Numerical Analysis of Rotor Systems with Aerostatic Journal Bearings

DISSERTATION

by

Antonín Skarolek

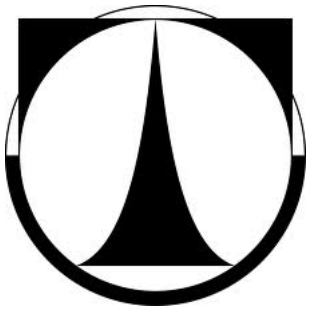

TECHNICAL UNIVERSITY OF LIBEREC

January 2012

Numerical Analysis of Rotor Systems with Aerostatic Journal Bearings

by

Antonín Skarolek

Supervisor: Doc. Ing. **Josef Mevald**, CSc., Technical University of Liberec, Liberec
Consultant: Ing. **Jan Kozánek**, CSc., Institute of Thermomechanics, CAS, Prague

Abstract:

This work delivers a set of mathematical tools for analysis of rotor systems supported in aerostatic journal bearings with special attention to thermal conditions of analysed system. Presented finite element thermo-hydrodynamic lubrication model of aerostatic bearings enables calculation of temperature distribution inside bearing air film and solid parts of rotor–bearing system. Test problem showed that the air film remains nearly isothermal, even if the average air film temperature is significantly higher than the ambient temperature as a result of power losses at high speed of journal. It also confirmed that Poiseuille part of the air flow does not contribute to increase of temperature. These findings suggest that isothermal bearing models are adequate, on condition that the average air film temperature is known. Steady state and transient isothermal hydrodynamic lubrication models of aerostatic bearings and a method of obtaining stiffness and damping coefficients corresponding to the lateral translational and angular displacements are also presented. Linearity of bearing models is discussed by means of obtained linear coefficients and by means of the response of the model to stochastic force excitation. This work also deals with reduction of defective, strongly gyroscopic rotor systems. Reduction of these systems is desirable for direct numerical integration of equations of motion of rotor supported by nonlinear bearings. Suitability of three feasible methods is evaluated.

Key words:

THDL, Thermo-hydrodynamic lubrication, Aerostatic journal bearing, Reduction of defective systems, Timoshenko rotating beam

Numerická analýza rotorových soustav s aerostatickými radiálními ložisky

Antonín Skarolek

Školitel: Doc. Ing. **Josef Mevald**, CSc., Technická univerzita v Liberci, Liberec
Konzultant: Ing. **Jan Kozánek**, CSc., Ústav Termomechaniky, ČAV, Praha

Abstrakt:

Tato práce přináší soubor matematických nástrojů pro analýzu rotorových soustav uložených v aerostatických radiálních ložiskách se zvláštním zřetelem na teplotní podmínky analyzovaného systému. Předložený konečněprvkový model termo-hydrodynamického mazání aerostatického ložiska umožňuje výpočet rozložení teploty uvnitř vzduchového filmu a pevných částí systému rotoru a ložiska. Testovací úloha ukázala, že vzduchový film zůstává téměř izotermický i tehdy, když je jeho průměrná teplota výrazně vyšší než teplota okolí v důsledku ztrátového výkonu při vysoké rychlosti čepu hřídele. Také potvrdila, že Poiseuilleova část proudění vzduchu nepřispívá ke zvýšení teploty. Tyto poznatky naznačují, že izotermické modely jsou vhodné za předpokladu známé průměrné teploty vzduchového filmu. Dále jsou prezentovány statické a dynamické modely isotermického hydrodynamického mazání aerostatických ložisek a metoda získání koeficientů tuhosti a tlumení odpovídajících bočním translačním a úhlovým výchylkám. Linearita modelu ložisek je diskutována pomocí získaných lineárních charakteristik a odezev dynamického modelu ložisek na stochastické silové buzení. Tato práce se také zabývá redukcí defektivních, silně gyroskopických rotorových soustav, jež je žádoucí pro přímé numerické řešení pohybových rovnic rotoru uloženého v nelineárních ložiskách. Hodnocena je vhodnost tří možných metod.

Klíčová slova:

THDL, Termo-hydrodynamické mazání, Aerostatické radiální ložisko, Redukce defektivních soustav, Timošenkův rotující nosník

Acknowledgments

At this point, I would like to thank all those who contributed to the creation of this work. First of all, I would like to thank my wonderful family that supported me throughout my studies from the beginning until now. I am also grateful to my supervisor Assoc. Prof. Josef Mevald for generous guidance of my work, number of valuable advice, fruitful discussions and moral support in difficult moments of this dissertation. To the consultant, Dr. Jan Kozánek, I am indebted for countless visits at his workplace. He was selflessly devoting time for many years and have passed down valuable knowledge and experience, from which I can profit for the rest of my life. Without the help of both, this work could not have been created. I would like to thank Dr. Jiří Šimek for provision of literature and consultations in the field of aerostatic bearings. Invaluable were also friendly discussions with Dr. Michal Hajžman, not only on rotor dynamics, but on the current applied science in general. I am obliged to him for providing valuable literature sources. I thank Ms Whitney Tallarico for friendly help with the English language. My thanks also belong to numerous former and current colleagues, whose friendly attitude and engineering enthusiasm have always been inspiring. Because of their large number and concerns that I might wrongfully omit someone, I hereby thank them all at once.

Poděkování

Na tomto místě bych rád poděkoval všem těm, kteří přispěli ke vzniku této práce. Na prvním místě bych rád poděkoval své skvělé rodině, která mě podporovala po celou dobu od počátků mých studií až doposud. Jsem též vděčen svému školiteli Doc. Ing. Josefu Mevaldovi, CSc. za velkorysé vedení mé práce, množství cenných rad, plodných diskuzí a morální podporu v těžších momentech vzniku této disertační práce. Konzultantovi, Ing. Janu Kozánkovi, CSc., jsem zavázán za bezpočet návštěv v jeho pracovišti, během kterých se mi po mnoho let nezištně věnoval a předával mi cenné zkušenosti a vědomosti, ze kterých mohu čerpat po zbytek života. Bez pomoci obou by tato práce nemohla nikdy vzniknout. Ing. Jiřímu Šimkovi, CSc. bych chtěl poděkovat za poskytnutí literatury a konzultace v oblasti aerostatických ložisek. Neocenitelné byly též přátelské diskuze s Dr. Michalem Hajžmanem, a to nejen o rotorové dynamice, ale o současné aplikované vědě obecně. I jemu jsem zavázán za poskytnutí cenných literárních pramenů. Slečně Whitney Tallarico děkuji za přátelskou pomoc s anglickým jazykem. Můj dík patří i bezpočtu bývalým i současným kolegům, jejichž přátelský přístup a inženýrské nadšení vždy byly inspirující. Vzhledem k jejich velkému počtu a obavám, abych nikoho neprávem neopomněl, jim tímto děkuji všem najednou.

Contents

List of Figures

Nomenclature

Symbol	Dimension	Description
$A(x)$	m^2	Cross section area
c	m	Radial bearing clearance
c_o	1	Discharge coefficient
c_p	$\mathrm{J\,kg^{-1}\,K^{-1}}$	Isobaric specific heat
c_v	$\mathrm{J\,kg^{-1}\,K^{-1}}$	Isochoric specific heat capacity
E	Pa	Young modulus of elasticity
$\mathbf{f}$	$\mathrm{Pa\,m^{-1}}$	External volume force
G	Pa	Shear modulus of elasticity
G_{x_1}, G_{x_2}	1	Turbulence coefficients
h	m	Thickness of fluid film
h_b	$\mathrm{W\,m^{-2}\,K^{-1}}$	Bushing heat convection rate
h_j	$\mathrm{W\,m^{-2}\,K^{-1}}$	Journal heat convection rate
i	$\mathrm{J\,kg^{-1}}$	Specific enthalpy
j	1	Imaginary unit; $j = \sqrt{-1}$
$J(x)$	m^4	Polar moment of inertia
k	$\mathrm{W\,m^{-1}\,K^{-1}}$	Heat conductivity
k_b	$\mathrm{W\,m^{-1}\,K^{-1}}$	Bushing heat conductivity
k_j	$\mathrm{W\,m^{-1}\,K^{-1}}$	Journal heat conductivity
k_l	$\mathrm{W\,m^{-1}\,K^{-1}}$	Lubricant heat conductivity
Kn	1	Knudsen number
L	m	Bearing length
$\dot{m}_i$	$\mathrm{kg\,s^{-1}}$	Inlet mass flow
$\dot{m}_{it}$	$\mathrm{kg\,s^{-1}}$	Theoretic inlet mass flow
p	Pa	Pressure
p_a	Pa	Ambient pressure
p_s	Pa	Supply pressure
P	Pa	Dimensionless pressure
Pr	1	Prandtl number
Q_d	W	Dissipative heat rate
r	$\mathrm{J\,kg^{-1}\,K^{-1}}$	Specific gas constant
R	m	Radius of bearing
Re_c	1	Couette Reynolds number
Re_s	1	Squeeze Reynolds number
t	s	Time

T	K	Temperature
Ta	1	Taylor number
T_i	K	Inlet temperature
T_r	K	Reference temperature
$u(x)$	m	Axial displacement
$\mathbf{v} = (v_1, v_2, v_3)$	$\mathrm{m\,s^{-1}}$	Velocity
v_ξ, v_η, v_ζ	1	Dimensionless velocities
$v(x)$, $w(x)$	m	Lateral displacements
$\mathbf{V} = (U, V)^{\mathrm{T}}$	$\mathrm{m\,s^{-1}}$	Boundary velocity
α_H	1	Hysteretic damping coefficient
α_v	1	Viscous damping coefficient
β^*	1	Critical pressure ratio
δ_{ij}	1	Kronecker delta
Δt	s	Time step
κ	Pa s	Bulk viscosity (Chapter 1)
κ	1	Shear correction coefficient (Chapter 2)
κ	1	Ratio of specific heats (Exc. chapter 1&2)
λ	Pa s	Second viscosity
λ_f	m	Mean free path of gas particles
Λ	1	Bearing (compressibility) number
μ	Pa s	Dynamic viscosity
μ_r	Pa s	Reference viscosity
ν	1	Poisson constant
ξ, η, ζ	1	Dimensionless spatial coordinates
ρ	$\mathrm{kg\,m^{-3}}$	Density
τ	1	Dimensionless time
τ_{ij}	Pa	Stress tensor
τ_S	Pa	Mean shear stress
$\tau(y, z)$	Pa	Shear stress
τ'_{ij}	Pa	Deviatoric stress tensor component
$\varphi(x)$	1	Angle of torsional rotation
Φ	$\mathrm{W\,m^{-3}}$	Dissipation function (Exc. chapter 2)
Φ	1	Shear deformation coefficient (Chapter 2)
$\psi(x)$, $\vartheta(x)$	1	Angles of lateral rotations
ω	$\mathrm{s^{-1}}$	Journal angular velocity (Exc. pages 18–64)
ω	$\mathrm{s^{-1}}$	Excitation angular velocity (Pages 18–64)
ω_0	$\mathrm{s^{-1}}$	Shaft angular velocity

Chapter 1

Introduction

1.1 The Air Lubrication

It has been over 150 years since Gustaph Adolph Hirn published results of his experimental work with bearing friction using various lubricants, having been the first who observed that air might behave as sufficient lubricant. Several decades later Albert Kingsbury performed his impressive experiments with externally pressurized air bearing. The physical explanation of load-carrying capacity of fluid film during hydrodynamic lubrication based on work of Osborne Reynolds is also known for over one century. Despite the long period since the first valuable experiments were carried out as well as their physical explanation was provided, there were practically no applications using air bearings until second half of twentieth century [1]. The precise manufacture with close tolerances, necessary for air bearings production, together with the lack of practical design directions were the main reasons restraining them from broader practical introduction. Meantime, the improving quality of steel materials used for rolling element bearings allowed them to prevail over classical journal bearings and later even other plain joints, which trend continues and is noticeable even today for instance in machining tool and turbo-machinery industry. However the rolling element bearings were great improvement against plain bearings and still experience evolution, there are certain borders difficult to pass. Thermal behaviour, bearing endurance and life of rolling element bearings are some of the limiting factors at very high speed of modern machinery [2],[3]. Nonlinear microscopic behaviour of the rolling elements [4] means another limitation with respect to increasing demands for ultra-precision operation [5]. Gas bearings offer noticeable benefits, especially for ultra-precise and very fast applications.

Gas bearings can be divided into two basic categories. Bearings operating exclusively on the principle of hydrodynamic lubrication are referred to as aerodynamic or self-acting bearings. These bearings use the pressure profile of lubricant within wedge shaped clearance that is formed by means of reciprocal movement of moving and static body. They do not need external supply of pressurized gas, but can only operate after exceeding certain speed of relative motion of parts that generate the wedge gap. Their apparent advantage of low running

cost is counterbalanced by inability of operation at rest, generally low carrying capacity and stiffness in comparison with aerostatic bearings. Aerostatic bearings, also referred to as externally pressurized bearings, work with supply of pressurized gas incoming into narrow gap between two surfaces, where the gas consequently expands and leaves the bearing. These bearings operate at rest as well as during reciprocal motion of both faces.

The previously mentioned effect of hydrodynamic lubrication also takes place in the case of aerostatic bearings at higher speed. It may even dominate the bearing load. This principle is utilized in hybrid bearings that operate with supply of pressurized gas at low speed, but act as aerodynamic bearings at operational conditions. Compressed gas can be delivered only during start up and shut down. These hybrid bearings commonly incorporate surface features, for instance the so-called herringbone grooves on journal surface.

1.1.1 Aerodynamic Journal Bearings

From the geometry point of view, the basic aerostatic journal bearings are similar to oil-operating hydrodynamic bearings. However, the working substance has significantly different properties. Liquids have bulk modulus higher of several orders of magnitude than gases. Whilst the liquids are often treated as incompressible continuum, the gases have bulk modulus dependent on pressure. Viscosity of gases is also substantially smaller than viscosity of liquids and it increases with temperature. Another considerable distinction from oil-operating bearings is the absence of gaseous and vaporous cavitation. Aerostatic bearings require smaller clearances between sliding surfaces than oil bearings while offering a fraction of their damping abilities, therefore a special attention must be paid to dynamic stability of the bearing system. Without the presence of liquid lubricant even short contact of parts at full speed can end up with severe damage of precision surfaces. Aerodynamic bearings often necessitate special materials in order to capable of dry run during start up and shut down phase.

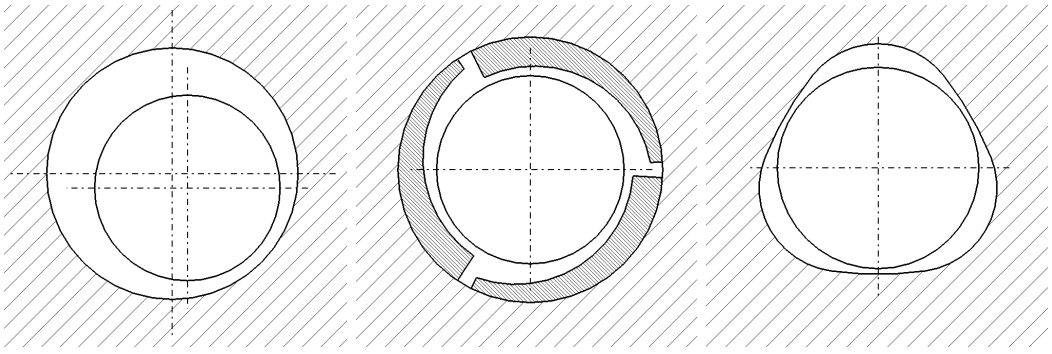

Figure 1.1: a) Plain Bearing, b) Fixed-Pad Bearing, c) Multilobe Bearing

Fig. 1.1 shows three shapes of bearings with rigid geometry. Plane aerodynamic bearings overpay their simplest geometry by very low load capacity for bigger clearances and tendencies to unstable behaviour. Application of this design is typically restricted to very light

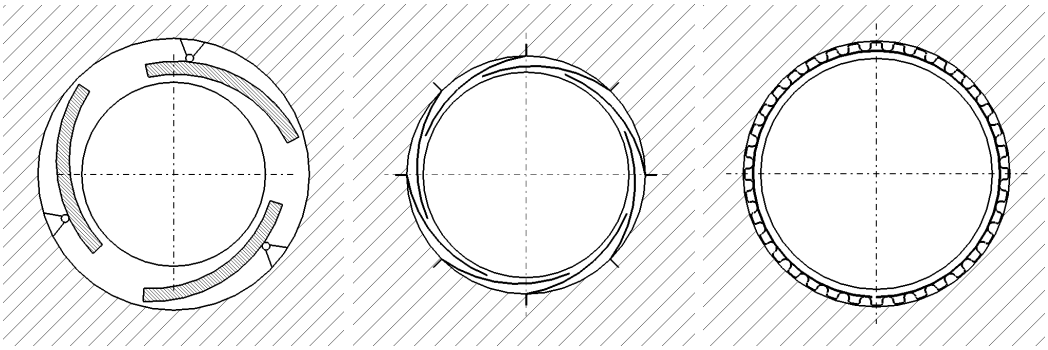

Figure 1.2: a) Tilting Pad Bearing, b) Multileaf Bearing, c) Bump Foil Bearing

rotors. The work of Piekos [6] provides performance study of plain bearings used in MEMS (Micro-Electro-Mechanical-Systems), where the implementation of more complex bearing geometries is limited by manufacturing process. Another study of micro bearing combining thrust and journal faces can be found in [7]. For larger, but still rather light devices, journal with so-called herringbone grooves is often used in order to improve the stability of plain bearing [8, 9]. The two remaining schemes in the figure 1.1 present geometrically preloaded bearings. The preload is ensured by multiple wedge shape.

Fig. 1.2 depicts three types of aerodynamic journal bearings with variable geometry. The tilting pad bearing design is already widely used in broad range of machinery. Authors Šimek et al. [10] present the use of tilting pad journal bearings and spiral groove thrust bearing system in several industrial applications ranging from the size of 80 g turbine expander for helium liquefaction running on 350,000 rpm to 100 kW industrial turboblower. The more recent aerodynamic bearing designs incorporate thin foils to allow accommodation of the film thickness to actual conditions of the bearing. A flexible element that acts as one of the sliding faces improves the load capacity and allows journal to move on orbits exceeding in radius the base clearance [11]. The foil bearings may incorporate multiple foil leafs [12] or the corrugated (often called bump) foil covered by plain top foil [13]. Both of the mentioned cases use the foils configurations, where the deflection of foil is caused by bending, instead of foil tension that was used in older foil bearings [14]. Further improvements on the bump foil bearings are available. For instance, the bearings that use multiple layers of corrugated foils that provides a piecewise stiffness support to the top foil [15], or bearings with viscoelastic foil made from acrylic polymers inserted between corrugated and top foil in order to ensure higher damping of bearing [16]. The top foil is in contact with journal during run up and shut down, therefore an appropriate foil coating is necessary, primarily for high temperature operating bearings [17].

1.1.2 Aerostatic Journal Bearings

Aerostatic bearings generate load capacity by means of gas pressure, which is supplied from the outside of bearing. Gas flows to the area of bearing gap via feeding system of orifices or flows through porous material, see fig. 1.3. The gas is throttled within the narrow gap. Actual thickness of the air film corresponds with resistance against air flow out of the bearing and thus with local magnitude of pressure. These bearings work exclusively on this principle at low speed of journal. At higher speed, the aerodynamic effect increases the bearing load, but also promotes instability of the bearing. Aerostatic bearings can also incorporate a noncircular shape design, similarly to the aerodynamic bearings, in order to deal with instability at high speed. Other problems may be caused by inappropriate arrangement of feeding system, when instability called pneumatic hammer may occur. This is typical for bearings with pocketed orifices. Experimental investigation of pneumatic hammer on orifice-compensated air bearings can be found in the work of Talukder and Stowell [18]. Porous aerostatic bearings are generally less prone to this phenomenon.

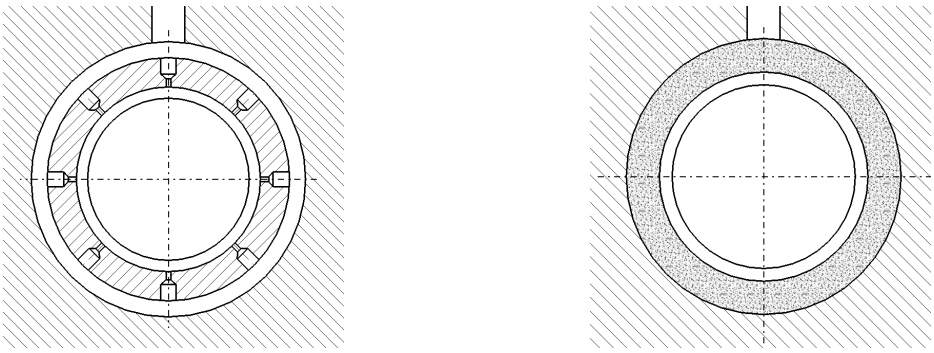

Figure 1.3: a) Aerostatic bearing with simple orifices, b) Porous aerostatic bearing

The necessity of delivering pressurized gas is the biggest drawback of aerostatic bearings. Beside the purchase costs of an aggregate that produces sufficient amount pressurized air the energy consumed by this process means significant expenses. Compared to the aerodynamic bearings, we additionally get feasibility of running the bearings at zero journal speed, higher and controllable stiffness and load capacity. Flow of the compressed air through the bearing also helps in dirt removal from the working space of the bearing. High stiffness and precision, together with feasibility of running at high speed practically without mechanical wear, are the main advantages of aerostatic bearings.

1.2 Fundamentals of Lubrication Theory

1.2.1 Navier–Stokes Equations

Navier–Stokes equations are fundamental equations of viscous fluid dynamics. Consecutive assumptions and simplifications relevant to specific conditions of bearings lead to Reynolds equation of classical lubrication theory. This way of deriving Reynolds equation allows us to observe all simplifications along the process and to judge their validity. The Navier–Stokes equations are represented by set of three components of momentum transfer [19]:

$$\rho\left(\frac{\partial \mathbf{v}}{\partial t}+\mathbf{v}\cdot\nabla\mathbf{v}\right)=-\nabla p+\nabla\cdot\tau'_{ij}+\mathbf{f}. \tag{1.1}$$

The volume inertia forces on the left-hand side consist of density ρ multiplied by acceleration written as a convective derivative of velocity $\mathbf{v}$. This force is equal to the sum of the external volume forces $\mathbf{f}$ and the surface forces acting upon boundaries of volume element. These forces can be separated into normal and tangential components. The former are represented by pressure gradient, the latter by tensor derivative of deviatoric stress tensor τ'_{ij}. For assumed Newtonian fluid, the stress tensor is established as a linear function of strain rates

$$\tau'_{ij}=\mu\left(\frac{\partial v_i}{\partial x_j}+\frac{\partial v_j}{\partial x_i}\right)+\delta_{ij}\lambda\nabla\cdot\mathbf{v}, \tag{1.2}$$

where symbol μ is dynamic viscosity; λ is coefficient of second viscosity. δ_{ij} means Kronecker delta. Assuming those coefficients constant, the term for coefficient of second viscosity: $\lambda=\kappa-\frac{2}{3}\mu$, the momentum equation can be rewritten to

$$\rho\left(\frac{\partial \mathbf{v}}{\partial t}+\mathbf{v}\cdot\nabla\mathbf{v}\right)=-\nabla p+\mu\Delta\mathbf{v}+\left(\kappa+\frac{1}{3}\mu\right)\nabla\left(\nabla\cdot\mathbf{v}\right)+\mathbf{f}. \tag{1.3}$$

The third term on the right-hand side is called second viscosity term, κ is called bulk coefficient of viscosity. Bulk coefficient of viscosity κ can be left out, so the second viscosity term becomes $\lambda=-\frac{2}{3}\mu$. This is exact for monoatomic gases, although it is usually used for viscous fluids regardless to internal structure [19]. In cited book, this simplification is explained by following contemplation. Full stress tensor τ_{ij} is a sum of its deviatoric and hydrostatic components. Deviatoric part of tensor τ'_{ij} is defined as equation (1.2). From Navier–Stokes equation (1.1), we can see that full stress tensor is

$$\tau_{ij}=-\delta_{ij}\,p+\tau'_{ij}=-\delta_{ij}\,p+\mu\left(\frac{\partial v_i}{\partial x_j}+\frac{\partial v_j}{\partial x_i}\right)+\delta_{ij}\lambda\nabla\cdot\mathbf{v}. \tag{1.4}$$

Contraction of stress tensor provides invariant

$$\tau_{ii}=\tau_{11}+\tau_{22}+\tau_{33}=-3\,p+(3\,\lambda+2\,\mu)\,\frac{\partial\,v_j}{\partial\,x_j}. \tag{1.5}$$

Last term $\frac{\partial v_j}{\partial x_j}$ is velocity divergence (Einstein summation convention is used in this work, unless it is explicitly emphasized otherwise), which essentially equals zero for incompressible fluids. In that case, it can be said that the local pressure is negative mean value of principle stresses or mean value of normal stresses acting upon any three perpendicular planes at given point. Should this requirement be satisfied even for compressible viscous fluid, the second viscosity must follow

$$\lambda = -\frac{2}{3}\,\mu. \tag{1.6}$$

The other equations of viscous fluid dynamics are the continuity equation expressing conservation of mass

$$\frac{\partial \rho}{\partial t} + \nabla \cdot (\rho \mathbf{v}) = 0, \tag{1.7}$$

and the conservation of total energy, written in differential form Brdička et al. [19]:

$$\rho c_v \left(\frac{\partial T}{\partial t} + \mathbf{v} \cdot \nabla T \right) - \frac{p}{\rho} \left(\frac{\partial \rho}{\partial t} + \mathbf{v} \cdot \nabla \rho \right) = \nabla \cdot (k \nabla T) + \Phi, \tag{1.8}$$

where k is heat conductivity, c_v isochoric heat capacity and Φ dissipation function

$$\Phi = \lambda (\nabla \cdot \mathbf{v})^2 + 2\mu e_{ij}^{\cdot} e_{ij}^{\cdot}, \qquad e_{ij}^{\cdot} = \frac{1}{2} \left(\frac{\partial v_i}{\partial x_j} + \frac{\partial v_j}{\partial x_i} \right). \tag{1.9}$$

The above energy conservation equation can be expressed in terms of specific enthalpy i (assuming that continuum obeys state equation of ideal gas)

$$\rho \left(\frac{\partial i}{\partial t} + \mathbf{v} \cdot \nabla i \right) = \frac{\partial p}{\partial t} + \mathbf{v} \cdot \nabla p + \nabla \cdot (k \nabla T) + \Phi. \tag{1.10}$$

Dissipation function broken down to its components:

$$\begin{aligned} \Phi = \mu \Bigg(& 2 \left(\frac{\partial v_1}{\partial x_1} \right)^2 + 2 \left(\frac{\partial v_2}{\partial x_2} \right)^2 + 2 \left(\frac{\partial v_3}{\partial x_3} \right)^2 + \left(\frac{\partial v_2}{\partial x_1} + \frac{\partial v_1}{\partial x_2} \right)^2 + \left(\frac{\partial v_3}{\partial x_2} + \frac{\partial v_2}{\partial x_3} \right)^2 + \\ & + \left(\frac{\partial v_1}{\partial x_3} + \frac{\partial v_3}{\partial x_1} \right)^2 \Bigg) + \lambda (\nabla \cdot \mathbf{v})^2. \end{aligned} \tag{1.11}$$

Ideal gas equation of state provides relation among density, pressure and temperature

$$p = \rho\, r\, T, \tag{1.12}$$

where r is specific gas constant, for dry air $r = 286.7\,\mathrm{J\,kg^{-1}K^{-1}}$. Material properties for specific continuum material enclose entire system.

The complex set of equations described above is to be simplified by relevant preconditions. Assumption of isothermal flow leads to omission of the equation (1.8). By substitution to density from ideal gas equation of state, the Navier–Stokes equations of isothermal flow and

the mass conservation become

$$\frac{p}{r\,T}\left(\frac{\partial \mathbf{v}}{\partial t}+\mathbf{v}\cdot\nabla\mathbf{v}\right)=-\nabla p+\mu\Delta\mathbf{v}+\frac{1}{3}\mu\nabla\left(\nabla\cdot\mathbf{v}\right)+\mathbf{f}, \tag{1.13}$$

$$\frac{\partial p}{\partial t}+\nabla\cdot(p\mathbf{v})=0. \tag{1.14}$$

1.2.2 Stokes Flow

Considering only flow with low Reynolds number, we are allowed to leave out nonlinear advective term of acceleration. Remaining members of Navier–Stokes equations (1.13) form unsteady Stokes equations for compressible flow

$$\frac{p}{r\,T}\frac{\partial \mathbf{v}}{\partial t}=-\nabla p+\mu\Delta\mathbf{v}+\frac{1}{3}\mu\nabla\left(\nabla\cdot\mathbf{v}\right)+\mathbf{f}. \tag{1.15}$$

Steady form of Stokes equation for compressible fluid become

$$\mathbf{0}=-\nabla p+\mu\Delta\mathbf{v}+\frac{1}{3}\mu\nabla\left(\nabla\cdot\mathbf{v}\right), \tag{1.16}$$

from (1.15) by not considering of external and inertia volume forces. Equation now represents balance of normal and shear surface forces, written in components related to individual coordinates:

$$0=-\frac{\partial p}{\partial x_1}+\mu\left(\frac{\partial^2 v_1}{\partial x_1^2}+\frac{\partial^2 v_1}{\partial x_2^2}+\frac{\partial^2 v_1}{\partial x_3^2}\right)+\frac{1}{3}\,\mu\left(\frac{\partial^2 v_1}{\partial x_1^2}+\frac{\partial^2 v_2}{\partial x_2\,\partial x_1}+\frac{\partial^2 v_3}{\partial x_3\,\partial x_1}\right), \tag{1.17}$$

$$0=-\frac{\partial p}{\partial x_2}+\mu\left(\frac{\partial^2 v_2}{\partial x_1^2}+\frac{\partial^2 v_2}{\partial x_2^2}+\frac{\partial^2 v_2}{\partial x_3^2}\right)+\frac{1}{3}\,\mu\left(\frac{\partial^2 v_1}{\partial x_1\,\partial x_2}+\frac{\partial^2 v_2}{\partial x_2^2}+\frac{\partial^2 v_3}{\partial x_3\,\partial x_2}\right), \tag{1.18}$$

$$0=-\frac{\partial p}{\partial x_3}+\mu\left(\frac{\partial^2 v_3}{\partial x_1^2}+\frac{\partial^2 v_3}{\partial x_2^2}+\frac{\partial^2 v_3}{\partial x_3^2}\right)+\frac{1}{3}\,\mu\left(\frac{\partial^2 v_1}{\partial x_1\,\partial x_3}+\frac{\partial^2 v_2}{\partial x_2\,\partial x_3}+\frac{\partial^2 v_3}{\partial x_3^2}\right). \tag{1.19}$$

1.2.3 Reynolds Equation

Balance of surface forces (1.16) does not contain external and inertia forces. Acceleration as an inertia volume force is justifiably omitted as long as Reynolds number keeps at low level. With respect to journal bearings, small ratio of clearance to bearing diameter is considered. Journal can experience very high speed, therefore the centripetal acceleration acting on dragged air can be enormous, but very small film thickness makes it radially almost uniform. Both the small thickness and low density of air make it negligible, as well as effect of gravity, which does not show measurable effect on technical proportions.

Thin fluid film orientation is depicted in the fig. 1.4. Thickness of the lubricant film is aligned to x_3 coordinate and it is assumed to be much smaller than the other two dimensions. Assuming these conditions, velocity derivatives with respect to the x_3 coordinate has

predominant effect in former two equations (1.17, 1.18). The third equation of momentum transfer (1.19) is omitted by presuming constant pressure across film thickness.

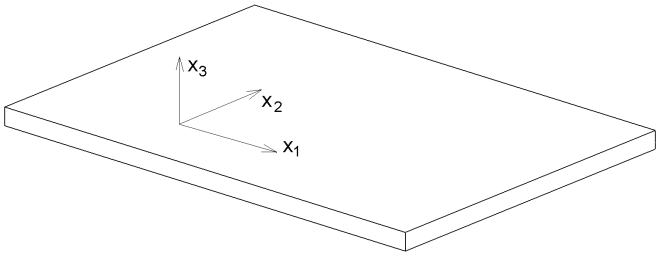

Figure 1.4: Orientation of thin fluid film

Equations (1.17, 1.18) are reduced to

$$\frac{\partial p}{\partial x_1} = \mu \frac{\partial^2 v_1}{\partial x_3^2}, \tag{1.20}$$

$$\frac{\partial p}{\partial x_2} = \mu \frac{\partial^2 v_2}{\partial x_3^2}. \tag{1.21}$$

These equations with help of continuity equation (1.14) are starting point for Reynolds equation. Introducing no-slip condition for velocities v_1, v_2 on boundaries of film $x_3 = 0$ and $x_3 = h(x_1, x_2, t)$

$$v_1 = 0, \quad v_2 = 0 \qquad for \qquad x_3 = 0, \tag{1.22}$$

$$v_1 = U, \quad v_2 = V \qquad for \qquad x_3 = h, \tag{1.23}$$

allows velocity profiles to be solved by integration of both equations:

$$v_1 = \frac{1}{2\,\mu} \frac{\partial p}{\partial x_1} \left(x_3^2 - h x_3 \right) + U \, \frac{x_3}{h}, \tag{1.24}$$

$$v_2 = \frac{1}{2\,\mu} \frac{\partial p}{\partial x_2} \left(x_3^2 - h x_3 \right) + V \, \frac{x_3}{h}. \tag{1.25}$$

Integration of continuity equation across thickness of fluid film

$$\int_0^h \frac{\partial p}{\partial t} \mathrm{d}x_3 + \int_0^h \left(\frac{\partial (p\, v_1)}{\partial x_1} + \frac{\partial (p\, v_2)}{\partial x_2} + \frac{\partial (p\, v_3)}{\partial x_3} \right) \mathrm{d}x_3 = 0 \tag{1.26}$$

with regard to that $h = h(x_1, x_2, t)$ yields

$$\frac{\partial}{\partial t}(ph) - p\frac{\partial h}{\partial t} + \frac{\partial}{\partial x_1}\left(p\int_0^h v_1 \,\mathrm{d}x_3\right) - p\frac{\partial h}{\partial x_1}\cdot v_1\Big|_h + \frac{\partial}{\partial x_2}\left(p\int_0^h v_2 \,\mathrm{d}x_3\right) - p\frac{\partial h}{\partial x_2}\cdot v_2\Big|_h + p\cdot v_3\Big|_h - p\cdot v_3\Big|_0 = 0. \tag{1.27}$$

Boundary conditions for v_1 and v_2 are already established and then

$$v_3\Big|_0 = 0, \quad v_3\Big|_h = \frac{\partial h}{\partial t} + \frac{\partial h}{\partial x_1}U + \frac{\partial h}{\partial x_2}V. \tag{1.28}$$

The equation (1.27) leads after integration to Reynolds equation of classical lubrication theory

$$\frac{\partial}{\partial t}(ph) + \frac{1}{2}\frac{\partial}{\partial x_1}(phU) + \frac{1}{2}\frac{\partial}{\partial x_2}(phV) - \frac{1}{12\mu}\left(\frac{\partial}{\partial x_1}\left(ph^3\frac{\partial p}{\partial x_1}\right) + \frac{\partial}{\partial x_2}\left(ph^3\frac{\partial p}{\partial x_2}\right)\right) = 0, \tag{1.29}$$

which can be written in vector notation:

$$\frac{\partial}{\partial t}(ph) = \frac{1}{12\mu}\nabla\cdot\left(ph^3\nabla p\right) - \frac{1}{2}\nabla\cdot(ph\mathbf{V}), \tag{1.30}$$

where $\mathbf{V} = (U, V)^{\mathrm{T}}$ is vector of top surface velocities. The derived Reynolds equation is nonlinear because of pressure term p in the first divergence of the right-hand side of (1.30).

If mass conservation law for incompressible flow $\nabla\cdot\mathbf{v} = 0$ is used, the Reynolds equation turnes into simpler elliptic linear form

$$0 = \frac{1}{12\mu}\nabla\cdot\left(h^3\nabla p\right) - \frac{1}{2}\nabla\cdot(h\mathbf{V}) - \frac{\partial h}{\partial t}, \tag{1.31}$$

referred to as Reynolds equation for incompressible fluid or less formal as *incompressible* Reynolds equation. There is no term of pressure time derivative in the equation (1.31). This equation cannot be directly used for gas bearings due to high velocities of air and big variations of pressure and density within air film.

1.3 Limitations of Classical Reynolds Equation in Air Lubrication Problems

Reynolds equation is widely used in lubrication theory and belongs to well studied problems. Two dimensional form makes it computationally friendly, but it should be borne on mind that results obtained from (1.29) are trustworthy only as far as respective conditions are satisfied. Following list shows all the prerequisites to Reynolds equation in previous section:

1. Fluid is Newtonian
2. State equation of ideal gas is valid for used fluid
3. Fluid behaves as continuum; no-slip condition on top and bottom boundary surfaces is valid
4. The inertia and body forces are negligibly small against viscous and pressure forces, the flow is laminar
5. The fluid film thickness is small compared to lateral dimensions, pressure is assumed constant across fluid film, gradient of velocity is strongly dominant in direction of film thickness
6. The processes in the film are isothermal, viscosity is independent to pressure and is therefore constant

Assumptions number 1 and 2 have appeared valid for air over wide range of conditions. The other limitations are less apparent. The premise 3, which expects air to act as a continuum is reasonable at large scale, where mean free path of molecules is insignificant compared to spatial dimensions. In view of small air film thickness an effect of particular structure may become important. Points 4 and 5 are basically conditions on bearing geometry. Air velocity in the bearings can approach very high speed and small thickness of fluid film is needed to ensure that Reynolds number is low enough. Thin film is also required to reduce three dimensional problem to the two dimensional one. The last item on the list is the assumption saying that only isothermal processes occur in the air film. Heat conduction is expected to effectively carry out dissipative heat from the fluid to material of journal and bush. Uniform temperature is expected across thickness as well as along circumferential and axial coordinates.

1.3.1 Rarefaction

For very narrow gaps, where the mean free path of air particles becomes significant, the gaseous rarefaction must be taken into account. Gas dynamics cannot be directly described by continuum transport. Measure of rarefaction effect is described by Knudsen number as the ratio between the mean free path of gas particles and the characteristic length.

$$Kn = \frac{\lambda_f}{h}. \tag{1.32}$$

Mean free path λ_f is inversely proportional to pressure p and thus

$$Kn = \frac{\lambda_{f0}\, p_0}{h\, p}, \tag{1.33}$$

where λ_{f0} is the mean free path at pressure p_0.

Value of Knudsen number is commonly used to classify rarefied gas flow into several regimes. Continuum flow for $Kn < 0.01$, molecular flow for $Kn > 10$ and transitional between those limits. Transitional regime with lower Knudsen numbers $Kn < 0.1$ is often called slip-flow regime, where continuum approach is still used, but no-slip boundary condition for velocity is no longer considered.

As can be seen from (1.33), the meaning of term *very narrow gap* changes with air pressure. Mean free path for air at normal atmospheric conditions is approximately $\lambda_{f0} = 80\,\mathrm{nm}$. Fig. 1.5 shows critical characteristic lengths for pressure range typical for gas bearings. Relevant to viscous flow regime, the critical thickness is approximately 8μm at atmospheric pressure. This value is satisfied for most of common sized bearings, in view of the fact that the minimum pressure in the bearing occurs at the location of maximum film thickness, but it is usually exceeded in case of MEMS devices.

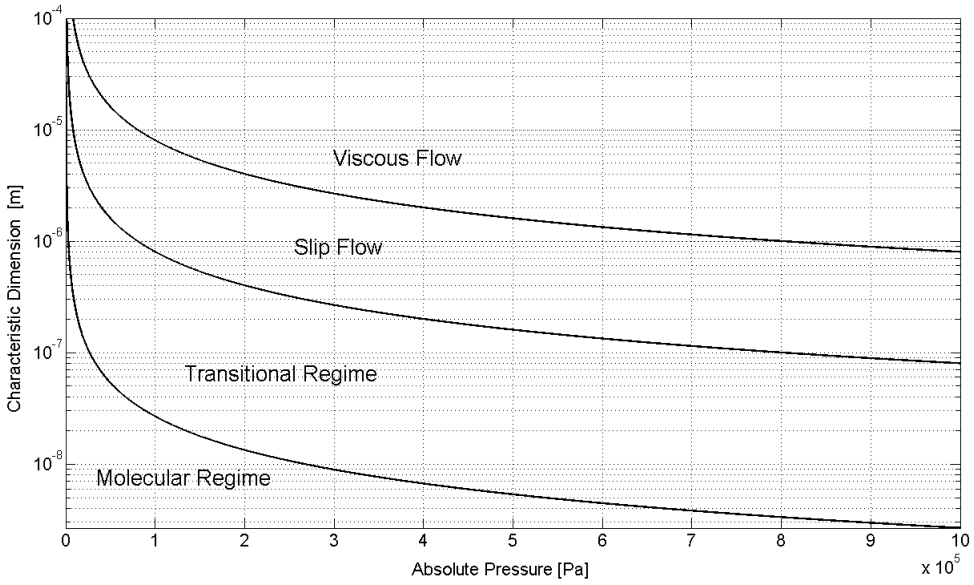

Figure 1.5: Rarefaction: flow regimes

Many slip flow models of various capabilities of describing flow at high Knudsen numbers have been developed. After integration of continuum equation with new velocity profiles, the effective viscosity is often utilized to Reynolds equation as a nonlinear function of Knudsen number. Alternative ways to obtain effective viscosity are to use Boltzmann equation or experimental data fitting. List of models of effective viscosity can be found in dissertation of Younis [20].

Introduction of slip velocity on the boundaries as a function of Knudsen number is also used in generalized models. Multi-coefficient slip-corrected Reynolds equation in comparison with slip models up to the second order is presented in the work of Ng and Liu [21]. Cited model is claimed suitable at wide range of Knudsen number covering slip to transition regimes.

1.3.2 Inertial Forces versus Film Thickness

To justify elimination of inertia from momentum transport, it is useful to introduce following dimensionless variables:

$$\xi = \frac{x_1}{R}, \quad \eta = \frac{x_2}{R}, \quad \zeta = \frac{x_3}{c}, \quad \tau = \omega\, t. \tag{1.34}$$

To keep the system consistent, then dimensionless velocities should be

$$v_\xi = \frac{v_1}{R\,\omega}, \quad v_\eta = \frac{v_2}{R\,\omega}, \quad v_\zeta = \frac{v_3}{c\,\omega}. \tag{1.35}$$

Dimensionless pressure can be set independently as

$$P = \frac{p}{p_a}, \tag{1.36}$$

where p_a is reference pressure. It may be the ambient pressure or the feeding pressure in the case of aerostatic bearings. For our general purpose, it is convenient to use the standard atmospheric pressure. All of dimensionless variables should be of the same order of magnitude of 1.

Substitution of newly introduced variables into continuity equation (1.14) shows that the equation preserves its general form

$$\frac{\partial\, P}{\partial\, \tau} + \frac{\partial\, P\, v_\xi}{\partial\, \xi} + \frac{\partial\, P\, v_\eta}{\partial\, \eta} + \frac{\partial\, P\, v_\zeta}{\partial\, \zeta} = 0. \tag{1.37}$$

Now, the Navier–Stokes equations (1.13) can be written by means of dimensionless variables:

$$\rho\,\frac{\omega\, c^2}{\mu}\left(\frac{\partial\, v_\xi}{\partial\, \tau} + v_\xi\frac{\partial\, v_\xi}{\partial\, \xi} + v_\eta\frac{\partial\, v_\xi}{\partial\, \eta} + v_\zeta\frac{\partial\, v_\xi}{\partial\, \zeta}\right) = -\frac{p_a\, c^2}{R^2\,\mu\,\omega}\frac{\partial P}{\partial \xi} + \frac{\partial^2 v_\xi}{\partial \zeta^2} + \frac{c^2}{R^2}\left(\frac{\partial^2 v_\xi}{\partial \xi^2} + \frac{\partial^2 v_\xi}{\partial \eta^2}\right) + \frac{c^2}{3\,R^2}\left(\frac{\partial^2 v_\xi}{\partial \xi^2} + \frac{\partial^2 v_\eta}{\partial \eta\,\partial \xi} + \frac{\partial^2 v_\zeta}{\partial \zeta\,\partial \xi}\right), \tag{1.38}$$

$$\rho\,\frac{\omega\, c^2}{\mu}\left(\frac{\partial\, v_\eta}{\partial\, \tau} + v_\xi\frac{\partial\, v_\eta}{\partial\, \xi} + v_\eta\frac{\partial\, v_\eta}{\partial\, \eta} + v_\zeta\frac{\partial\, v_\eta}{\partial\, \zeta}\right) = -\frac{p_a\, c^2}{R^2\,\mu\,\omega}\frac{\partial P}{\partial \eta} + \frac{\partial^2 v_\eta}{\partial \zeta^2} + \frac{c^2}{R^2}\left(\frac{\partial^2 v_\eta}{\partial \xi^2} + \frac{\partial^2 v_\eta}{\partial \eta^2}\right) + \frac{c^2}{3\,R^2}\left(\frac{\partial^2 v_\xi}{\partial \xi\,\partial \eta} + \frac{\partial^2 v_\eta}{\partial \eta^2} + \frac{\partial^2 v_\zeta}{\partial \zeta\,\partial \eta}\right), \tag{1.39}$$

$$\rho\,\frac{\omega\, c^2}{\mu}\left(\frac{\partial\, v_\zeta}{\partial\, \tau} + v_\xi\frac{\partial\, v_\zeta}{\partial\, \xi} + v_\eta\frac{\partial\, v_\zeta}{\partial\, \eta} + v_\zeta\frac{\partial\, v_\zeta}{\partial\, \zeta}\right) = -\frac{p_a}{\mu\, c}\frac{\partial P}{\partial \zeta} + \frac{\omega}{c}\frac{\partial^2 v_\zeta}{\partial \zeta^2} + \frac{c\,\omega}{R^2}\left(\frac{\partial^2 v_\zeta}{\partial \xi^2} + \frac{\partial^2 v_\zeta}{\partial \eta^2}\right) + \frac{\omega}{3\,c}\left(\frac{\partial^2 v_\xi}{\partial \xi\,\partial \zeta} + \frac{\partial^2 v_\eta}{\partial \eta\,\partial \zeta} + \frac{\partial^2 v_\zeta}{\partial \zeta^2}\right). \tag{1.40}$$

Right-hand sides of first two momentum equations contain terms multiplied by $\frac{c^2}{R^2}$. Typical value of ratio between clearance and radius is approximately 0.001. Square of this ratio is negligibly small compared to 1 or even to the value of $\frac{p_a\, c^2}{R^2\, \mu\, \omega}$. Effect of second viscosity and shear stress in plane of film layer would become significant if $p_a \sim \mu\, \omega$. Common conditions are far from this relation. In the last equation, pressure gradient strongly dominates over many orders of magnitude, thus momentum transport becomes

$$Re_s \left(\frac{\partial\, v_\xi}{\partial\, \tau} + v_\xi \frac{\partial\, v_\xi}{\partial\, \xi} + v_\eta \frac{\partial\, v_\xi}{\partial\, \eta} + v_\zeta \frac{\partial\, v_\xi}{\partial\, \zeta} \right) = -\frac{6}{\Lambda} \frac{\partial P}{\partial \xi} + \frac{\partial^2 v_\xi}{\partial \zeta^2}, \tag{1.41}$$

$$Re_s \left(\frac{\partial\, v_\eta}{\partial\, \tau} + v_\xi \frac{\partial\, v_\eta}{\partial\, \xi} + v_\eta \frac{\partial\, v_\eta}{\partial\, \eta} + v_\zeta \frac{\partial\, v_\eta}{\partial\, \zeta} \right) = -\frac{6}{\Lambda} \frac{\partial P}{\partial \eta} + \frac{\partial^2 v_\eta}{\partial \zeta^2}, \tag{1.42}$$

$$0 = \frac{\partial P}{\partial \zeta}. \tag{1.43}$$

Parameter Re_s is called the squeeze Reynolds number. It is Reynolds number based on radial motion of journal with amplitude c and angular frequency of journal ω. Λ is called the bearing number or the compressibility number.

$$Re_s = \rho\, \frac{\omega\, c^2}{\mu} = Re_c\, \frac{c}{R}, \qquad \Lambda = \frac{6\, \mu\, \omega\, R^2}{p_a\, c^2}. \tag{1.44}$$

From the definition of squeeze Reynolds number it is clear that inertia effects would be significant if $\omega \sim \frac{\mu}{\rho\, c^2}$, hence the elimination of left-hand side is justified for most cases. Momentum equations are simplified to

$$0 = -\frac{6}{\Lambda} \frac{\partial P}{\partial \xi} + \frac{\partial^2 v_\xi}{\partial \zeta^2}, \tag{1.45}$$

$$0 = -\frac{6}{\Lambda} \frac{\partial P}{\partial \eta} + \frac{\partial^2 v_\eta}{\partial \zeta^2}, \tag{1.46}$$

$$0 = \frac{\partial P}{\partial \zeta}. \tag{1.47}$$

These equations are identical to those used in deriving Reynolds equation (1.20),(1.21).

1.3.3 Turbulence

Turbulent flow can occur at high Reynolds numbers, when destabilising inertia forces outweigh stabilizing viscous forces. Transition from laminar flow to fully turbulent is usually preceded by flow instability. Two basic forms of flow instability are the circumferential instability and the parallel flow instability.

The circumferential instability can occur in flows with curved streamlines, when destabilising effect of centrifugal force cannot be suppressed by viscous forces anymore. This instability is characterized by a steady secondary laminar flow often referred as Taylor vortices. Taylor vortex flow is characterized by series of toroidal vortices equally spaced along cylinder axis. This phenomenon has been studied for the flow between rotating cylinders. Experiments showed that the flow is stable against centrifugal disturbances if the outer cylinder rotates while the inner one is stationary. If the outer cylinder is at rest and the inner one rotates, the laminar flow can become unstable depending on value of Taylor number

$$Ta = \left(\frac{c}{R}\right) Re_c^2. \tag{1.48}$$

Critical value of Taylor number $Ta = 1707.8$ is valid for concentric cylinders. Bearing eccentricity raises the value of critical Taylor number. Additional Poiseuille flow, caused either by an external axial pressure gradient or circumferential pressure gradient, also makes the critical value of Taylor number higher. As Taylor number increases above the critical value the vortex cells become distorted and parallel flow instability takes place as a transient to the fully turbulent regime. Widely accepted value of Reynolds number when flow becomes turbulent due to parallel flow instability is $Re_c = 2,000$, however this critical value does not reflect axial flow caused by imposed pressure gradient.

The way how the turbulent flow is developed within bearing depends on which critical value is reached first. If the first exceeded critical value is the Taylor number, Taylor vortices occur until the critical Reynolds number is reached. Otherwise the direct transient to fully turbulent regime will happen at around $Re_c = 2,000$. For critical values given above, the relative eccentricity $c/R = 4.27 \cdot 10^{-4}$ is the boundary case.

The turbulent-flow model as well as the effects of inertia forces can be found in the work of Frêne et al. [22]. Comparison of three turbulent models applied to tilting pad journal bearing is provided by Bouard et al. [23]. Experimental observation of Taylor vortices instability for Newtonian and Non-Newtonian fluids was done by Dumont et al. [24], who used direct visualization technique and electro-diffusion probes. Widely used turbulent model based on works of Constatinescu can be found e.g. in Chun [25]:

$$\frac{\partial}{\partial x_1}\left(\frac{\rho h^3}{\mu} G_{x_1} \frac{\partial p}{\partial x_1}\right) + \frac{\partial}{\partial x_2}\left(\frac{\rho h^3}{\mu} G_{x_2} \frac{\partial p}{\partial x_2}\right) = \frac{U}{2} \frac{\partial (\rho h)}{\partial x_1}, \tag{1.49}$$

where values of the parameters G_{x_1} and G_{x_2} are given in the range $1000 \leq Re \leq 30000$ as

$$G_{x_1} = \frac{1}{12 + 0.0136 \left(\frac{\rho h U}{\mu}\right)^{0.9}}, \tag{1.50}$$

$$G_{x_2} = \frac{1}{12 + 0.0043 \left(\frac{\rho h U}{\mu}\right)^{0.96}}. \tag{1.51}$$

1.3.4 Anisothermal Flow

The last item of the list of necessary conditions for validitity of classical Reynolds equation, summarized on the page 9, constitutes widely used assumption undertaken wherever the classical form of Reynolds equation is used. It renders the temperature and viscosity constant around entire volume of lubricant. Searching for appropriate temperature can be complicated, especially with lack of experimental data. In general, the phenomena influencing lubricant temperature are dissipative heat generation by viscous friction, heat transfer between film and rigid boundaries, heat carried by inlet/outlet flow, convection and conduction of heat within film and expansion work of compressible continuum. Last term will not be present for case of incompressible fluids. If the temperatures of bearing surfaces and inlet lubricant are known, the simple lumped-mass quasistatic heat balance calculation can be iteratively performed along the solution of Reynolds equation.

$$c_p \dot{m}_i \left(T_i - T\right) + Q_d + S_1 h_1 \left(T_1 - T\right) + S_2 h_2 \left(T_2 - T\right) = 0. \tag{1.52}$$

The first term is the balance of heat carried in and out of control volume by medium, Q_d is dissipative heat that can be computed from the results of Reynolds equation, heat convection through boundaries is represented by the last two terms. S_1, S_2 mean boundary areas, h_1 and h_2 are heat convection rates. The heat convection rates can be estimated by means of Prandtl number and thickness of laminar boundary layer taken equal to bearing radial clearance.

$$h_{1,2} = \frac{3}{2} \frac{k_l}{c} Pr^{1/3}, \qquad Pr = \frac{\mu\, c_p}{k_l}, \tag{1.53}$$

c is radial clearance, k_l is lubricant thermal conductivity. It is worth realizing that the Prandtl number of air within expectable range of temperature is lower than 1, see fig. (1.6), what renders the thickness of temperature boundary layer greater than thickness of laminar boundary layer. On this condition, the relation (1.53) cannot be used for calculation of heat convection in air operating bearings. The temperature boundary layer should be thinner than the half of the radial clearance, what would happen provided $Pr > 8$. More detailed analysis needs to account for more or less simplified equation of energy conservation (1.8).

Despite the fact, that the gas bearings are in minority compared to bearing using liquid lubricants, it is surprising how little information on thermal analysis of gas bearing can be

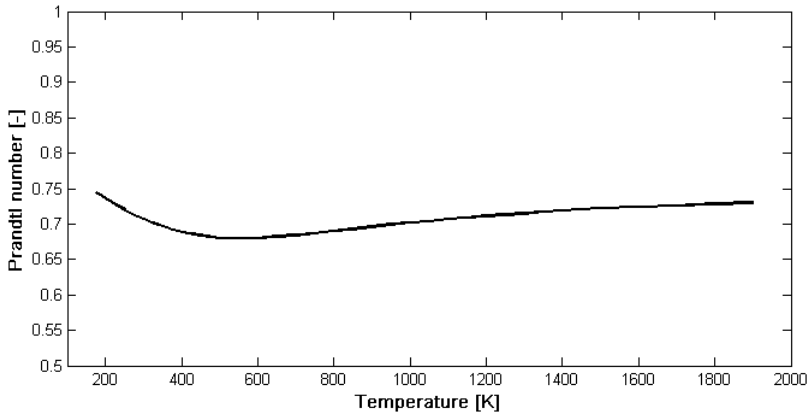

Figure 1.6: Prandtl number for dry air

found in literature. One of the reasons might be that the gas bearings have been believed to experience only little heat generation because of low viscosity of operating medium, which effect is in the case of aerostatic bearings further reduced by expansion work of gas passing the orifice system. With increasing speed of machinery using gas bearings, the energy balance within bearings should be taken into consideration.

Experimental observation of temperature profiles within aerostatic bearing supporting a spindle of 60 mm in diameter and rotating up to the 20,000 rpm has been carried out by Ohishi and Matsuzaki [26]. This isolated work brings unique data on thermal behaviour of entire bearing system. The experimental setup comprised 94 thermocouples to measure the temperature of bearing housing, bush and the air film. Thermocouples used for measuring temperatures of metal parts were fitted in blind drillings. Those used for the air film temperatures were inserted into plugs pressed through the wall of bearing bush, which was consequently lapped. Authors logged transient data for 300 minutes from rotor start up. One of the observed facts was that the air bearing was nearly isothermal. Only small variations in temperature along circumferential dimension were found in the air film; however, the variations could be promoted by feeding with cooler air. The nearly constant temperature of air film around the circumference is discussed to be attributed to the used feeding system of twelve evenly distributed orifices. Bush and housing temperature variations were more affected. the air film temperature measurements showed that the outlet air temperature closely represents the average temperature within air film. This information is of considerable practical use. Another important observation was that the Poiseuille flow, which is still present when spindle is at rest did not cause measurable temperature rise and thus entire heat generation comes from the shear rate in Couette flow. This is in accordance with measured temperature rise that was proportional to the square of spindle speed, which was about 30 K at 20,000 rpm.

Author did not find any article dealing with analytical modelling of temperature effects for journal gas bearing. There exist a few papers approaching special cases of air bearings in terms of thermal analysis. One of such is the work of Zhang and Bogy [27], where a solution of heat transfer model of thin slider/disk air bearing system of magnetoresistive transducer is presented. This specific design of self-acting slider air bearing works with $Kn = 0.02 \div 1$, what implies wall slip to transitional flow regime. Authors used simplified Stokes equation and applied boundary conditions for velocity and temperature derived from kinetic theory of gases. However, the air properties were assumed constant over bearing geometry and all nonlinear terms of energy conservation was neglected. These significant simplifications were reasonable for obtaining heat flux coefficient within this bearing, but would not serve well for the case of externally pressurized bearing.

There can be found significantly more papers on thermal analysis, approaching the problem both analytically and experimentally, of bearings with liquid lubricant that can be treated as incompressible medium. Andres et al. [28] provides bearing model with two-dimensional energy equation supplemented by global energy balance at recessed oil inlet pocket, considering the convection, oil mixing and energy dissipation in the recess. Another example of numerical observation of the temperature and the velocity profiles is introduced in Kumar et al. [29]. The finite element method was used on thermo-hydrodynamic problem of pad slider bearing. The problem was restricted to two spatial dimensions, thus only one-dimensional Reynolds equation was used (infinite width of the pad), but full energy conservation was involved. Solution for incompressible fluid has been provided with density and viscosity as functions of temperature. Authors Yang and Jeng [30] have studied thermal effects in conical-cylindrical bearing lubricated by incompressible fluid. They have added the effect of viscosity rise due to pressure that has shown important in the temperature-pressure-viscosity interaction at isothermal, convective and adiabatic boundary conditions. Chun and Ha [31] studied the thermal variability of high speed oil bearings with axial feeding groove at turbulent flow condition. The Reynolds equation was solved with two-dimensional energy equation with isothermal, convective and adiabatic boundary conditions of temperatures at wall surfaces.

Reynolds boundary condition was incorporated in order to account for cavitation. Mixing of recirculated and inlet oil was considered for different oil inlet conditions. Syverud [32] maintained experimental study of surface temperature in the cavitated region of oil bearings. The measured temperature distribution along circumferential coordinate has shown temperature fall in the oil undergoing the pressure drop. The fall in the temperature is discussed to be caused by evaporation of the oil with certain contribution of isentropic expansion of gas released from oil due to cavitation. The work of Santos and Nicoletti [33] analyses the hybrid tilting pad bearing with various configurations of oil inlet orifices. Variation of viscosity along circumferential and axial dimension is considered in Reynolds equation. The energy equation uses calculated velocity profiles and it is implemented in two-dimensional form after integration of the energy equation across the film thickness. This approach allows time efficient

calculation, but gives up on considering thermal variations across film thickness. Adiabatic boundary conditions have been adopted in this paper. Kumar et al. [34] and Sharma et al. [35] provide elasto-thermo-hydrodynamic solution for hybrid bearing with elastic bush. This work uses finite element formulation of the Reynolds equation, energy conservation equation and problem of thermo-elastic deformation of the bush. The effect of design of inlet flow restrictors on the stability of rotor is studied. This complex study on analytical modelling of bearing considers steady state solution. Adiabatic solution of energy for elliptic journal bearings can be found in the work of Mishra et al. [36]. Fillon and Bouyer [37] studied temperature distribution in worn plain bearings. The solution is provided by means of steady form of the energy equation for incompressible fluid. Results for different level of local circular worn out have shown significant fall in temperature for wear of above the 30% of bearing radial clearance.

1.4 Mathematical Models of Flexible Rotors

Apart from traditional analytic models, Transfer Matrix Method used to be popular in the past. This method provides the solution directly in the frequency domain, which was beneficial because of limited power of available computers. Nowadays, it is used rather rarely, being superseded by Finite Elements Method (FEM). FEM is more universal, because it builds equations of motion in the time domain, what is necessary for dealing with strongly nonlinear problems. Power of today's computers is not a limitation for transition of these models to frequency or frequency-modal domains.

Standard approach to derive FEM formulation of rotor system is to establish kinetic and potential energy of shaft element by means of nodal values of generalized displacements followed by application of Lagrange equations in order to obtain equations of motion. For assumed small displacements, these equations are linear and can be represented by matrices of mass, stiffness, and generalized damping involving gyroscopic effects. Assembled into global matrices they provide numerical model of the shaft that can be supplemented by lumped matrices of rigid discs, linear bearings etc. These models can be generalized to cover the use of flexible discs, turbine blades, fatigue crack propagation, inertial reference frame etc. Most of available extensions of classical rotor FEM models are out of scope of this work, which restricts the use of flexible rotor model to FEM model of axisymmetric rotor with rigid discs.

1.4.1 Rayleigh Shaft Finite Elements

This model is adopted from the book [38]. It uses Navier's hypothesis of non-deformable cross section of the beam, which remains perpendicular to the neutral axis of the beam. This condition assumes negligible contribution of shear to the potential deformation energy, which is applicable in the case of slender beams. This model is shortly presented here, as the work of cited authors Slavík et al. [38], because this model is to be extended to respect also the

contribution of shear deformation potential energy. Author refers to the mentioned book for full details about derivation of these Rayleigh shaft elements.

Shaft is treated as one-dimensional continuum divided by nodes into a number of finite elements. Generalized displacements of single shaft element of length l are defined as per figure 1.7.

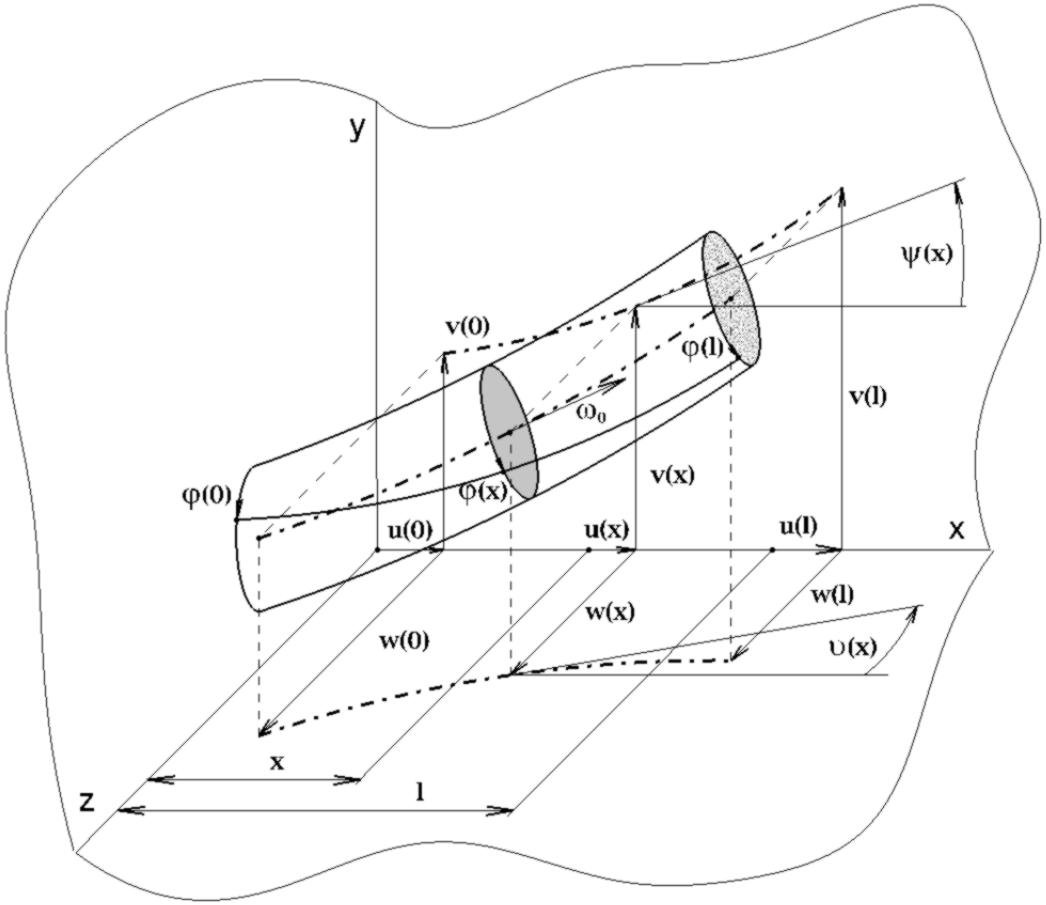

Figure 1.7: Configuration of shaft finite element

Finite base representation of transversal displacements along the length of the element is held by means of polynomials of third order

$$v(x) = \mathbf{P}_3\,\mathbf{c}_1, \quad w(x) = \mathbf{P}_3\,\mathbf{c}_2, \quad \mathbf{P}_3 = (1, x, x^2, x^3). \tag{1.54}$$

Angular displacements are then

$$\psi(x) = \frac{\mathrm{d}\,v(x)}{\mathrm{d}x} = \frac{\mathrm{d}\,\mathbf{P}_3}{\mathrm{d}x}\,\mathbf{c}_1, \quad \vartheta(x) = -\frac{\mathrm{d}\,w(x)}{\mathrm{d}x} = -\frac{\mathrm{d}\,\mathbf{P}_3}{\mathrm{d}x}\,\mathbf{c}_2. \tag{1.55}$$

Axial and torsional angular displacements are represented by linear functions

$$u(x) = \mathbf{P}_1\,\mathbf{c}_3, \quad \varphi(x) = \mathbf{P}_1\,\mathbf{c}_4, \quad \mathbf{P}_1 = (1, x). \tag{1.56}$$

Vector of nodal values fully defines the configuration of the element:

$$\mathbf{q}^e = \left(\mathbf{q}_1^{\mathrm{T}}, \mathbf{q}_2^{\mathrm{T}}, \mathbf{q}_3^{\mathrm{T}}, \mathbf{q}_4^{\mathrm{T}}\right)^{\mathrm{T}}, \tag{1.57}$$

where

$$\mathbf{q}_1 = \begin{pmatrix} v(0) \\ \psi(0) \\ v(l) \\ \psi(l) \end{pmatrix}, \quad \mathbf{q}_2 = \begin{pmatrix} w(0) \\ \vartheta(0) \\ w(l) \\ \vartheta(l) \end{pmatrix}, \quad \mathbf{q}_3 = \begin{pmatrix} u(0) \\ u(l) \end{pmatrix}, \quad \mathbf{q}_4 = \begin{pmatrix} \varphi(0) \\ \varphi(l) \end{pmatrix}. \tag{1.58}$$

Relations between nodal values and deformations approached by selected polynomials (1.54), (1.55), (1.56),

$$\begin{aligned} v(x) &= \mathbf{P}_3\,\mathbf{S}_1^{-1}\,\mathbf{q}_1, & w(x) &= \mathbf{P}_3\,\mathbf{S}_2^{-1}\,\mathbf{q}_2, & \psi(x) &= \frac{\mathrm{d}\mathbf{P}_3}{\mathrm{d}x}\,\mathbf{S}_1^{-1}\,\mathbf{q}_1, \\ \vartheta(x) &= -\frac{\mathrm{d}\mathbf{P}_3}{\mathrm{d}x}\,\mathbf{S}_2^{-1}\,\mathbf{q}_2, & u(x) &= \mathbf{P}_1\,\mathbf{S}_3^{-1}\,\mathbf{q}_3, & \varphi(x) &= \mathbf{P}_1\,\mathbf{S}_3^{-1}\,\mathbf{q}_4, \end{aligned} \tag{1.59}$$

are determined by transformation matrices

$$\mathbf{S}_1 = \begin{pmatrix} 1 & 0 & 0 & 0 \\ 0 & 1 & 0 & 0 \\ 1 & l & l^2 & l^3 \\ 0 & 1 & 2l & 3l^2 \end{pmatrix}, \quad \mathbf{S}_2 = \begin{pmatrix} 1 & 0 & 0 & 0 \\ 0 & -1 & 0 & 0 \\ 1 & l & l^2 & l^3 \\ 0 & -1 & -2l & -3l^2 \end{pmatrix}, \quad \mathbf{S}_3 = \begin{pmatrix} 1 & 0 \\ 1 & l \end{pmatrix}. \tag{1.60}$$

Local matrices are now constructed as follows

$$\begin{aligned} \mathbf{M}^e &= \begin{pmatrix} \mathbf{S}_1^{-\mathrm{T}}\,(\mathbf{I}_1 + \mathbf{I}_2)\,\mathbf{S}_1^{-1} & \mathbf{0} & \mathbf{0} & \mathbf{0} \\ \mathbf{0} & \mathbf{S}_2^{-\mathrm{T}}\,(\mathbf{I}_1 + \mathbf{I}_2)\,\mathbf{S}_2^{-1} & \mathbf{0} & \mathbf{0} \\ \mathbf{0} & \mathbf{0} & \mathbf{S}_3^{-\mathrm{T}}\mathbf{I}_4\mathbf{S}_3^{-1} & \mathbf{0} \\ \mathbf{0} & \mathbf{0} & \mathbf{0} & \mathbf{S}_3^{-\mathrm{T}}\mathbf{I}_5\mathbf{S}_3^{-1} \end{pmatrix}, \\ \mathbf{G}^e &= \begin{pmatrix} \mathbf{0} & 2\mathbf{S}_1^{-\mathrm{T}}\mathbf{I}_2\mathbf{S}_2^{-1} & \mathbf{0} & \mathbf{0} \\ -2\mathbf{S}_1^{-\mathrm{T}}\mathbf{I}_2\mathbf{S}_2^{-1} & \mathbf{0} & \mathbf{0} & \mathbf{0} \\ \mathbf{0} & \mathbf{0} & \mathbf{0} & \mathbf{0} \\ \mathbf{0} & \mathbf{0} & \mathbf{0} & \mathbf{0} \end{pmatrix}, \\ \mathbf{K}^e &= \begin{pmatrix} \mathbf{S}_1^{-\mathrm{T}}\mathbf{I}_3\mathbf{S}_1^{-1} & \mathbf{0} & \mathbf{0} & \mathbf{0} \\ \mathbf{0} & \mathbf{S}_2^{-\mathrm{T}}\mathbf{I}_3\mathbf{S}_2^{-1} & \mathbf{0} & \mathbf{0} \\ \mathbf{0} & \mathbf{0} & \mathbf{S}_3^{-\mathrm{T}}\mathbf{I}_6\mathbf{S}_3^{-1} & \mathbf{0} \\ \mathbf{0} & \mathbf{0} & \mathbf{0} & \mathbf{S}_3^{-\mathrm{T}}\mathbf{I}_7\mathbf{S}_3^{-1} \end{pmatrix}. \end{aligned} \tag{1.61}$$

Material and geometric properties of the element are contained in

$$\begin{aligned}
\mathbf{I}_1 &= \int_0^l \rho\, A(x)\, \mathbf{P}_3^{\mathrm{T}}\, \mathbf{P}_3 \,\mathrm{d}x, & \mathbf{I}_2 &= \int_0^l \rho\, J(x)\, \frac{\mathrm{d}\,\mathbf{P}_3}{\mathrm{d}x}^{\mathrm{T}} \frac{\mathrm{d}\,\mathbf{P}_3}{\mathrm{d}x}\,\mathrm{d}x, \\
\mathbf{I}_3 &= \int_0^l E\, J(x)\, \frac{\mathrm{d}^2\,\mathbf{P}_3}{\mathrm{d}x^2}^{\mathrm{T}} \frac{\mathrm{d}^2\,\mathbf{P}_3}{\mathrm{d}x^2}\,\mathrm{d}x, & \mathbf{I}_4 &= \int_0^l \rho\, A(x)\, \mathbf{P}_1^{\mathrm{T}}\, \mathbf{P}_1 \,\mathrm{d}x, \\
\mathbf{I}_5 &= 2\int_0^l \rho\, J(x)\, \mathbf{P}_1^{\mathrm{T}}\, \mathbf{P}_1 \,\mathrm{d}x, & \mathbf{I}_6 &= \int_0^l E\, A(x)\, \frac{\mathrm{d}\,\mathbf{P}_1}{\mathrm{d}x}^{\mathrm{T}} \frac{\mathrm{d}\,\mathbf{P}_1}{\mathrm{d}x}\,\mathrm{d}x, \\
\mathbf{I}_7 &= 2\int_0^l G\, J(x)\, \frac{\mathrm{d}\,\mathbf{P}_1}{\mathrm{d}x}^{\mathrm{T}} \frac{\mathrm{d}\,\mathbf{P}_1}{\mathrm{d}x}\,\mathrm{d}x.
\end{aligned} \tag{1.62}$$

For prismatic shaft element these integrals will become

$$\begin{aligned}
\mathbf{I}_1 &= \rho A l \begin{pmatrix} 1 & l/2 & l^2/3 & l^3/4 \\ & l^2/3 & l^3/4 & l^4/5 \\ & & l^4/5 & l^5/6 \\ sym. & & & l^6/7 \end{pmatrix} & \mathbf{I}_2 &= \rho J l \begin{pmatrix} 0 & 0 & 0 & 0 \\ & 1 & l & l^2 \\ & & 4l^2/3 & 3l^3/2 \\ sym. & & & 9l^4/5 \end{pmatrix} \\
\mathbf{I}_3 &= EJl \begin{pmatrix} 0 & 0 & 0 & 0 \\ & 0 & 0 & 0 \\ & & 4 & 6l \\ sym. & & & 12l^2 \end{pmatrix} & \mathbf{I}_4 &= \rho A l \begin{pmatrix} 1 & l/2 \\ l/2 & l^2/3 \end{pmatrix} \\
\mathbf{I}_5 &= 2\rho J l \begin{pmatrix} 1 & l/2 \\ l/2 & l^2/3 \end{pmatrix}, & \mathbf{I}_6 &= EAl \begin{pmatrix} 0 & 0 \\ 0 & l \end{pmatrix}, & \mathbf{I}_7 &= 2GJl \begin{pmatrix} 0 & 0 \\ 0 & l \end{pmatrix}.
\end{aligned} \tag{1.63}$$

Reordering the components of vector of nodal displacements $\mathbf{q}^e$ to the

$$\tilde{\mathbf{q}}^e = (u(0),\, v(0),\, \psi(0),\, w(0),\, \vartheta(0),\, \varphi(0), u(l),\, v(l),\, \psi(l),\, w(l),\, \vartheta(l),\, \varphi(l))^{\mathrm{T}} \tag{1.64}$$

by means of permutation matrix $\mathbf{T} = [T_{ij}]$

$$\mathbf{q}^e = \mathbf{T}\,\tilde{\mathbf{q}}^e, \tag{1.65}$$

where

$$T_{ij} = \begin{cases} 1 & \text{for } i,j = 1,2; 2,3; 3,8; 4,9; 5,4; 6,5; 7,10; 8,11; 9,1; 10,7; 11,6; 12,12 \\ 0 & \text{else,} \end{cases} \tag{1.66}$$

leads to the new local matrices

$$\tilde{\mathbf{M}}^e = \mathbf{T}^{\mathrm{T}}\mathbf{M}^e\,\mathbf{T}, \quad \tilde{\mathbf{G}}^e = \mathbf{T}^{\mathrm{T}}\mathbf{G}^e\,\mathbf{T}, \quad \tilde{\mathbf{K}}^e = \mathbf{T}^{\mathrm{T}}\mathbf{K}^e\,\mathbf{T}. \tag{1.67}$$

If only transversal degrees of freedom are of concern, then the model can be simplified by leaving out relevant rows and columns from matrices (1.67). This can be done during assembly of local matrices what simplifies the relations (1.61) to

$$\begin{aligned}
\mathbf{M}^e &= \begin{pmatrix} \mathbf{S}_1^{-\mathrm{T}} (\mathbf{I}_1 + \mathbf{I}_2) \mathbf{S}_1^{-1} & \mathbf{0} \\ \mathbf{0} & \mathbf{S}_2^{-\mathrm{T}} (\mathbf{I}_1 + \mathbf{I}_2) \mathbf{S}_2^{-1} \end{pmatrix}, \\
\mathbf{G}^e &= \begin{pmatrix} \mathbf{0} & 2\mathbf{S}_1^{-\mathrm{T}} \mathbf{I}_2 \mathbf{S}_2^{-1} \\ -2\mathbf{S}_1^{-\mathrm{T}} \mathbf{I}_2 \mathbf{S}_2^{-1} & \mathbf{0} \end{pmatrix}, \\
\mathbf{K}^e &= \begin{pmatrix} \mathbf{S}_1^{-\mathrm{T}} \mathbf{I}_3 \mathbf{S}_1^{-1} & \mathbf{0} \\ \mathbf{0} & \mathbf{S}_2^{-\mathrm{T}} \mathbf{I}_3 \mathbf{S}_2^{-1} \end{pmatrix}.
\end{aligned} \tag{1.68}$$

Elements of the permutation matrix $\mathbf{T}$ are now

$$T_{ij} = \begin{cases} 1 & \text{for } i,j = 1,1; 2,2; 3,5; 4,6; 5,3; 6,4; 7,7; 8,8 \\ 0 & \text{else,} \end{cases} \tag{1.69}$$

with respect to the vector of nodal displacements

$$\tilde{\mathbf{q}}^e = (v(0),\, \psi(0),\, w(0),\, \vartheta(0),\, v(l),\, \psi(l),\, w(l),\, \vartheta(l))^{\mathrm{T}}. \tag{1.70}$$

The global matrices $\mathbf{K}$,$\mathbf{G}$,$\mathbf{M}$ are built in the typical way by adding up local matrices, respecting the node positions of the particular elements. The FEM model of free, undamped rotating shaft can be written as

$$\mathbf{M}\,\ddot{\mathbf{q}}(t) + \omega_0\,\mathbf{G}\,\dot{\mathbf{q}}(t) + \mathbf{K}\,\mathbf{q}(t) = \mathbf{f}(\dot{\mathbf{q}}, \mathbf{q}, t). \tag{1.71}$$

1.4.2 Rigid Discs

Rigid discs mounted centrically and perpendicular with respect to the shaft axis can be incorporated into rotor model by updating the global matrices $\tilde{\mathbf{M}}^e$ and $\tilde{\mathbf{G}}^e$ by lumped mass and gyroscopic matrices. For Rayleigh rotor model, the matrices are constructed as

$$\mathbf{M}_d = \begin{pmatrix} m_d & 0 & 0 & 0 & 0 & 0 \\ & m_d & m_d\, x_T & 0 & 0 & 0 \\ & & I_d + m_d\, x_T^2 & 0 & 0 & 0 \\ & & & m_d & -m_d\, x_T & 0 \\ & & & & I_d + m_d\, x_T^2 & 0 \\ sym. & & & & & I_{d0} \end{pmatrix}, \tag{1.72}$$

$$\mathbf{G}_d = \begin{pmatrix} 0 & 0 & 0 & 0 & 0 & 0 \\ 0 & 0 & 0 & 0 & 0 & 0 \\ 0 & 0 & 0 & 0 & -I_{d0} & 0 \\ 0 & 0 & 0 & 0 & 0 & 0 \\ 0 & 0 & I_{d0} & 0 & 0 & 0 \\ 0 & 0 & 0 & 0 & 0 & 0 \end{pmatrix}. \tag{1.73}$$

For models involving lateral generalized displacements only, the first and the sixth raws and columns of the matrices (1.72) and (1.73) will be left out. List of disc's parameters is following: m_d –mass of the disc; x_T –distance from attachment node to disc's centre of mass; I_d –transversal mass moment of inertia; I_{d0} –axial mass moment of inertia.

1.4.3 Bearings and External Forces

If it is possible to consider the bearings linear, then the bearing reactions can be represented as

$$\mathbf{f}_{bi} = \mathbf{K}_{bi}\,\mathbf{q}_{bi} + \mathbf{B}_{bj}\,\dot{\mathbf{q}}_{bi}. \tag{1.74}$$

Vector $\mathbf{q}_{bi}$ contains generalized displacements of the node at which i-th bearing reaction acts. Matrices $\mathbf{K}_{bi}$ and $\mathbf{B}_{bi}$ are bearing stiffness and damping matrices. Their properties depend on the specific kind of bearing and its parameters, but in general, these matrices are full and unsymmetrical, what introduces cross-coupling between particular degrees of freedom. Elements of these bearing matrices can be added to the system matrices of the rotor model to the respective positions. This linear model can be treated by means of modal analysis and frequency response calculations. Methods of obtaining bearing stiffness and damping coefficients are discussed later in this work.

Non-linear bearing reactions as well as other external forces can be put in the force vector $\mathbf{f}(\dot{\mathbf{q}}, \mathbf{q}, t)$. Solution of the system is then accessible by time domain analyses only.

An important kind of force excitation of rotor system is the one caused by inertial reactions from eccentrically and askew mounted discs. On condition of small angle of skewness γ and eccentricity e_T of the disc, the inertial reaction can be expressed as following force vector

$$\mathbf{f}_d = \begin{pmatrix} f_y \\ M_\psi \\ f_z \\ M_\vartheta \end{pmatrix} = \begin{pmatrix} m_d\, e_T\, \omega_0^2 \\ \left((I_d - I_{d0})\,\gamma + m_d\, e_T\, x_T\right)\,\omega_0^2 \\ -j\, m_d\, e_T\, \omega_0^2 \\ j\,\left((I_d - I_{d0})\,\gamma + m_d\, e_T\, x_T\right)\,\omega_0^2 \end{pmatrix} \cdot \mathrm{e}^{j\omega_0\, t}. \tag{1.75}$$

This force excitation is valid for constant or only slowly changing ω_0. For fast transition analysis, the torsional degrees of freedom should be taken into account, which would introduce cross-coupling between torsional and lateral degrees of freedom. Real part of $\mathbf{f}_d$ is taken for time domain analyses.

1.5 Modal Analysis of Rotor Systems

In comparison with conservative non-rotating structures or such structures with light proportional damping, there are some differences in terms of applicability of spectral decomposition on matrices describing rotor systems. The most important ones are listed below.

1. Coefficient matrices describing rotor system are dependent on angular speed of rotor, therefore also eigenvalues and eigenvectors are dependent on rotor angular speed
2. System in the state space is non-self-adjoint owing to the presence of skew-symmetric parts of coefficient matrices. Pair of complex eigenvectors describes one degree of freedom instead of real eigenvectors
3. Defective system may occur, thus preventing direct the use of spectral decomposition in the form of full diagonalization of matrices of the problem

The last item of the list comes into play when rigid body modes of rotor system with gyroscopic effects are solved for. These modes would be useful for modal reduction of rotor supported by nonlinear bearings.

1.5.1 Linear Eigenvalue Problem of Non-Self-Adjoint Diagonalizable System

Linear dynamic system, representing a rotor system supported in linear bearings:

$$\mathbf{M}\,\ddot{\mathbf{q}}(t) + (\mathbf{B} + \omega_0\,\mathbf{G})\;\dot{\mathbf{q}}(t) + \mathbf{K}\,\mathbf{q}(t) = \mathbf{f}(\dot{\mathbf{q}}, \mathbf{q}, t). \tag{1.76}$$

The equation (1.76) contains matrices, which have following properties: $\mathbf{M}$ is real, symmetric positive definite, $\mathbf{G}$ is real skew-symmetric. Considering that rotor is supported in linear bearings then $\mathbf{K}$ is only regular. The damping matrix $\mathbf{B}$ contains so far only a few bearing damping coefficients. (Accounting for internal damping models is not vital at this point.)

Equation (1.76) can be, by adding identity, expressed in state space as

$$\mathbf{N}\,\dot{\mathbf{u}} + \mathbf{P}\,\mathbf{u} = \mathbf{F}, \quad \mathbf{F} = \left(\mathbf{f}^{\mathrm{T}}, \mathbf{0}^{\mathrm{T}}\right)^{\mathrm{T}}, \tag{1.77}$$

where

$$\mathbf{N} = \begin{pmatrix} \mathbf{M} & \mathbf{0} \\ \mathbf{0} & \mathbf{M} \end{pmatrix}, \quad \mathbf{P} = \begin{pmatrix} \mathbf{B} + \omega_0\,\mathbf{G} & \mathbf{K} \\ -\mathbf{M} & \mathbf{0} \end{pmatrix}, \quad \mathbf{u} = \begin{pmatrix} \dot{\mathbf{q}} \\ \mathbf{q} \end{pmatrix}. \tag{1.78}$$

It is possible to assembly matrices $\mathbf{N}, \mathbf{P}$ and vector $\mathbf{u}$ in alternative forms. Advantage of presented structure is that matrix $\mathbf{N}$ is regular, symmetric positive definite as long as the mass matrix $\mathbf{M}$ holds these properties. Fundamental solution of linear differential equations is expected, hence for

$$\mathbf{q} = \hat{q}\,\mathrm{e}^{s\,t}, \qquad \dot{\mathbf{q}} = s\hat{q}\,\mathrm{e}^{s\,t} \tag{1.79}$$

can the homogenous system associated to (1.77) be expressed as

$$(\mathbf{A} - s\mathbf{I})\,\mathbf{v} = \mathbf{0}, \quad \mathbf{A} = -\mathbf{N}^{-1}\mathbf{P}, \tag{1.80}$$

which is the linear eigenvalue problem. Since the matrix $\mathbf{A}$ is not symmetric, there is no orthogonal system of real eigenvectors. It is therefore necessary to take eigenvalue problem of adjoint system into account in order to obtain complete set of eigenvectors. Adjoint system can be understood in two manners, expressed by means of *left* eigenvectors

$$\mathbf{v}_L^{\mathrm{T}}\,(\mathbf{A} - s\mathbf{I}) = \mathbf{0}^{\mathrm{T}}, \tag{1.81}$$

or

$$\mathbf{w}^{\mathrm{T}}\,(\mathbf{A}_* - s\mathbf{I}) = \mathbf{0}^{\mathrm{T}}, \quad \mathbf{A}_* = -\mathbf{P}\mathbf{N}^{-1}. \tag{1.82}$$

The first one is clearly the eigenvalue problem adjoint to (1.80), the second one is adjoint to generalized eigenvalue problem of homogenous system associated with (1.77). Whether to choose (1.81) or (1.82) depends on which matrices are desired to diagonalize, $\mathbf{A}$, or $\mathbf{N}$ and $\mathbf{P}$. Eigenvalue problems defined by (1.80) and (1.81) provides biorthogonal system of eigenvectors with respect to matrix $\mathbf{A}$. Generalized problem established by (1.80) and (1.82) will provide system of biorthogonal eigenvectors $\mathbf{v}$ and $\mathbf{w}$ with respect to $\mathbf{N}$. Normalization of eigenvectors could be done in several ways, but it should obey following relations (no summation over indexes)

$$\mathbf{w}_i^{\mathrm{T}}\,\mathbf{N}\,\mathbf{v}_j = \delta_{ij}, \quad \mathbf{w}_i^{\mathrm{T}}\,\mathbf{P}\,\mathbf{v}_j = -\delta_{ij}\,s_i. \tag{1.83}$$

This condition can be used directly for searching left eigenvectors as

$$\mathbf{W}^{\mathrm{T}} = (\mathbf{N}\mathbf{V})^{-1}\,. \tag{1.84}$$

It is convenient to sort the eigenvalues in spectral matrix according to their ascending imaginary parts. Supposing there are no real eigenvalues then

$$\mathbf{S}_p = \begin{pmatrix} \mathbf{S} & \\ & \bar{\mathbf{S}} \end{pmatrix}, \qquad \mathbf{S} = \begin{pmatrix} s_1 & & \\ & s_2 & \\ & & \ddots \end{pmatrix}. \tag{1.85}$$

Modal matrices will get following block structures

$$\mathbf{V} = \begin{pmatrix} \mathbf{U}\mathbf{S} & \bar{\mathbf{U}}\bar{\mathbf{S}} \\ \mathbf{U} & \bar{\mathbf{U}} \end{pmatrix}, \quad \mathbf{W} = \begin{pmatrix} \mathbf{Y} & \bar{\mathbf{Y}} \\ \mathbf{X} & \bar{\mathbf{X}} \end{pmatrix}. \tag{1.86}$$

System of equations of motion (1.77) is transformed from physical coordinates to modal ones by means of modal matrices $\mathbf{V}$ and $\mathbf{W}$

$$\mathbf{W}^{\mathrm{T}}\mathbf{N}\mathbf{V}\,\dot{\mathbf{c}}(t) + \mathbf{W}^{\mathrm{T}}\mathbf{P}\mathbf{V}\,\mathbf{c}(t) = \mathbf{W}^{\mathrm{T}}\mathbf{f}(t), \quad \mathbf{u}(t) = \mathbf{V}\mathbf{c}(t). \tag{1.87}$$

This is a set of decoupled ordinary differential equations. It can be treated in time domain with opportunity to reduce the model by considering only modes, the eigenfrequencies of which lie within certain range of frequency.

Steady state response of the system (1.77) subjected to harmonic excitation $\mathbf{F}(t) = \hat{\mathbf{F}}\,\mathrm{e}^{j\omega t}$ is

$$\hat{\mathbf{u}} = \mathbf{V}\hat{\mathbf{c}} = \mathbf{V}\left(j\omega\mathbf{I} - \mathbf{S}_p\right)^{-1}\mathbf{W}^{\mathrm{T}}\hat{\mathbf{F}} = \mathbf{H}_u(j\omega)\,\hat{\mathbf{F}}. \tag{1.88}$$

Given (1.86), the complex amplitudes of displacements are

$$\hat{\mathbf{q}} = \mathbf{U}\left(j\omega\mathbf{I} - \mathbf{S}\right)^{-1}\mathbf{Y}^{\mathrm{T}}\hat{\mathbf{f}} + \bar{\mathbf{U}}\left(j\omega\mathbf{I} - \bar{\mathbf{S}}\right)^{-1}\bar{\mathbf{Y}}^{\mathrm{T}}\hat{\mathbf{f}} = \mathbf{H}_q(j\omega)\,\hat{\mathbf{f}}. \tag{1.89}$$

Transfer matrix $\mathbf{H}_u(j\omega)$ or $\mathbf{H}_q(j\omega)$ fully describes the response of studied linear system.

Modal analysis shortly described in this section is applicable to a system of rotor equations of motion only if the system matrix $\mathbf{A}$ is diagonalizable. If the matrix $\mathbf{A}$ has any eigenvalue s with algebraic multiplicity greater than the nullity of the matrix $\mathbf{A} - s\mathbf{I}$, then the set of eigenvectors does not form a complete base, in which the matrix $\mathbf{A}$ would become a diagonal matrix.

From previous it appears that matrix $\mathbf{M}$ and therefore also matrix $\mathbf{N}$ is always regular, positive definite matrix. Stiffness matrix $\mathbf{K}_{n\times n}$ is singular with rank $n-4$, unless it contains stiffness coefficients of linear bearings. If it does, than $\mathbf{K}$ is also regular. If rotor angular speed $\omega_0 = 0$, than gyroscopic matrix $\mathbf{G}$ is ruled out of matrix $\mathbf{P}$, as well as circulatory part of stiffness matrix $\mathbf{K}$. If $\mathbf{K}$ is regular owing to bearing stiffnesses, then there are no rigid modes present and the $\mathbf{A}$ is diagonalizable by means of eigenvectors defined in (1.80) and (1.82). For $\omega_0 = 0$, there are pairs of eigenvalues with equal values, but each pair has eigenspace of dimension two. Two linearly independent vectors can be stated to span this eigenspace. Such situation is identical to beam bending in two independent planes. If $\omega_0 > 0$, then each pair of identical eigenvalues splits into two distinct ones, each inevitably having its own eigenvector. They are usually related to forward and backward whirl modes, however mixed forward-backward whirl modes can occur for e.g. strongly dissimilar coefficients of bearings. Classification of eigenmodes, whether they belong to plane bending, forward, backward or mixed whirl is enclosed as the appendix B.

1.5.2 Defectiveness of Free Rotor with Gyroscopic Effects

Situation becomes more complicated when stiffness matrix $\mathbf{K}$ is singular. Rotor system without gyroscopic effects (slow, or standstill rotor) can be diagonalized by generalized eigenvalue

problem. This approach is identical to decomposition of system of static structures defined by mass and stiffness matrices as follows

$$\mathbf{Kq} = -s^2\mathbf{Mq}. \tag{1.90}$$

However the calculation of eigenvalues s^2 may exhibit numerical difficulties, there exists a set of four linearly independent eigenvectors for multiple zero eigenvalue, so it is possible to find a system of eigenvectors that diagonalizes both the matrices $\mathbf{M}$ and $\mathbf{K}$. It is possible to use generalized formulation of the eigenproblem, since matrix $\mathbf{K}$ is symmetric and $\mathbf{M}$ is positive definite symmetric matrix. Cholesky decomposition in `LAPACK` routine `DSYGV` is used by Matlab, when command `eig(K,M)` is called and the entire process stays in real numbers.

If gyroscopic effects are present, we have to describe the problem in the state space. One of the rigid modes relates to the free precession with corresponding eigenvalue becoming non-zero. Gyroscopic effects bound the rotational lateral displacements of rigid shaft together, and there is only subspace of dimension two left for zero eigenvalue with multiplicity of three. However, Matlab routine `DGGEV` provides matrices $\mathbf{V}$ and $\mathbf{D}$ that satisfy $\mathbf{AV} = \mathbf{VD}$. Matrix $\mathbf{W}$ can be calculated by equation (1.84) (numerically and only owing to round-off errors), what enforces the diagonalization of matrix $\mathbf{N}$, but not matrix $\mathbf{P}$. To compare what remains in matrix $\mathbf{W}^{\mathrm{T}}\mathbf{PV}$ for this degenerated case and the case of constrained shaft with regular stiffness matrix $\mathbf{K}$ we can define residual matrix

$$\mathbf{R} = \mathbf{W}^{\mathrm{T}}\mathbf{PV} + \mathbf{S}_p. \tag{1.91}$$

This matrix should contain only numbers of small magnitudes, caused by round-off errors and problem conditioning. Suitable norm of matrix $\mathbf{R}$ can serve as a criterion of quality of diagonalization process. Maximum norm has been chosen in this case. For numerical example, let us consider steel prismatic rotor 300 mm long with full circular cross-section with diameter 15 mm. Values for system with regular stiffness matrix, obtained by supporting this shaft at the both ends in linear isotropic bearing of stiffness $10^7\,\mathrm{Nm}^{-1}$ and defective system of free shaft are $\|\mathbf{R}\| = 8.9 \cdot 10^{-6}$ and $\|\mathbf{R}\| = 0.29$ respectively. Former value is acceptable according to condition number of the problem, the latter one shows that matrix $\mathbf{P}$ has not been diagonalized. Profiles of the residual matrices are displayed in the figure 1.8, where shade of gray of each cell is determined by decadic logarithm of absolute value of number at corresponding position. From the fig. 1.8b) it can be seen that residuals of high order of magnitude are cumulated at two block columns, corresponding to the positions where four rigid modes would be present in case of non-gyroscopic free rotor.

All square matrices, including all defective ones, can be put in Jordan canonical form. Considering the rigid modes only, Jordan canonical form and generalized eigenvectors can be expressed symbolically. Equations of motion of free rigid prismatic shaft, including gyroscopic effects and considering only small displacements measured at the centre of mass, can be

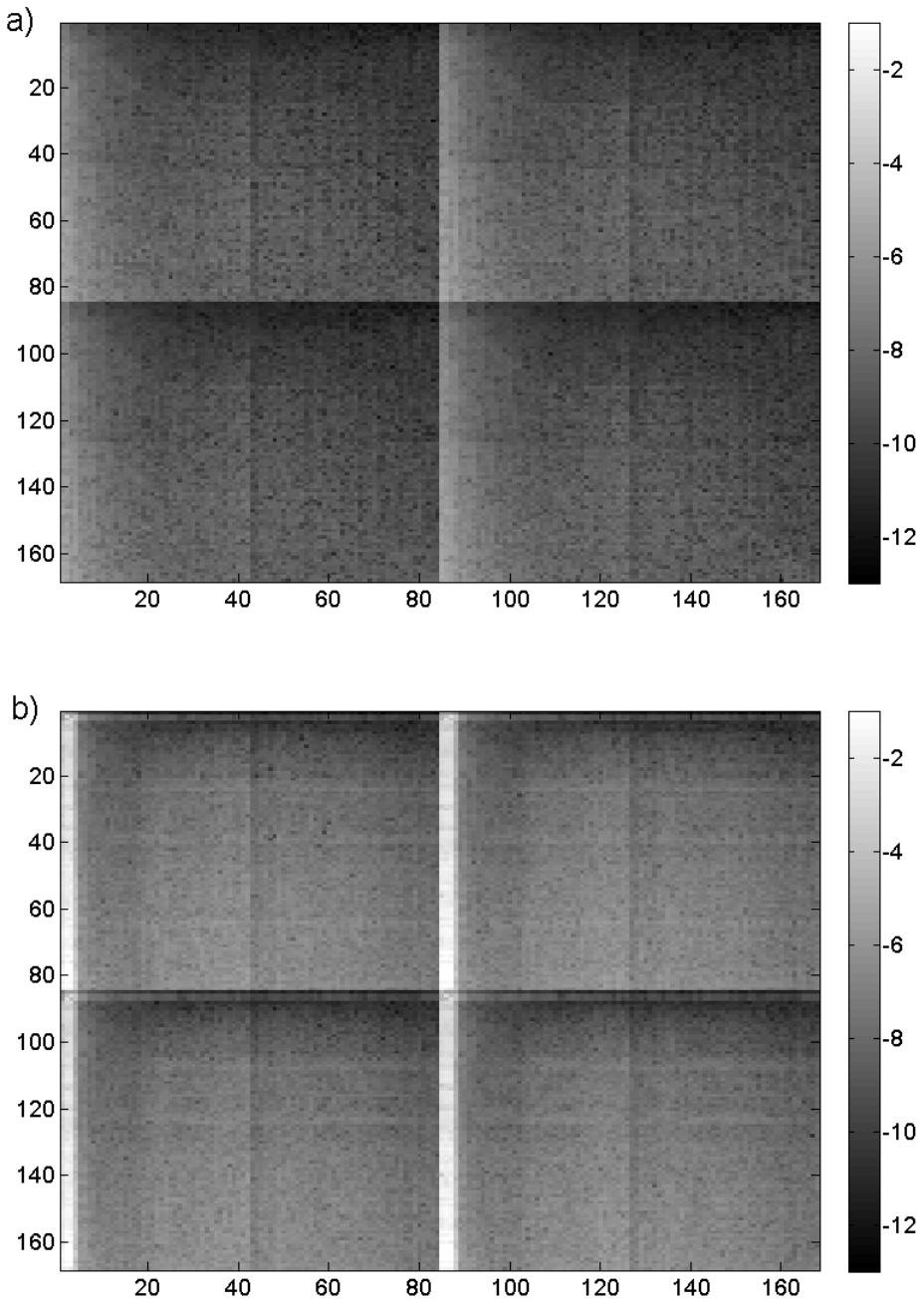

Figure 1.8: Profiles of residual matrices $\mathbf{R}$ – Orders of magnitudes of the elements; a) Regular stiffness matrix, b) Singular stiffness matrix (defective system); 20 finite elements, $\omega_0 = 10000\,\mathrm{rad\,s^{-1}}$

written in matrix form as

$$\mathbf{M}\ddot{\mathbf{q}} + \omega_0 \mathbf{G}\dot{\mathbf{q}} = \mathbf{0}, \tag{1.92}$$

where

$$\mathbf{M} = \begin{pmatrix} m & 0 & 0 & 0 \\ 0 & I & 0 & 0 \\ 0 & 0 & m & 0 \\ 0 & 0 & 0 & I \end{pmatrix}, \quad \mathbf{G} = \begin{pmatrix} 0 & 0 & 0 & 0 \\ 0 & 0 & 0 & -I_0 \\ 0 & 0 & 0 & 0 \\ 0 & I_0 & 0 & 0 \end{pmatrix}, \quad \mathbf{q} = \begin{pmatrix} v \\ \psi \\ w \\ \vartheta \end{pmatrix}. \tag{1.93}$$

Linearization of the system (1.92) gives again

$$\mathbf{N}\,\dot{\mathbf{u}} + \mathbf{P}\,\mathbf{u} = \mathbf{0}, \quad \mathbf{u} = (\dot{\mathbf{q}},\, \mathbf{q})^{\mathrm{T}}, \tag{1.94}$$

with matrices $\mathbf{N}$ and $\mathbf{P}$ constructed as

$$\mathbf{N} = \begin{pmatrix} \mathbf{M} & \mathbf{0} \\ \mathbf{0} & \mathbf{M} \end{pmatrix}, \quad \mathbf{P} = \begin{pmatrix} \omega_0\,\mathbf{G} & \mathbf{0} \\ -\mathbf{M} & \mathbf{0} \end{pmatrix}. \tag{1.95}$$

Jordan canonical form of matrix $\mathbf{A} = -\mathbf{N}^{-1}\mathbf{P}$ is

$$\mathbf{J} = \mathbf{Q}^{-1}\mathbf{A}\mathbf{Q}. \tag{1.96}$$

For this particular case of defective system are

$$\mathbf{J} = \begin{pmatrix} 0 & 0 & 0 & 0 & 0 & 0 & 0 & 0 \\ 0 & 0 & 1 & 0 & 0 & 0 & 0 & 0 \\ 0 & 0 & 0 & 0 & 0 & 0 & 0 & 0 \\ 0 & 0 & 0 & \frac{i\,\omega_0 I_0}{I} & 0 & 0 & 0 & 0 \\ 0 & 0 & 0 & 0 & 0 & 0 & 0 & 0 \\ 0 & 0 & 0 & 0 & 0 & 0 & 1 & 0 \\ 0 & 0 & 0 & 0 & 0 & 0 & 0 & 0 \\ 0 & 0 & 0 & 0 & 0 & 0 & 0 & -\frac{i\,\omega_0 I_0}{I} \end{pmatrix}, \tag{1.97}$$

$$\mathbf{Q} = \begin{pmatrix} 0 & 0 & 1 & 0 & 0 & 0 & 0 & 0 \\ 0 & 0 & 0 & \frac{1}{2} & 0 & 0 & 0 & \frac{1}{2} \\ 0 & 0 & 1 & 0 & 0 & 0 & 1 & 0 \\ 0 & 0 & 0 & \frac{i}{2} & 0 & 0 & 0 & \frac{-i}{2} \\ 0 & 1 & 0 & 0 & 0 & 0 & 0 & 0 \\ \frac{I}{\omega_0 I_0} & 0 & \frac{I}{\omega_0 I_0} & \frac{-iI}{2\omega_0 I_0} & 0 & 0 & \frac{I}{\omega_0 I_0} & \frac{iI}{2\omega_0 I_0} \\ 0 & 1 & 0 & 0 & 0 & 1 & 0 & 0 \\ 0 & 0 & \frac{-I}{\omega_0 I_0} & \frac{I}{2\omega_0 I_0} & \frac{I}{\omega_0 I_0} & 0 & \frac{-I}{\omega_0 I_0} & \frac{I}{2\omega_0 I_0} \end{pmatrix}. \tag{1.98}$$

Jordan canonical form **J** contains two Jordan blocks of dimension two for zero eigenvalues of algebraic multiplicity two, another two independent zero eigenvalues and two non-zero eigenvalues. The last two are complex conjugated and they belong to regular synchronous precession, corresponding generalized eigenvectors in the fourth and eighth column of matrix **Q** are also conjugated and satisfy the structure introduced in (1.86). They can therefore be understood as regular eigenvectors.The geometric meaning of related normal modes of regular synchronous precession is a spherical motion with its centre of motion located in the centre of mass of the shaft body. The axis of rotation ω_0 moves conically with angular frequency determined by the ratio of moments of inertia and the shaft's angular speed. The rest of generalized eigenvectors do not have structure of the regular eigenvectors. As can be seen in the matrix **Q**, it is clear how they use up *allowed* degrees of freedom; static translational and angular displacements and translational movement. An unenforced angular motion of the free rotating shaft, with exception of the regular synchronous precession, is not a part of the general solution, because vector describing such motion does not belong to linear space of basis **Q**.

1.6 Motivation and Objectives

1.6.1 Thermal Aspects of Aerostatic Bearings

Only limited attention has been paid to thermal analysis of gas bearings so far and there are minimal scientific publications in literature sources on the subject. This is probably because there is not an extended use of gas bearings in comparison with oil bearings or bearings with rolling elements. In view of the low viscosity of air, the heat generation due to shear rate seems negligible at a glance. However, the fact is that for modern high-speed machinery, the temperature conditions are important. The concerns are not only the heat generated via shear rate, but also the heat transfer through bearings, which fulfil their cooling duty in many applications. Cited experimental work of Ohishi and Matsuzaki [26] has shown that temperature rise in bearing can easily exceed 30 °C at a relatively low speed of 20,000 rpm. In addition to air properties, the bearing geometry also changes with temperature, especially when materials with different temperature dilatation coefficients are used for journal and bearing bush. These changes are significant, considering the small radial clearance. Often a water cooling system is implemented to high speed devices using gas bearings. During the design stage of such devices, the information on thermal behaviour of journal-bush-housing system is valuable, especially for equipment where operating precision is a critical parameter.

The graph in fig. 1.9 illustrates typical clearance change (relative clearance $c/R = 0.001$) for steel shaft and bronze bush drawn together with changes of selected air properties at atmospheric pressure. 275 K was used as the nominal temperature. It is evident from this graph that a change in bearing operating temperature is likely to alter the bearing performance. On the other hand, Ohishi and Matsuzaki [26] found aerostatic bearings working with small

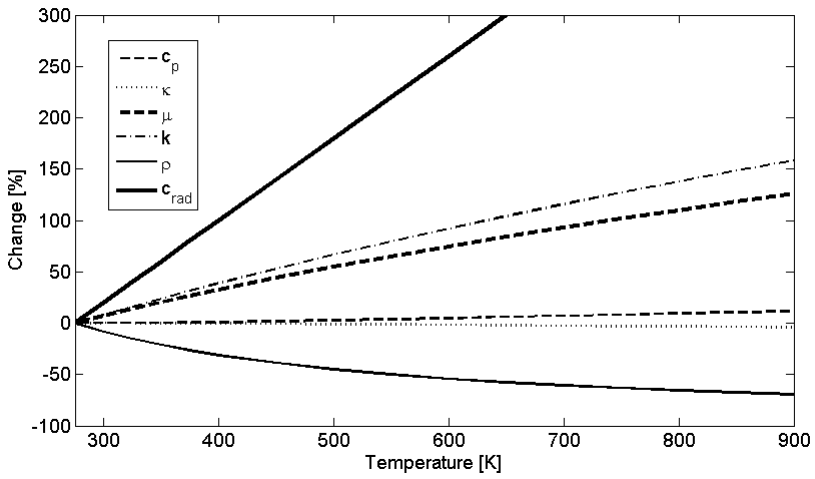

Figure 1.9: Change of bearing clearance and air properties with temperature. c_p – Isobaric specific heat capacity, κ – Ratio of specific heats, μ – Dynamic viscosity, k – Thermal conductivity, ρ – Density, c – Bearing radial clearance for combination steel-bronze at $c/R = 0.001$

variations of temperature of the air film. This finding suggests that if the bearing operating temperature is known, then isothermal models will produce adequate results. The one of the aims of this dissertation is to develop a thermo-hydrodynamic lubrication model of aerostatic bearings that could be capable of predicting the bearing operating temperature and to assess the suitability of using isothermal bearing models.

1.6.2 Isothermal Aerostatic Bearings Properties

Isothermal models of aerostatic bearings with orifice restrictors contain noticeable nonlinearities that are caused by nonlinear Reynolds equation of classical lubrication theory and nonlinearity of equations driving air inlet flow. Transient solver could be used to calculate the pressure distribution inside the air film and bearing reaction. However, that would involve the solving of Reynolds equation in the time domain. The former use of aerostatic bearings has rendered them closely linear within the certain eccentricities. Bearings at these conditions can therefore be represented by a set of linear coefficients of stiffness and damping. Such coefficients can be obtained by various methods, presented in literature: Czolczyński [39], Han et al. [40], Czolczyński [41]. The next two objectives of this work are to develop an isothermal aerostatic bearing model for transient analysis and to establish a feasible method of evaluation of bearing linearity at specific conditions. The applicability of linear bearing coefficients will be based on the results of this linearity assessment. While the methods presented in the literature focus on only coefficients related to lateral translations, this dissertation will cover linear stiffness and damping coefficients corresponding to lateral translational displace-

ments, as well as the angular displacements and the coefficients of cross-coupling between translational and angular displacements.

1.6.3 Models of Rotors Supported by Aerostatic Bearings

If bearings can be considered linear and the rotor model is free from nonlinearities of other origin, then determination of the response of the rotor system by means of spectral decomposition is applicable. Rotors supported in strongly nonlinear bearings can be, for the purpose of transient analysis, treated as free rotors with bearing reactions acting as excitation forces. Finite element models of such rotors are accessible by numerical solvers in the physical domain, although the number of degrees of freedom might be unnecessarily high for an adequate description of system dynamics. These systems with the singular stiffness matrix and gyroscopic generalized damping are defective and cannot be treated by spectral decomposition.

Although there are some algorithms of numerical Jordan decomposition (working with floating point arithmetics) published in the literature the task is commonly perceived as very difficult, ill-posed and extremely sensitive to numerical errors. The author of this work did not test such algorithms, because the relevant matrices of rotor systems are usually large and always poorly conditioned, even if they are not defective. He has decided to leave the numerical algorithms of Jordan decomposition out of the scope of this work, even though it is admittable that such an algorithm, consistently and reliably working on large matrices of his interest, would be of great value. Another objective of this work is to investigate and test available options of the reduction of defective systems generated by gyroscopic rotor models with singular stiffness matrices. This work presents a Timoshenko rotating beam (shaft) element that has a rotation of cross-section treated as an independent degree of freedom. Internal viscous damping of this model is also incorporated.

Chapter 2

Rotordynamics of Flexible Rotors

2.1 Chapter Outline

This chapter documents the main parts of program MEROT that has been built to provide models of elastic rotors constructed by finite element method and respective analysis tools of rotordynamics. It has been built entirely in MATLAB as a set of routines that can be used in a modular way to suite the analysed problem. Instead of detailed description of the code, that would likely to occupy entire volume of the text, an higher altitude image is offered, leaving enough space to deal with particularly important topics with occasional excursions beyond the implemented features to discuss potential extension related to specific rotordynamics problems.

Apart from standard analyses of rotor models supported in linear bearings, the transient solver of equations of motion of rotor supported by nonlinear bearings is provided. Models of aerostatic bearings developed and described in the next chapter can be linked to this solver.

Transient analysis can be performed on full set of equations of motion, or it can run on reduced models of rotor. Those deserve serious attention owing to problems linked with spectral decomposition of free (unsupported) rotor with gyroscopic effects. Unlike the rotor constrained to the inertial frame by linear stiffness of the bearings, the free rotor generates defective, non-diagonalizable system matrix. In such case, spectral decomposition and modal reduction cannot be used directly, which is the reason, why transient analyses are usually performed in the physical space. Three possible methods of reduction of defective systems are described and evaluated in the text of this chapter.

Attention is also paid to eigenvalue problem conditioning, quality of finite element model representation and differences between Rayleigh and Timoshenko rotating beam models in terms of selected eigenvalues.

2.2 Concept of MEROT Routine Package

Structure of the program is drawn in the figure 2.1. It contains procedures for creating FEM models of rotors based on Rayleigh and Timoshenko finite elements as described in following sections. It also contains tools for analysis and further treatment of these models: Modal analysis of rotors with linear bearings, calculation of critical speed maps, whirl maps, frequency response functions to harmonic excitation by unbalance and transfer functions for calculation of response to general time-dependent excitation of the linear system.

The ellipse labelled "Non-linear forces" is an external routine that provides vector of forces dependent on actual state vector of the rotor system and the time. It can conclude nonlinear bearing models as well as any arbitrary excitation forces. It is used in connection with transient solvers (4th order Runge-Kutta and Newmark-β method). The analysed models can be composed of several coupled rotors, using either full systems of equations of motion or Craig-Bampton reduced systems.

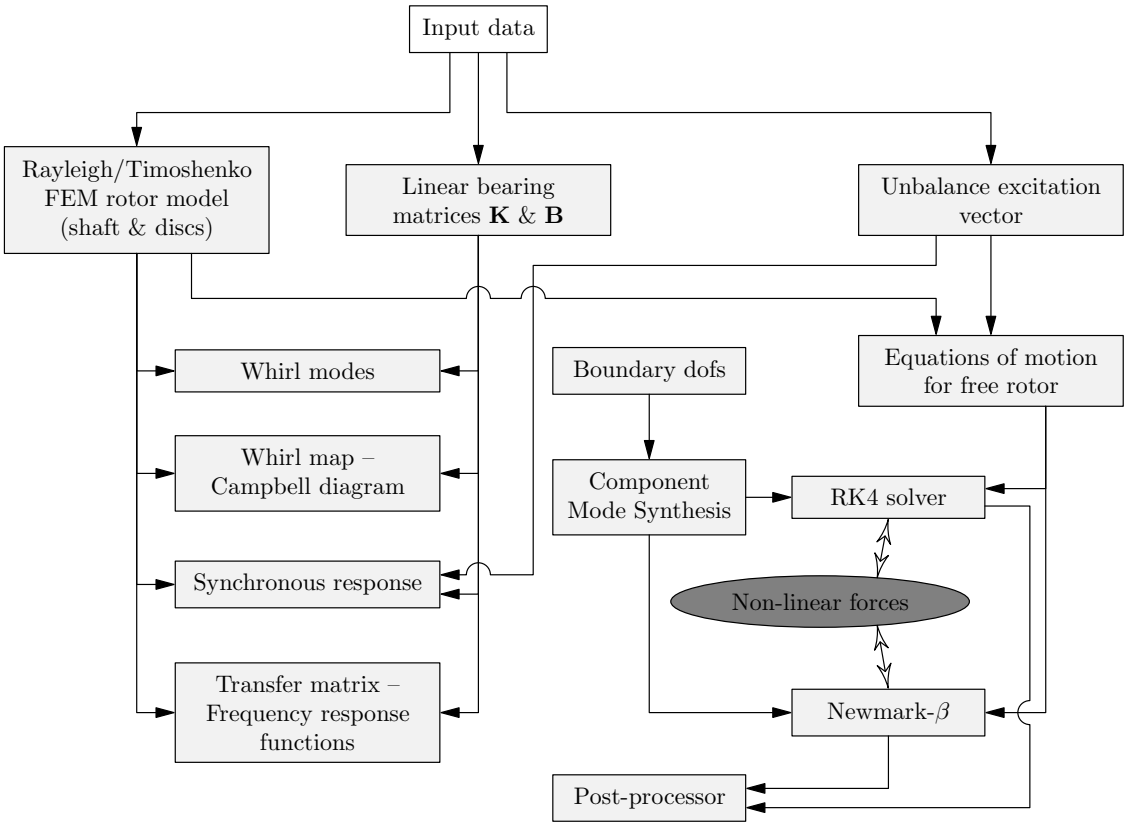

Figure 2.1: MEROT scheme

2.2.1 Timoshenko Shaft Finite Elements

One assumption of Euler-Bernoulli beam theory is that planar cross section of beam remains planar and perpendicular to the neutral axis during bending deformation of the beam. This assumption (Navier's hypothesis) is appropriate in the case of slender beams, where contribution of shear deformation to the total deformation energy is negligible. Beam slenderness can be quantified by means of shear deformation coefficient Φ defined as the ratio of the bending and the shear stiffness

$$\Phi = \frac{12\,E\,J}{\kappa\,A\,G\,l_b^2}, \tag{2.1}$$

where κ is shear correction coefficient depending on the cross section. If $\Phi \ll 1$ than Euler-Navier hypothesis is valid. In the case of thicker beams that do not obey this assumption, Timoshenko beam model should be implemented to respect additional shear deformation. The length l_b should not be understood only as the length of the beam, defined by beam supports, but it should be considered as a reduced length, defined by deflection mode of the beam. For dynamic analysis of beam/shaft structures, where higher vibration modes are of concern, is its value driven by wavelength of particular mode. In such case, the beam that appears slender from static point of view may become thick, when dynamic analysis is applied. Respecting the shear deformation as well as the bending one, deplanation of beam cross-section takes place, because of uneven distribution of shear stress upon cross-section. Cross-section warping is neglected in Timoshenko model by assuming constant shear stress τ_S, for what the κ coefficient is introduced in order to satisfy

$$\int_A \tau(y,z)\mathrm{d}A = \kappa\tau_S\,A = \kappa AG\delta. \tag{2.2}$$

For full circular cross section is

$$\kappa = \frac{6\,(1+\nu)}{7+6\nu} \tag{2.3}$$

and for hollow circular cross section

$$\kappa = \frac{6\,(1+\nu)\left(1+m^2\right)^2}{(7+6\nu)\left(1+m^2\right)^2 + (20+20\nu)\;m^2}, \tag{2.4}$$

where ν denotes the Poisson constant of shaft material and m is the ratio of inner to outer radii. [42]. Constant shear stress causes rotation of the cross section additional to the angle caused by pure bending. This situation is depicted in figure 2.2.

Finite elements of rotating shafts respecting shear deformation can be found e.g. in the book of Byrtus et al. [43], or in the papers of Qin and Mao [44], Mohiuddin and Khulief [45], Lee et al. [46], and L.-W.Chen and Peng [47].

Finite elements presented in [43], [44], [45], [46] do respect that the slope of deflection curve of shaft element is generally different from the angle of rotation of element's cross section, but do not treat shear induced rotation of cross section as independent degree of

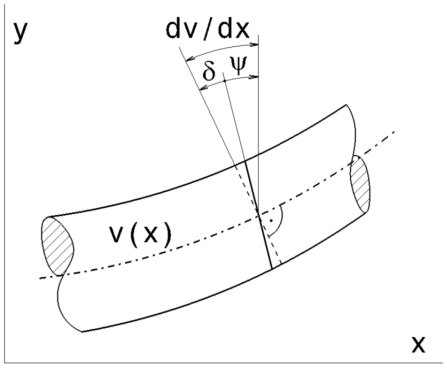

Figure 2.2: Rotation of cross section of Timoshenko beam due to shear stress

freedom. Instead, the equation

$$EJ\,\frac{\partial^2 \psi}{\partial\, x^2} + \kappa GA\,\delta = 0, \tag{2.5}$$

is used to couple shear and bending contributions to the rotation of element's cross section. This equation is valid for static deflection of the shaft and it can be incorporated into Rayleigh model formulation. These shaft elements are referred in this work to as quasistatic Timoshenko finite elements. Preserving the formalism of FEM model in [38], quasistatic finite elements, expressed in the non-rotating coordinates are enclosed in appendix A. More general formulation of these quasistatic elements in co-rotating coordinates can be found in the cited book [43].

Without the equation (2.5), the shear and the bending deformations of a shaft element are independent degrees of freedom, which will double the number of independent state variables of model of elastic shaft. Non-rotating Timoshenko beam finite element models can be found in [48] and [49]. Authors L.-W.Chen and Peng [47] deliver the finite element model of rotating Timoshenko beam in co-rotating coordinates. Description of the model in co-rotating coordinates was beneficial in their particular study, because they investigated shafts with dissimilar lateral moments of inertia. Not having that in scope, the equations of motion in static coordinates are more convenient, especially when anisotropic bearings are planned to be incorporated. Both the independent variables, the lateral displacements and the shear induced rotation, are approached by third order polynomials. Using lower order of approximation would lead to shear lock phenomenon [50], where constant shear rotation angle over single element does not create adequate contribution to the deformation energy. This results in overestimated stiffness of an element.

the lateral generalized displacements v,ψ and w,ϑ are now four independent variables. State of the element is described by vector of nodal displacements

$$\mathbf{q}^e = \left(\mathbf{q}_v^{\mathrm{T}}, \mathbf{q}_\psi^{\mathrm{T}}, \mathbf{q}_w^{\mathrm{T}}, \mathbf{q}_\vartheta^{\mathrm{T}} \right)^{\mathrm{T}}, \tag{2.6}$$

where

$$\mathbf{q}_v = \begin{pmatrix} v(0) \\ \frac{\mathrm{d}v}{\mathrm{d}x}(0) \\ v(l) \\ \frac{\mathrm{d}v}{\mathrm{d}x}(l) \end{pmatrix}, \quad \mathbf{q}_\psi = \begin{pmatrix} \psi(0) \\ \frac{\mathrm{d}\psi}{\mathrm{d}x}(0) \\ \psi(l) \\ \frac{\mathrm{d}\psi}{\mathrm{d}x}(l) \end{pmatrix}, \quad \mathbf{q}_w = \begin{pmatrix} w(0) \\ \frac{\mathrm{d}w}{\mathrm{d}x}(0) \\ w(l) \\ \frac{\mathrm{d}w}{\mathrm{d}x}(l) \end{pmatrix}, \quad \mathbf{q}_\vartheta = \begin{pmatrix} \vartheta(0) \\ \frac{\mathrm{d}\vartheta}{\mathrm{d}x}(0) \\ \vartheta(l) \\ \frac{\mathrm{d}\vartheta}{\mathrm{d}x}(l) \end{pmatrix}. \tag{2.7}$$

Shaft generalized displacements are approached by third order polynomial

$$v(x) = \mathbf{N}\mathbf{q}_v, \quad \psi(x) = \mathbf{N}\mathbf{q}_\psi, \quad w(x) = \mathbf{N}\mathbf{q}_w, \quad \vartheta(x) = \mathbf{N}\mathbf{q}_\vartheta, \quad \mathbf{N} = \mathbf{P}_3\,\mathbf{S}_1^{-1}, \tag{2.8}$$

$$\begin{aligned} N_1 &= 1 - 3\,\tfrac{x^2}{l^2} + 2\,\tfrac{x^3}{l^3}, & N_2 &= x - 2\,\tfrac{x^2}{l} + \tfrac{x^3}{l^2}, \\ N_3 &= 3\,\tfrac{x^2}{l^2} - 2\,\tfrac{x^3}{l^3}, & N_4 &= -\tfrac{x^2}{l} + \tfrac{x^3}{l^2}. \end{aligned} \tag{2.9}$$

Potential strain energy of shaft element contains both the bending and the shear components

$$U^e = \frac{1}{2}\int_0^l \left(EJ(x) \left(\left(\frac{\partial \psi}{\partial x} \right)^2 + \left(\frac{\partial \vartheta}{\partial x} \right)^2 \right) + \kappa GA(x) \left(\left(\frac{\partial v}{\partial x} - \psi \right)^2 + \left(\frac{\partial w}{\partial x} + \vartheta \right)^2 \right) \right) \mathrm{d}x, \tag{2.10}$$

written in terms of nodal displacements

$$\begin{aligned} U^e = \frac{1}{2}\int_0^l \Bigg(& EJ(x) \left(\mathbf{q}_\psi^{\mathrm{T}} \frac{\partial \mathbf{N}^{\mathrm{T}}}{\partial x} \frac{\partial \mathbf{N}}{\partial x} \mathbf{q}_\psi + \mathbf{q}_\vartheta^{\mathrm{T}} \frac{\partial \mathbf{N}^{\mathrm{T}}}{\partial x} \frac{\partial \mathbf{N}}{\partial x} \mathbf{q}_\vartheta \right) \\ & + \kappa GA(x) \left(\mathbf{q}_v^{\mathrm{T}} \frac{\partial \mathbf{N}^{\mathrm{T}}}{\partial x} \frac{\partial \mathbf{N}}{\partial x} \mathbf{q}_v - 2\mathbf{q}_v^{\mathrm{T}} \frac{\partial \mathbf{N}^{\mathrm{T}}}{\partial x} \mathbf{N}\mathbf{q}_\psi + \mathbf{q}_\psi^{\mathrm{T}} \mathbf{N}^{\mathrm{T}} \mathbf{N}\mathbf{q}_\psi \right. \\ & \left. + \mathbf{q}_w^{\mathrm{T}} \frac{\partial \mathbf{N}^{\mathrm{T}}}{\partial x} \frac{\partial \mathbf{N}}{\partial x} \mathbf{q}_w + 2\mathbf{q}_w^{\mathrm{T}} \frac{\partial \mathbf{N}^{\mathrm{T}}}{\partial x} \mathbf{N}\mathbf{q}_\vartheta + \mathbf{q}_\vartheta^{\mathrm{T}} \mathbf{N}^{\mathrm{T}} \mathbf{N}\mathbf{q}_\vartheta \right) \Bigg) \mathrm{d}x. \end{aligned} \tag{2.11}$$

Kinetic energy of the element

$$T^e = \frac{1}{2}\int_0^l \left(\rho A(x) \left(\dot{v}^2 + \dot{w}^2 \right) + \rho J(x) \left(\dot{\psi}^2 + \dot{\vartheta}^2 \right) + \rho J_p(x) \omega_0 \left(2\,\dot{\vartheta}\,\psi + 1 \right) \right) \mathrm{d}x \tag{2.12}$$

written by means of nodal displacements

$$\begin{aligned} T^e = \frac{1}{2}\int_0^l & \left(\rho A(x) \left(\dot{\mathbf{q}}_v^{\mathrm{T}} \mathbf{N}^{\mathrm{T}} \mathbf{N} \dot{\mathbf{q}}_v + \dot{\mathbf{q}}_w^{\mathrm{T}} \mathbf{N}^{\mathrm{T}} \mathbf{N} \dot{\mathbf{q}}_w \right) + \rho J(x) \left(\dot{\mathbf{q}}_\psi^{\mathrm{T}} \mathbf{N}^{\mathrm{T}} \mathbf{N} \dot{\mathbf{q}}_\psi + \dot{\mathbf{q}}_\vartheta^{\mathrm{T}} \mathbf{N}^{\mathrm{T}} \mathbf{N} \dot{\mathbf{q}}_\vartheta \right) \right. \\ & \left. + \rho\, J_p(x)\, \omega_0 \, \left(2 \dot{\mathbf{q}}_\vartheta^{\mathrm{T}} \mathbf{N}^{\mathrm{T}} \mathbf{N} \mathbf{q}_\psi + 1 \right) \right) \mathrm{d}x. \end{aligned} \tag{2.13}$$

Application of Lagrange equations to potential and kinetic energy

$$\frac{\mathrm{d}}{\mathrm{d}t}\left(\frac{\partial T^e}{\partial \dot{\mathbf{q}}^e}\right) - \frac{\partial T^e}{\partial \mathbf{q}^e} + \frac{\partial U^e}{\partial \mathbf{q}^e} = \mathbf{M}_T^e\,\ddot{\mathbf{q}}^e + \omega_0\,\mathbf{G}_T^e\,\dot{\mathbf{q}}^e + \mathbf{K}_T^e\,\mathbf{q}^e \tag{2.14}$$

renders

$$\mathbf{M}_T^e = \begin{pmatrix} \mathbf{I}_1 & \mathbf{0} & \mathbf{0} & \mathbf{0} \\ \mathbf{0} & \mathbf{I}_2 & \mathbf{0} & \mathbf{0} \\ \mathbf{0} & \mathbf{0} & \mathbf{I}_1 & \mathbf{0} \\ \mathbf{0} & \mathbf{0} & \mathbf{0} & \mathbf{I}_2 \end{pmatrix}, \quad \mathbf{G}_T^e = \begin{pmatrix} \mathbf{0} & \mathbf{0} & \mathbf{0} & \mathbf{0} \\ \mathbf{0} & \mathbf{0} & \mathbf{0} & -2\mathbf{I}_2 \\ \mathbf{0} & \mathbf{0} & \mathbf{0} & \mathbf{0} \\ \mathbf{0} & 2\mathbf{I}_2^{\mathrm{T}} & \mathbf{0} & \mathbf{0} \end{pmatrix}, \tag{2.15}$$

and

$$\mathbf{K}_T^e = \begin{pmatrix} \mathbf{I}_3 & -\mathbf{I}_4 & \mathbf{0} & \mathbf{0} \\ -\mathbf{I}_4^{\mathrm{T}} & \mathbf{I}_5 + \mathbf{I}_6 & \mathbf{0} & \mathbf{0} \\ \mathbf{0} & \mathbf{0} & \mathbf{I}_3 & \mathbf{I}_4 \\ \mathbf{0} & \mathbf{0} & \mathbf{I}_4^{\mathrm{T}} & \mathbf{I}_5 + \mathbf{I}_6 \end{pmatrix}. \tag{2.16}$$

Auxiliary integrals are

$$\begin{aligned} &\mathbf{I}_1 = \int_0^l \rho A \mathbf{N}^{\mathrm{T}}\mathbf{N}\mathrm{d}x, \quad \mathbf{I}_2 = \int_0^l \rho J \mathbf{N}^{\mathrm{T}}\mathbf{N}\mathrm{d}x, \quad \mathbf{I}_3 = \int_0^l \kappa G A \frac{\partial \mathbf{N}^{\mathrm{T}}}{\partial x}\frac{\partial \mathbf{N}}{\partial x}\mathrm{d}x, \\ &\mathbf{I}_4 = \int_0^l \kappa G A \frac{\partial \mathbf{N}^{\mathrm{T}}}{\partial x}\mathbf{N}\mathrm{d}x, \quad \mathbf{I}_5 = \int_0^l E J \frac{\partial \mathbf{N}^{\mathrm{T}}}{\partial x}\frac{\partial \mathbf{N}}{\partial x}\mathrm{d}x, \quad \mathbf{I}_6 = \int_0^l \kappa G A \mathbf{N}^{\mathrm{T}}\mathbf{N}\mathrm{d}x. \end{aligned} \tag{2.17}$$

For prismatic circular shaft element, it is possible to evaluate these integrals as

$$\mathbf{I}_1 = \rho A \begin{pmatrix} \frac{13l}{35} & \frac{11l^2}{210} & \frac{9l}{70} & \frac{-13l^2}{420} \\ & \frac{l^3}{105} & \frac{13l^2}{420} & \frac{-l^3}{140} \\ & & \frac{13l}{35} & \frac{-11l^2}{210} \\ sym. & & & \frac{l^3}{105} \end{pmatrix}, \quad \mathbf{I}_2 = \rho J \begin{pmatrix} \frac{13l}{35} & \frac{11l^2}{210} & \frac{9l}{70} & \frac{-13l^2}{420} \\ & \frac{l^3}{105} & \frac{13l^2}{420} & \frac{-l^3}{140} \\ & & \frac{13l}{35} & \frac{-11l^2}{210} \\ sym. & & & \frac{l^3}{105} \end{pmatrix}, \tag{2.18}$$

$$\mathbf{I}_3 = \kappa G A \begin{pmatrix} \frac{6}{5l} & \frac{1}{10} & \frac{-6}{5l} & \frac{1}{10} \\ & \frac{2l}{15} & \frac{-1}{10} & \frac{-l}{30} \\ & & \frac{6}{5l} & \frac{-1}{10} \\ sym. & & & \frac{2l}{15} \end{pmatrix}, \quad \mathbf{I}_4 = \kappa G A \begin{pmatrix} \frac{-1}{2} & \frac{-l}{10} & \frac{-1}{2} & \frac{l}{10} \\ \frac{l}{10} & 0 & \frac{-l}{10} & \frac{l^2}{60} \\ \frac{1}{2} & \frac{l}{10} & \frac{1}{2} & \frac{-l}{10} \\ \frac{-l}{10} & \frac{-l^2}{60} & \frac{l}{10} & 0 \end{pmatrix}, \tag{2.19}$$

$$\mathbf{I}_5 = EJ \begin{pmatrix} \frac{6}{5l} & \frac{1}{10} & \frac{-6}{5l} & \frac{1}{10} \\ & \frac{2l}{15} & \frac{-1}{10} & \frac{-l}{30} \\ & & \frac{6}{5l} & \frac{-1}{10} \\ sym & & & \frac{2l}{15} \end{pmatrix}, \quad \mathbf{I}_6 = \kappa G A \begin{pmatrix} \frac{13l}{35} & \frac{11l^2}{210} & \frac{9l}{70} & \frac{-13l^2}{420} \\ & \frac{l^3}{105} & \frac{13l^2}{420} & \frac{-l^3}{140} \\ & & \frac{13l}{35} & \frac{-11l^2}{210} \\ sym. & & & \frac{l^3}{105} \end{pmatrix}. \tag{2.20}$$

Transformation to global displacement coordinates

$$\tilde{\mathbf{q}}^e = \Big(v(0),\, \tfrac{\mathrm{d}v}{\mathrm{d}x}(0),\, \psi(0),\, \tfrac{\mathrm{d}\psi}{\mathrm{d}x}(0),\, w(0),\, \tfrac{\mathrm{d}w}{\mathrm{d}x}(0),\, \vartheta(0),\, \tfrac{\mathrm{d}\vartheta}{\mathrm{d}x}(0),\\ v(l),\, \tfrac{\mathrm{d}v}{\mathrm{d}x}(l),\, \psi(l),\, \tfrac{\mathrm{d}\psi}{\mathrm{d}x}(l),\, w(l),\, \tfrac{\mathrm{d}w}{\mathrm{d}x}(l),\, \vartheta(l),\, \tfrac{\mathrm{d}\vartheta}{\mathrm{d}x}(l)\Big)^{\mathrm{T}} \tag{2.21}$$

is again done via permutation matrix $\mathbf{T}$ with elements

$$T_{ij} = \begin{cases} 1 & \text{for } i,j = 1,1;2,2;3,9;4,10;5,3;6,4;7,11;8,12;\\ & \qquad 9,5;10,6;11,13;12,14;13,7;14,8;15,15;16,16 \\ 0 & \text{else,} \end{cases} \tag{2.22}$$

For quasistatic Timoshenko model, derived in appendix A, the matrices (1.72) can be used, which assumes that angular displacements of the discs are driven by actual angles of shaft cross section. This is rightful expectation in the case of very thin disc, especially if it makes one piece with the shaft. For disc the length of which is comparable to shaft diameter, the angular displacements should be derived rather from the slope of shaft deflection. Disc matrices for Timoshenko model derived in this section are similar to those of Rayleigh model (1.72). Angular displacements of disc, the slope of deflection curve or angular displacement of shaft cross section are both possible to respect. In both cases, only rows and columns of zero vectors have to be added to the matrices (1.72).

2.2.2 Rotor Damping

Damping of mechanical structures has complicated nature and basic linear models are strong simplification of complex reality. Detailed studies on damping of rotating structures are beyond the scope of this work. However, it is worth noticing that some new phenomena arise in the case of damping of rotating structures in comparison to the non-rotating ones. In the case of rotating structures, the damping effects can be separated into two parts: the internal and the external damping. The internal damping consists mainly of material hysteretic damping due to elastic deformation of the shaft and of structural dry friction between components of the rotor. The origin of external damping is in the interaction of rotor and surrounding media, e.g. compressor wheels, turbines, and especially bearings. The effects of internal and external damping, hysteretic damping, and structural dry friction on stability as well as the enforced vibration of rotors are analytically studied in the famous book of Tondl [51]. Detailed study of rotor internal damping instability can be found in doctoral thesis of Kandil [52].

For its complexity in nature and nonlinearity, damping is often considered as viscous damping i.e. linear function of velocity. External damping forces act in the inertial coordinates, in which the presented rotor models are formulated, so that forces acting upon shaft element at inertial coordinates, such as bearing reactions or drag forces induced by interaction between impellers and surrounding media, can be directly linearized with respect to vector $\dot{\mathbf{q}}$.

Internal viscous damping, incorporated into the model of elastic rotor described as (1.71), can be constructed by means of Rayleigh dissipation function in co-rotating coordinates defined as

$$\begin{pmatrix} x_R \\ y_R \\ z_R \end{pmatrix} = \begin{pmatrix} 1 & 0 & 0 \\ 0 & \cos\omega_0 t & \sin\omega_0 t \\ 0 & -\sin\omega_0 t & \cos\omega_0 t \end{pmatrix} \begin{pmatrix} x \\ y \\ z \end{pmatrix}. \tag{2.23}$$

For quasistatic Timoshenko elements, similar to model in appendix A, can be the implementation of internal viscous damping found in [43]. For 16 degree of freedom version of Timoshenko shaft finite element, presented in this chapter, the Rayleigh dissipation function is constructed with help of potential function similar to strain potential energy (2.10). For viscoelastic material, the viscous part of potential function can be considered

$$\begin{aligned} D_R^e = \frac{\alpha_V}{2} \int_0^l \Bigg(& EJ(x) \left(\left(\frac{\partial \dot{\psi}_R}{\partial x} \right)^2 + \left(\frac{\partial \dot{\vartheta}_R}{\partial x} \right)^2 \right) \\ & + \kappa GA(x) \left(\left(\frac{\partial \dot{v}_R}{\partial x} - \dot{\psi}_R \right)^2 + \left(\frac{\partial \dot{w}_R}{\partial x} + \dot{\vartheta}_R \right)^2 \right) \Bigg) \, \mathrm{d}x, \end{aligned} \tag{2.24}$$

written in terms of nodal displacements in co-rotating coordinate system

$$\begin{aligned} D_R^e = \frac{\alpha_V}{2} \int_0^l \Bigg(& EJ(x) \left(\dot{\mathbf{q}}_{\psi R}^{\mathrm{T}} \frac{\partial \mathbf{N}^{\mathrm{T}}}{\partial x} \frac{\partial \mathbf{N}}{\partial x} \dot{\mathbf{q}}_{\psi R} + \dot{\mathbf{q}}_{\vartheta R}^{\mathrm{T}} \frac{\partial \mathbf{N}^{\mathrm{T}}}{\partial x} \frac{\partial \mathbf{N}}{\partial x} \dot{\mathbf{q}}_{\vartheta R} \right) \\ & + \kappa GA(x) \left(\dot{\mathbf{q}}_{vR}^{\mathrm{T}} \frac{\partial \mathbf{N}^{\mathrm{T}}}{\partial x} \frac{\partial \mathbf{N}}{\partial x} \dot{\mathbf{q}}_{vR} - 2\dot{\mathbf{q}}_{vR}^{\mathrm{T}} \frac{\partial \mathbf{N}^{\mathrm{T}}}{\partial x} \mathbf{N} \dot{\mathbf{q}}_{\psi R} + \dot{\mathbf{q}}_{\psi R}^{\mathrm{T}} \mathbf{N}^{\mathrm{T}} \mathbf{N} \dot{\mathbf{q}}_{\psi R} \right. \\ & \left. + \dot{\mathbf{q}}_{wR}^{\mathrm{T}} \frac{\partial \mathbf{N}^{\mathrm{T}}}{\partial x} \frac{\partial \mathbf{N}}{\partial x} \dot{\mathbf{q}}_{wR} + 2\dot{\mathbf{q}}_{wR}^{\mathrm{T}} \frac{\partial \mathbf{N}^{\mathrm{T}}}{\partial x} \mathbf{N} \dot{\mathbf{q}}_{\vartheta R} + \dot{\mathbf{q}}_{\vartheta R}^{\mathrm{T}} \mathbf{N}^{\mathrm{T}} \mathbf{N} \dot{\mathbf{q}}_{\vartheta R} \right) \Bigg) \, \mathrm{d}x. \end{aligned} \tag{2.25}$$

Vectors of nodal displacements in co-rotating frame are constructed as

$$\mathbf{q}_R^e = \left(\mathbf{q}_{vR}^{\mathrm{T}}, \mathbf{q}_{\psi R}^{\mathrm{T}}, \mathbf{q}_{wR}^{\mathrm{T}}, \mathbf{q}_{\vartheta R}^{\mathrm{T}} \right)^{\mathrm{T}}, \tag{2.26}$$

where

$$\mathbf{q}_{vR} = \begin{pmatrix} v_R(0) \\ \frac{\mathrm{d}v_R}{\mathrm{d}x}(0) \\ v_R(l) \\ \frac{\mathrm{d}v_R}{\mathrm{d}x}(l) \end{pmatrix}, \quad \mathbf{q}_{\psi R} = \begin{pmatrix} \psi_R(0) \\ \frac{\mathrm{d}\psi_R}{\mathrm{d}x}(0) \\ \psi_R(l) \\ \frac{\mathrm{d}\psi_R}{\mathrm{d}x}(l) \end{pmatrix}, \quad \mathbf{q}_{wR} = \begin{pmatrix} w_R(0) \\ \frac{\mathrm{d}w_R}{\mathrm{d}x}(0) \\ w_R(l) \\ \frac{\mathrm{d}w_R}{\mathrm{d}x}(l) \end{pmatrix}, \quad \mathbf{q}_{\vartheta R} = \begin{pmatrix} \vartheta_R(0) \\ \frac{\mathrm{d}\vartheta_R}{\mathrm{d}x}(0) \\ \vartheta_R(l) \\ \frac{\mathrm{d}\vartheta_R}{\mathrm{d}x}(l) \end{pmatrix}. \tag{2.27}$$

Transformation of nodal quantities from non-rotating coordinates to co-rotating coordinates is

$$\mathbf{q}_R^e = \mathbf{T}_R(t) \, \mathbf{q}^e, \tag{2.28}$$

where transformation matrix $\mathbf{T}_R(t)$ is unitary matrix of structure

$$\mathbf{T}_R(t) = \begin{pmatrix} \mathbf{C} & \mathbf{0} & \mathbf{S} & \mathbf{0} \\ \mathbf{0} & \mathbf{C} & \mathbf{0} & -\mathbf{S} \\ -\mathbf{S} & \mathbf{0} & \mathbf{C} & \mathbf{0} \\ \mathbf{0} & \mathbf{S} & \mathbf{0} & \mathbf{C} \end{pmatrix}, \quad \mathbf{C} = \mathbf{I}\cos\omega_0 t, \quad \mathbf{S} = \mathbf{I}\sin\omega_0 t. \tag{2.29}$$

Rayleigh dissipative term in non-rotating coordinates is then

$$\frac{\partial D^e}{\partial \dot{\mathbf{q}}^e} = \mathbf{T}_R^{\mathrm{T}}(t)\,\frac{\partial D_R^e}{\partial \dot{\mathbf{q}}_R^e}, \tag{2.30}$$

where

$$\frac{\partial D_R^e}{\partial \dot{\mathbf{q}}_R^e} = \mathbf{B}_{ITR}^e \dot{\mathbf{q}}_R^e. \tag{2.31}$$

Matrix of internal viscous damping in co-rotating frame $\mathbf{B}_{ITR}^e$ is

$$\mathbf{B}_{ITR}^e = \alpha_V\,\mathbf{K}_T^e. \tag{2.32}$$

Using transformation (2.28), the Rayleigh dissipative term in non-rotating frame becomes

$$\frac{\partial D^e}{\partial \dot{\mathbf{q}}^e} = \alpha_V \mathbf{T}_R^{\mathrm{T}}(t)\,\mathbf{K}_T^e \dot{\mathbf{T}}_R(t)\,\mathbf{q}^e + \alpha_V \mathbf{T}_R^{\mathrm{T}}(t)\,\mathbf{K}_T^e \mathbf{T}_R(t)\,\dot{\mathbf{q}}^e = \omega_0\,\mathbf{K}_{CT}^e \mathbf{q}^e + \mathbf{B}_{IT}^e \dot{\mathbf{q}}^e \tag{2.33}$$

introducing new local matrices. Matrix $\mathbf{K}_{CT}^e$ is circulatory stiffness matrix and $\mathbf{B}_{IT}^e$ is internal damping matrix. Both these matrices are constant in time. Owing to the properties of unitary transformation and the symmetry of matrix $\mathbf{K}_T^e$, the forms of the matrices (using the auxiliary integrals from (2.17)) are

$$\mathbf{B}_{IT}^e = \alpha_V \mathbf{K}_T^e = \alpha_V \begin{pmatrix} \mathbf{I}_3 & -\mathbf{I}_4 & \mathbf{0} & \mathbf{0} \\ -\mathbf{I}_4^{\mathrm{T}} & \mathbf{I}_5 + \mathbf{I}_6 & \mathbf{0} & \mathbf{0} \\ \mathbf{0} & \mathbf{0} & \mathbf{I}_3 & \mathbf{I}_4 \\ \mathbf{0} & \mathbf{0} & \mathbf{I}_4^{\mathrm{T}} & \mathbf{I}_5 + \mathbf{I}_6 \end{pmatrix},$$

$$\mathbf{K}_{CT}^e = \alpha_V \begin{pmatrix} \mathbf{0} & \mathbf{0} & \mathbf{I}_3 & \mathbf{I}_4 \\ \mathbf{0} & \mathbf{0} & -\mathbf{I}_4^{\mathrm{T}} & -(\mathbf{I}_5 + \mathbf{I}_6) \\ -\mathbf{I}_3 & \mathbf{I}_4 & \mathbf{0} & \mathbf{0} \\ -\mathbf{I}_4^{\mathrm{T}} & \mathbf{I}_5 + \mathbf{I}_6 & \mathbf{0} & \mathbf{0} \end{pmatrix}. \tag{2.34}$$

Full set of equations of motion of elements are

$$\frac{\mathrm{d}}{\mathrm{d}t}\left(\frac{\partial T^e}{\partial \dot{\mathbf{q}}^e}\right) - \frac{\partial T^e}{\partial \mathbf{q}^e} + \frac{\partial U^e}{\partial \mathbf{q}^e} + \frac{\partial D^e}{\partial \dot{\mathbf{q}}^e} = \mathbf{M}_T^e \ddot{\mathbf{q}}^e + (\omega_0\,\mathbf{G}_T^e + \alpha_V \mathbf{K}_T^e)\,\dot{\mathbf{q}}^e + (\mathbf{K}_T^e + \omega_0\,\mathbf{K}_{CT}^e)\,\mathbf{q}^e. \tag{2.35}$$

Internal damping effects are represented by two parts. The first one represented by matrix $\mathbf{B}^e_{IT}$ is the classical proportional damping. The second one, described by anti-symmetric circulatory matrix increases with rotor speed and has destabilizing effect.

Traditional approach to linear hysteretic, frequency-independent damping that uses complex stiffness matrix in the form

$$\mathbf{K}_H = \mathbf{K}\,(1 + j\alpha_H) \tag{2.36}$$

would lead in the case of rotor system to the equations of motion

$$\mathbf{M}\,\ddot{\mathbf{q}}(t) + \omega_0\,\mathbf{G}\,\dot{\mathbf{q}}(t) + \mathbf{K}\,(1 + j\alpha_H)\;\mathbf{q}(t) = \mathbf{f}(\dot{\mathbf{q}}, \mathbf{q}, t), \tag{2.37}$$

in which the material damping forces are independent on frequency and proportional to displacements. The equation (2.37) is viable only in the case of single-frequency steady state sinusoidal motion [52], which assumption can be expressed as

$$\mathbf{q}(t) = \mathbf{q}\mathrm{e}^{j\omega t}, \qquad \dot{\mathbf{q}}(t) = j\omega\mathbf{q}(t). \tag{2.38}$$

This condition can be satisfied during spectral decomposition process, so the equation (2.37) can be used for calculation of eigenmodes and frequency response functions, but it is unsuitable for numerical integration in the time domain. For time domain numerical solution, the internal damping can be implemented as non-linear forces. Overview of such models of internal damping can be found in the thesis of Kandil [52].

Another serious problem of hysteretic damping concept used in rotordynamics is that it tends to overestimate damping for very low frequencies of vibration. This frequency vanishes at synchronous whirl and thus the use of hysteretic damping leads to inconsistent results [53]. The paper of Genta and Amati [53] shows that the use of equivalent viscous damping to approach hysteretic damping of rotor systems gives agreement in natural frequencies and decay rates only for standstill rotor. With increasing speed, the decay rates of eigenmodes differ and this equivalent damping concept is not adequate for rotors running above critical speeds. To obtain good agreement in terms of decay rates as well, nonviscous models of damping must be introduced in the time domain formulation. The nonviscous damping model with finite number of viscous dampers that allows for writing equations of motion in the time domain is provided, with examples of application, in the referred article [53].

2.2.3 Finite Element Representation and Convergence of Eigenvalues

Effect of number of finite elements used for discretization of rotating shaft on the error of eigenvalues is investigated in this section. It is naturally assumed that computed eigenvalues converge to exact values as the number of elements increases, until of course the effects of numerical process of spectral decomposition become important. Higher number of elements

means higher influence of round-off errors and higher condition number for the eigenvalue problem of matrix **A**.

Convergence of eigenvalues is studied for both the Rayleigh and the Timoshenko shaft models. Prismatic circular shaft of 15 mm in diameter and length of 300 mm is used as a trial rotor. Material properties match the properties of steel: $E = 2.05\,\mathrm{MPa}$, $\nu = 0.3$, $\rho = 7860\,\mathrm{kgm}^{-3}$. The shaft is supported by isotropic linear bearings with stiffness $K_b = 1 \cdot 10^7\,\mathrm{Nm}^{-1}$ at both ends. Finite element models have been coded up in program Matlab. Spectral decomposition method is chosen by Matlab automatically based on the type of input matrix. For this particular case, `LAPACK` routine `DGEEV` is used. The matrix **A** is balanced first in order to reduce the condition number, QR algorithm follows. Condition number corresponding to the eigenvalue problem of matrix A is determined as `cond(V)`, which means condition number with respect to inversion of modal matrix.

$$\mathrm{cond}_{\mathrm{eig}}(\mathbf{A}) = \mathrm{cond}(\mathbf{V}) = \|\mathbf{V}\| \cdot \|\mathbf{V}^{-1}\|. \tag{2.39}$$

Condition numbers for this shape of system matrix are relatively high even for small number of elements. The actual values for trial case are displayed in fig. 2.3.

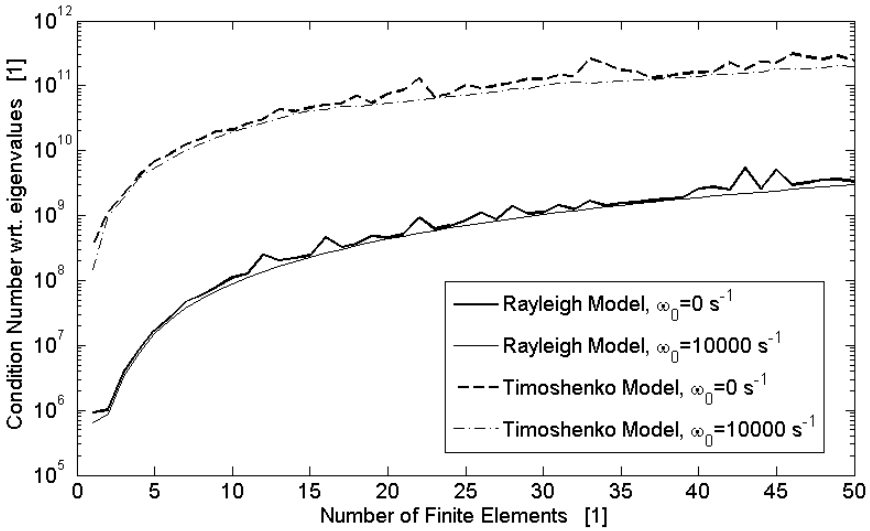

Figure 2.3: Condition numbers with respect to eigenvalues vs. number of finite elements

Rates of eigenvalues' convergence are depicted in figures 2.4 and 2.5 for Rayleigh and Timoshenko models. Relative differences of the lowest twenty imaginary parts of eigenvalues with respect to the values calculated for the highest number of elements are there plotted against number of elements used. From both these chart can be seen that minimum number of elements for relevant representation of eigenmodes corresponds to the half of the highest order of modes of the interest. The eigenmodes occur in pairs, so at least one element per

half-wave of the highest mode is necessary. Beyond this point the eigenfrequencies converge with similar speed for all eigenvalues, noticeably faster for Timoshenko model.

Shift of eigenfrequencies due to additional shear deformation is drawn in fig. 2.6 in ascending order of eigenvalues. The same differences drawn against the values of eigenfrequencies of Rayleigh model are in the fig. 2.7.

2.3 Numerical Methods of ODE Integration

Two basic methods for numerical integration of ordinary differential equations were implemented. the explicit 4th order Runge-Kutta method and the implicit A-stable Newmark-β method. An advantage of the former one is the higher order of error, but it is not suitable for stiff systems due to the fact that stability of this method is limited by highest eigenvalues of linearized system of solved equations. FEM models of rotor systems typically belong to highly stiff systems, what makes this numerical method feasible only for reduced systems. The latter method is suitable for stiff systems, owing to the unconditional stability for linear systems.

Runge-Kutta method is used to solve first order system in the state space

$$\mathbf{N}\dot{\mathbf{u}} + \mathbf{P}\mathbf{u} = \mathbf{F}. \tag{2.40}$$

For given time step Δt and known current state of the system $\mathbf{u}_t$, the next step is calculated as

$$\mathbf{u}_{t+\Delta t} = \mathbf{u}_t + \tfrac{\Delta t}{6}\left(\mathbf{k}_1 + 2\left(\mathbf{k}_2 + \mathbf{k}_3\right) + \mathbf{k}_4\right), \tag{2.41}$$

where

$$\begin{aligned}
\mathbf{k}_1 &= \mathbf{N}^{-1}\left(\mathbf{F}(t) - \mathbf{P}\mathbf{u}_t\right), \\
\mathbf{k}_2 &= \mathbf{N}^{-1}\left(\mathbf{F}(t + \tfrac{\Delta t}{2}) - \mathbf{P}\left(\mathbf{u}_t + \mathbf{k}_1\tfrac{\Delta t}{2}\right)\right), \\
\mathbf{k}_3 &= \mathbf{N}^{-1}\left(\mathbf{F}(t + \tfrac{\Delta t}{2}) - \mathbf{P}\left(\mathbf{u}_t + \mathbf{k}_2\tfrac{\Delta t}{2}\right)\right), \\
\mathbf{k}_4 &= \mathbf{N}^{-1}\left(\mathbf{F}(t + \Delta t) - \mathbf{P}\left(\mathbf{u}_t + \mathbf{k}_3\Delta t\right)\right).
\end{aligned} \tag{2.42}$$

Inverse matrix $\mathbf{N}^{-1}$ is calculated just once before own process.

Newmark-β method is used for solving directly a set of differential equations of second order

$$\mathbf{M}\,\ddot{\mathbf{q}}(t) + \left(\mathbf{B} + \omega_0\,\mathbf{G}\right)\,\dot{\mathbf{q}}(t) + \mathbf{K}\,\mathbf{q}(t) = \mathbf{f}(\dot{\mathbf{q}}, \mathbf{q}, t). \tag{2.43}$$

It uses following approximation of displacements and velocities within single time step

$$\dot{\mathbf{q}}_{t+\Delta t} = \dot{\mathbf{q}}_t + \Delta t\left(\left(1-\gamma\right)\ddot{\mathbf{q}}_t + \gamma\ddot{\mathbf{q}}_{t+\Delta t}\right), \tag{2.44}$$

$$\mathbf{q}_{t+\Delta t} = \mathbf{q}_t + \Delta t\dot{\mathbf{q}}_t + \Delta t^2\left(\left(\frac{1}{2} - \beta\right)\ddot{\mathbf{q}}_t + \beta\ddot{\mathbf{q}}_{t+\Delta t}\right). \tag{2.45}$$

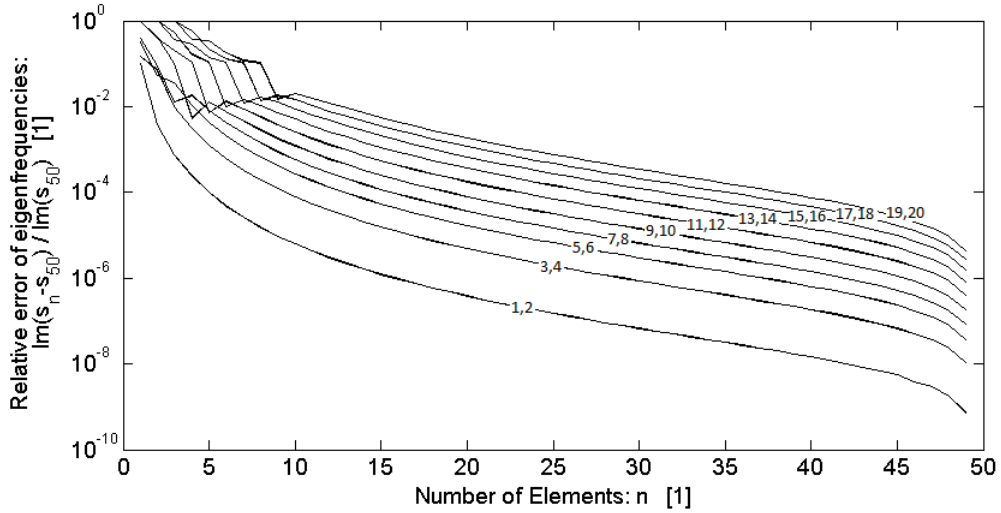

Figure 2.4: Convergence of eigenfrequencies of Rayleigh shaft model, $\omega_0 = 10000\,\mathrm{s}^{-1}$

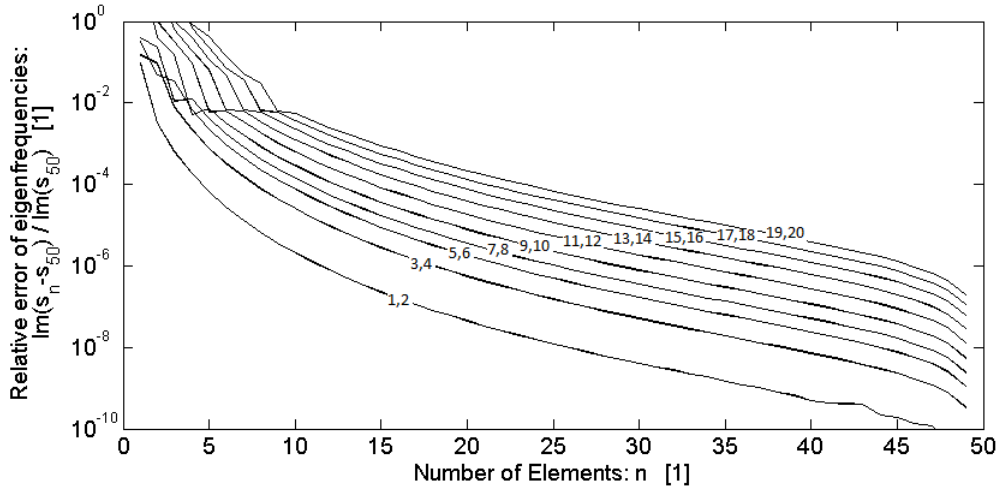

Figure 2.5: Convergence of eigenfrequencies of Timoshenko shaft model, $\omega_0 = 10000\,\mathrm{s}^{-1}$

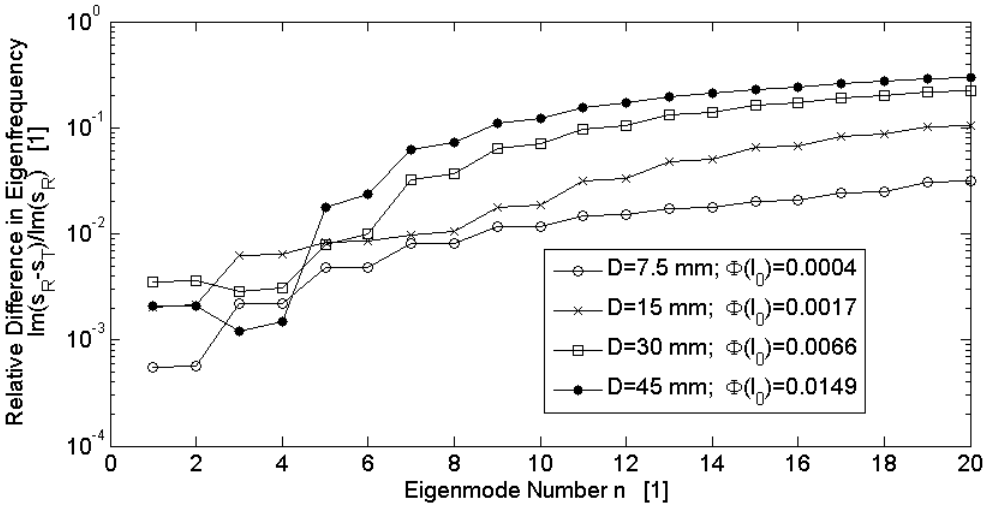

Figure 2.6: Difference in eigenfrequencies between Rayleigh and Timoshenko models, slenderness $\Phi(l_0)$ is based on full length of the shaft, $\omega_0 = 10000\,\mathrm{s}^{-1}$

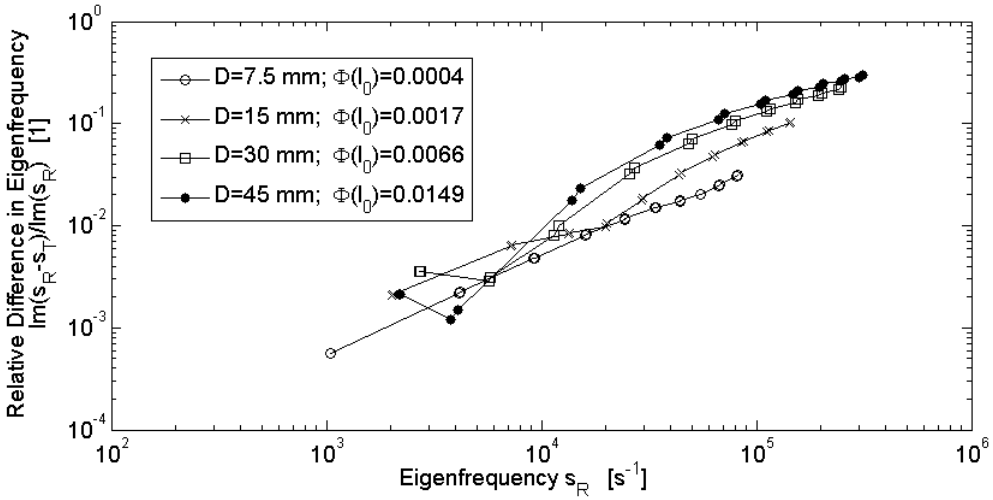

Figure 2.7: Difference in eigenfrequencies between Rayleigh and Timoshenko models, slenderness $\Phi(l_0)$ is based on full length of the shaft, $\omega_0 = 10000\,\mathrm{s}^{-1}$

Parameters γ and β are chosen with respect to desired unconditional stability of the method. The most popular variant of this method uses $\gamma = 1/2$ and $\beta = 1/4$. With these values, the acceleration within single time step is held constant as an average of initial and final value

$$\ddot{\mathbf{q}} = \frac{1}{2}\left(\ddot{\mathbf{q}}_t + \ddot{\mathbf{q}}_{t+\Delta t}\right). \tag{2.46}$$

From (2.44) and (2.45), final values of acceleration and velocity

$$\ddot{\mathbf{q}}_{t+\Delta t} = \frac{4}{\Delta t^2}\left(\mathbf{q}_{t+\Delta t} - \mathbf{q}_t\right) - \frac{4}{\Delta t}\dot{\mathbf{q}}_t - \ddot{\mathbf{q}}_t, \tag{2.47}$$

$$\dot{\mathbf{q}}_{t+\Delta t} = \frac{2}{\Delta t}\left(\mathbf{q}_{t+\Delta t} - \mathbf{q}_t\right) - \dot{\mathbf{q}}_t \tag{2.48}$$

are substituted into

$$\mathbf{M}\,\ddot{\mathbf{q}}_{t+\Delta t} + \left(\mathbf{B} + \omega_0\,\mathbf{G}\right)\,\dot{\mathbf{q}}_{t+\Delta t} + \mathbf{K}\,\mathbf{q}_{t+\Delta t} = \mathbf{f}(\dot{\mathbf{q}}_{t+\Delta t}, \mathbf{q}_{t+\Delta t}, t+\Delta t). \tag{2.49}$$

Resulting set of algebraic equations

$$\begin{aligned}\left(\frac{4}{\Delta t^2}\mathbf{M} + \frac{2}{\Delta t}\left(\mathbf{B} + \omega_0\,\mathbf{G}\right) + \mathbf{K}\right)\mathbf{q}_{t+\Delta t} &= \mathbf{M}\ddot{\mathbf{q}}_t + \left(\frac{4}{\Delta t}\mathbf{M} + \mathbf{B} + \omega_0\,\mathbf{G}\right)\dot{\mathbf{q}}_t \\ &+ \left(\frac{4}{\Delta t^2}\mathbf{M} + \frac{2}{\Delta t}\left(\mathbf{B} + \omega_0\,\mathbf{G}\right)\right)\mathbf{q}_t + \mathbf{f}(\dot{\mathbf{q}}_{t+\Delta t}, \mathbf{q}_{t+\Delta t}, t+\Delta t)\end{aligned} \tag{2.50}$$

is solved for $\mathbf{q}_{t+\Delta t}$. Velocity is updated using (2.48), acceleration is obtained from (2.49). The algebraic system (2.50) is nonlinear due to its last term on the right-hand side, what makes the finding of $\mathbf{q}_{t+\Delta t}$ more complicated.

Author Musil [54] used following linearization of set of algebraic equations given by Newmark method. Let us have function $\mathbf{f}(\dot{\mathbf{q}}, \mathbf{q}, t)$ split into $\mathbf{f}(\dot{\mathbf{q}}, \mathbf{q}, t) = \mathbf{f}_h(\dot{\mathbf{q}}, \mathbf{q}) + \mathbf{f}_r(t)$. The nonlinear part of function $\mathbf{f}(\dot{\mathbf{q}}, \mathbf{q}, t)$, representing hydrodynamic forces of bearings is a function of displacement and velocities only, $\mathbf{f}_h(\dot{\mathbf{q}}, \mathbf{q})$. Remaining parts of function $\mathbf{f}$ are functions of time only. Musil proposes first order linearization of $\mathbf{f}_h$ with respect to initial time as

$$\mathbf{f}_h(\dot{\mathbf{q}}_{t+\Delta t}, \mathbf{q}_{t+\Delta t}) \approx \mathbf{f}_h(\dot{\mathbf{q}}_t, \mathbf{q}_t) + \mathbf{D}_{\mathbf{q}}\left(\mathbf{q}_{t+\Delta t} - \mathbf{q}_t\right) + \mathbf{D}_{\dot{\mathbf{q}}}\left(\dot{\mathbf{q}}_{t+\Delta t} - \dot{\mathbf{q}}_t\right), \tag{2.51}$$

where Jacobi matrices are

$$\mathbf{D}_{\mathbf{q}\,i,j} = \frac{\partial \mathbf{f}_h(\dot{\mathbf{q}}, \mathbf{q})_i}{\partial \mathbf{q}_j}\Big|_{\dot{\mathbf{q}}_t, \mathbf{q}_t}, \qquad \mathbf{D}_{\dot{\mathbf{q}}\,i,j} = \frac{\partial \mathbf{f}_h(\dot{\mathbf{q}}, \mathbf{q})_i}{\partial \dot{\mathbf{q}}_j}\Big|_{\dot{\mathbf{q}}_t, \mathbf{q}_t}. \tag{2.52}$$

Approximation (2.51) substituted back into (2.50) gives a linear set of equations. This step turns the solver to explicit single step numerical method, with all its drawbacks. It is time efficient approach, but the local error is controlled by time step only. First order approximation is used here, which may lead to very small time step to ensure stability of this method,

especially for higher bearing eccentricities, where slopes of hydrodynamic forces rise very quickly.

To preserve the implicitness of the Newmark-β method, some method of solving nonlinear set of equations has to be implemented. Newton-Raphson method can be implemented as follows. The set of equations (2.50) can be written as

$$\mathbf{A}\mathbf{q}_{t+\Delta t} - \mathbf{c} - \mathbf{f}_h(\dot{\mathbf{q}}_{t+\Delta t}, \mathbf{q}_{t+\Delta t}) = \mathbf{0}, \tag{2.53}$$

where $\mathbf{c}$ and $\mathbf{A}$ are constants

$$\mathbf{c} = \mathbf{M}\ddot{\mathbf{q}}_t + \left(\frac{4}{\Delta t}\mathbf{M} + \mathbf{B} + \omega_0\,\mathbf{G}\right)\dot{\mathbf{q}}_t + \left(\frac{4}{\Delta t^2}\mathbf{M} + \frac{2}{\Delta t}\left(\mathbf{B} + \omega_0\,\mathbf{G}\right)\right)\mathbf{q}_t + \mathbf{f}_r(t+\Delta t), \tag{2.54}$$

$$\mathbf{A} = \left(\frac{4}{\Delta t^2}\mathbf{M} + \frac{2}{\Delta t}\left(\mathbf{B} + \omega_0\,\mathbf{G}\right) + \mathbf{K}\right). \tag{2.55}$$

Vector $\mathbf{q}_{t+\Delta t}$ is iteratively searched by solving set of linear equations

$$\mathbf{J}^{\{k\}}\left(\mathbf{q}_{t+\Delta t}^{\{k+1\}} - \mathbf{q}_{t+\Delta t}^{\{k\}}\right) = -\left(\mathbf{A}\mathbf{q}_{t+\Delta t}^{\{k\}} - \mathbf{c} - \mathbf{f}_h(\dot{\mathbf{q}}_{t+\Delta t}^{\{k\}}, \mathbf{q}_{t+\Delta t}^{\{k\}})\right). \tag{2.56}$$

Jacobian $\mathbf{J}^{\{k\}}$ is constructed as

$$J_{ij}^{\{k\}} = A_{ij} - \frac{\partial f_h(\dot{\mathbf{q}}, \mathbf{q})_i}{\partial q_j}\Big|_{\dot{\mathbf{q}}_t^{\{k\}}, \mathbf{q}_t^{\{k\}}}. \tag{2.57}$$

After each iteration (2.56), the velocity is updated according to

$$\dot{\mathbf{q}}_{t+\Delta t}^{\{k+1\}} = \frac{2}{h}\left(\mathbf{q}_{t+\Delta t}^{\{k+1\}} - \mathbf{q}_t\right) - \dot{\mathbf{q}}_t. \tag{2.58}$$

Despite the Newton-Raphson method usually converges quickly, it is highly time consumptive method. Especially if Jacobi matrix $\mathbf{J}$ has to be estimated numerically each step of iterative process. However, if the Newton-Raphson method converges, then this method does not compromise the stability and local accuracy of Newmark-β ODE solver.

Presented approach to set of nonlinear equations assumes that there exist derivatives of function $\mathbf{f}_h(\dot{\mathbf{q}}, \mathbf{q})$ and that they form total differentials

$$\mathrm{d}f_h(\dot{\mathbf{q}}, \mathbf{q})_i = \frac{\partial f_h(\dot{\mathbf{q}}, \mathbf{q})_i}{\partial q_j}\mathrm{d}q_j + \frac{\partial f_h(\dot{\mathbf{q}}, \mathbf{q})_i}{\partial \dot{q}_j}\mathrm{d}\dot{q}_j. \tag{2.59}$$

By other words, the function $\mathbf{f}_h$ is time-independent. In connotation to hydrodynamic bearings that means that reaction forces are free from memory effect. This may be satisfied by using Reynolds equation for incompressible lubricant to model the pressure distribution within fixed geometry bearings. If the pressure distribution is a product of some dynamic process, as it is for gas lubricated bearings due to compressibility of the gas, then such approach cannot be applied generally without ignoring internal dynamics of the bearing model.

Such dynamic models of gas bearings can be numerically solved simultaneously to the model of the rotor and provide only the instantaneous force. The system of nonlinear equations of Newmark-β method can be approached by fixed-point iterations. Slow convergence of this method may enforce more iterations than the case of Newton-Raphson, but one step of this method is much less time consumptive, in view of the fact that Jacobi matrix is never constructed and instead of solving the linear system (2.56) only matrix multiplication takes place. The fixed-point iteration is used on set of (2.50), that can be rewritten as

$$\mathbf{q}_{t+\Delta t} = \mathbf{A}_f \left(\mathbf{e} + \mathbf{f}(\dot{\mathbf{q}}_{t+\Delta t}, \mathbf{q}_{t+\Delta t}, t+\Delta t) \right), \tag{2.60}$$

with constants

$$\mathbf{A}_f = \left(\frac{4}{\Delta t^2}\mathbf{M} + \frac{2}{\Delta t}\left(\mathbf{B} + \omega_0 \mathbf{G}\right) + \mathbf{K} \right)^{-1}, \tag{2.61}$$

$$\mathbf{e} = \mathbf{M}\ddot{\mathbf{q}}_t + \left(\frac{4}{\Delta t}\mathbf{M} + \mathbf{B} + \omega_0 \mathbf{G} \right) \dot{\mathbf{q}}_t + \left(\frac{4}{\Delta t^2}\mathbf{M} + \frac{2}{\Delta t}\left(\mathbf{B} + \omega_0 \mathbf{G}\right) \right) \mathbf{q}_t. \tag{2.62}$$

Iterative process proceeds according to formula

$$\mathbf{q}_{t+\Delta t}^{\{k+1\}} = \mathbf{g}(\dot{\mathbf{q}}_{t+\Delta t}^{\{k\}}, \mathbf{q}_{t+\Delta t}^{\{k\}}, t+\Delta t) = \mathbf{A}_f \mathbf{e} + \mathbf{A}_f \mathbf{f}(\dot{\mathbf{q}}_{t+\Delta t}^{\{k\}}, \mathbf{q}_{t+\Delta t}^{\{k\}}, t+\Delta t). \tag{2.63}$$

Velocity is updated using (2.58).

Conditions guarantying convergence of this method are quite restrictive. First of all, the function $\mathbf{f}$ is defined only within bearing clearance, but it can theoretically gain infinite values. The matrix $\mathbf{A}_f$ would have to project the vector $\mathbf{e}+\mathbf{f}$ back inside the range defined by bearing clearances for respective degrees of freedom. If $\mathbf{f}$ contains values higher than certain limit, then the iterative process inevitably fails. Second necessary condition is that the projection $\mathbf{g}(\mathbf{q}, t)$ is contractive, hence

$$\left\| \frac{\partial \mathbf{g}(\mathbf{q}, t)_i}{\partial \mathbf{q}_j} \right\| = \left\| \mathbf{A}_f \frac{\partial \mathbf{f}(\mathbf{q}, t)_i}{\partial \mathbf{q}_j} \right\| < 1. \tag{2.64}$$

Again, the slopes of bearing reactions contained within function $\mathbf{f}$ grows infinitely with increase of bearing eccentricity, what causes iterative algorithm to fail if certain limit is reached. Fortunately, matrix $\mathbf{A}_f$ contains time step Δt which sets up such limits. Time step of Newmark-β method is thus driven by character of external forces rather than by accuracy of the Newmark-β method itself, because the limitation coming from convergence of fixed-point iterative method is more stringent as numerical experiments with this method have shown.

2.4 Decomposition of Free Flexible Rotor System with Gyroscopic Effects

As shown in the introduction in section 1.5.2, free flexible rotor system with gyroscopic effects is defective and such fact does not allow spectral decomposition to be used directly for modal reduction of the model. However, reduction of the system is desirable when system is to be treated by numerical integration. Although it is possible to directly integrate full set of equations of motion obtained from finite element methods, it brings strong limitations to applicable numerical methods. Presence of very high frequencies in such system disqualifies more accurate methods of higher order, either explicit or implicit, because of their limited stability. Stability conditions of these methods could be satisfies only for very small time step, so that transient analysis would often need unreasonable machine time. Some A-stable implicit method must be used instead to solve such system more efficiently, but unconditional stability of these methods is outweighed by low order of integrator rule that harms accuracy of the method.

2.4.1 Real Modes Partial Decoupling

This approach uses normal modes of rotor system without gyroscopic effects. Simplicity of this method and benefit of using real modes has its drawback of gyroscopic part of motion equations not being diagonalized and therefore entire system not being fully decoupled.

$$\mathbf{M}\,\ddot{\mathbf{q}}(t) + \omega_0\,\mathbf{G}\,\dot{\mathbf{q}}(t) + \mathbf{K}\,\mathbf{q}(t) = \mathbf{f}(\dot{\mathbf{q}}, \mathbf{q}, t). \tag{2.65}$$

Eigenvalue problem (1.90) is solved for spectral $\mathbf{D}$ and modal $\mathbf{V_r}$ matrices. This problem is self-adjoint, so after normalization of eigenvectors $\mathbf{W_r} = (\mathbf{MV_r})^{-\mathrm{T}}$ can be the previous equation transformed into modal space as

$$\mathbf{W_r}^{\mathrm{T}}\mathbf{M}\mathbf{V_r}\,\ddot{\mathbf{c}}(t) + \omega_0\,\mathbf{W_r}^{\mathrm{T}}\mathbf{G}\mathbf{V_r}\,\dot{\mathbf{c}}(t) + \mathbf{W_r}^{\mathrm{T}}\mathbf{K}\mathbf{V_r}\,\mathbf{c}(t) = \mathbf{W_r}^{\mathrm{T}}\mathbf{f}(\dot{\mathbf{q}}, \mathbf{q}, t). \tag{2.66}$$

Matrices $\mathbf{W_r}^{\mathrm{T}}\mathbf{M}\mathbf{V_r}$ and $\mathbf{W_r}^{\mathrm{T}}\mathbf{K}\mathbf{V_r}$ are fully diagonalized. Matrix $\mathbf{W_r}^{\mathrm{T}}\mathbf{G}\mathbf{V_r}$ remains full.

Profile of this matrix, calculated for two trial rotors is plotted in the figures 2.9 and 2.10 as orders of magnitude of its elements. Prismatic circular shaft (see page 43) corresponds to figure 2.9. The same shaft, but supplemented by rigid disc positioned in the 3/10-th of its length serves as the second case of trial rotor. The parameters of the disc are: $m = 0.5\,\mathrm{kg}$, $I = 7.81 \cdot 10^{-5}\,\mathrm{kgm}^2$, $I_0 = 1.56 \cdot 10^{-4}\,\mathrm{kgm}^2$. This second case was selected to promote effects of gyroscopic matrix on eigenfrequencies of the system, see Campbell plot in fig. 2.8.

Figures 2.9 and 2.10 clearly show that normal modes are strongly coupled via gyroscopic effects, even if they are distant in term of corresponding eigenvalues. Presented reduction of this system ignores these distant couplings between preserved and omitted modes.

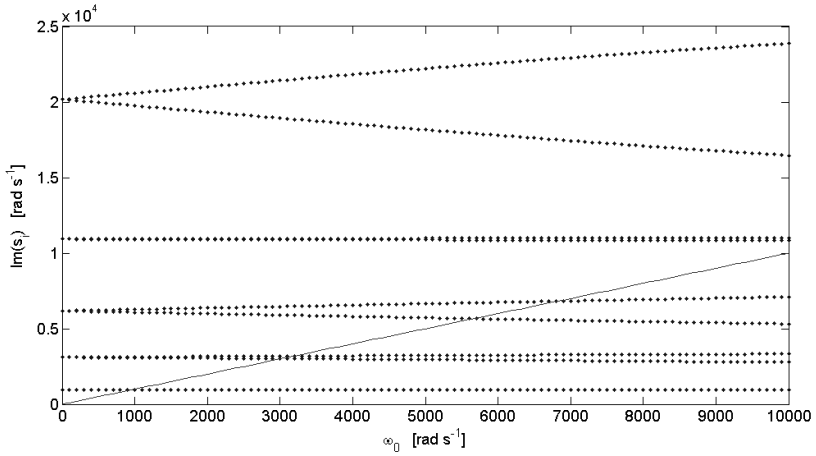

Figure 2.8: Campbell plot of trial rotor with disc; 20 finite elements

To check on consistency of previous simple method as well as to assess numerical errors, normal modes and their frequencies of constrained rotor were calculated and compared with those obtained by modal analysis in the state space that was directly applied to the full system. Validity of this reduction process for defective system of unconstrained rotor system was tested in the time domain. Trial case of rotor with disc is used in all following numerical analyses. System of equations (2.65) is reduced and put into state space

$$\mathbf{N}_R\,\dot{\mathbf{z}} + \mathbf{P}_R\,\mathbf{z} = \mathbf{F}_R, \tag{2.67}$$

where

$$\mathbf{N}_R = \begin{pmatrix} \mathbf{W}_R^{\mathrm{T}}\mathbf{M}\mathbf{V}_R & \mathbf{0} \\ \mathbf{0} & \mathbf{W}_R^{\mathrm{T}}\mathbf{M}\mathbf{V}_R \end{pmatrix}, \quad \mathbf{P}_R = \begin{pmatrix} \omega_0\mathbf{W}_R^{\mathrm{T}}\mathbf{G}\mathbf{V}_R & \mathbf{W}_R^{\mathrm{T}}\mathbf{K}\mathbf{V}_R \\ -\mathbf{W}_R^{\mathrm{T}}\mathbf{M}\mathbf{V}_R & \mathbf{0} \end{pmatrix}, \tag{2.68}$$

and

$$\mathbf{F}_R = \begin{pmatrix} \mathbf{W}_R^{\mathrm{T}}\mathbf{f} \\ \mathbf{0} \end{pmatrix}, \quad \mathbf{z} = \begin{pmatrix} \dot{\mathbf{c}} \\ \mathbf{c} \end{pmatrix}, \quad \begin{pmatrix} \dot{\mathbf{q}} \\ \mathbf{q} \end{pmatrix} = \begin{pmatrix} \mathbf{V}_R\,\dot{\mathbf{c}} \\ \mathbf{V}_R\,\mathbf{c} \end{pmatrix}. \tag{2.69}$$

$\mathbf{V}_R$ and $\mathbf{W}_R$ are reduced modal matrices, columns of which consist of reduced set of eigenvectors of $\mathbf{K}$, $\mathbf{M}$ eigenvalue problem. Full set of eigenvectors creates the matrices $\mathbf{V}_r$ and $\mathbf{W}_r$. Now, it is possible to solve eigenvalue problem using reduced matrices $\mathbf{N}_R$ and $\mathbf{P}_R$ and compare the eigenvalues of selected low frequency modes to those of the original system, taking $\mathbf{N}$ and $\mathbf{P}$ matrices.

The convergence of imaginary parts of eigenvalues for the lowest ten modes is depicted in the fig. 2.11. To assess the effect of this reduction to eigenvectors obtained from reduced system $\mathbf{N}_R$ and $\mathbf{P}_R$, let us calculate following matrix $\mathbf{R}$

$$\mathbf{R} = \mathbf{I} - \mathbf{W}_n^{\mathrm{T}}\mathbf{N}\mathbf{V}^*, \tag{2.70}$$

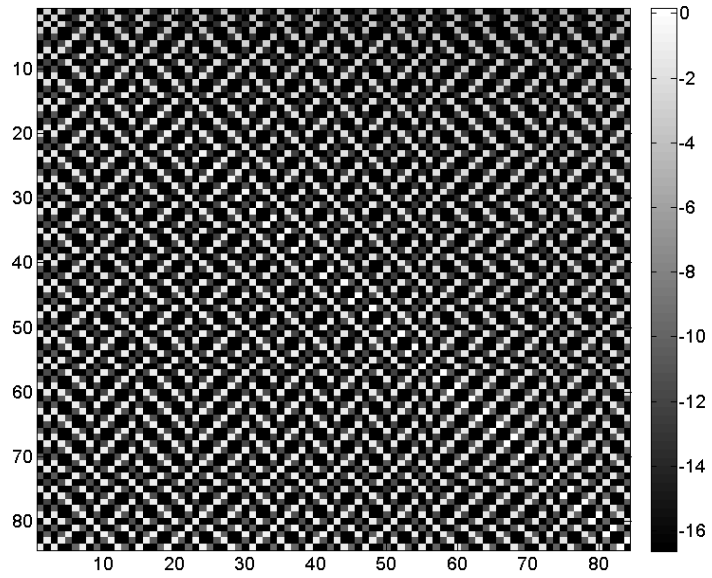

Figure 2.9: Profile of $\mathbf{W}_r^{\mathrm{T}}\mathbf{G}\mathbf{V}_r$; Orders of magnitudes of the elements; 20 finite elements, $\omega_0 = 10000\,\mathrm{rad\,s^{-1}}$; Prismatic trial rotor

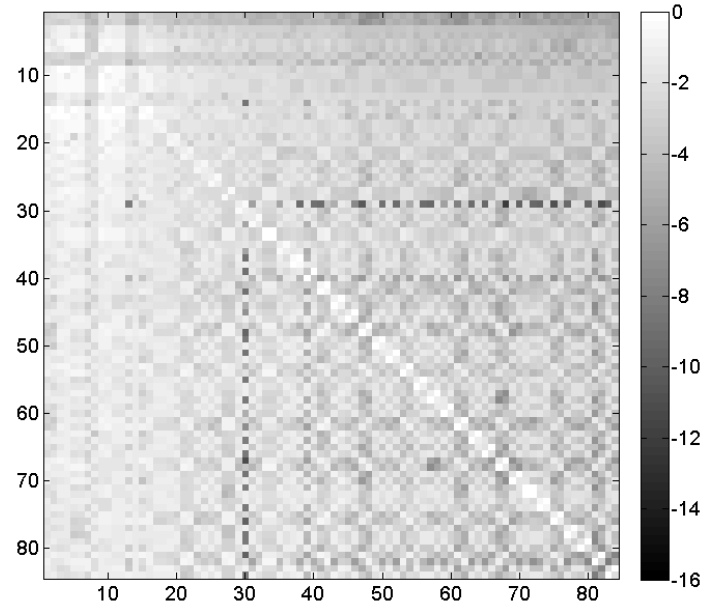

Figure 2.10: Profile of $\mathbf{W}_r^{\mathrm{T}}\mathbf{G}\mathbf{V}_r$; Orders of magnitudes of the elements; 20 finite elements, $\omega_0 = 10000\,\mathrm{rad\,s^{-1}}$; Trial rotor with disc

where $\mathbf{W}_n$ is a matrix that consists of n left eigenvectors of the unreduced original system, and matrix $\mathbf{V}^*$ is the approximation of the right eigenvectors, but calculated from reduced system using matrices $\mathbf{N}_R$ and $\mathbf{P}_R$

$$\mathbf{V}^* = \begin{pmatrix} \mathbf{V}_R & \mathbf{0} \\ \mathbf{0} & \mathbf{V}_R \end{pmatrix} \mathbf{V}^{**}. \tag{2.71}$$

The matrix $\mathbf{V}^{**}$ is the modal matrix obtained by solving eigenvalue problem determined by matrices $\mathbf{N}_R$ and $\mathbf{P}_R$. The diagonal elements of matrix $\mathbf{R}$ indicate the level of generalized biorthogonality of eigenvectors of original and reduced system. Their values tend to zero with increasing number of eigenmodes taken into reduction process, see figure 2.12.

As it can be seen from both figures 2.11 and 2.12, relatively small number of normal bending modes taken for reduction gives reasonable approximation of ten modes of the original rotor model. These tests were done for diagonalizable system; the rotor was supported by linear bearings. The process applied on non-diagonalizable system without these supports was tested in the time domain. Equation (2.66) was constructed and then solved by means of Newmark-β solver. For detail about this method see section 2.3. Reactions of the bearings were applied at each time step of the method as an excitation forces. Full set of equations of motion of the original system was solved for comparison. Transient vibration of the rotor was solved with initial conditions of zero displacements and velocities for all nodes, synchronous unbalance of 10^{-6} g m was applied at disc location. Damping of the system was neglected in both cases in order to promote potential differences in the results. Orbit plots of midplane node of the shaft are plotted in the figures 2.13 and 2.14.

2.4.2 Component Mode Synthesis

Component mode synthesis (CMS) or substructure coupling methods are the names for wide set of methods applicable to various problems of structure vibrations. These methods treat the complex problems divided into substructures with defined coupling between them, leading to reduction of degrees of freedom of the problem. This topic has been extensively discussed in the literature over decades and many variations to the original methods have been presented. According to review of these methods made by Craig et al. [55], a CMS method can be classified as belonging into one of the following groups:

- Fixed-Interface methods
- Free-Interface methods
- Loaded-Interface methods
- Hybrid methods

Craig-Bampton method is almost certainly the most popular member of the first category. Each substructure is treated by means of so-called boundary (also sometimes referred to

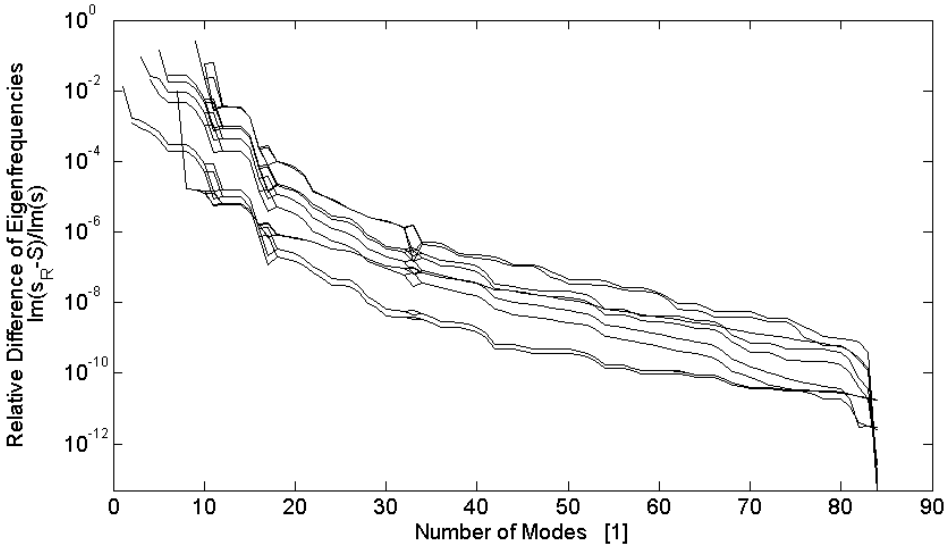

Figure 2.11: Convergence of eigenvalues; Partial decoupling of rotor system; 20 finite elements, $\omega_0 = 10000\,\mathrm{rad\,s^{-1}}$

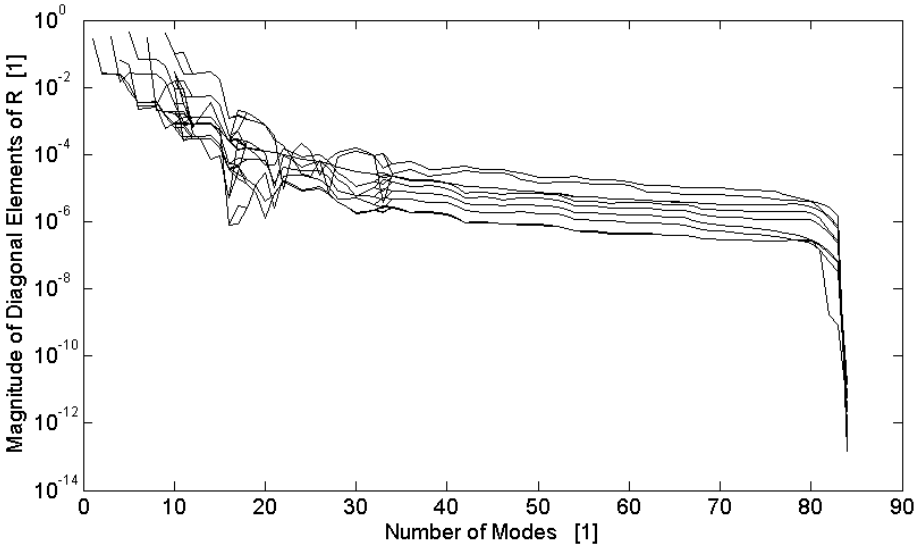

Figure 2.12: Diagonal elements of matrix **R**; Partial decoupling of rotor system; 20 finite elements, $\omega_0 = 10000\,\mathrm{rad\,s^{-1}}$

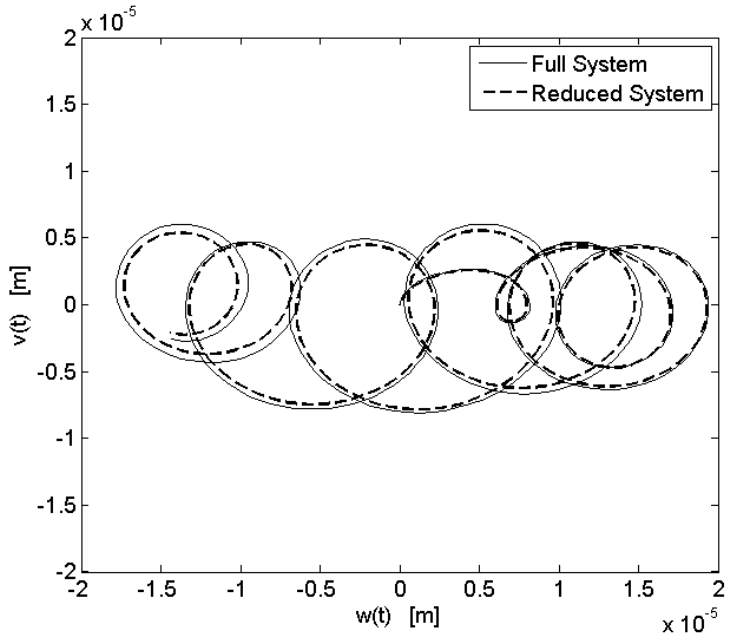

Figure 2.13: Orbit plots for full and reduced (10 degrees of freedom total) rotor model; Real modes partial decoupling

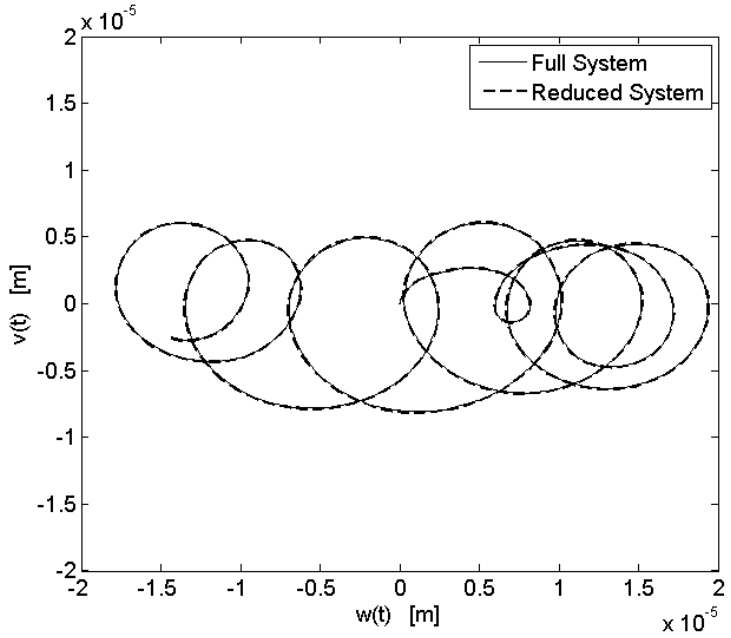

Figure 2.14: Orbit plots for full and reduced (20 degrees of freedom total) rotor model; Real modes partial decoupling

as static, interface, constraint, or attachment) modes, and a set of normal modes. Normal modes of particular substructure are calculated with boundary degrees of freedom fixed. Normal modes are supplemented by boundary modes, which are calculated as deflections of the substructure when unit displacement is enforced at respective degree of freedom (having the rest of boundary dofs fixed). Unlike the other three categories, it does not use rigid body modes in description of substructure dynamics, what means that issue of defectiveness of our particular system is avoided.

The latter three kinds of substructuring methods use rigid body modes in the case of unconstrained problems. To deal with rotors, defective due to gyroscopic effects, similar partial decoupling as described in the last section can be introduced. This approach to hybrid fixed-free interface CMS neglecting the gyroscopic matrix is presented in the work of Shanmugam and Padmanabhan [56]. Similar free-interface method has been delivered by Wang et al. [57]. Another example is hybrid method of coupling between rigid and flexible modes of rotating beams using beam and solid finite elements by Hu et al. [58]. In that work, centrifugal forces are taken into account, but the models do not consider gyroscopic effects.

In next sections, fixed-interface substructuring methods based on Craig-Bampton approach are used to decompose the defective rotor systems.

2.4.3 Real Modes Craig-Bampton Method

Classical Craig-Bampton method can be used on rotor system, neglecting the gyroscopic matrix. Boundary and internal modes are then identical to those of non-rotating beam problem. Resultant transformation matrices are then used to reduce size of all matrices $\mathbf{M}$, $\mathbf{K}$, $\mathbf{G}$.

Starting from (2.65), displacement vector is reordered by unitary transformation matrix to achieve following structure of new state vector

$$\mathbf{z} = \begin{pmatrix} \mathbf{q}_\mathrm{B} \\ \mathbf{q}_\mathrm{I} \end{pmatrix} = \mathbf{T}^\mathrm{T}\mathbf{q}. \tag{2.72}$$

Index B denotes boundary degrees of freedom, index I denotes internal degrees of freedom. Mass and stiffness matrices are transformed to the new configuration

$$\tilde{\mathbf{M}} = \mathbf{T}^\mathrm{T}\mathbf{M}\mathbf{T}, \qquad \tilde{\mathbf{K}} = \mathbf{T}^\mathrm{T}\mathbf{K}\mathbf{T}. \tag{2.73}$$

The transformed part of the system is now

$$\begin{pmatrix} \tilde{\mathbf{M}}_\mathrm{BB} & \tilde{\mathbf{M}}_\mathrm{BI} \\ \tilde{\mathbf{M}}_\mathrm{IB} & \tilde{\mathbf{M}}_\mathrm{II} \end{pmatrix} \begin{pmatrix} \dot{\mathbf{q}}_\mathrm{B}(t) \\ \dot{\mathbf{q}}_\mathrm{I}(t) \end{pmatrix} + \begin{pmatrix} \tilde{\mathbf{K}}_\mathrm{BB} & \tilde{\mathbf{K}}_\mathrm{BI} \\ \tilde{\mathbf{K}}_\mathrm{IB} & \tilde{\mathbf{K}}_\mathrm{II} \end{pmatrix} \begin{pmatrix} \mathbf{q}_\mathrm{B}(t) \\ \mathbf{q}_\mathrm{I}(t) \end{pmatrix} = \begin{pmatrix} \mathbf{f}_\mathrm{B}(t) \\ \mathbf{f}_\mathrm{I}(t) \end{pmatrix}. \tag{2.74}$$

The idea of Craig-Bampton method is to represent state vector $\mathbf{z}(t)$ as a sum of static $\mathbf{z}_\mathrm{s}(t)$ and dynamic $\mathbf{z}_\mathrm{d}(t)$ components. Static part is based on vectors of static deflections

(boundary modes) that span the subspace of rigid body modes, dynamic part is based on contribution of set of selected normal modes with fixed boundary degrees of freedom.

Static reduction can be implemented to calculate static modes. State vector has been reordered in such way, that term $\mathbf{f}_{\mathrm{I}}(t)$ is zero vector, so static part of the equations (2.74) is

$$\tilde{\mathbf{K}}_{\mathrm{IB}}\mathbf{q}_{\mathrm{B}} + \tilde{\mathbf{K}}_{\mathrm{II}}\mathbf{q}_{\mathrm{I}} = \mathbf{0}. \tag{2.75}$$

This equation states the relation between the boundary degrees of freedom and the internal degrees of freedom

$$\mathbf{q}_{\mathrm{I}} = -\tilde{\mathbf{K}}_{\mathrm{II}}^{-1}\tilde{\mathbf{K}}_{\mathrm{IB}}\mathbf{q}_{\mathrm{B}}. \tag{2.76}$$

Static modes contribution is then

$$\mathbf{z}_{\mathrm{s}}(t) = \begin{pmatrix} \mathbf{I}_{\mathrm{BB}} \\ \mathbf{R}_{\mathrm{IB}} \end{pmatrix} \mathbf{q}_{\mathrm{B}}(t), \tag{2.77}$$

where matrix $\mathbf{I}_{\mathrm{BB}}$ is identity with dimension equal to number of boundary degrees of freedom B, and matrix $\mathbf{R}_{\mathrm{IB}} = -\tilde{\mathbf{K}}_{\mathrm{II}}^{-1}\tilde{\mathbf{K}}_{\mathrm{IB}}$.

Dynamic modes are now calculated from matrices $\tilde{\mathbf{K}}_{\mathrm{II}}$ and $\tilde{\mathbf{M}}_{\mathrm{II}}$

$$\left(-\tilde{\mathbf{M}}_{\mathrm{II}}^{-1}\tilde{\mathbf{K}}_{\mathrm{II}} - s\mathbf{I}_{\mathrm{II}}\right)\mathbf{v} = \mathbf{0}. \tag{2.78}$$

Dynamic part of state vector written by means of modal participation vector $\mathbf{c}_{\mathrm{I}}$

$$\mathbf{z}_{\mathrm{d}}(t) = \begin{pmatrix} \mathbf{0}_{\mathrm{BI}} \\ \mathbf{V}_{\mathrm{II}} \end{pmatrix} \mathbf{c}_{\mathrm{I}}(t) \tag{2.79}$$

is reduced by taking only k normal modes, so the vector $\mathbf{z}(t)$ will become

$$\mathbf{z}(t) = \begin{pmatrix} \mathbf{I}_{\mathrm{BB}} & \mathbf{0}_{\mathrm{BK}} \\ \mathbf{R}_{\mathrm{IB}} & \mathbf{V}_{\mathrm{IK}} \end{pmatrix} \begin{pmatrix} \mathbf{q}_{\mathrm{B}}(t) \\ \mathbf{c}_{\mathrm{K}}(t) \end{pmatrix} = \mathbf{R}\mathbf{u}(t). \tag{2.80}$$

Self-adjointness of this $\mathbf{K}$, $\mathbf{M}$ problem leads to the final transformation

$$\mathbf{M}_{cb} = \mathbf{R}^{\mathrm{T}}\mathbf{T}^{\mathrm{T}}\,\mathbf{M}\,\mathbf{T}\mathbf{R}, \qquad \mathbf{K}_{cb} = \mathbf{R}^{\mathrm{T}}\mathbf{T}^{\mathrm{T}}\,\mathbf{K}\,\mathbf{T}\mathbf{R}, \qquad \mathbf{G}_{cb} = \mathbf{R}^{\mathrm{T}}\mathbf{T}^{\mathrm{T}}\,\mathbf{G}\,\mathbf{T}\mathbf{R}. \tag{2.81}$$

The original system of equations is finally reduced to

$$\mathbf{M}_{cb}\,\ddot{\mathbf{u}}(t) + \omega_0\mathbf{G}_{cb}\,\dot{\mathbf{u}}(t) + \mathbf{K}_{cb}\,\mathbf{u}(t) = \left(\mathbf{f}_{\mathrm{B}}^{\mathrm{T}}(t), \mathbf{0}^{\mathrm{T}}\right)^{\mathrm{T}}. \tag{2.82}$$

Gyroscopic matrix of the system has been blindly treated as stiffness and mass matrices, but the gyroscopic coupling between preserved modes is still preserved. Profiles of these matrices that generate reduced system (20 degrees of freedom of reduced model) of trial rotor with disc (page 50) are depicted in figures 2.15 to 2.17.

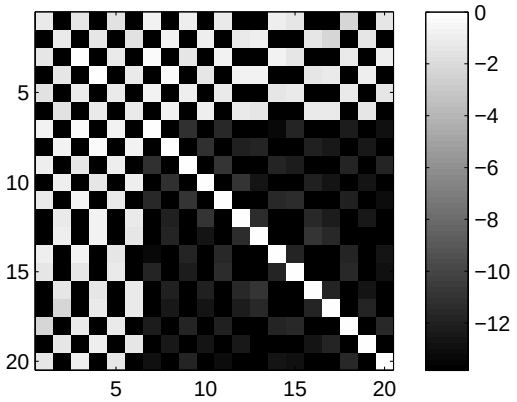

Figure 2.15: Profile of $\mathbf{M}_{cb}$; Orders of magnitudes of the elements; 20 finite elements, $\omega_0 = 10000\,\mathrm{rad\,s^{-1}}$

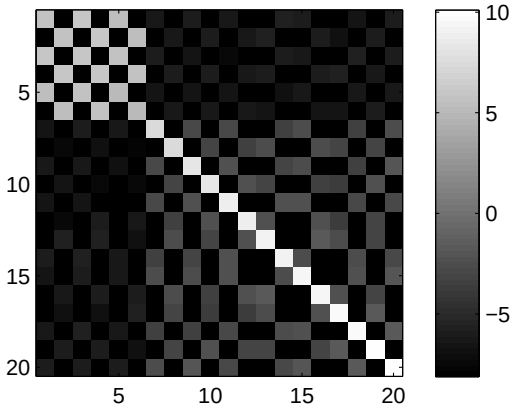

Figure 2.16: Profile of $\mathbf{K}_{cb}$; Orders of magnitudes of the elements; 20 finite elements, $\omega_0 = 10000\,\mathrm{rad\,s^{-1}}$

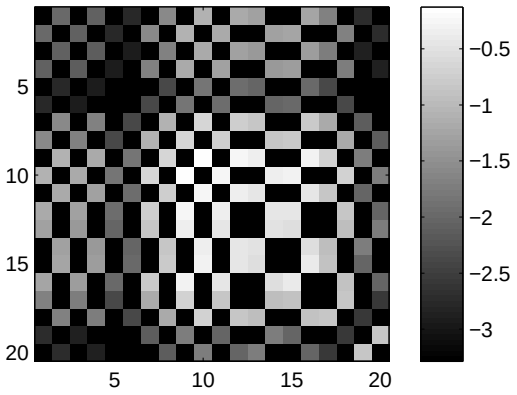

Figure 2.17: Profile of $\mathbf{G}_{cb}$; Orders of magnitudes of the elements; 20 finite elements, $\omega_0 = 10000\,\mathrm{rad\,s^{-1}}$

Convergence of eigenfrequencies of reduced model to those calculated with full system is shown in fig. 2.18. Figure 2.19, as a graph of diagonal elements of matrix $\mathbf{R}_{cb}$, represents the convergence of eigenvectors. Matrix $\mathbf{R}_{cb}$ is constructed as follows:

$$\mathbf{R}_{cb} = \mathbf{I} - \mathbf{W}_n^{\mathrm{T}} \mathbf{N} \mathbf{V}^*, \tag{2.83}$$

where the approximation of the system eigenvectors $\mathbf{V}^*$ is obtained by

$$\mathbf{V}^* = \begin{pmatrix} \mathbf{TR} & \mathbf{0} \\ \mathbf{0} & \mathbf{TR} \end{pmatrix} \mathbf{V}^{**}. \tag{2.84}$$

Matrix $\mathbf{V}^{**}$ is right-hand side modal matrix of reduced system in state space defined by matrices $\mathbf{P}_{cb}$ and $\mathbf{N}_{cb}$, which are for this method

$$\mathbf{N}_{cb} = \begin{pmatrix} \mathbf{M}_{cb} & \mathbf{0} \\ \mathbf{0} & \mathbf{M}_{cb} \end{pmatrix}, \qquad \mathbf{P}_{cb} = \begin{pmatrix} \omega_0 \, \mathbf{G}_{cb} & \mathbf{K}_{cb} \\ -\mathbf{M}_{cb} & \mathbf{0} \end{pmatrix}. \tag{2.85}$$

Results of numerical example of rotor transient vibrations, identical to test problem of previous reduction method are drawn in figures 2.20 to 2.21.

2.4.4 Craig-Bampton Method for General Damping

Craig-Bampton substructuring technique, originally designed for reduction of conservative structures or structures with small proportional damping, can be used in the state space for systems with gyroscopic effects or systems with general damping. This variation of the method can be found in [59]. In this section, the idea of Craig-Bampton method will be applied on the rotor system with gyroscopic effects as a specific case of system damping.

Dynamic system given as

$$\mathbf{M}\ddot{\mathbf{q}}(t) + \omega_0 \mathbf{G}\dot{\mathbf{q}}(t) + \mathbf{K}\mathbf{q}(t) = \mathbf{f}(t) \tag{2.86}$$

can be put into the state space as first order system

$$\mathbf{N}\dot{\mathbf{y}}(t) + \mathbf{P}\mathbf{y}(t) = \mathbf{g}(t), \tag{2.87}$$

where

$$\mathbf{N} = \begin{pmatrix} \mathbf{M} & \mathbf{0} \\ \mathbf{0} & \mathbf{M} \end{pmatrix}, \qquad \mathbf{P} = \begin{pmatrix} \omega_0 \mathbf{G} & \mathbf{K} \\ -\mathbf{M} & \mathbf{0} \end{pmatrix}, \qquad \mathbf{y}(t) = \begin{pmatrix} \dot{\mathbf{q}}(t) \\ \mathbf{q}(t) \end{pmatrix}, \qquad \mathbf{g}(t) = \begin{pmatrix} \mathbf{f}(t) \\ \mathbf{0} \end{pmatrix}. \tag{2.88}$$

Matrices $\mathbf{N}$ and $\mathbf{P}$ have structure as introduced earlier in order to keep the consistency with rest of the code. Degrees of freedom of entire structure are separated into the set of boundary degrees of freedom, where any type of constraint or external force is to be applied, and the

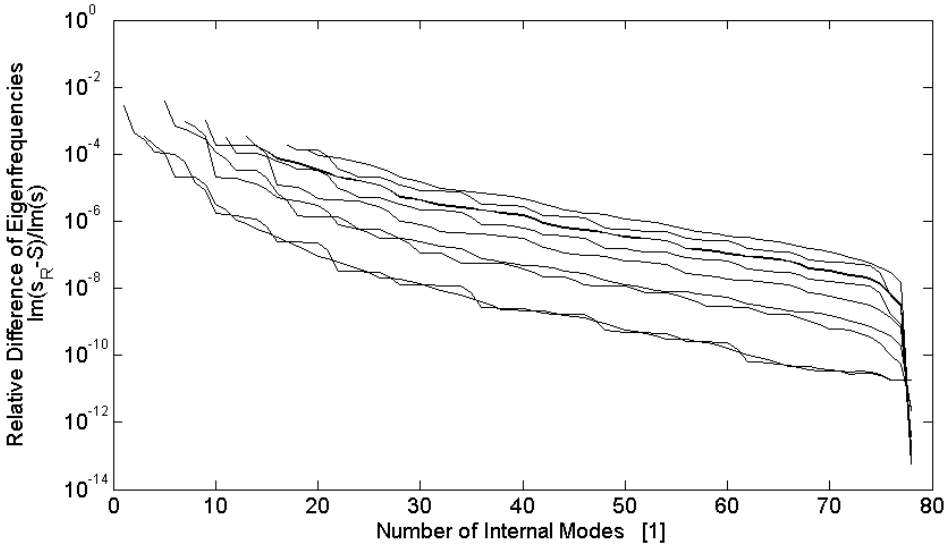

Figure 2.18: Convergence of eigenvalues; Real modes Craig-Bampton substructuring; 20 finite elements, $\omega_0 = 10000\,\mathrm{rad\,s^{-1}}$

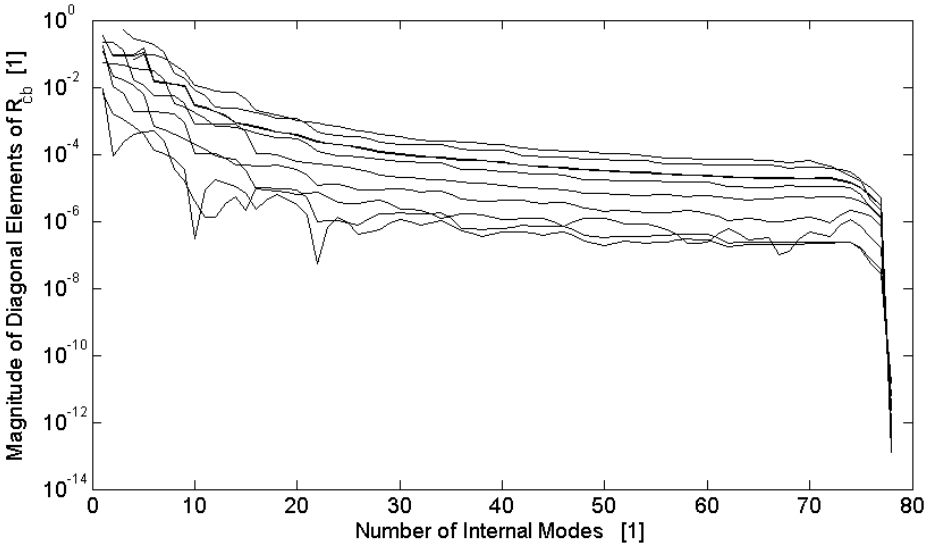

Figure 2.19: Diagonal elements of matrix $\mathbf{R}_{cb}$; Real modes Craig-Bampton substructuring; 20 finite elements, $\omega_0 = 10000\,\mathrm{rad\,s^{-1}}$

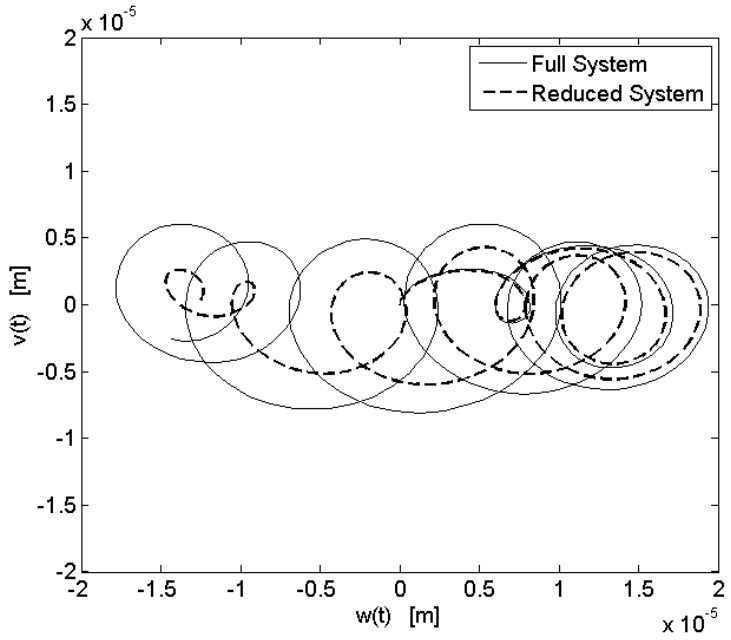

Figure 2.20: Orbit plots for full and reduced (10 degrees of freedom total) rotor model; Real modes Craig-Bampton substructuring

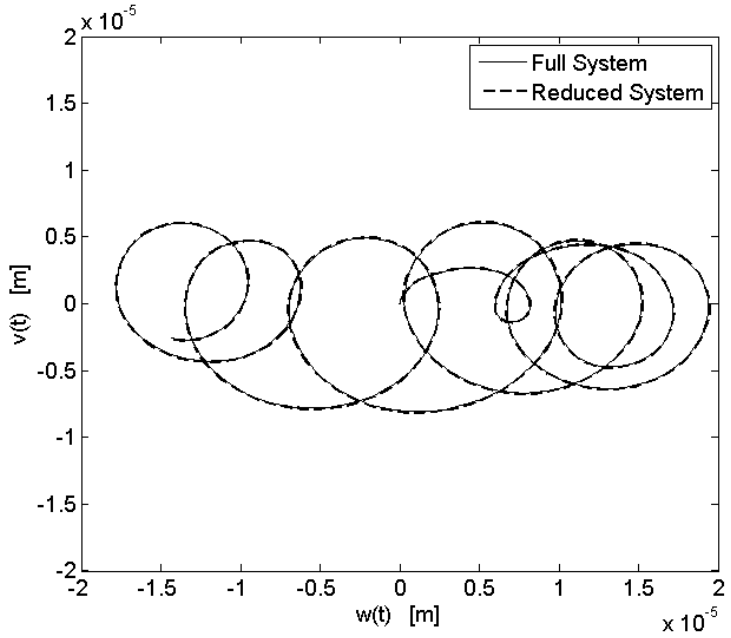

Figure 2.21: Orbit plots for full and reduced (20 degrees of freedom total) rotor model; Real modes Craig-Bampton substructuring

rest of internal degrees of freedom. State vector $\mathbf{y}(t)$ is now reordered

$$\mathbf{z}(t) = \mathbf{T}^{\mathrm{T}}\mathbf{y}(t), \tag{2.89}$$

to achieve following structure of new state vector

$$\mathbf{z}(t) = \begin{pmatrix} \mathbf{z}_{\mathrm{B}}(t) \\ \mathbf{z}_{\mathrm{I}}(t) \end{pmatrix} = \begin{pmatrix} \dot{\mathbf{q}}_{\mathrm{B}}(t) \\ \mathbf{q}_{\mathrm{B}}(t) \\ \dot{\mathbf{q}}_{\mathrm{I}}(t) \\ \mathbf{q}_{\mathrm{I}}(t) \end{pmatrix}. \tag{2.90}$$

Transformed matrices $\mathbf{N}$ and $\mathbf{P}$ are then

$$\tilde{\mathbf{N}} = \mathbf{T}^{\mathrm{T}}\mathbf{N}\mathbf{T}, \qquad \tilde{\mathbf{P}} = \mathbf{T}^{\mathrm{T}}\mathbf{P}\mathbf{T}, \tag{2.91}$$

and entire system has now following structure

$$\begin{pmatrix} \tilde{\mathbf{N}}_{\mathrm{BB}} & \tilde{\mathbf{N}}_{\mathrm{BI}} \\ \tilde{\mathbf{N}}_{\mathrm{IB}} & \tilde{\mathbf{N}}_{\mathrm{II}} \end{pmatrix} \begin{pmatrix} \dot{\mathbf{z}}_{\mathrm{B}}(t) \\ \dot{\mathbf{z}}_{\mathrm{I}}(t) \end{pmatrix} + \begin{pmatrix} \tilde{\mathbf{P}}_{\mathrm{BB}} & \tilde{\mathbf{P}}_{\mathrm{BI}} \\ \tilde{\mathbf{P}}_{\mathrm{IB}} & \tilde{\mathbf{P}}_{\mathrm{II}} \end{pmatrix} \begin{pmatrix} \mathbf{z}_{\mathrm{B}}(t) \\ \mathbf{z}_{\mathrm{I}}(t) \end{pmatrix} = \begin{pmatrix} \mathbf{g}_{\mathrm{B}}(t) \\ \mathbf{g}_{\mathrm{I}}(t) \end{pmatrix}. \tag{2.92}$$

Static relation between boundary and internal displacements (2.76) is used also in this case. Derivation of this equation gives

$$\dot{\mathbf{q}}_{\mathrm{I}} = -\tilde{\mathbf{K}}_{\mathrm{II}}^{-1}\tilde{\mathbf{K}}_{\mathrm{IB}}\dot{\mathbf{q}}_{\mathrm{B}}. \tag{2.93}$$

Static modes contribution is then

$$\mathbf{z}_{\mathrm{s}}(t) = \begin{pmatrix} \mathbf{I}_{\mathrm{BB}} \\ \mathbf{R}_{\mathrm{IB}} \end{pmatrix} \mathbf{z}_{\mathrm{B}}(t), \tag{2.94}$$

where matrix $\mathbf{I}_{\mathrm{BB}}$ is identity with dimension equal to number of boundary degrees of freedom B, and matrix $\mathbf{R}_{\mathrm{IB}}$ is

$$\mathbf{R}_{\mathrm{IB}} = \begin{pmatrix} -\tilde{\mathbf{K}}_{\mathrm{II}}^{-1}\tilde{\mathbf{K}}_{\mathrm{IB}} & \mathbf{0} \\ \mathbf{0} & -\tilde{\mathbf{K}}_{\mathrm{II}}^{-1}\tilde{\mathbf{K}}_{\mathrm{IB}} \end{pmatrix}. \tag{2.95}$$

Dynamic modes are standard normal modes of the system having all boundary modes suppressed, so they can be calculated only from matrices $\tilde{\mathbf{P}}_{\mathrm{II}}$ and $\tilde{\mathbf{N}}_{\mathrm{II}}$ by solving eigenvalue problem

$$\left(-\tilde{\mathbf{N}}_{\mathrm{II}}^{-1}\tilde{\mathbf{P}}_{\mathrm{II}} - s\mathbf{I}_{\mathrm{II}}\right)\mathbf{v} = \mathbf{0}. \tag{2.96}$$

Dynamic part of state vector $\mathbf{z}_{\mathrm{d}}(t)$ can be written by means of modal participation vector $\mathbf{c}_{\mathrm{I}}$ as

$$\mathbf{z}_{\mathrm{d}}(t) = \begin{pmatrix} \mathbf{0}_{\mathrm{BI}} \\ \mathbf{V}_{\mathrm{II}} \end{pmatrix} \mathbf{c}_{\mathrm{I}}(t). \tag{2.97}$$

Zero matrix $\mathbf{0}_{\mathrm{BI}}$ represents locked boundary degrees of freedom, modal matrix $\mathbf{V}_{\mathrm{II}}$ consists of eigenvectors of problem (2.96). System reduction strategy is based upon taking only selected eigenmodes into consideration and neglecting contribution of the others. Considering only k normal modes, the state vector $\mathbf{z}(t)$ will become

$$\mathbf{z}(t) = \begin{pmatrix} \mathbf{I}_{\mathrm{BB}} \\ \mathbf{R}_{\mathrm{IB}} \end{pmatrix} \mathbf{z}_{\mathrm{B}}(t) + \begin{pmatrix} \mathbf{0}_{\mathrm{BK}} \\ \mathbf{V}_{\mathrm{IK}} \end{pmatrix} \mathbf{c}_{\mathrm{K}}(t) = \begin{pmatrix} \mathbf{I}_{\mathrm{BB}} & \mathbf{0}_{\mathrm{BK}} \\ \mathbf{R}_{\mathrm{IB}} & \mathbf{V}_{\mathrm{IK}} \end{pmatrix} \begin{pmatrix} \mathbf{z}_{\mathrm{B}}(t) \\ \mathbf{c}_{\mathrm{K}}(t) \end{pmatrix} = \mathbf{R}\mathbf{u}(t). \tag{2.98}$$

The matrix $\mathbf{R}$ is based on right-hand side static modes and eigenvectors. The system with gyroscopic matrix $\mathbf{G}$ is non-self-adjoint, so the left-hand-side decomposition matrix $\mathbf{L}$ is constructed identically as with modal decomposition in state space. Structure of matrix $\mathbf{L}$ is identical to matrix $\mathbf{R}$, but it is based on adjoint system with matrices $\mathbf{N}^{\mathrm{T}}$ and $\mathbf{P}^{\mathrm{T}}$ instead of $\mathbf{N}$ and $\mathbf{P}$. Matrix $\mathbf{L}$ can be written as

$$\mathbf{L} = \begin{pmatrix} \mathbf{I}_{\mathrm{BB}} & \mathbf{0}_{\mathrm{BK}} \\ \mathbf{L}_{\mathrm{IB}} & \mathbf{W}_{\mathrm{IK}} \end{pmatrix}. \tag{2.99}$$

Using substitution (2.98) and multiplying by matrix $\mathbf{L}^{\mathrm{T}}$ from the left, the system (2.92) will become

$$\mathbf{N}_{cb}\dot{\mathbf{u}}(t) + \mathbf{P}_{cb}\mathbf{u}(t) = \mathbf{L}^{\mathrm{T}}\tilde{\mathbf{g}}(t). \tag{2.100}$$

Reduced matrices $\mathbf{N}_{cb}$ and $\mathbf{P}_{cb}$ are

$$\mathbf{N}_{cb} = \mathbf{L}^{\mathrm{T}}\tilde{\mathbf{N}}\mathbf{R}, \qquad \mathbf{P}_{cb} = \mathbf{L}^{\mathrm{T}}\tilde{\mathbf{P}}\mathbf{R}, \tag{2.101}$$

with the following structure

$$\mathbf{N}_{cb} = \begin{pmatrix} \tilde{\mathbf{N}}_{\mathrm{BB}} + \tilde{\mathbf{N}}_{\mathrm{BI}}\mathbf{R}_{\mathrm{IB}} + \mathbf{L}_{\mathrm{IB}}^{\mathrm{T}}\tilde{\mathbf{N}}_{\mathrm{IB}} + \mathbf{L}_{\mathrm{IB}}^{\mathrm{T}}\tilde{\mathbf{N}}_{\mathrm{II}}\mathbf{R}_{\mathrm{IB}} & \tilde{\mathbf{N}}_{\mathrm{BI}}\mathbf{V}_{\mathrm{IK}} + \mathbf{L}_{\mathrm{IB}}^{\mathrm{T}}\tilde{\mathbf{N}}_{\mathrm{II}}\mathbf{V}_{\mathrm{IK}} \\ \mathbf{W}_{\mathrm{IK}}^{\mathrm{T}}\tilde{\mathbf{N}}_{\mathrm{IB}} + \mathbf{W}_{\mathrm{IK}}^{\mathrm{T}}\tilde{\mathbf{N}}_{\mathrm{II}}\mathbf{R}_{\mathrm{IB}} & \mathbf{W}_{\mathrm{IK}}^{\mathrm{T}}\tilde{\mathbf{N}}_{\mathrm{II}}\mathbf{V}_{\mathrm{IK}} \end{pmatrix}, \tag{2.102}$$

$$\mathbf{P}_{cb} = \begin{pmatrix} \tilde{\mathbf{P}}_{\mathrm{BB}} + \tilde{\mathbf{P}}_{\mathrm{BI}}\mathbf{R}_{\mathrm{IB}} + \mathbf{L}_{\mathrm{IB}}^{\mathrm{T}}\tilde{\mathbf{P}}_{\mathrm{IB}} + \mathbf{L}_{\mathrm{IB}}^{\mathrm{T}}\tilde{\mathbf{P}}_{\mathrm{II}}\mathbf{R}_{\mathrm{IB}} & \tilde{\mathbf{P}}_{\mathrm{BI}}\mathbf{V}_{\mathrm{IK}} + \mathbf{L}_{\mathrm{IB}}^{\mathrm{T}}\tilde{\mathbf{P}}_{\mathrm{II}}\mathbf{V}_{\mathrm{IK}} \\ \mathbf{W}_{\mathrm{IK}}^{\mathrm{T}}\tilde{\mathbf{P}}_{\mathrm{IB}} + \mathbf{W}_{\mathrm{IK}}^{\mathrm{T}}\tilde{\mathbf{P}}_{\mathrm{II}}\mathbf{R}_{\mathrm{IB}} & \mathbf{W}_{\mathrm{IK}}^{\mathrm{T}}\tilde{\mathbf{P}}_{\mathrm{II}}\mathbf{V}_{\mathrm{IK}} \end{pmatrix}. \tag{2.103}$$

Bottom right blocks $\mathbf{W}_{\mathrm{IK}}^{\mathrm{T}}\tilde{\mathbf{N}}_{\mathrm{II}}\mathbf{V}_{\mathrm{IK}}$ and $\mathbf{W}_{\mathrm{IK}}^{\mathrm{T}}\tilde{\mathbf{P}}_{\mathrm{II}}\mathbf{V}_{\mathrm{IK}}$ are naturally diagonal. Right-hand side of the equation

$$\mathbf{L}^{\mathrm{T}}\tilde{\mathbf{g}}(t) = \begin{pmatrix} \mathbf{I}_{\mathrm{BB}}\,\mathbf{g}_{\mathrm{B}}(t) + \mathbf{L}_{\mathrm{IB}}^{\mathrm{T}}\,\mathbf{g}_{\mathrm{I}}(t) \\ \mathbf{W}_{\mathrm{IK}}^{\mathrm{T}}\,\mathbf{g}_{\mathrm{I}}(t) \end{pmatrix} \tag{2.104}$$

shows the pleasant property of the Craig-Bampton method. Degrees of freedom have been reordered in such way that $\mathbf{g}_{\mathrm{I}}(t)$ equals to zero vector, so that right-hand side of the reduced system consists of only $(\mathbf{g}_{\mathrm{B}}^{\mathrm{T}}(t), \mathbf{0}^{\mathrm{T}})^{\mathrm{T}}$.

Profiles of the matrices $\mathbf{N}_{cb}$ and $\mathbf{P}_{cb}$ are plotted in figures 2.22 and 2.23, for case of trial rotor with disc and 20 degrees of freedom of the reduced system. Convergence of eigenvalues for trial rotor (see page 50), used also for testing other two decoupling methods is drawn in the fig. 2.24. Convergence of eigenvectors' approximation is tested by means of matrix $\mathbf{R}_{cb}$, which is for this method defined as

$$\mathbf{R}_{cb} = \mathbf{I} - \mathbf{W}_n^{\mathrm{T}}\mathbf{N}\mathbf{V}^*, \tag{2.105}$$

where matrix $\mathbf{V}^*$ is an approximation of eigenmodes of the system calculated from

$$\mathbf{V}^* = \mathbf{T}\mathbf{R}\mathbf{V}^{**} \tag{2.106}$$

with matrix $\mathbf{V}^{**}$ being modal matrix obtained by solving eigenvalue problem determined by matrices $\mathbf{N}_{cb}$ and $\mathbf{P}_{cb}$. Graph of diagonal elements of matrix $\mathbf{R}_{cb}$ is in the figure 2.25. Comparisons of the time domain solutions of identical problem as in previous subsection are in the figures 2.26 and 2.27.

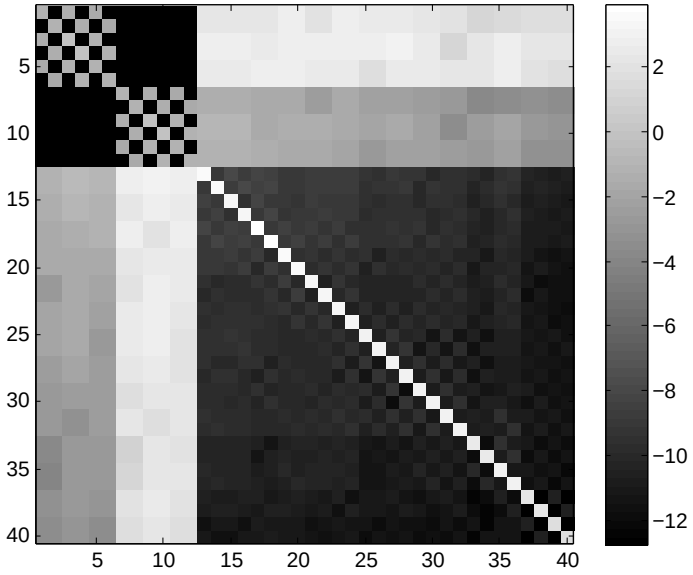

Figure 2.22: Profile of $\mathbf{N}_{cb}$; Orders of magnitudes of the elements; 20 finite elements, $\omega_0 = 10000\,\mathrm{rad\,s^{-1}}$

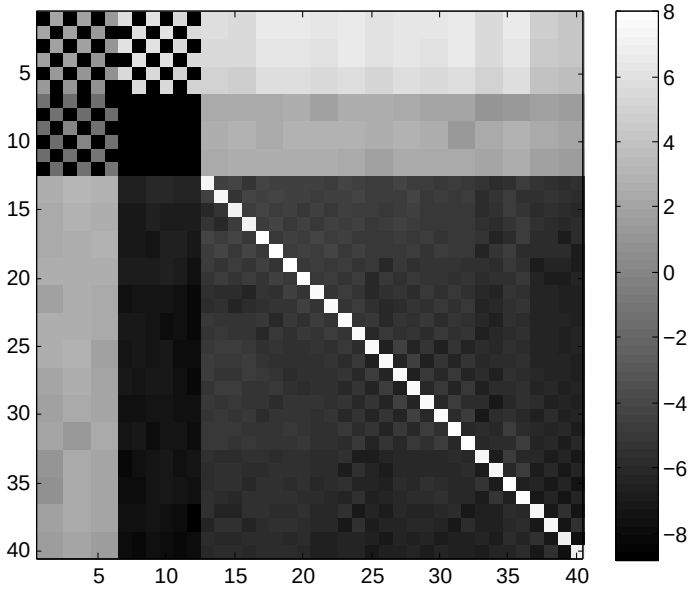

Figure 2.23: Profile of $\mathbf{P}_{cb}$; Orders of magnitudes of the elements; 20 finite elements, $\omega_0 = 10000\,\mathrm{rad\,s^{-1}}$

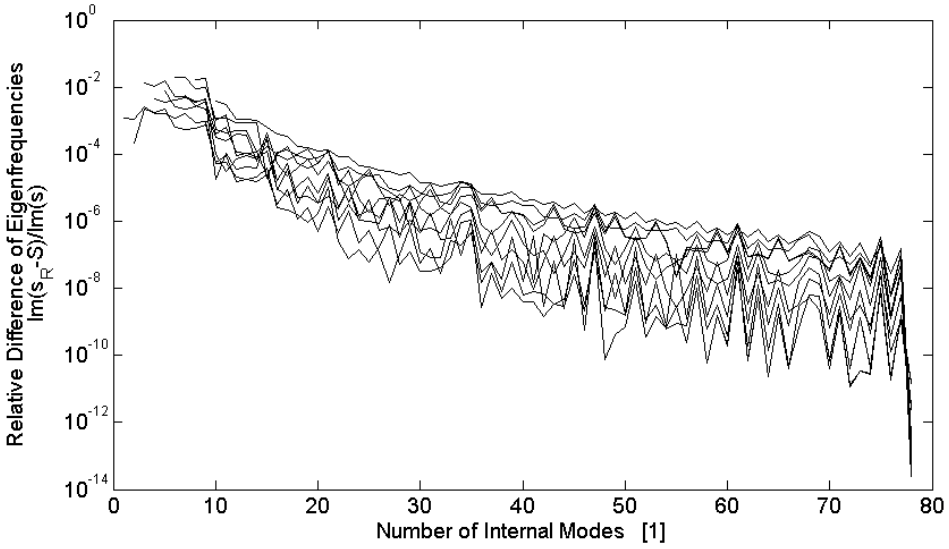

Figure 2.24: Convergence of eigenvalues; Craig-Bampton method for general damping; 20 finite elements, $\omega_0 = 10000\,\mathrm{rad\,s^{-1}}$

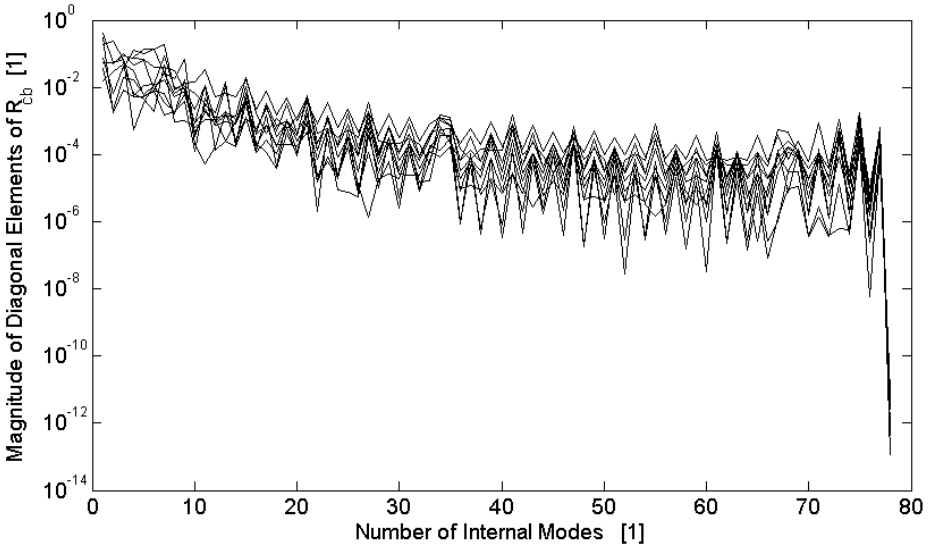

Figure 2.25: Diagonal elements of matrix $\mathbf{R}_{cb}$; Craig-Bampton method for general damping; 20 finite elements, $\omega_0 = 10000\,\mathrm{rad\,s^{-1}}$

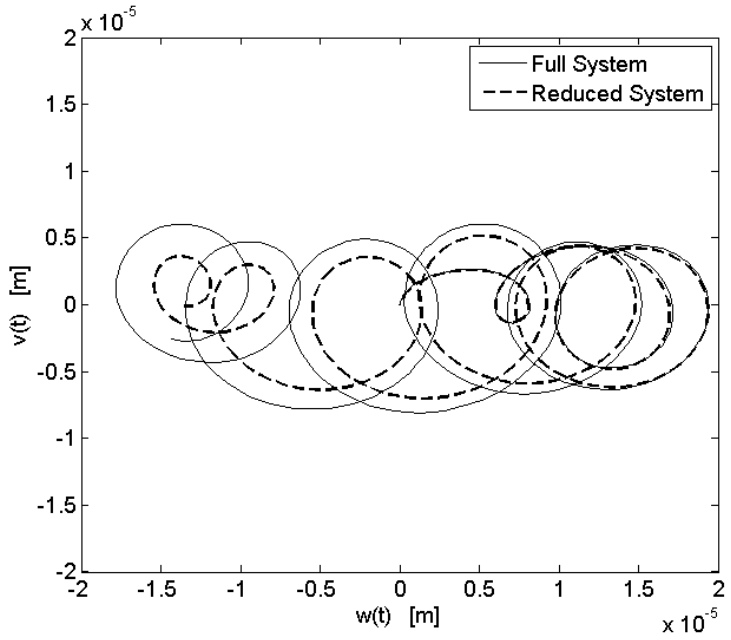

Figure 2.26: Orbit plots for full and reduced (10 degrees of freedom total) rotor model; Craig-Bampton method for general damping

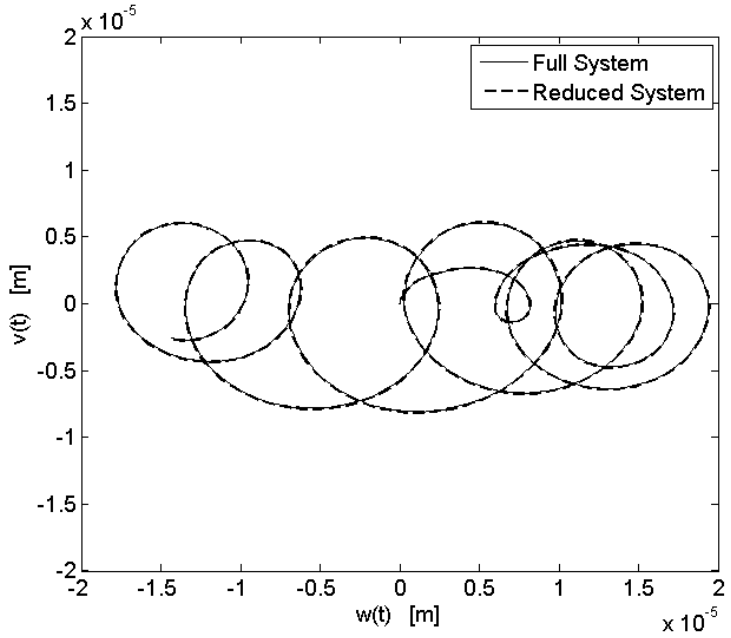

Figure 2.27: Orbit plots for full and reduced (20 degrees of freedom total) rotor model; Craig-Bampton method for general damping

Chapter 3

Isothermal Models of Aerostatic Bearings

3.1 Chapter Outline

This chapter documents the isothermal models of aerostatic bearings with orifice restrictors. The presented models have been developed by means of finite element method and finite difference method and programmed in order to investigate their suitability for steady state and transient numerical solvers. Steady state bearing models are helpful during the pre-design stage of new bearings. These models help with selection of adequate bearing dimensions in relation to load capacity, air consumptions, and power loss. A method of using transient numerical solver to obtain the stiffness and damping coefficients that corresponds not only to the lateral translational displacements, but also to the angular displacements, and the coefficients of cross-coupling between translational and angular displacements is presented. This method has been developed as an extension of existing method of Czolczyński [39]. The last part of this chapter discusses the methods of linearity assessment for aerostatic bearings in terms of obtained linear coefficients and response of the bearing transient model to a stochastic force excitation.

3.2 Aerostatic Bearing Geometry

Circular aerostatic bearing with single row of simple orifices is drawn in the fig. 3.1. The radial clearance is determined by difference of bearing and journal radii $c = R - R_j$. Figure 3.2 defines chosen orientation of coordinates' system. The centre of journal is misaligned from bearing centre by eccentricity $e = \sqrt{(v^2 + w^2)}$. Thickness of air layer is the radial distance measured between surfaces of the bearing bushing and the journal. Air pressure acting upon journal surface results in bearing reaction that consists of two force components F_y, F_z and two moments, M_y and M_z. The moments are oriented according to the figure 3.3 in order to preserve right-hand orientation of coordinate system (x, y, z). These moment components occur if the pressure distribution is not symmetric with respect to the bearing midplane, what happens if bushing and journal axes are not parallel or in the case of bearings with

non-symmetric geometry. Tilt of the journal with respect to bushing is described by angles ψ and ϑ.

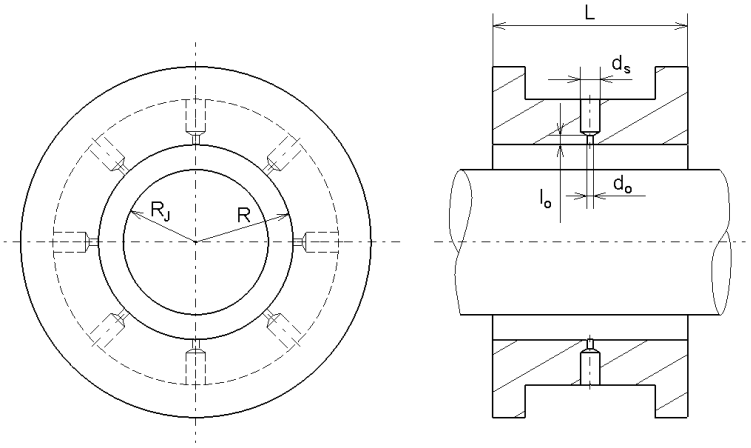

Figure 3.1: Circular aerostatic journal bearing with single row of simple orifices

Annular inlet orifice geometry is characterised by orifice diameter d_o and length l_o. Alternatively, the orifices can be supplemented with feed pockets to produce high stiffness bearings. An example of pocket's geometry is depicted in the figure 3.4.

3.3 Hydrodynamic Model of Aerostatic Journal Bearings

Pressure distribution inside the bearing air film is described by Reynolds equation that was derived and discussed in the introduction chapter. In the case of aerostatic bearings, the Reynolds equation is supplemented by mass flow through feeding system:

$$\frac{\partial}{\partial t}(ph) + \frac{R\omega}{2}\frac{\partial}{\partial x_1}(ph) - \frac{1}{12\mu}\left(\frac{\partial}{\partial x_1}\left(ph^3\frac{\partial p}{\partial x_1}\right) + \frac{\partial}{\partial x_2}\left(ph^3\frac{\partial p}{\partial x_2}\right)\right) = rT\frac{\partial \dot{m}_i}{\partial x_1\,\partial x_2}. \tag{3.1}$$

The right-hand side of this equation is non-zero only at the locations of feedholes and air pockets. The term $\frac{\partial \dot{m}_i}{\partial x_1\,\partial x_2}$ denotes the intake velocity of the air flow multiplied by air density. Using following non-dimensional quantities

$$\xi = \frac{x_1}{R}, \quad \eta = \frac{x_2}{R}, \quad H = \frac{h}{c}, \quad P = \frac{p}{p_a}, \quad \tau = \frac{\omega\, t}{2}, \tag{3.2}$$

the equation (3.1) can be rewritten to

$$\frac{\partial}{\partial \tau}(PH) + \frac{\partial}{\partial \xi}(PH) - \frac{1}{\Lambda}\left(\frac{\partial}{\partial \xi}\left(PH^3\frac{\partial P}{\partial \xi}\right) + \frac{\partial}{\partial \eta}\left(PH^3\frac{\partial P}{\partial \eta}\right)\right) = \frac{2rT}{c\omega R^2 p_a}\frac{\partial \dot{m}_i}{\partial \xi\,\partial \eta}. \tag{3.3}$$

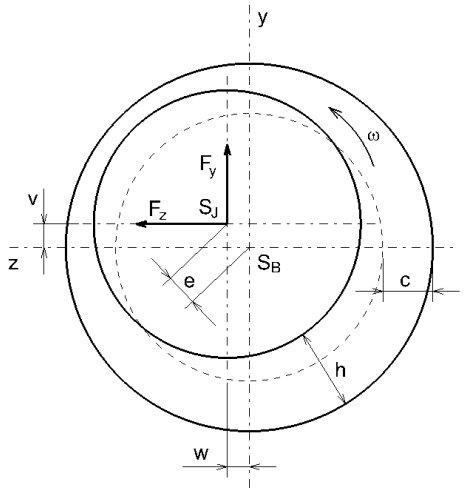

Figure 3.2: Bearing midplane cross section

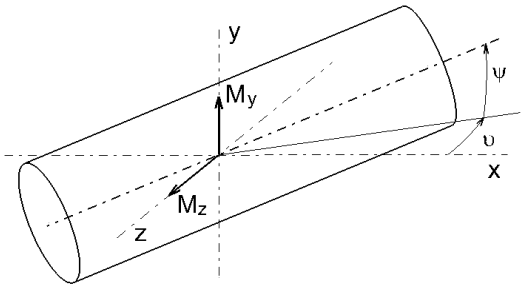

Figure 3.3: Orientation of journal tilt angles and bearing reactive torques

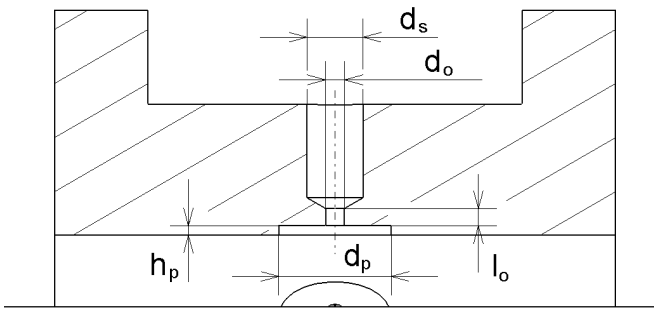

Figure 3.4: Dimensions of feed pocket

This form of equation is used for numerical models together with the appropriate equations controlling air mass flow $\dot{m}_i$. This equation can be discretized by method of finite differences providing a system of ordinary differential equations. The system can be then treated by various numerical methods to obtain time evolution of pressure distribution or steady state solution for fixed journal positions. Variations of these methods can be found in Czolczyński [39], Han et al. [40], Lo et al. [60] and Chen et al. [61]. The biggest advantage of these straightforward methods is the ease of implementation. However they are mostly perceived as old-fashioned outside the field of theory of lubrication, they are still widely used in connection with the Reynolds equation.

3.3.1 Air Inlet Flow

An important part of aerostatic bearing modelling technique is the model of air flow feeding the air film between bushing and journal. Mass flow through feeding system of orifice compensated bearings can be approached by equations of isentropic flow. Theoretical value of isentropic mass flow is

$$\dot{m}_{it} = A_o\, p_s \sqrt{\frac{\kappa}{\kappa-1}\frac{2}{r\,T_0}\left(\left(\frac{p}{p_s}\right)^{\frac{2}{\kappa}} - \left(\frac{p}{p_s}\right)^{\frac{\kappa+1}{\kappa}}\right)}, \tag{3.4}$$

for the pressure ratio greater than critical, $\frac{p}{p_s} > \beta^*$. For smaller pressure ratios, $\frac{p}{p_s} \leq \beta^*$, flow becomes critical and mass flow reaches

$$\dot{m}_{it} = A_o\, p_s \sqrt{\frac{\kappa}{\kappa+1}\frac{2}{r\,T_0}\left(\frac{2}{\kappa+1}\right)^{\frac{2}{\kappa-1}}}. \tag{3.5}$$

A_o is cross section area of the orifice, p_s is supply pressure, p is pressure near the outlet of orifice, κ is ratio of specific heats, r is specific gas constant and T_0 is stagnation temperature. The critical pressure ratio is

$$\beta^* = \left(\frac{2}{\kappa+1}\right)^{\frac{\kappa}{\kappa-1}}. \tag{3.6}$$

Real value of air mass flow is given by

$$\dot{m}_i = c_o\, \dot{m}_{it}, \tag{3.7}$$

where c_o is discharge coefficient obtained experimentally. This work has been recently undertaken by Belforte et al. [62]. Authors tested simple orifice flow restrictors and flow restrictors with feed pockets. They measured air flow and pressure profile in the air film. Obtained discharge coefficients for annular orifice restrictors were approximated by formula

$$c_o = 0.85\left(1 - \mathrm{e}^{-8.2\,\frac{h+h_p}{d_o}}\right). \tag{3.8}$$

This approximation is said acceptable even for feed pocketed annular orifices, if the pocket is no deeper than limit given by condition $\frac{h+h_p}{d_o} < 0.1$. For more recessed pockets, but still satisfying relation $\frac{h+h_p}{d_o} < 0.2$, the discharge coefficient can be estimated by updated relation involving Reynolds number based on orifice diameter

$$c_o = 0.85 \left(1 - \mathrm{e}^{-8.2\,\frac{h+h_p}{d_o}}\right) \left(1 - \mathrm{e}^{-0.001\,Re_o\,\frac{h+h_p}{h+4h_p}}\right), \tag{3.9}$$

where

$$Re_o = \frac{4\dot{m}_i}{\pi d_o \mu}. \tag{3.10}$$

If a feed pocket is deep enough such that $\frac{h+h_p}{d_o} \geq 0.2$, it is necessary to consider the pressure inside feed pocket as an independent variable p_p, because it would be significantly different from the pressure of the air surrounding feed pocket. Mass flow is determined by two subsequent restrictors with the pressure drops p_s–p_p and p_p–p. Mass flow through the former one is calculated the same way using equations (3.4), (3.5), (3.7) and (3.9) substituting p_p for p. Mass flow through annular pocket restrictor also satisfies isentropic flow equations (3.4), (3.5), but with pressure p_p used instead of p_s and with passage area $A_p = \pi d_p h$ instead of orifice cross section A_o. Real value of mass flow is obtained from theoretic one by

$$\dot{m}_i = c_p\,\dot{m}_{it}. \tag{3.11}$$

Pocket discharge coefficient c_p was found to follow

$$c_p = 1.05 \left(1 - \mathrm{e}^{-0.005\,Re_p}\right), \tag{3.12}$$

with Reynolds number Re_p now based on the air film thickness

$$Re_p = \frac{\dot{m}_i}{\pi d_p \mu}. \tag{3.13}$$

Both the mass flows, the one passing from orifice to the pocket and the second one leaving the pocket, are equal one another. This relation determines the value of pocket pressure p_p.

Authors Belforte et al. [62] encountered phenomenon called pressure depression near outlet of a simple orifice. The passage area is suddenly reduced when air reaches the film, and inertia volume forces are dominant for the flow. Pressure drops to a local minimum, then increases again as the air continues through the gap where laminar flow develops owing to prevailing viscous forces. The pressure depression phenomenon is depicted in the fig. 3.5 using actual data from [62]. Local maximum pressure p is used in isentropic flow equations (3.4), (3.5). Computational Fluid Dynamics (CFD) analysis of the air flow through feeding system of air bearing has been recently done by Chen and He [63], showing the pressure depression phenomenon for rectangular recess of the orifice.

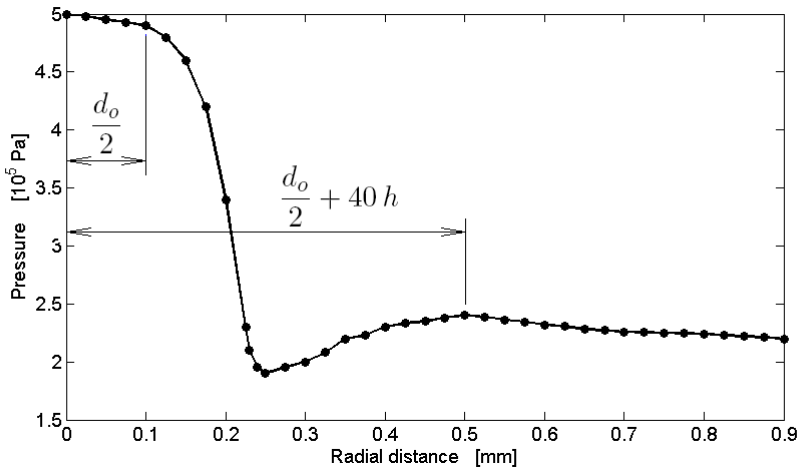

Figure 3.5: Pressure depression phenomenon according to Belforte et al. [62]

3.3.2 FEM Formulation

Galerkin formulation was used to obtain a set of ordinary differential equations from (3.3). For a set of basis functions N_i, weak formulation of Reynolds equation is

$$\int_\Omega N_i \frac{\partial}{\partial \tau}(PH)\,\mathrm{d}\Omega + \int_\Omega N_i \frac{\partial}{\partial \xi}(PH)\,\mathrm{d}\Omega - \frac{1}{\Lambda}\int_\Omega N_i \frac{\partial}{\partial \xi}\left(PH^3\frac{\partial P}{\partial \xi}\right)\mathrm{d}\Omega - \frac{1}{\Lambda}\int_\Omega N_i \frac{\partial}{\partial \eta}\left(PH^3\frac{\partial P}{\partial \eta}\right)\mathrm{d}\Omega = \frac{2rT}{R^2 c p_a \omega}\int_\Omega \frac{\partial \dot{m}_i}{\partial \xi\,\partial \eta} N_i \mathrm{d}\Omega. \tag{3.14}$$

Ω is the region determined by dimensions of the bearing: $\Omega = \{(\xi,\eta) : \xi \in \langle 0, 2\pi), \eta \in \langle 0, L/R\rangle\}$. This rectangular area is meshed by bi-linear quadrilateral finite elements. Orientation and position of single element with respect to coordinates, ξ and η, are displayed in the figure 3.6. Basis functions of this type of element are

$$N_1 = \frac{\xi_b\eta_b - \xi\,\eta_b - \eta\,\xi_b + \xi\,\eta}{(\eta_b - \eta_a)(\xi_b - \xi_a)}, \qquad N_2 = \frac{-\xi_a\eta_b + \eta\,\xi_a + \xi\,\eta_b - \xi\,\eta}{(\eta_b - \eta_a)(\xi_b - \xi_a)},$$
$$N_3 = \frac{-\xi_b\eta_a + \xi\,\eta_a + \eta\,\xi_b - \xi\,\eta}{(\eta_b - \eta_a)(\xi_b - \xi_a)}, \qquad N_4 = \frac{\xi_a\eta_a - \xi\,\eta_a - \eta\,\xi_a + \xi\,\eta}{(\eta_b - \eta_a)(\xi_b - \xi_a)}. \tag{3.15}$$

Derivatives of basis functions with respect to ξ and η are

$$\frac{\partial N_1}{\partial \xi} = \frac{-\eta_b + \eta}{(\eta_b - \eta_a)(\xi_b - \xi_a)}, \qquad \frac{\partial N_2}{\partial \xi} = \frac{\eta_b - \eta}{(\eta_b - \eta_a)(\xi_b - \xi_a)},$$
$$\frac{\partial N_3}{\partial \xi} = \frac{\eta_a - \eta}{(\eta_b - \eta_a)(\xi_b - \xi_a)}, \qquad \frac{\partial N_4}{\partial \xi} = \frac{-\eta_a + \eta}{(\eta_b - \eta_a)(\xi_b - \xi_a)}, \tag{3.16}$$

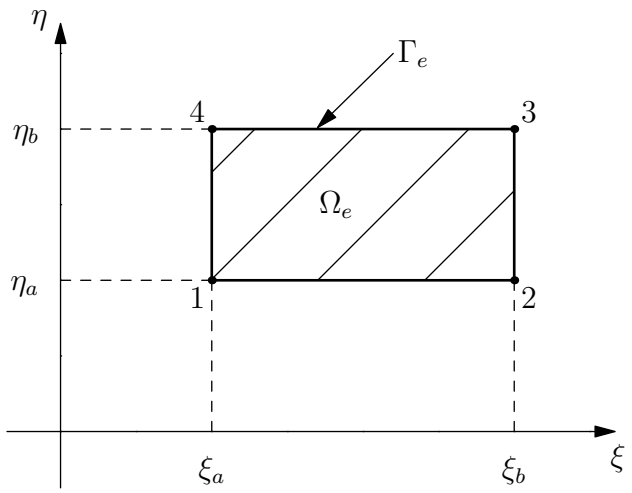

Figure 3.6: Orientation of quadrilateral finite elements

$$\frac{\partial N_1}{\partial \eta} = \frac{-\xi_b + \xi}{(\eta_b - \eta_a)(\xi_b - \xi_a)}, \qquad \frac{\partial N_2}{\partial \eta} = \frac{\xi_a - \xi}{(\eta_b - \eta_a)(\xi_b - \xi_a)},$$
$$\frac{\partial N_3}{\partial \eta} = \frac{\xi_b - \xi}{(\eta_b - \eta_a)(\xi_b - \xi_a)}, \qquad \frac{\partial N_4}{\partial \eta} = \frac{-\xi_a + \xi}{(\eta_b - \eta_a)(\xi_b - \xi_a)}. \tag{3.17}$$

Let us use following approximations of physical quantities

$$P \approx P_i\, N_i, \qquad H \approx H_i\, N_i, \qquad PH^3 = Q \approx Q_i\, N_i \qquad i = 1, 2, 3, 4. \tag{3.18}$$

Integration of (3.14) over single element gives

$$\begin{aligned} &\frac{\partial P_j}{\partial \tau} \int_{\Omega_e} N_i\, N_j\, H_k\, N_k \,\mathrm{d}\Omega_e + \frac{\partial H_j}{\partial \tau} \int_{\Omega_e} N_i\, N_j\, P_k\, N_k \,\mathrm{d}\Omega_e + \int_{\Gamma_e} N_i\, PH\, \mathbf{n}_\xi \,\mathrm{d}s - \\ &P_j \int_{\Omega_e} H_k\, N_k \frac{\partial N_i}{\partial \xi}\, N_j \,\mathrm{d}\Omega_e - \frac{1}{\Lambda} \int_{\Gamma_e} N_i Q \frac{\partial P}{\partial \xi}\, \mathbf{n}_\xi \,\mathrm{d}s + \frac{P_j}{\Lambda} \int_{\Omega_e} Q_k\, N_k \frac{\partial N_i}{\partial \xi} \frac{\partial N_j}{\partial \xi} \,\mathrm{d}s - \\ &\frac{1}{\Lambda} \int_{\Gamma_e} N_i Q \frac{\partial P}{\partial \eta}\, \mathbf{n}_\eta \,\mathrm{d}s + \frac{P_j}{\Lambda} \int_{\Omega_e} Q_k\, N_k \frac{\partial N_i}{\partial \eta} \frac{\partial N_j}{\partial \eta} \,\mathrm{d}\Omega_e = \frac{2rT\,\dot{m}_i}{AR^2 c p_a \omega} \int_{\Omega_e} N_i \,\mathrm{d}\Omega_e. \end{aligned} \tag{3.19}$$

Unexpanded line integrals along element boundary Γ_e will cancel out when assembling system of equations for entire domain Ω because of the opposite directions of integration paths of adjacent elements. The exceptions are the boundary elements with edges on $\eta = 0$ and $\eta = L/R$. (ξ is a cyclic coordinate with boundary condition $P_{(\xi=0)} = P_{(\xi=2\pi)}$.) For those elements, only third line integral remains and can be simplified to

$$\frac{1}{\Lambda} \int_{\Gamma_e} N_i Q \frac{\partial P}{\partial \eta}\, \mathbf{n}_\eta \,\mathrm{d}s = \frac{P_j}{\Lambda} \int_{\xi_a}^{\xi_b} N_i Q_k N_k \frac{\partial N_j}{\partial \eta} \,\mathrm{d}\xi. \tag{3.20}$$

If Dirichlet conditions are applied along bearing ends, also the contribution of this integral becomes zero. Equation (3.19) can be written in the matrix form as

$$M_{ij}^{e}\frac{\partial P_j}{\partial \tau} + B_{ij}^{e}\frac{\partial H_j}{\partial \tau} + K_{ij}^{e}P_j = F_j, \tag{3.21}$$

with elemental matrices calculated neglecting line integrals as

$$\begin{aligned} M_{ij}^{e} &= \sum_{k=1}^{4} H_k \int_{\xi_a}^{\xi_b}\int_{\eta_a}^{\eta_b} N_i\, N_j\, N_k \,\mathrm{d}\eta\,\mathrm{d}\xi, \qquad B_{ij}^{e} = \sum_{k=1}^{4} P_k \int_{\xi_a}^{\xi_b}\int_{\eta_a}^{\eta_b} N_i\, N_j\, N_k \,\mathrm{d}\eta\,\mathrm{d}\xi, \\ K_{ij}^{e} &= \sum_{k=1}^{4} \left(H_k \int_{\xi_a}^{\xi_b}\int_{\eta_a}^{\eta_b} N_j \frac{\partial N_i}{\partial \xi}\, N_k \,\mathrm{d}\eta\,\mathrm{d}\xi + \frac{Q_k}{\Lambda}\int_{\xi_a}^{\xi_b}\int_{\eta_a}^{\eta_b} N_k \left(\frac{\partial N_i}{\partial \xi}\frac{\partial N_j}{\partial \xi} + \frac{\partial N_i}{\partial \eta}\frac{\partial N_j}{\partial \eta} \right) \mathrm{d}\eta\,\mathrm{d}\xi \right). \end{aligned} \tag{3.22}$$

The double integrals can be expressed in close algebraic form. This approach has been used to build elemental matrices in the Matlab code. It is also possible to evaluate these integrals numerically by means of Gauss quadrature rule or other suitable numerical method. Right-hand side vector is zero for all elements except of those positioned at air inlet orifices, for which

$$F_i^{e} = \frac{2rT\,\dot{m}_i}{AR^2 c p_a \omega} \int_{\xi_a}^{\xi_b}\int_{\eta_a}^{\eta_b} N_i \,\mathrm{d}\eta\,\mathrm{d}\xi. \tag{3.23}$$

In the last equation, the index at $\dot{m}_i$ does not mean a summation index. Set of all elemental equations (3.21) forms global system of equations

$$M_{ij}\frac{\partial P_j}{\partial \tau} + B_{ij}\frac{\partial H_j}{\partial \tau} + K_{ij}P_j = F_i \tag{3.24}$$

the solution of which provides the weak solution of original Reynolds equation. Global matrices are composed of individual elemental matrices, and modified by Dirichlet boundary condition for those nodes at the ends of bearing, where the ambient pressure is expected.

3.3.3 Steady State Solver

Static pressure distribution for stationary position of journal is obtained from the equation (3.24), considering both the time derivatives of pressure and the film thickness zero. The stiffness matrix K_{ij} is a function of pressure P_j, thus a set of nonlinear algebraic equation

$$K_{ij}P_j - F_i = 0 \tag{3.25}$$

has to be solved. Newton-Raphson method was implemented to iteratively approach the weak solution for pressure distribution by solving

$$J_{ij}^{\{k\}} \left(P_j^{\{k+1\}} - P_j^{\{k\}} \right) = - \left(K_{ij}^{\{k\}} P_j^{\{k\}} - F_i^{\{k\}} \right). \tag{3.26}$$

Jacobian $J_{ij}^{\{k\}}$ is calculated in each iteration:

$$J_{ij}^{\{k\}} = K_{ij}^{\{k\}} - \frac{\partial F_i^{\{k\}}}{\partial P_j}. \tag{3.27}$$

The second term on the the right-hand side is obtained numerically, but since the vector F_i contains non-zero elements only at a few positions that corresponds to the nodes of elements at inlet orifices, this process can be done effectively with minimum time requirements.

An example of static pressure distribution, calculated by developed numerical method, is shown in the fig. 3.7. The pressure was calculated for bearing operating at relative eccentricity $\varepsilon = 0.6$, with eight inherently compensated orifices of diameter $d_o = 0.2\,\mathrm{mm}$ evenly distributed at bearing midplane section. Air supply pressure: $p_s = 0.5\,\mathrm{MPa}$, angular velocity $\omega = 1000\,\mathrm{s}^{-1}$. Dimensions of the bearing: $L = 30\,\mathrm{mm}$, $R = 15\,\mathrm{mm}$, $c = 20\,\mu\mathrm{m}$.

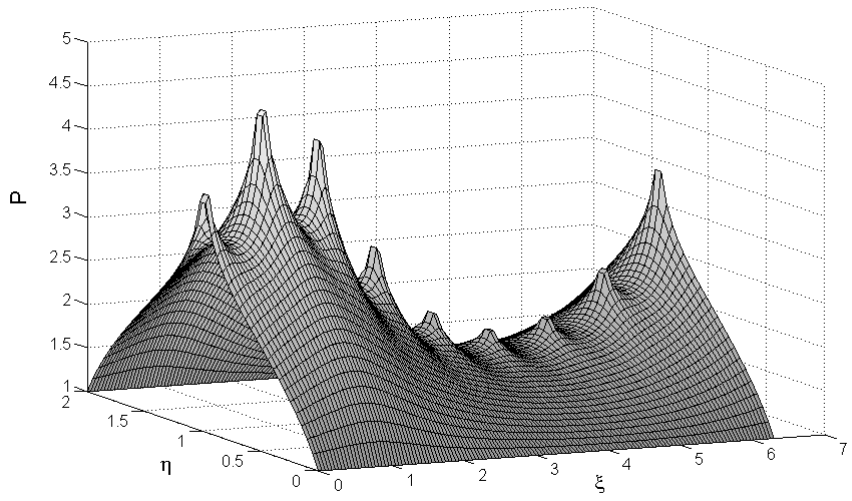

Figure 3.7: Pressure distribution of aerostatic bearing with 8 inherently compensated orifices

The convergence of Newton-Raphson steady state solver applied on this particular bearing design is depicted in the figure 3.8. It shows that pressure distribution converge rapidly, and that the speed of convergence is practically unaffected by the number of finite elements used for spatial discretization.

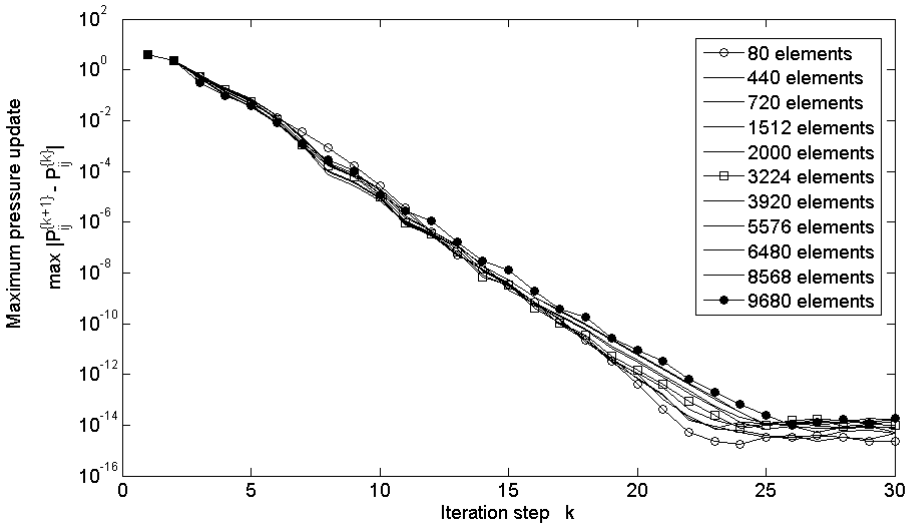

Figure 3.8: Convergence of Newton-Raphson steady state solver

3.3.4 Bearing Load Capacity

The pressure distribution inside bearing air film is driven by bearing geometry and operating conditions of the bearing, involving air supply pressure, angular speed of journal, and position of journal with respect to bushing. For stationary operating conditions, the balance between bearing load and reaction determines the operating point of the bearing. Bearing reactions are the lateral components of the resultant of the air film pressure acting upon shaft journal

$$\begin{aligned} F_y &= -p_a\, R^2 \int_0^{2\pi} \int_0^{\frac{L}{R}} P \cos\xi \,\mathrm{d}\eta \,\mathrm{d}\xi, \quad M_y = p_a\, R^3 \int_0^{2\pi} \int_0^{\frac{L}{R}} P \sin\xi \left(\eta - \frac{L}{2R}\right) \mathrm{d}\eta \,\mathrm{d}\xi, \\ F_z &= -p_a\, R^2 \int_0^{2\pi} \int_0^{\frac{L}{R}} P \sin\xi \,\mathrm{d}\eta \,\mathrm{d}\xi, \quad M_z = -p_a\, R^3 \int_0^{2\pi} \int_0^{\frac{L}{R}} P \cos\xi \left(\eta - \frac{L}{2R}\right) \mathrm{d}\eta \,\mathrm{d}\xi. \end{aligned} \tag{3.28}$$

For given eccentricity, bearing reactions determine the bearing load capacity W. It is the maximum static load applicable to the bearing on condition that the journal position does not exceed the respective eccentricity.

$$W(\varepsilon) = \sqrt{F_y^2 + F_z^2}. \tag{3.29}$$

The load capacity of the bearing design specified above, versus maximum relative eccentricity, is drawn in the figure 3.9. It shows the increase of bearing reaction force for greater speed of journal due to hydrodynamic effect. Such operating conditions may not be always stable, even though the steady state solver converges. Figures 3.10 and 3.11 show the effects

of the orifice diameter and bearing radial clearance on bearing load capacity and air consumption. These graphs show the relation between orifice diameter and radial clearance for the maximum load capacity achievable. Smaller diameter of the orifices reduces the air consumption, but smaller radial clearance, corresponding to the maximum load capacity, does not only bring limitations to the production process in terms of precision and surface quality, but also reduces the stability margin at higher speeds. Convergence of load capacity obtained by finite element solver is depicted in the figure 3.13.

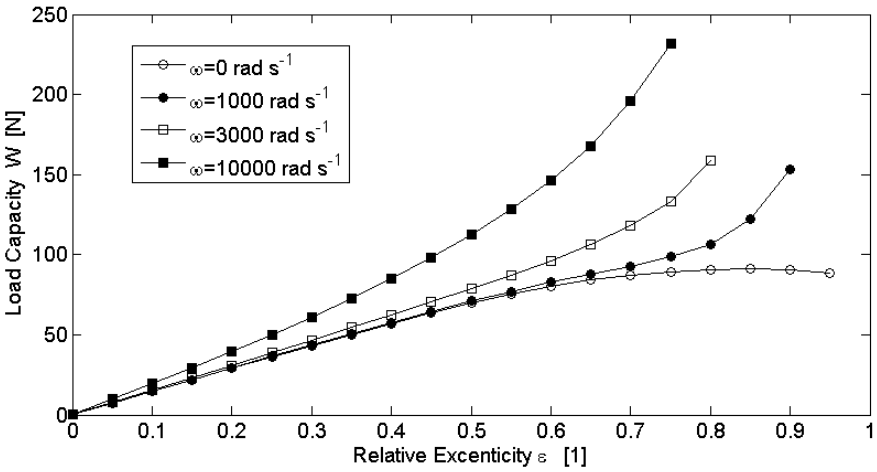

Figure 3.9: Load capacity $W(\varepsilon)$

3.3.5 Drag Torque and Power Loss

Bearing drag torque and power loss can be obtained from static pressure distribution by means of following post-process formulae. Drag torque contribution from single element

$$M_d^e = R^3 \int_{\Omega_e} \frac{Hcp_a}{2R} \frac{\partial P}{\partial \xi} + \frac{\mu R \omega}{Hc} \, \mathrm{d}\xi \, \mathrm{d}\eta \tag{3.30}$$

gives the contribution to total bearing power loss from single element as

$$P_l^e = \omega M_d^e. \tag{3.31}$$

3.3.6 Transient Solver

The transient solver using FEM model of aerostatic bearing works with system of first order differential equations

$$M_{ij} \frac{\partial P_j}{\partial \tau} + K_{ij} P_j = F_j - B_{ij} \frac{\partial H_j}{\partial \tau} \tag{3.32}$$

describing time evolution of the pressure distribution of the bearing. The system matrices are dependent on actual thickness function H, its time derivative, and, due to nonlinearity of

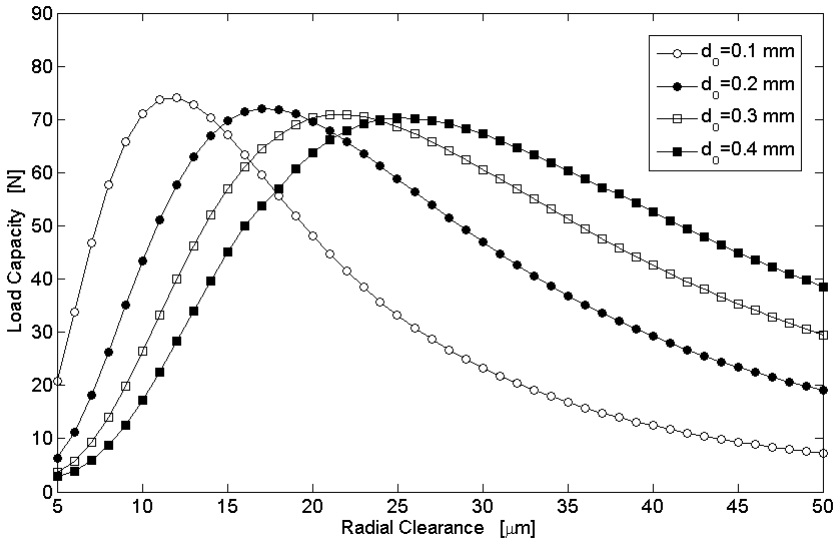

Figure 3.10: Load capacity versus radial clearance and orifice diameter, relative eccentricity $\varepsilon = 0.5$

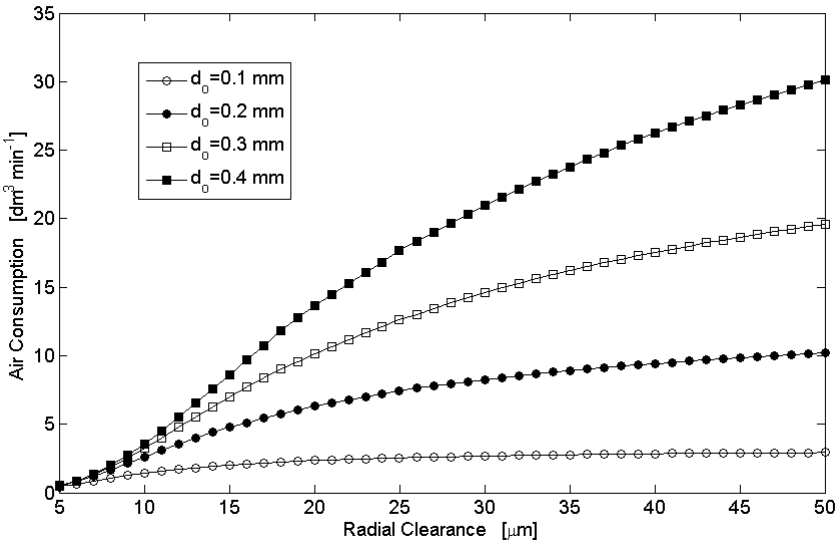

Figure 3.11: Air consumption versus radial clearance and orifice diameter, relative eccentricity $\varepsilon = 0.5$

the problem, also on the actual pressure P. This fact leads to necessity of re-building these matrices each time step, which is extremely time-consuming for bigger number of elements. However the dimensionless Reynolds equation was used for development of the system (3.32), the time step of transient solver remains limited due to the inlet mass flow conditions contained in vector F_j on the right-hand side of the equation. Numerical experiments revealed that the reasonable time step for 4th order Runge-Kutta and 2nd order Adams-Moulton methods should not exceed order of magnitude $\Delta\tau = 10^{-6}\omega$.

Alternatively, the time evolution of the pressure determined by the Reynolds equation (3.3) can be approached by finite difference method. Area of the air gap $\Omega \in \{\xi \times \eta; \xi \in \langle 0, 2\pi), \eta \in \langle 0, L/R\rangle\}$ is divided into $(n+2) \times (m+1)$ rectangular regions. The uniform mesh contains extra rows of nodes outside the solved region in order to implement boundary conditions. Two extra columns of nodes are used for enforcing the periodicity condition in η direction, see figure 3.12.

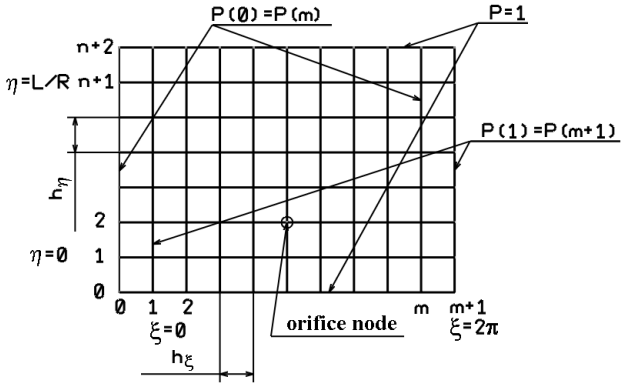

Figure 3.12: Mesh of air gap region – FDM

Replacing the spatial derivatives in (3.3) by approximative differences of second order leads to the set of nonlinear differential equations (3.33), which describes the nodal values of pressure and their time changes that both depend on the functions describing air film thickness and its time derivative obtained from instantaneous position and velocity of journal inside bearing. This FDM transient solver, in conjunction with rigid rotor dynamics, has been presented by author of this work, Skarolek [64]. Similar modelling technique can be found in the work of Lo et al. [60].

$$\frac{\partial P}{\partial \tau}(i,j) = \frac{\Lambda}{H_{i,j}} \left(P_{i,j} H_{i,j}^3 \frac{P_{i+1,j} - 2P_{i,j} + P_{i-1,j}}{h_\xi^2} + P_{i,j} H_{i,j}^3 \frac{P_{i,j+1} - 2P_{i,j} + P_{i,j+1}}{h_\eta^2} + \right.$$
$$H_{i,j}^3 \left(\frac{P_{i+1,j} - P_{i-1,j}}{2h_\xi} \right)^2 + H_{i,j}^3 \left(\frac{P_{i,j+1} - P_{i,j-1}}{2h_\eta} \right)^2 + 3P_{i,j} H_{i,j}^2 \frac{\partial H}{\partial \xi}(i,j) \frac{P_{i+1,j} - P_{i-1,j}}{2h_\xi} +$$
$$3P_{i,j} H_{i,j}^2 \frac{\partial H}{\partial \eta}(i,j) \frac{P_{i,j+1} - P_{i,j-1}}{2h_\eta} - \Lambda \left(H_{i,j} \frac{P_{i+1,j} - P_{i-1,j}}{2h_\xi} + P_{i,j} \frac{\partial H}{\partial \xi}(i,j) \right) -$$
$$\left. \frac{P_{i,j}}{\Lambda} \frac{\partial H}{\partial \tau}(i,j) + \frac{12\mu r T_0}{p_a c^3} \frac{c_o A_o p_s}{h_\xi \, h_\eta} \sqrt{\frac{2\kappa}{\kappa - 1} \frac{1}{r T_0} \left(1 - \left(\frac{P_{i,j}}{P_s} \right)^{\frac{\kappa-1}{\kappa}} \right)} \left(\frac{P_{i,j}}{P_s} \right)^{\frac{1}{\kappa}} \right). \tag{3.33}$$

Transient numerical schemes can also be used for calculation of steady state pressure profile. Pressure profiles for two bearing designs marked A & B, both fed with pressure $p_s = 0.6\,\mathrm{MPa}$, and running at eccentricity $\varepsilon = 0.5$ are plotted in the figures 3.14 to 3.17. Both bearing variants share parameters: $R = 15\,\mathrm{mm}, L = 30\,\mathrm{mm}, c = 20\,\mu\mathrm{m}, d_o = 0.2\,\mathrm{mm}$. Bearing A has eight orifices at bearing midplane evenly distributed around circumference. Bearing B has two rows of evenly distributed orifices positioned at planes at the first and the third quarter of bearing length. Bearing A: Fig. 3.14 for stationary shaft and fig. 3.15 for 30,000 rpm. Bearing B: Fig. 3.16 for stationary shaft and fig. 3.17 for 30,000 rpm.

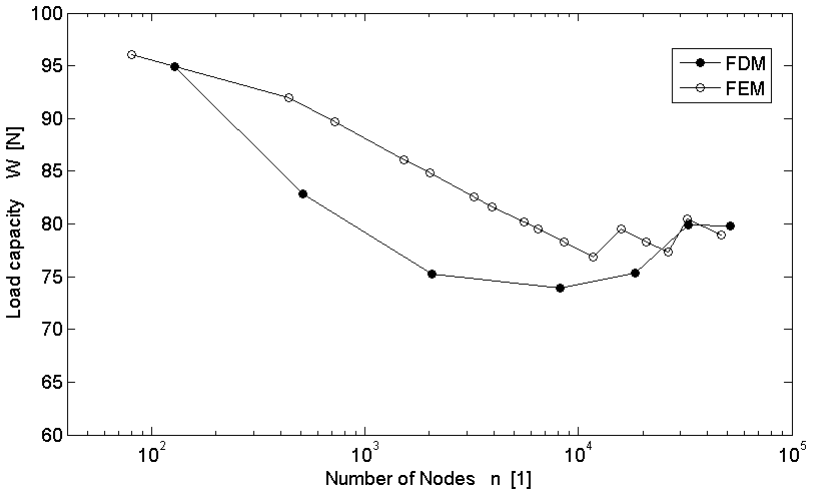

Figure 3.13: Convergence of load capacity W – FDM & FEM, $\varepsilon = 0.6$, $\omega = 1000\,\mathrm{s}^{-1}$

The convergence of bearing load capacity calculated by means transient FDM solver is plotted in fig. 3.13. Values of load capacity obtained by steady state FEM solver are added to the picture. In both cases, the results show that it is necessary to work with relatively fine meshes to obtain acceptably accurate estimation of bearing reactions. The non-monotonic convergence to the limit values of both is likely caused by implementation of discharge coef-

ficient according to the section 3.3.1. In view of rather slow convergence of bearing reactions, the FDM solver is preferable option for transient analysis owing to significantly faster algorithm for greater number of elements/nodes.

3.4 Dynamic Bearing Characteristics

Authors Han et al. [40] used for obtaining linear stiffness and damping coefficients of the aerostatic bearing harmonic the perturbations of film thickness and pressure profile applied to the Reynolds equation that was discretized by finite difference method. This linearization method provides the coefficients at the limit case of small amplitudes of the rotor journal. Paper of Czolczyński [41] and the book of the same author [39] describe approach based on direct numerical solution of the journal equations of motion and the Reynolds equation. The calculated time series of bearing reactions, journal positions and velocities are subjected to regression in order to find the best fit of the bearing coefficients. This method assumes harmonic motion of the journal of given amplitude and returns a set of bearing stiffness and damping coefficients. These coefficients are not limited to the linear model of bearing, but contain also higher components of bearing forces treated as a polynomials of displacements and velocities of journal up to the third order. This author uses various time series calculated based on following situations: free vibrations, forced vibrations, step-jump journal displacement and harmonic motion of the shaft. The former three are said inconvenient for described method. The last one brings the advantage of possibility of enforcing a harmonic vibrations of the journal in specific directions separately. This is important because of linear independence of the vectors of displacements and velocities. In the case of journal undergoing circular orbit motion, the vectors of v and $\dot{w}$ and vice versa are not linearly independent.

3.4.1 Translational Stiffness and Damping Coefficients

The method of direct numerical solution restricted to linear coefficients is explained in this subsection. This method has been previously published at national conference by author of this work, Skarolek and Kozánek [65].

Journal equations of motion

$$m\ddot{v} = F_y - mg, \qquad m\ddot{w} = F_z \tag{3.34}$$

contain gravity force acting on the journal and the bearing reactions F_y,F_z, which are calculated by transient solver of Reynolds equation. Firstly, by solving these equations, the equilibrium position of journal y^e, z^e is calculated. This position depends on mass of the journal and its angular velocity for given bearing. See the fig. 3.18.

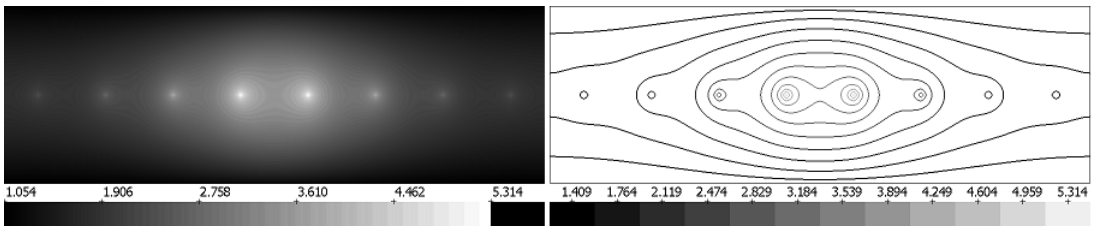

Figure 3.14: Pressure distribution, isobars: Bearing A, 0 rpm

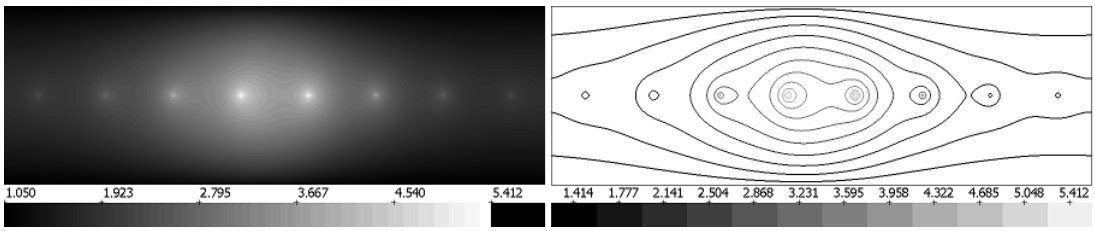

Figure 3.15: Pressure distribution, isobars: Bearing A, 30000 rpm

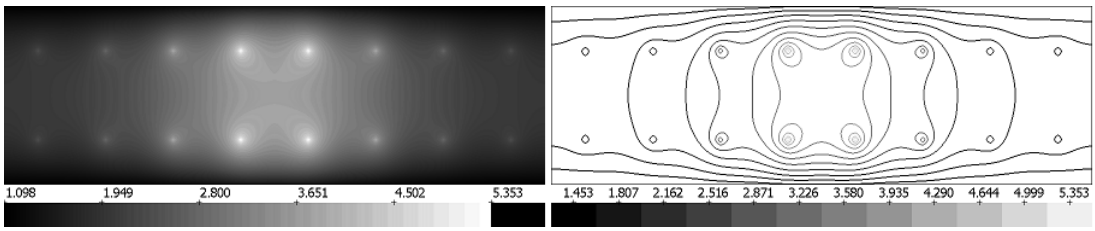

Figure 3.16: Pressure distribution, isobars: Bearing A, 0 rpm

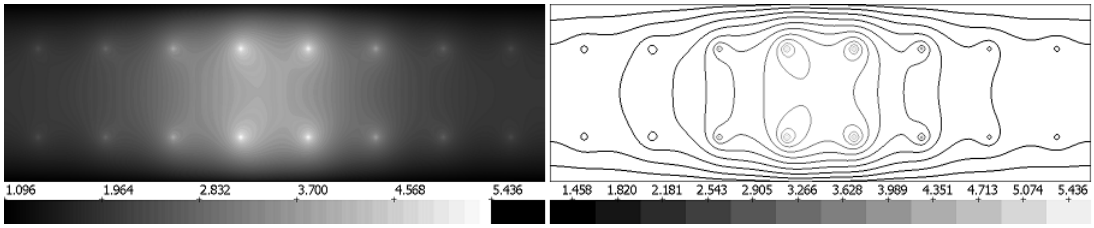

Figure 3.17: Pressure distribution, isobars: Bearing B, 30000 rpm

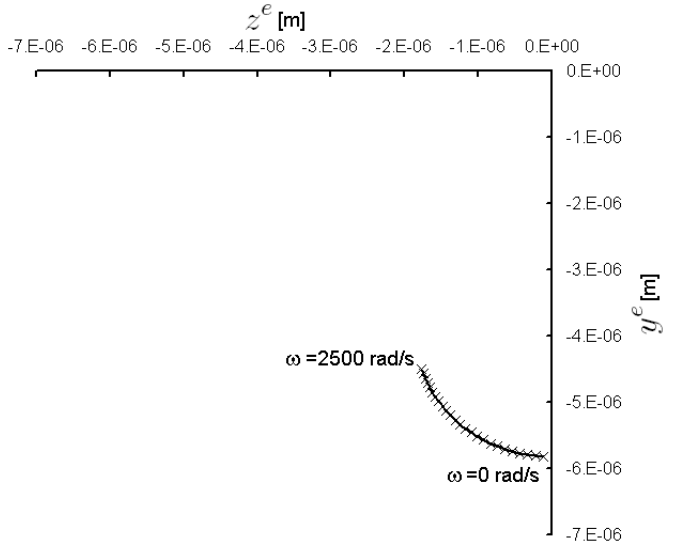

Figure 3.18: Equilibrium position of journal

Linear model of bearing expects reaction forces written in matrix form as

$$\begin{pmatrix} F_y - F_y^e \\ F_z - F_z^e \end{pmatrix} = -\begin{pmatrix} k_{yy} & k_{yz} \\ k_{zy} & k_{zz} \end{pmatrix} \begin{pmatrix} v - y^e \\ w - z^e \end{pmatrix} - \begin{pmatrix} b_{yy} & b_{yz} \\ b_{zy} & b_{zz} \end{pmatrix} \begin{pmatrix} \dot{v} \\ \dot{w} \end{pmatrix}, \tag{3.35}$$

where F_y^e, F_z^e are reaction forces acting upon journal at equilibrium position y^e, z^e. The journal is than forced to harmonic motion of amplitude A, separately in directions of y and z axes.

$$\begin{aligned} \tilde{v} &= v - y^e = A \cdot sin(\omega t), \qquad \dot{\tilde{v}} = \dot{v} = A\omega \cdot cos(\omega t), \\ \tilde{w} &= w - z^e = A \cdot sin(\omega t), \qquad \dot{\tilde{w}} = \dot{w} = A\omega \cdot cos(\omega t). \end{aligned} \tag{3.36}$$

During these enforced motions of shaft journal, the bearing reactions are stored together with displacements and velocities of journal.

It is convenient to divide equation (3.35) into four independent ones before applying least square regression for bearing coefficients:

$$\begin{aligned} -F_{yy} &= k_{yy} \cdot \tilde{v} + b_{yy} \cdot \dot{\tilde{v}}, \qquad -F_{zy} = k_{zy} \cdot \tilde{v} + b_{zy} \cdot \dot{\tilde{v}}, \\ -F_{yz} &= k_{yz} \cdot \tilde{w} + b_{yz} \cdot \dot{\tilde{w}}, \qquad -F_{zz} = k_{zz} \cdot \tilde{w} + b_{zz} \cdot \dot{\tilde{w}}. \end{aligned} \tag{3.37}$$

It is evident that due to harmonic motion the vectors $\tilde{v}$ and $\dot{\tilde{v}}$ as well as $\tilde{w}$ and $\dot{\tilde{w}}$ are orthogonal, hence the least square fitting is well posed problem. The increase of angular speed promotes cross-coupling coefficients of stiffness and damping due to non-symmetry of the pressure profile. Cross-coupling stiffness coefficient k_{yz} and k_{yz} have major impact to

stability of equilibrium position. It can be easily shown that without taking damping into equations, the equilibrium cannot be stable for $\omega > 0$.

3.4.2 Experimental Validation of Bearing Dynamic Parameters

Authors Kozánek and Půst [66] have recently published paper dealing with identification of aerostatic bearing parameters based on experiments. Details on the identification methods as well as on used experimental setup can be found also in Kozánek et al. [67],[68]. Experimental results of diagonal stiffness and damping coefficients of bearing similar to bearing design referred to as B are compared with the results obtained by algorithm presented in this work. The bearing design differs from bearing design B by length $L = 45\,\mathrm{mm}$ and radial clearance $c = 40\,\mu\mathrm{m}$. The air supply pressure was $p_s = 0.2\,\mathrm{MPa}$. The experimental and calculated stiffness and damping parameters are displayed in the figures 3.19, 3.20.

The figures 3.19 and 3.20 show reasonable agreement of calculated and experimental data. Differences in diagonal stiffness coefficients, K_{yy}, K_{zz}, reach slightly over 20 percent. In the case of damping coefficients, B_{yy}, B_{zz}, the calculated parameters lie inside the range, spanned by experimentally obtained data. Observed differences are not considered excessive, because they involve entire chain of inevitable uncertainties: Manufacturing tolerances of the test bearing, achievable precision of test rig setup, numerical errors of measurement, identification and simulation processes, and estimation of discharge coefficients used in bearing transient solver. From engineering standpoint, this level of accuracy of estimation of bearing parameters is satisfactory; very often engineers have to accept uncertainties of similar or even greater level.

3.4.3 Angular and Lateral-Angular Cross-Coupling Coefficients

Previous direct simulation method of enforced harmonic vibration of journal is applicable to the extended case of searching stiffness and damping coefficients related not only to the lateral displacements v, w and their derivatives, but also the coefficients corresponding to tilt angles ϑ, ψ and to respective angular velocities. Bearing reactions are expected to be linear with displacement and velocities

$$\mathbf{R} = -\mathbf{K}\mathbf{u} - \mathbf{B}\dot{\mathbf{u}}, \tag{3.38}$$

where $\mathbf{R}$ is vector of bearing reactions, vector $\mathbf{u}$ comprise displacements. The previous equation, written in components, is then

$$\begin{pmatrix} \tilde{F}_y \\ \tilde{F}_z \\ \tilde{M}_y \\ \tilde{M}_z \end{pmatrix} = - \begin{pmatrix} k_{yy} & k_{yz} & k_{y\vartheta} & k_{y\psi} \\ k_{zy} & k_{zz} & k_{z\vartheta} & k_{z\psi} \\ k_{\vartheta y} & k_{\vartheta z} & k_{\vartheta\vartheta} & k_{\vartheta\psi} \\ k_{\psi y} & k_{\psi z} & k_{\psi\vartheta} & k_{\psi\psi} \end{pmatrix} \begin{pmatrix} \tilde{v} \\ \tilde{w} \\ \tilde{\vartheta} \\ \tilde{\psi} \end{pmatrix} - \begin{pmatrix} b_{yy} & b_{yz} & b_{y\vartheta} & b_{y\psi} \\ b_{zy} & b_{zz} & b_{z\vartheta} & b_{z\psi} \\ b_{\vartheta y} & b_{\vartheta z} & b_{\vartheta\vartheta} & b_{\vartheta\psi} \\ b_{\psi y} & b_{\psi z} & b_{\psi\vartheta} & b_{\psi\psi} \end{pmatrix} \begin{pmatrix} \dot{\tilde{v}} \\ \dot{\tilde{w}} \\ \dot{\tilde{\vartheta}} \\ \dot{\tilde{\psi}} \end{pmatrix}. \tag{3.39}$$

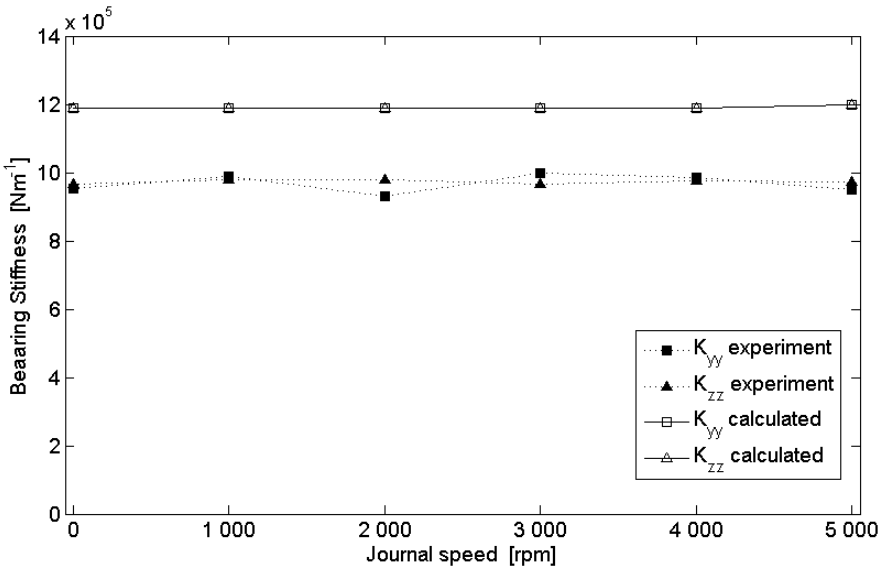

Figure 3.19: Bearing stiffness coefficients; Calculation vs. experiment

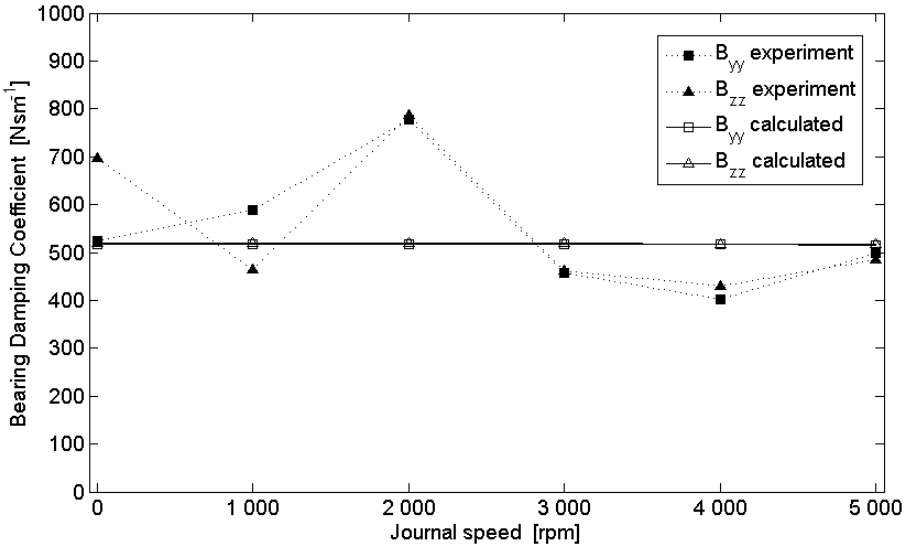

Figure 3.20: Bearing damping coefficients; Calculation vs. experiment

The off-diagonal blocks in **K** and **B** provide cross-coupling between translational and rotational degrees of freedom. The blocks bellow diagonal blocks are expected all zero for circular bearings, because while undergoing translational motion, the journal remains parallel to the bearing axis. The coefficients in the blocks above diagonal blocks may become non-zero for bearing running with certain eccentricity. However, their values are expected to be insignificant.

Harmonic motion of the journal is enforced separately for each degree of freedom according to

$$\begin{aligned}
\tilde{v} &= A \cdot sin(\omega t), & \dot{\tilde{v}} &= A\omega \cdot cos(\omega t),\\
\tilde{w} &= A \cdot sin(\omega t), & \dot{\tilde{w}} &= A\omega \cdot cos(\omega t),\\
\tilde{\vartheta} &= \frac{A}{2L} \cdot sin(\omega t), & \dot{\tilde{\vartheta}} &= \frac{A}{2L}\omega \cdot cos(\omega t),\\
\tilde{\psi} &= \frac{A}{2L} \cdot sin(\omega t), & \dot{\tilde{\psi}} &= \frac{A}{2L}\omega \cdot cos(\omega t).
\end{aligned} \tag{3.40}$$

For all the cases, the time series of journal positions, velocities and bearing reactions are obtained by means of transient solver. The bearing coefficients are calculated by least square regression applied to the time series using one of the following equations:

$$\begin{aligned}
-F_{yy} &= k_{yy} \cdot \tilde{v} + b_{yy} \cdot \dot{\tilde{v}}, & -F_{zy} &= k_{zy} \cdot \tilde{v} + b_{zy} \cdot \dot{\tilde{v}}, & -M_{yy} &= k_{\vartheta y} \cdot \tilde{v} + b_{\vartheta y} \cdot \dot{\tilde{v}},\\
-M_{zy} &= k_{\psi y} \cdot \tilde{v} + b_{\psi y} \cdot \dot{\tilde{v}}, & -F_{yz} &= k_{yz} \cdot \tilde{w} + b_{yy} \cdot \dot{\tilde{w}}, & -F_{zz} &= k_{zz} \cdot \tilde{w} + b_{zz} \cdot \dot{\tilde{w}},\\
-M_{yz} &= k_{\vartheta z} \cdot \tilde{w} + b_{\vartheta z} \cdot \dot{\tilde{w}}, & -M_{zz} &= k_{\psi z} \cdot \tilde{w} + b_{\psi z} \cdot \dot{\tilde{w}}, & -F_{y\vartheta} &= k_{y\vartheta} \cdot \tilde{\vartheta} + b_{y\vartheta} \cdot \dot{\tilde{\vartheta}},\\
-F_{z\vartheta} &= k_{z\vartheta} \cdot \tilde{\vartheta} + b_{z\vartheta} \cdot \dot{\tilde{\vartheta}}, & -M_{y\vartheta} &= k_{\vartheta\vartheta} \cdot \tilde{\vartheta} + b_{\vartheta\vartheta} \cdot \dot{\tilde{\vartheta}}, & -M_{z\vartheta} &= k_{\psi\vartheta} \cdot \tilde{\vartheta} + b_{\psi\vartheta} \cdot \dot{\tilde{\vartheta}},\\
-F_{y\psi} &= k_{y\psi} \cdot \tilde{\psi} + b_{y\psi} \cdot \dot{\tilde{\psi}}, & -F_{z\psi} &= k_{z\psi} \cdot \tilde{\psi} + b_{z\psi} \cdot \dot{\tilde{\psi}}, & -M_{y\psi} &= k_{\vartheta\psi} \cdot \tilde{\psi} + b_{\vartheta\psi} \cdot \dot{\tilde{\psi}},\\
-M_{z\psi} &= k_{\psi\psi} \cdot \tilde{\psi} + b_{\psi\psi} \cdot \dot{\tilde{\psi}}.
\end{aligned} \tag{3.41}$$

All of these equations work with harmonic vibration of single degree of freedom, so that functions of displacement and respective velocity are orthogonal.

3.4.4 Numerical Examples

Dynamic characteristics of both the bearing designs A & B, carrying 5 kg journal, have been investigated at four levels of air supply pressure: 0.3, 0.4, 0.5 and 0.6 MPa. Eccentricities of journal with respect to angular velocity and supply pressure are in the figures 3.21 and 3.22. The lowest pressure level is missing for bearing design A because of low load capacity of this configuration. The bearings were run to such angular speed, where the journal equilibrium position lost stability and the journal started to follow whirl orbit, similar to oil whirl of traditional hydrodynamic bearings.

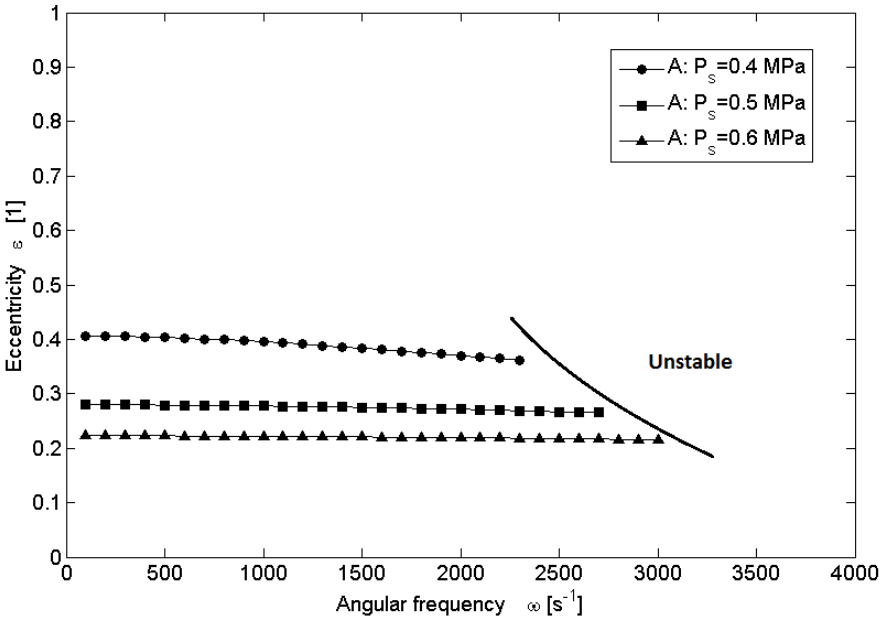

Figure 3.21: Bearing eccentricity v. angular velocity of journal ω, Bearing design A

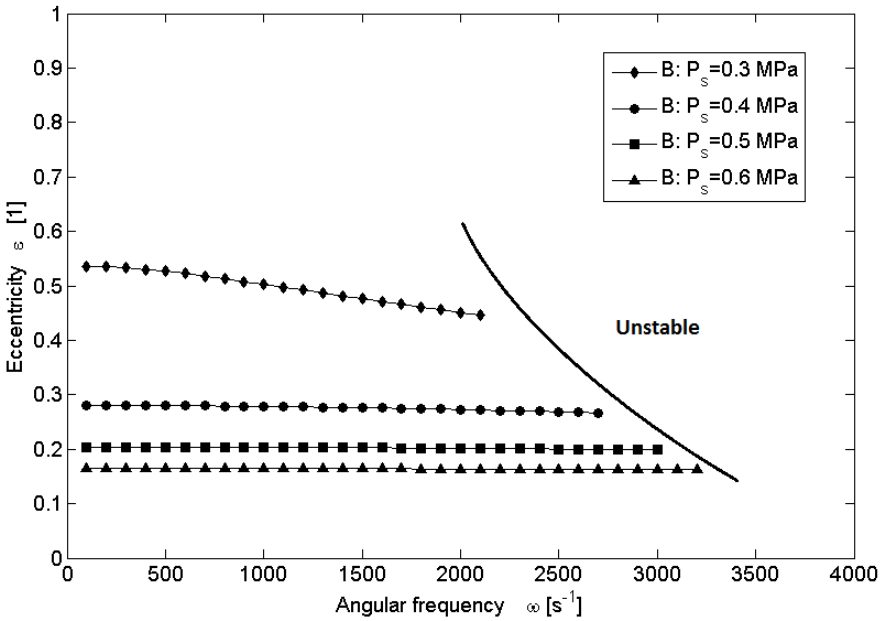

Figure 3.22: Bearing eccentricity v. angular velocity of journal ω, Bearing design B

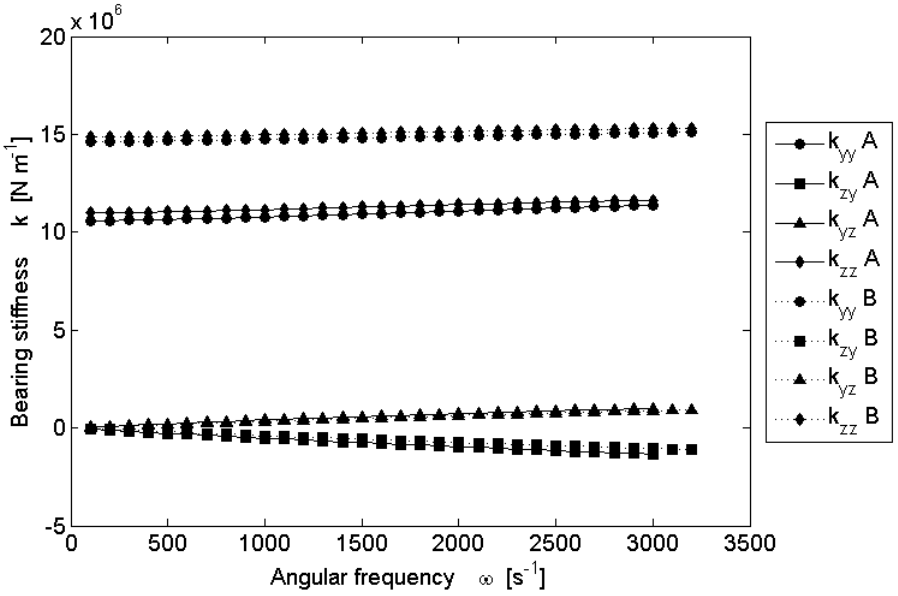

Figure 3.23: Translational stiffness v. angular velocity of journal ω, Bearing design A&B, Supply pressure $p_s = 0.6\,\mathrm{MPa}$

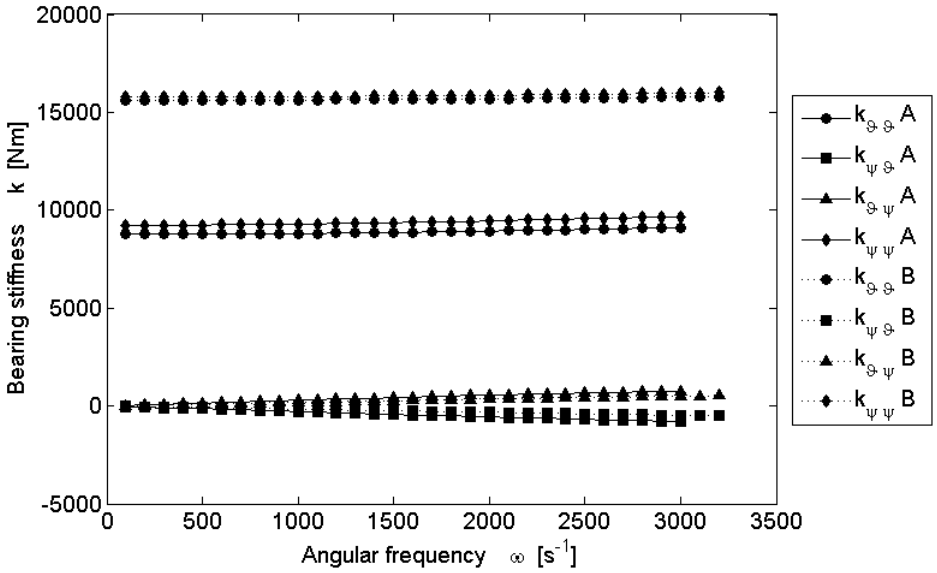

Figure 3.24: Angular stiffness v. angular velocity of journal ω, Bearing design A&B, Supply pressure $p_s = 0.6\,\mathrm{MPa}$

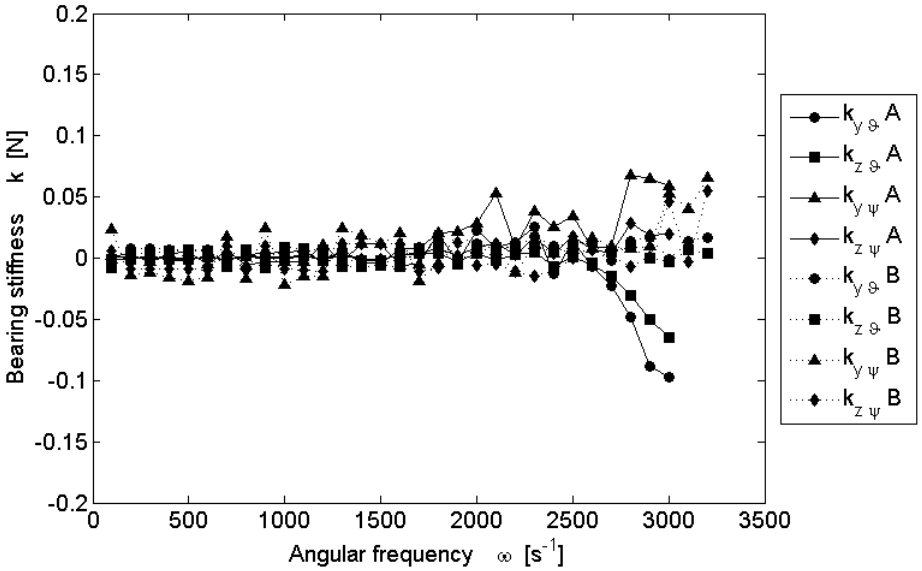

Figure 3.25: Cross-coupling stiffness v. angular velocity of journal ω, Bearing design A&B, Supply pressure $p_s = 0.6\,\mathrm{MPa}$

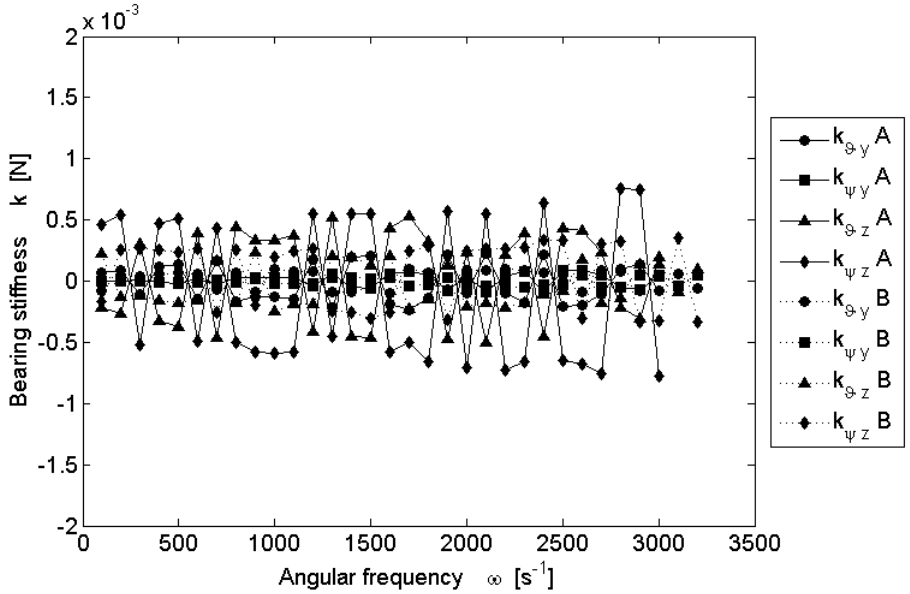

Figure 3.26: Cross-coupling stiffness v. angular velocity of journal ω, Bearing design A&B, Supply pressure $p_s = 0.6\,\mathrm{MPa}$

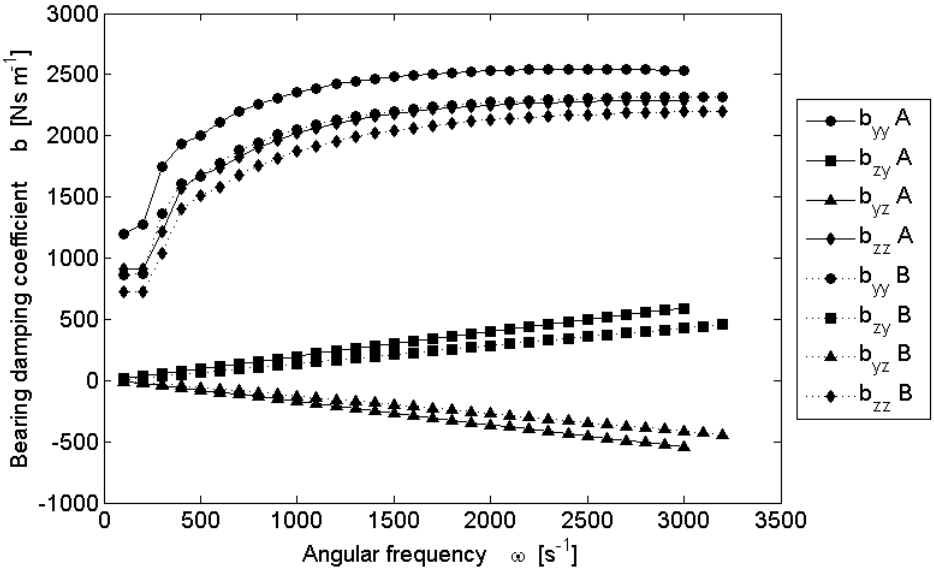

Figure 3.27: Translational damping coeff. v. angular velocity of journal ω, Bearing design A&B, Supply pressure $p_s = 0.6\,\mathrm{MPa}$

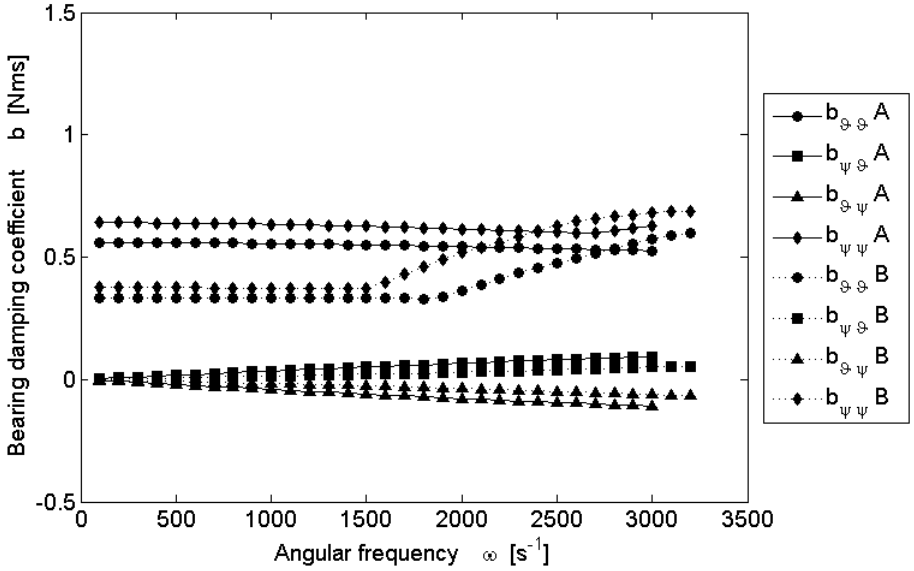

Figure 3.28: Angular damping coeff. v. angular velocity of journal ω, Bearing design A&B, Supply pressure $p_s = 0.6\,\mathrm{MPa}$

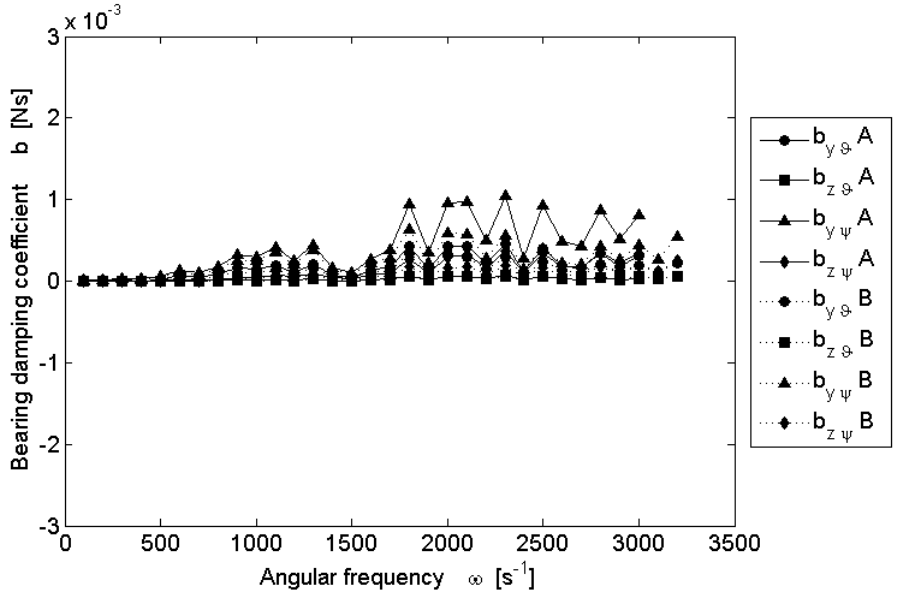

Figure 3.29: Cross-coupling damping coeff. v. angular velocity of journal ω, Bearing design A&B, Supply pressure $p_s = 0.6\,\mathrm{MPa}$

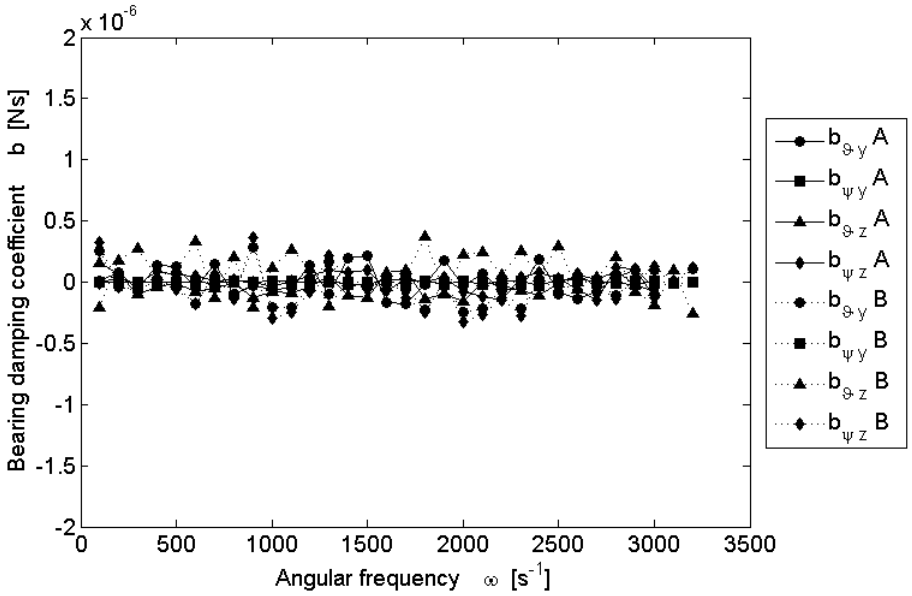

Figure 3.30: Cross-coupling damping coeff. v. angular velocity of journal ω, Bearing design A&B, Supply pressure $p_s = 0.6\,\mathrm{MPa}$

The process described in the previous subsection was applied at each of stable equilibrium, thus obtaining 32 dynamic coefficients from (3.39) for each point. For 0.6 MPa pressure level, the coefficients are plotted in the figures 3.23 to 3.30. Results for the other supply pressures are attached in the appendices as figures C.1 to C.16.

As expected, all cross-coupling coefficients –both the stiffness (figs. 3.25 and 3.26) and the damping (figs. 3.29 and 3.30) ones– that put in relation the translational degrees of freedom and the angular ones are negligible in comparison to the rest.

The translational and the angular stiffnesses (fig. 3.23 and 3.24) are of same character. The diagonal coefficients $k_{yy}, k_{zz}, k_{\vartheta\vartheta}, k_{\psi\psi}$ are mostly determined by supply pressure level and bearing design. The off-diagonal components $k_{zy}, k_{yz}, k_{\psi\vartheta}, k_{\vartheta\psi}$ gain their absolute values with increase of angular velocity due to bearing hydrodynamic effect, with lesser effect from the number of feeding orifices or the supply pressure. The greater differences in figures C.1 and C.3 are caused by greater difference between running eccentricities for both designs. Damping coefficients exhibit similar properties with exception of greater effect of angular velocity on diagonal coefficients $b_{yy}, b_{zz}, b_{\vartheta\vartheta}, b_{\psi\psi}$, see the figures 3.27 and 3.28.

3.5 Linearity of Aerostatic Bearing

According to the linearization technique from the previous section, the bearings running at given speed and load are described by using 16 linear coefficients (neglecting the nearly zero cross-coupling ones). This linearization technique assumes specific level of amplitudes of vibration and specific angular frequency of excitation. The most common is the synchronous excitation by unbalance. The nonlinearity of bearing at given conditions can be assessed by effect of different excitation frequency and vibration amplitudes to linear coefficients. Method of linearization by means of numerical simulation of Reynolds equation and enforced harmonic motion of journal can be used with various frequencies of journal motion $\nu\omega$ at several levels of amplitude A. The effects of frequency and amplitude for bearing design B, supplied with 0.6 MPa and running at angular frequency $\omega = 2000\,\mathrm{s}^{-1}$ is depicted in figures 3.31 to 3.46.

Figures 3.31 and 3.32 show that bearing diagonal stiffness coefficients k_{yy}, k_{zz}, $k_{\vartheta\vartheta}$, $k_{\psi\psi}$ tend to increase for higher frequency of journal vibration, meanwhile the off-diagonal ones k_{yz}, k_{zy}, $k_{\psi\vartheta}$, $k_{\vartheta\psi}$ decline in amplitudes; k_{yz}, k_{zy} even crossing zero value and swapping signs. Cross-coupling stiffnesses in the figures 3.33 and 3.34 appear oscillating along increasing vibration frequency. Their values remain small compared to diagonal coefficients and those oscillations seem to be of numerical origin. Diagonal damping coefficients b_{yy}, b_{zz}, $b_{\vartheta\vartheta}$, $b_{\psi\psi}$ also increase with vibration frequency, but all quickly saturate. The off-diagonal damping coefficients b_{yz}, b_{zy}, $b_{\psi\vartheta}$, $b_{\vartheta\psi}$ are practically unaffected by frequency. See figs. 3.35 and 3.36. The cross-coupling coefficients in the figure 3.37 and 3.38 are again of insignificant magnitudes.

Influence of the level of vibration (0.5 μm to 9.5 μm of 20 μm bearing radial clearance) on bearing stiffness coefficients is rather insignificant, with noticeable effect only to the translational stiffness coefficients, see the figures 3.39 to 3.42. Diagonal bearing damping coefficients

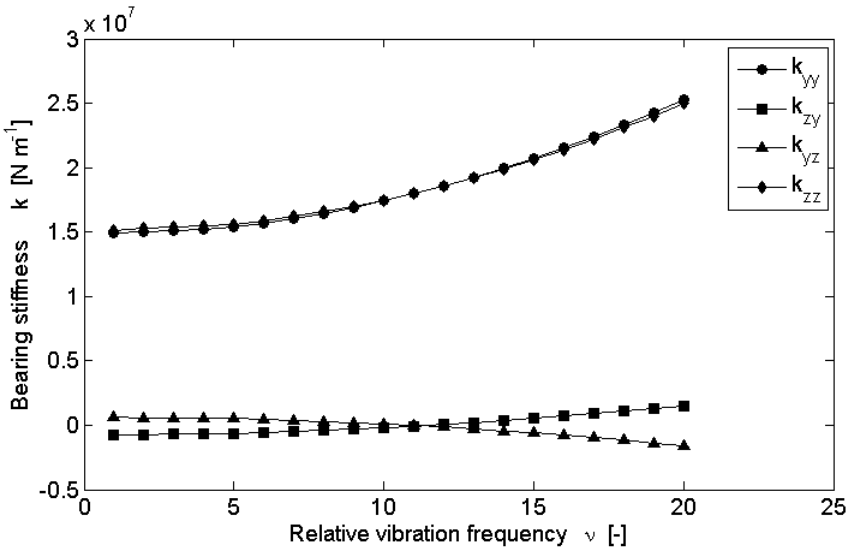

Figure 3.31: Translational stiffness v. relative vibration frequency, bearing B, $p_s = 0.6\,\mathrm{MPa}$

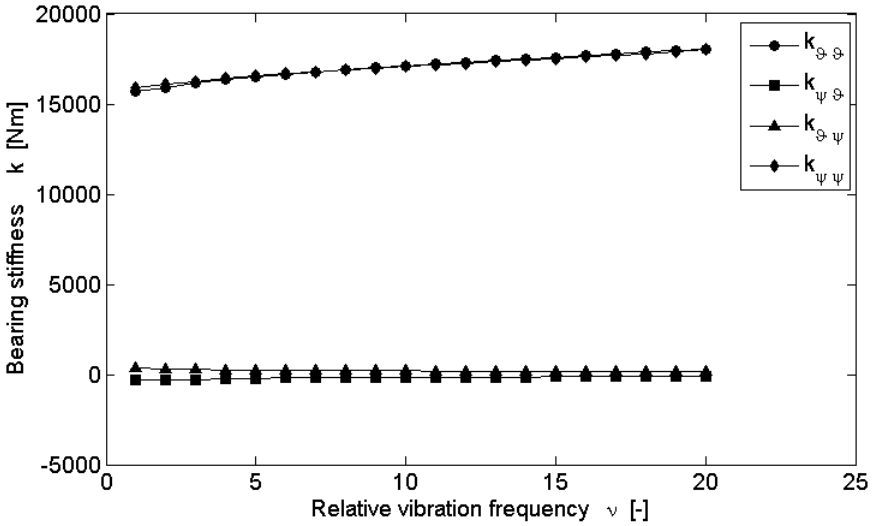

Figure 3.32: Angular stiffness v. relative vibration frequency, bearing B, $p_s = 0.6\,\mathrm{MPa}$

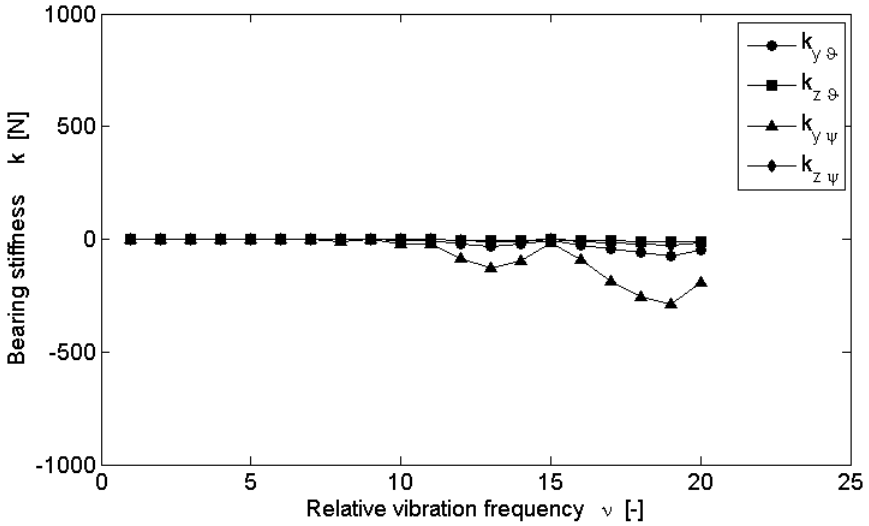

Figure 3.33: Cross-coupling stiffness v. relative vibration frequency, bearing B, $p_s = 0.6\,\mathrm{MPa}$

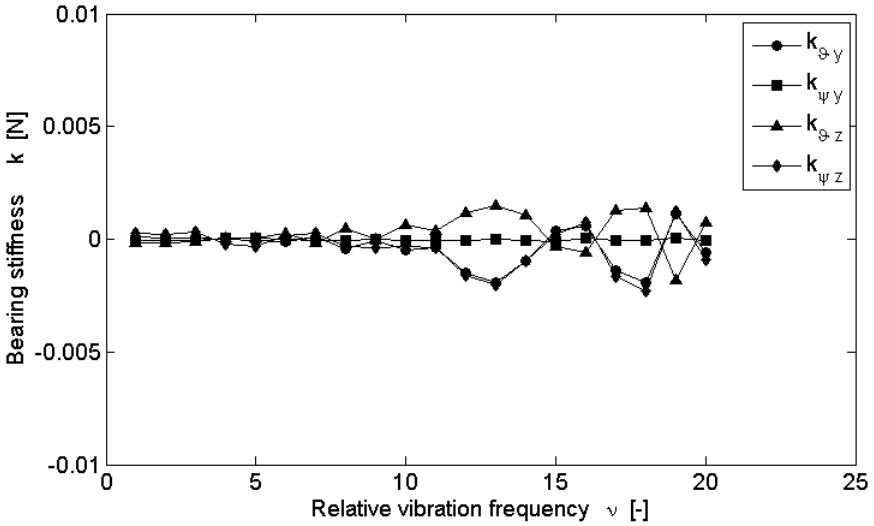

Figure 3.34: Cross-coupling stiffness v. relative vibration frequency, bearing B, $p_s = 0.6\,\mathrm{MPa}$

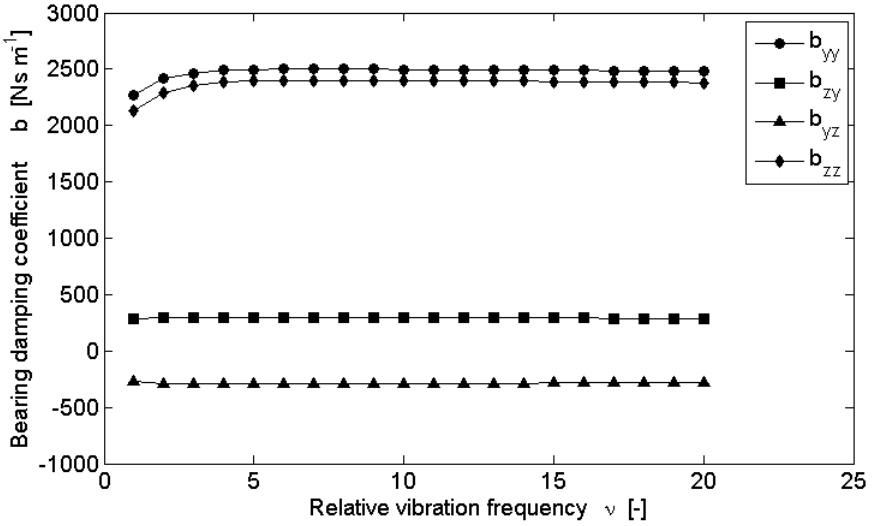

Figure 3.35: Translational damping coeff. v. relative vibration frequency, bearing B, $p_s = 0.6\,\mathrm{MPa}$

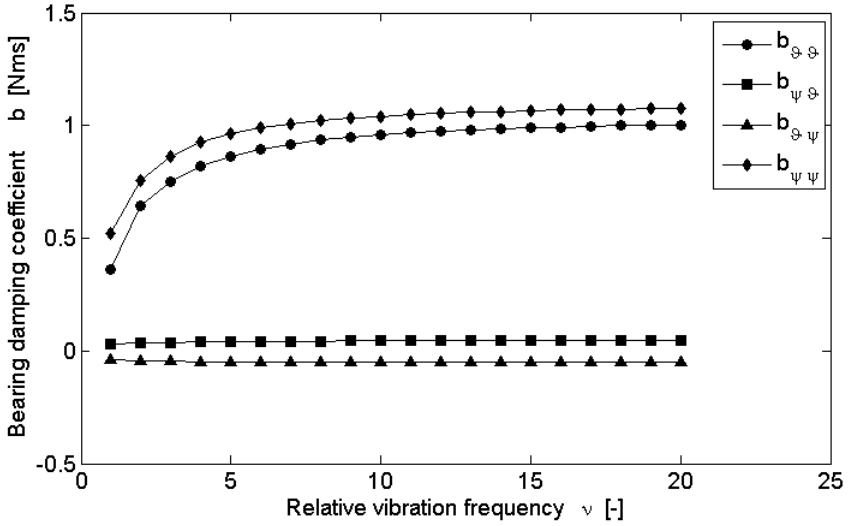

Figure 3.36: Angular damping coeff. v. relative vibration frequency, bearing B, $p_s = 0.6\,\mathrm{MPa}$

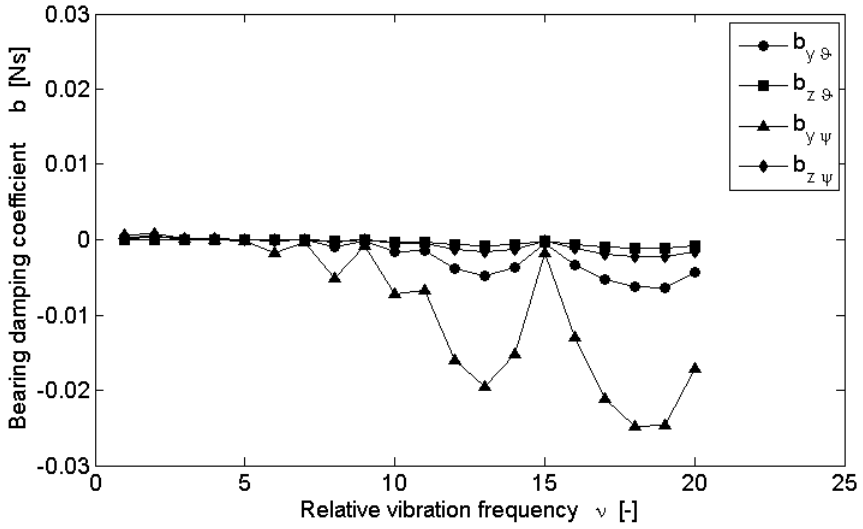

Figure 3.37: Cross-coupling damping coeff. v. relative vibration frequency, bearing B, p_s = 0.6 MPa

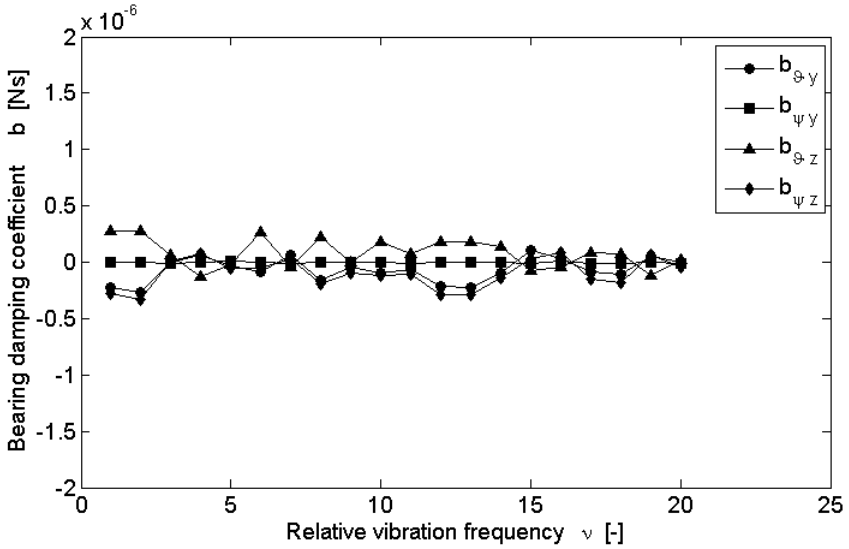

Figure 3.38: Cross-coupling damping coeff. v. relative vibration frequency, bearing B, p_s = 0.6 MPa

b_{yy}, b_{zz}, $b_{\vartheta\vartheta}$, $b_{\psi\psi}$ increase with amplitude, the rest of the coefficients are either unaffected or insignificant.

Presented numerical example indicates that the studied kind of aerostatic bearings running at lower eccentricity behave almost linearly with respect to the vibration amplitude (considering the *stiffness* part of their reactions). Linearized damping increase with amplitude, which effect is important when equilibrium point becomes unstable due to off-diagonal stiffnesses and self-excited vibration of journal occurs. Linearized bearing parameters are more sensitive to frequency of vibration, which fact should be considered in the case of non-synchronous excitation forces.

3.5.1 Transfer Function of Journal–Bearing System

The linearity of journal-bearing system can be also assessed by system response to random force excitation. The frequency response function estimated from simulation results can be compared to the transfer functions calculated by means of linearized bearing coefficients. Coherence functions can be used as a measure of system linearity. Journal-bearing system (3.34) employing the transient bearing solver (3.33) has been solved over period of 6 seconds, while external forces F_y and F_z were acting upon journal. Time series for these functions were constructed as a filtered white noise. Spectral density of these signals is in the figure 3.47.

Frequency response functions have been estimated by averaging of $N = 91$ peridograms, using Hann window with 50% overlap, symbolically by

$$G_{ij}(j\omega) = \frac{1}{N}\sum_{k=1}^{N}\frac{\mathrm{FFT}\left[w_H(t)\cdot g_i^{\{k\}}(t)\right]}{\mathrm{FFT}\left[w_H(t)\cdot f_j^{\{k\}}(t)\right]}, \tag{3.42}$$

where operator FFT $[\cdot]$ signs single-side amplitude spectrum normalized with respect to window function $w_H(t)$. Functions $f_j(t)$, $g_i(t)$ are j-th input resp. i-th output of the system. Superscript {k} signs k-th segment of given time-series. Transfer functions of linearized model were calculated directly as

$$G_{ij}(j\omega) = \left(\mathbf{K} + j\omega\mathbf{B} - \omega^2\mathbf{M}\right)^{-1}, \tag{3.43}$$

where matrices $\mathbf{K}$, $\mathbf{B}$ are the translational parts of bearing stiffness and damping matrix. $\mathbf{M}$ is diagonal matrix with journal mass on diagonal positions. These analyses have been done for both bearing designs A and B, running at identical conditions as previous analyses ($p_s = 0.6\,\mathrm{MPa}$, $m = 5\,\mathrm{kg}$, $\omega = 2,000\,\mathrm{s}^{-1}$). Transfer functions of the linearized model and estimated frequency response functions of nonlinear transient model are plotted in the figures 3.48 and 3.49. The results closely agree in terms of amplitude and phase, with minor discrepancies around amplitude peaks.

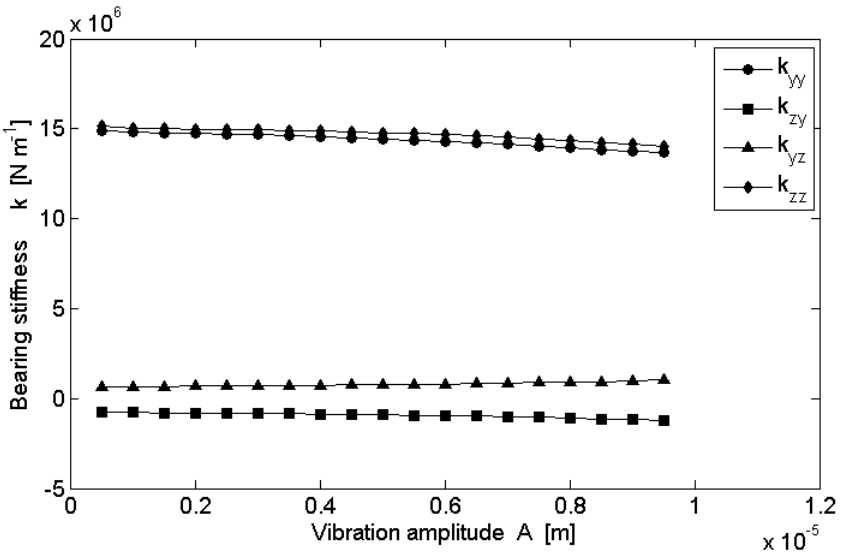

Figure 3.39: Translational stiffness v. vibration amplitude, bearing B, $p_s = 0.6\,\mathrm{MPa}$

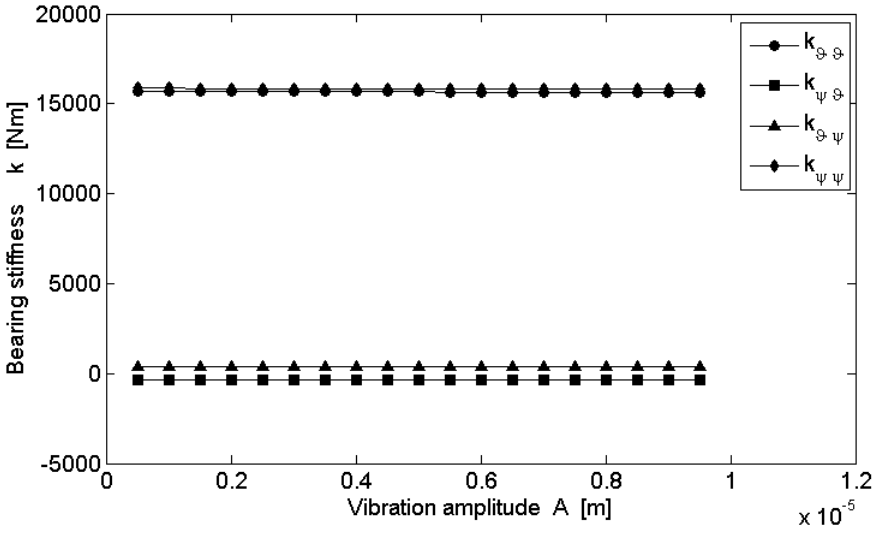

Figure 3.40: Angular stiffness v. vibration amplitude, bearing B, $p_s = 0.6\,\mathrm{MPa}$

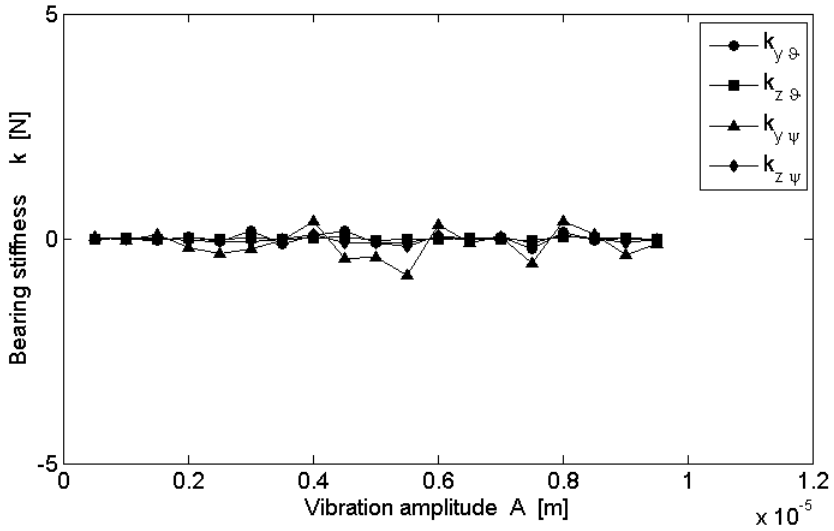

Figure 3.41: Cross-coupling stiffness v. vibration amplitude, bearing B, $p_s = 0.6\,\mathrm{MPa}$

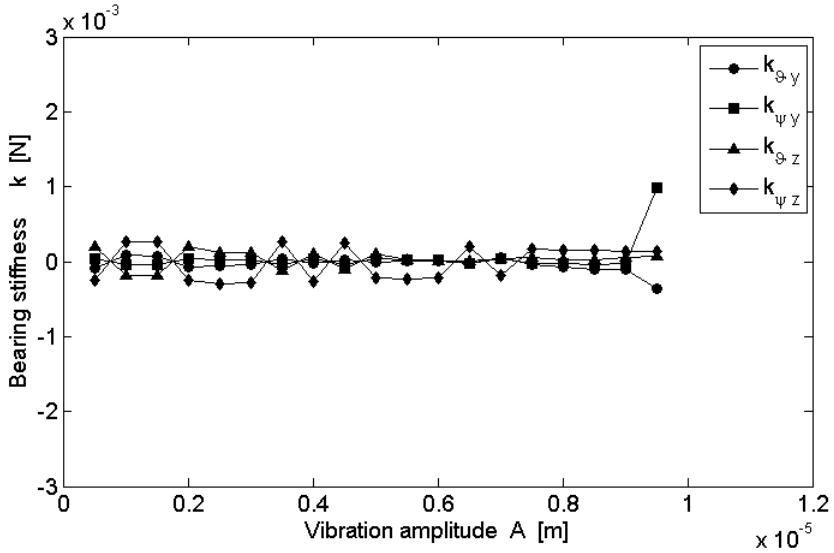

Figure 3.42: Cross-coupling stiffness v. vibration amplitude, bearing B, $p_s = 0.6\,\mathrm{MPa}$

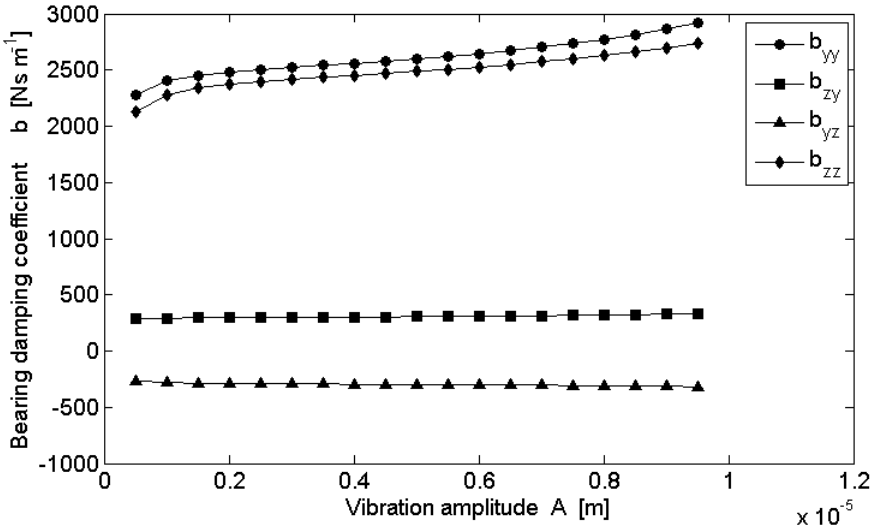

Figure 3.43: Translational damping coeff. v. vibration amplitude, bearing B, $p_s = 0.6\,\mathrm{MPa}$

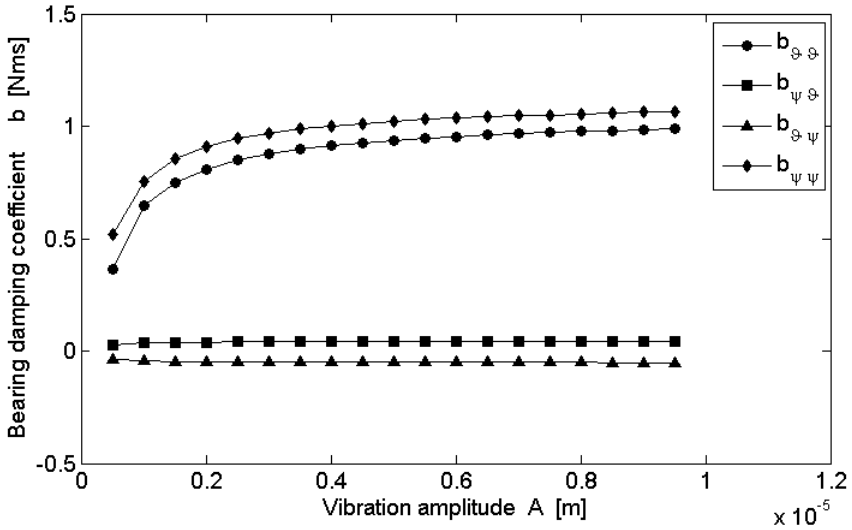

Figure 3.44: Angular damping coeff. v. vibration amplitude, bearing B, $p_s = 0.6\,\mathrm{MPa}$

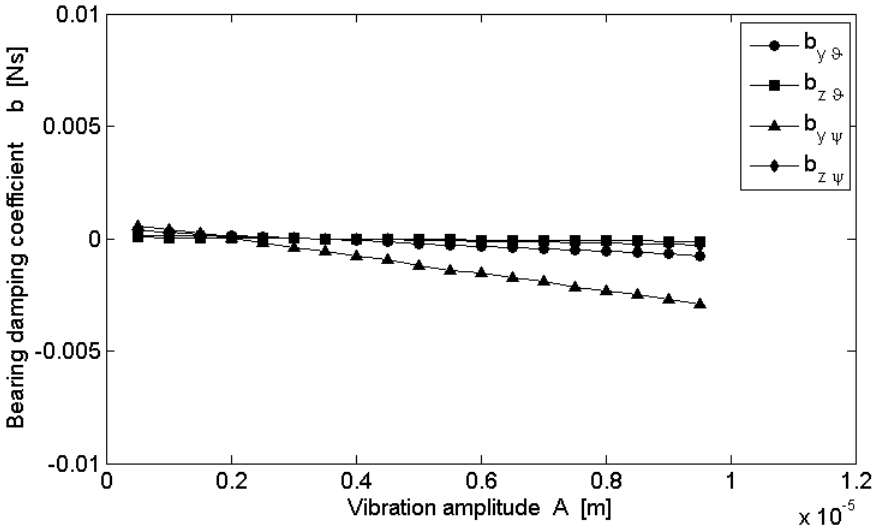

Figure 3.45: Cross-coupling damping coeff. v. vibration amplitude, bearing B, $p_s = 0.6\,\mathrm{MPa}$

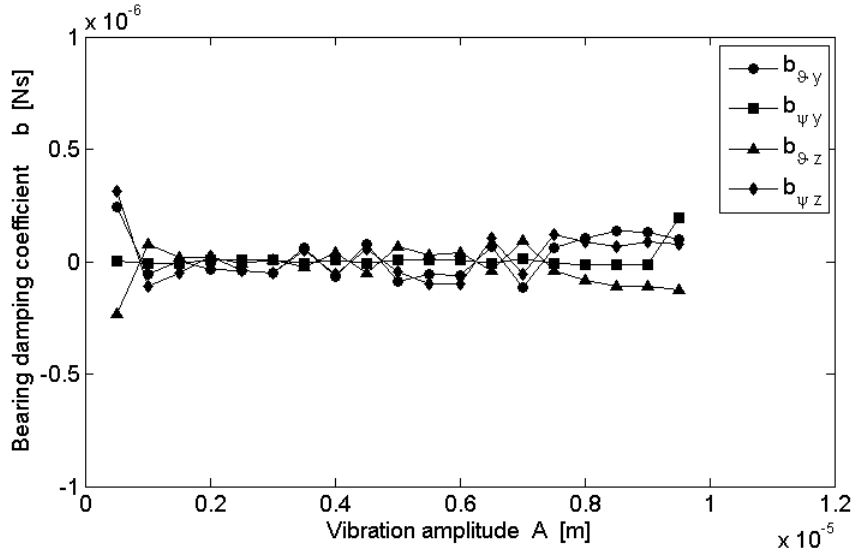

Figure 3.46: Cross-coupling damping coeff. v. vibration amplitude, bearing B, $p_s = 0.6\,\mathrm{MPa}$

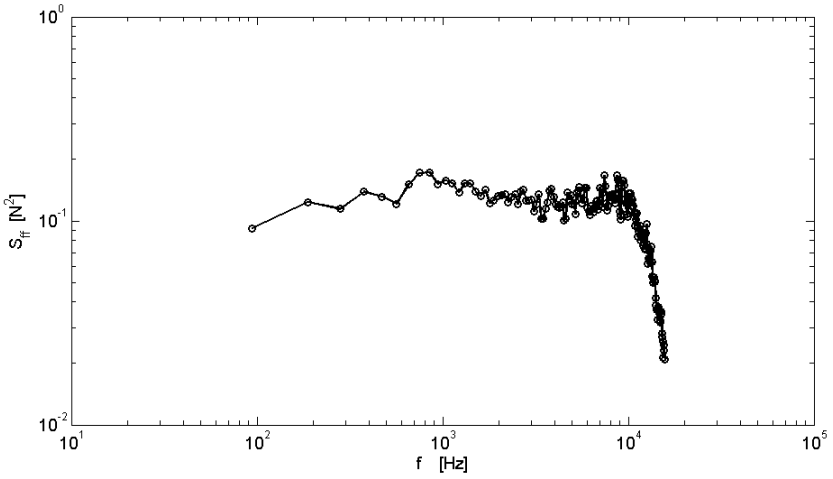

Figure 3.47: Spectrum density of signal used for excitation forces F_y, F_z

Another option of quantitative assessment of the validity of linear approximation of transient journal–bearing model is to calculate magnitude-square coherence of the force input and the displacement output of transient model. The magnitude-square coherence is calculated by means of spectral densities of signals as

$$\gamma_{ij}^2(\omega) = \frac{\left|\sum_{k=1}^{N} \mathrm{FFT}\left[w_H(t)\cdot f_j^{\{k\}}(t)\right]^* \cdot \mathrm{FFT}\left[w_H(t)\cdot g_i^{\{k\}}(t)\right]\right|^2}{\sum_{k=1}^{N}\left|\mathrm{FFT}\left[w_H(t)\cdot f_j^{\{k\}}(t)\right]\right|^2 \cdot \sum_{k=1}^{N}\left|\mathrm{FFT}\left[w_H(t)\cdot g_i^{\{k\}}(t)\right]\right|^2}, \tag{3.44}$$

where the numerator contains squared modulus of averaged cross-spectral density of output and input, whilst denominator contains averaged squared moduli of auto-spectral densities. Values of calculated coherences are depicted in the figures 3.50 and 3.51. On all of these graphs, local minima of coherence at around the peak amplitude occur. This is in correlation to discrepancies found in the comparisons of FRFs. Rapid decay at above 10^4 Hz of cross-coherences is caused by prevailing effect of numerical noise of integration methods, as the input signals had been limited by low pass filter at this frequency. At other regions, the values stay above 0.6; below the resonance and right above it closely approaching 1. For presented particular case of bearing systems, the calculated coherence functions show that linearized models reasonably approximate full transient nonlinear model, with some systematic errors at resonance due to nonlinearity of reaction forces in the displacement. Discrepancies at supersynchronous frequencies are not as significant, because frequency response functions rapidly tend to zero.

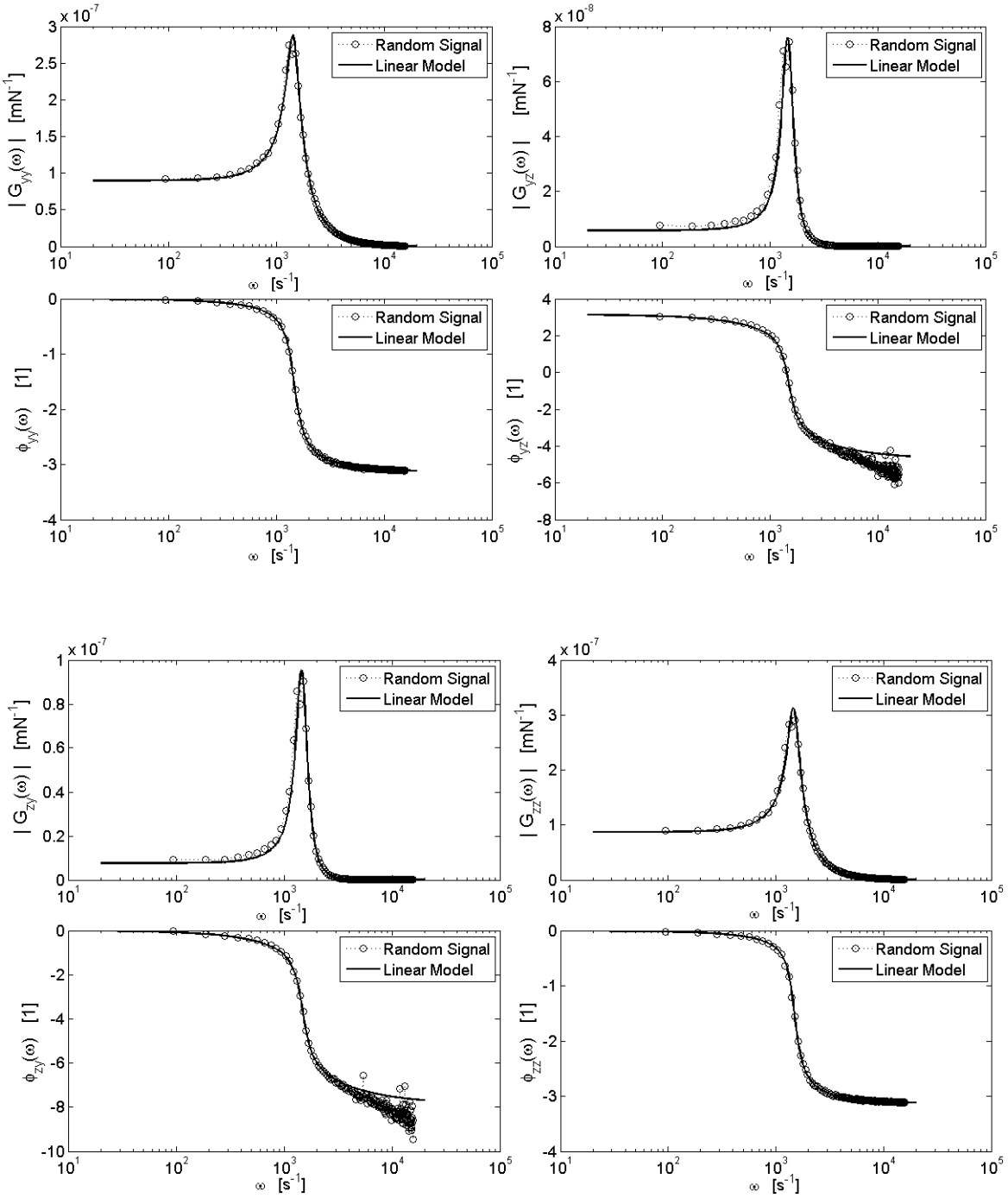

Figure 3.48: Transfer functions obtained using linear bearing coefficients and estimated from random signal excitation of transient bearing model, bearing A, $p_s = 0.6\,\mathrm{MPa}$

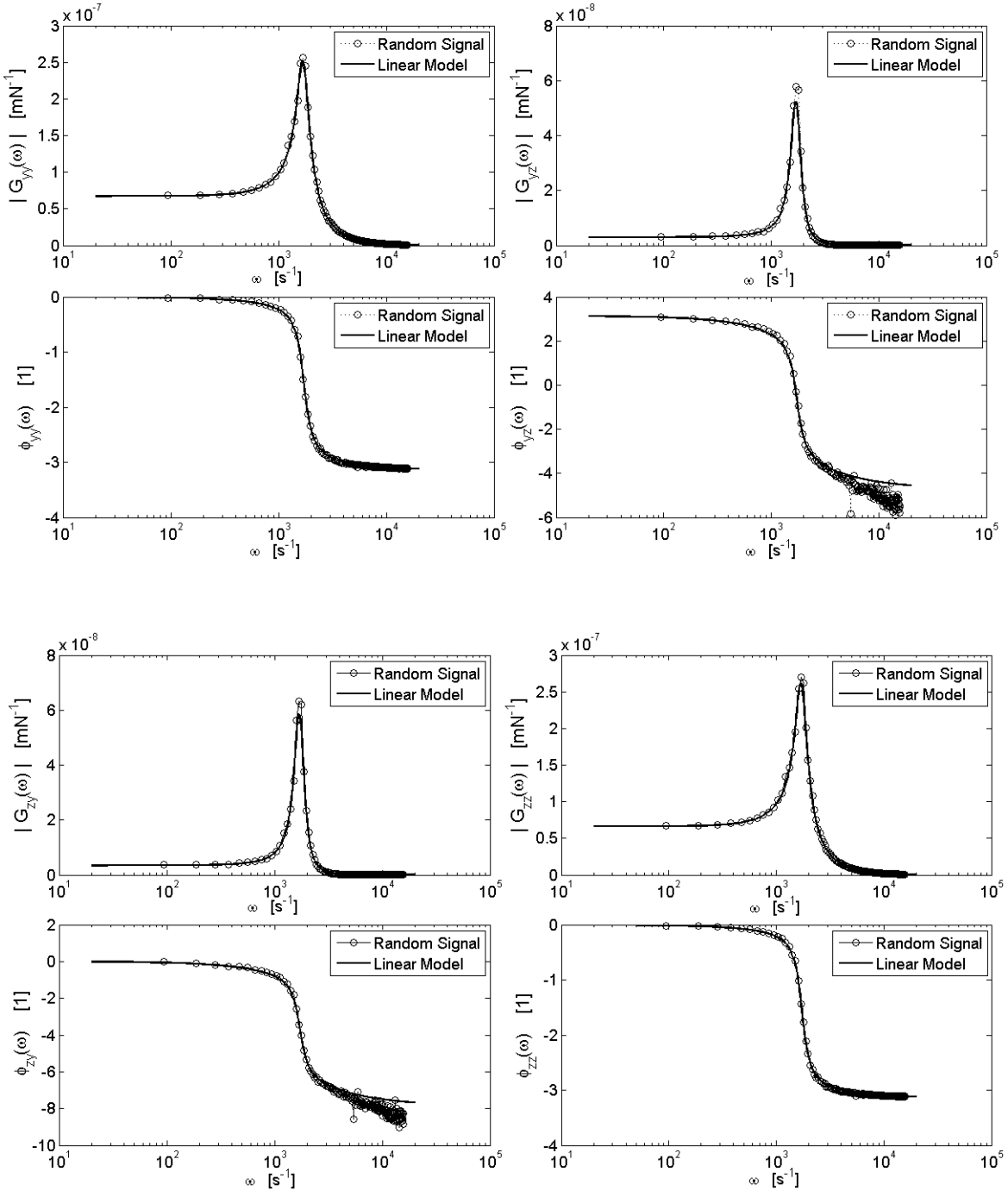

Figure 3.49: Transfer functions obtained using linear bearing coefficients and estimated from random signal excitation of transient bearing model, bearing B, $p_s = 0.6\,\mathrm{MPa}$

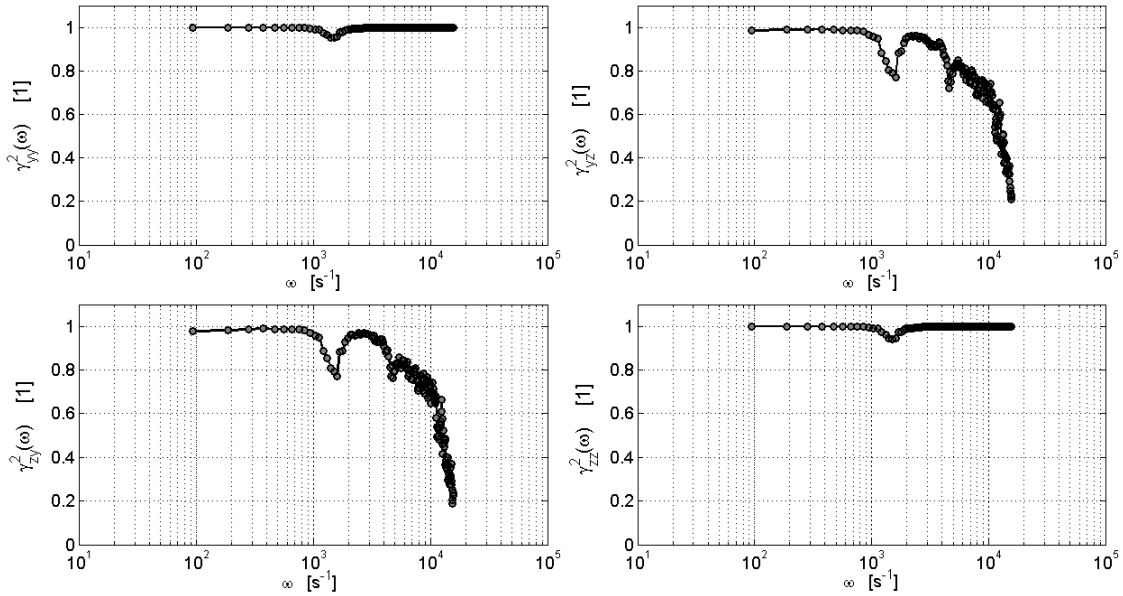

Figure 3.50: Magnitude-square coherence, bearing A, $p_s = 0.6\,\mathrm{MPa}$

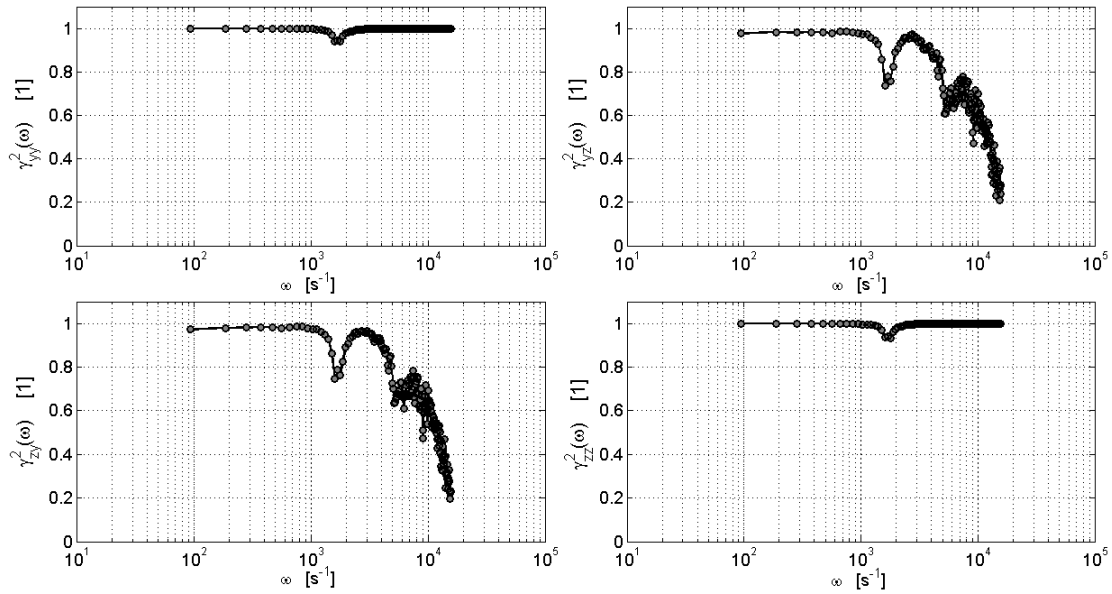

Figure 3.51: Magnitude-square coherence, bearing B, $p_s = 0.6\,\mathrm{MPa}$

Chapter 4

Thermal Analysis of Aerostatic Bearings

4.1 Chapter Outline

All models derived in the previous chapter expected the isothermal conditions of the air flow within the lubricant film. The rationale behind this assumption is discussed in the introduction chapter of this work. Summary of the recent research is provided in the section 1.3.4. the objective of this chapter is to document developed Thermo-Hydrodynamic Lubrication (THDL) model of aerostatic bearings, providing deeper insight into the thermal conditions of the bearings. The Reynolds equation of classical lubrication theory assumes isothermal processes of the lubricant film, thus a part of the THDL model is the generalized Reynolds equation that takes an uneven distribution of the temperature in all three spatial dimensions into account. Equation of conservation of energy is solved by finite element method in three dimensions in order to obtain the temperature distribution. The outcome of this analysis permits a quantitative assessment of validity of the previously accepted isothermal condition. On the top of this validity check, this model can be used for estimation of heat flow through the boundaries of the air film. Such data may be valuable in thespecific cases of design process, especially for machines operating with high temperature differences of its parts, e.g. turbines, machining spindles etc.

Complete Computational Fluid Dynamic (CFD) model of aerostatic bearings, solving directly the set of Navier-Stokes equations and mass and energy conservations is out of the scope of this work. Aerostatic bearings have the radial clearance typically thousand times smaller than the other two dimensions. The acceptable quality finite volume mesh would consists of enormous number of elements that would exceed available resources. The convergence of CFD analysis of such problem (compressible flow with strongly significant contribution of advective terms on an inconvenient mesh) has been also tested on simplified two-dimensional formulation without success. To this date, the author is not aware of any scientific paper delivering results of three-dimensional CFD solution of aerostatic bearings (including the heat conservation equation).

4.2 Thermo-Hydrodynamic Lubrication Model of Aerostatic Journal Bearings

4.2.1 Generalized Reynolds Equation

For obtaining the generalized Reynolds equation, let us consider the first five conditions from the page 10 satisfied. In addition to those conditions, let us assume that the temperature differences across film thickness are rather small, so the viscosity is little affected and it can be treated as nearly constant along radial coordinate (film thickness). This is strong assumption that restricts this model to small variations of temperature across the film thickness. It does not mean a limitation of viscosity variations in other two spatial directions nor its absolute value. The initial equations of mass and momentum conservation of thin fluid film are

$$\frac{\partial \rho}{\partial t} + \nabla \cdot (\rho \mathbf{v}) = 0, \quad \frac{\partial p}{\partial x_1} = \mu \frac{\partial^2 v_1}{\partial x_3^2}, \quad \frac{\partial p}{\partial x_2} = \mu \frac{\partial^2 v_2}{\partial x_3^2}. \tag{4.1}$$

The meaning of variables is as defined in the chapter 1. Substitution of boundary conditions for velocity components

$$\begin{aligned} v_1 = 0, \quad v_2 = 0 \quad at \quad x_3 = 0, \\ v_1 = R\omega, \quad v_2 = 0 \quad at \quad x_3 = h, \end{aligned} \tag{4.2}$$

into the momentum conservation equations renders the velocities v_1 a v_2

$$v_1 = \frac{1}{2\,\mu} \frac{\partial p}{\partial x_1} \left(x_3^2 - h x_3 \right) + R\omega \, \frac{x_3}{h}, \quad v_2 = \frac{1}{2\,\mu} \frac{\partial p}{\partial x_2} \left(x_3^2 - h x_3 \right). \tag{4.3}$$

Continuity equation 4.1 can now be integrated over film thickness

$$\int_0^h \frac{\partial \rho}{\partial t} \mathrm{d}x_3 + \int_0^h \frac{\partial (\rho\, v_1)}{\partial x_1} + \frac{\partial (\rho\, v_2)}{\partial x_2} + \frac{\partial (\rho\, v_3)}{\partial x_3} \mathrm{d}x_3 = 0. \tag{4.4}$$

Density of the air is replaced by the term

$$\rho = \frac{p}{rT} \tag{4.5}$$

coming from the state equation of ideal gas. Partial evaluation of the integrals in (4.4) leads to

$$\begin{aligned} &\frac{\partial}{\partial t} \left(p \int_0^h \frac{1}{T} \mathrm{d}x_3 \right) - \frac{p}{T} \frac{\partial h}{\partial t}\Big|_h + \frac{\partial}{\partial x_1} \left(p \int_0^h \frac{v_1}{T} \mathrm{d}x_3 \right) - \frac{p}{T} v_1 \frac{\partial h}{\partial x_1}\Big|_h \\ &+ \frac{\partial}{\partial x_2} \left(p \int_0^h \frac{v_2}{T} \mathrm{d}x_3 \right) - \frac{p}{T} v_2 \frac{\partial h}{\partial x_2}\Big|_h + p \left(\frac{v_3}{T}\Big|_h - \frac{v_3}{T}\Big|_0 \right) = 0. \end{aligned} \tag{4.6}$$

Boundary condition for the third component of velocity v_3

$$v_3\Big|_h = \frac{\partial h}{\partial t} + \frac{\partial h}{\partial x_1} R\omega \tag{4.7}$$

is added and further manipulation provides

$$\frac{\partial}{\partial t}\left(p\int_0^h \frac{1}{T}\mathrm{d}x_3\right) + \frac{\partial}{\partial x_1}\left(p\int_0^h \frac{v_1}{T}\mathrm{d}x_3\right) + \frac{\partial}{\partial x_2}\left(p\int_0^h \frac{v_2}{T}\mathrm{d}x_3\right) = p\left[\frac{v_3}{T}\right]_0. \tag{4.8}$$

In the case of isothermal situation, the integration after substitution for velocities would lead to classical Reynolds equation. For general temperature field, following auxiliary functions are introduced

$$Q_T = \int_0^h \frac{1}{T}\mathrm{d}x_3, \quad Q_{TC} = \int_0^h \frac{x_3}{T}\mathrm{d}x_3, \quad Q_{TP} = \int_0^h \frac{x_3^2}{T}\mathrm{d}x_3. \tag{4.9}$$

By means of these functions, the equation (4.8) is expressed as

$$\frac{\partial}{\partial t}\left(p\,Q_T\right) + \frac{1}{2}\frac{\partial}{\partial x_1}\left(\frac{p}{\mu}\frac{\partial p}{\partial x_1}\left(Q_{TP} - h\,Q_{TC}\right)\right) + R\omega\frac{\partial}{\partial x_1}\left(\frac{p}{h}Q_{TC}\right) + \frac{1}{2}\frac{\partial}{\partial x_2}\left(\frac{p}{\mu}\frac{\partial p}{\partial x_2}\left(Q_{TP} - h\,Q_{TC}\right)\right) = p\left[\frac{v_3}{T}\right]_0. \tag{4.10}$$

The auxiliary variables Q_T, Q_{TP}, Q_{TC} are functions of coordinates x_1, x_2 and time (owing to upper integrals' boundary h). Considering only static analysis, the film thickness function becomes time invariant and all the time derivatives can be left out. The generalized Reynolds equation can be put into steady state implicit form

$$\frac{1}{2}\frac{\partial}{\partial x_1}\left(A_Q\frac{\partial p}{\partial x_1}\right) + \frac{1}{2}\frac{\partial}{\partial x_2}\left(A_Q\frac{\partial p}{\partial x_2}\right) + R\omega\frac{\partial}{\partial x_1}\left(B_Q\,p\right) = p\left[\frac{v_3}{T}\right]_0, \tag{4.11}$$

where

$$A_Q = \frac{p}{\mu}\left(Q_{TP} - h\,Q_{TC}\right), \qquad B_Q = \frac{Q_{TC}}{h}. \tag{4.12}$$

The right-hand side of the equation (4.11) represents the air supplied through bearing orifices, symbolic form of this term stands for

$$p\left[\frac{v_3}{T}\right]_0 = \frac{\partial \dot{m}_i\, r}{\partial x_1\,\partial x_2}, \tag{4.13}$$

where $\dot{m}_i$ is mass flow rate through the orifice, the spatial differentials are understood as per section 3.3, page 69. The value of air mass flow is determined by equation of isentropic flow described in section 3.3.1 on page 71. Providing that the temperature field inside the air film is known, the auxiliary variables can be calculated and generalized Reynolds equation can be numerically solved.

4.2.2 Dimensionless Formulation of Generalized Reynolds Equation

Time dependent generalized Reynolds equation (4.10) can be put in the non-dimensional form

$$\frac{\partial}{\partial\tau}\left(P\,Q_T^*\right)+\frac{\partial}{\partial\xi}\left(\frac{P}{H}Q_{TC}^*\right)+\frac{3}{\Lambda}\frac{\partial}{\partial\xi}\left(\frac{P}{\mu^*}\frac{\partial P}{\partial\xi}\left(Q_{TP}^*-H\,Q_{TC}^*\right)\right)+ \frac{3}{\Lambda}\frac{\partial}{\partial\eta}\left(\frac{P}{\mu^*}\frac{\partial P}{\partial\eta}\left(Q_{TP}^*-H\,Q_{TC}^*\right)\right)=\frac{r\,T_r}{R^2\omega p_a c}\frac{\partial\dot{m}_i}{\partial\xi\,\partial\eta} \tag{4.14}$$

using dimensionless quantities defined as

$$P=\frac{p}{p_a},\quad H=\frac{h}{c},\quad Q_T^*=Q_T\frac{T_r}{c},\quad Q_{TC}^*=Q_{TC}\frac{T_r}{c^2},\quad Q_{TP}^*=Q_{TP}\frac{T_r}{c^3},$$
$$\mu^*=\frac{\mu}{\mu_r},\quad \xi=\frac{x_1}{R},\quad \eta=\frac{x_2}{R},\quad \zeta=\frac{x_3}{H\,c},\quad \tau=\omega\,t,\quad \Lambda=\frac{6R^2\omega\mu_r}{p_a\,c^2}. \tag{4.15}$$

The newly introduced variables T_r and μ_r are the reference temperature and the viscosity of the air, conveniently chosen according to bearing operation condition (ambient temperature and corresponding viscosity). From the equation (4.14), the pressure rate of change can be directly expressed as

$$\frac{\partial P}{\partial\tau}=\frac{1}{Q_T^*}\left(-P\frac{\partial Q_T^*}{\partial\tau}-\frac{\partial}{\partial\xi}\left(\frac{P}{H}Q_{TC}^*\right)-\frac{3}{\Lambda}\frac{\partial}{\partial\xi}\left(\frac{P}{\mu^*}\frac{\partial P}{\partial\xi}\left(Q_{TP}^*-H\,Q_{TC}^*\right)\right)- \frac{3}{\Lambda}\frac{\partial}{\partial\eta}\left(\frac{P}{\mu^*}\frac{\partial P}{\partial\eta}\left(Q_{TP}^*-H\,Q_{TC}^*\right)\right)+\frac{r\,T_r}{R^2\omega p_a c}\frac{\partial\dot{m}_i}{\partial\xi\,\partial\eta}\right). \tag{4.16}$$

4.2.3 FEM formulation of Steady State Generalized Reynolds Equation

Similarly to the section 3.3.2, the Galerkin method of creating weak formulation was used on this two-dimensional problem. In the physical coordinates the weak form of generalized Reynolds equation is

$$-\int_\Omega A_Q\left(\frac{\partial N_i}{\partial x_1}\frac{\partial N_j}{\partial x_1}+\frac{\partial N_i}{\partial x_2}\frac{\partial N_j}{\partial x_2}\right)p_j\mathrm{d}\Omega-2R\omega\int_\Omega B_Q\frac{\partial N_i}{\partial x_1}N_j p_j\mathrm{d}\Omega=2r\int_\Omega\frac{\partial\dot{m}_i}{\partial x_1\partial x_2}N_i\mathrm{d}\Omega. \tag{4.17}$$

Dirichlet boundary conditions for pressure are assumed at the bearing ends. The auxiliary variables A_Q and B_Q are approximated by their projection to the vector space with basis N_i of bi-linear quadrilateral finite elements.

$$A_Q\approx A_{Qi}\,N_i,\qquad B_Q\approx B_{Qi}\,N_i,\qquad i=1,2,3,4. \tag{4.18}$$

The coefficients of weak solution in the finite element basis are obtained by solving the equation

$$K_{ij}p_j=F_i. \tag{4.19}$$

Global matrix $\mathbf{K}$ and vector $\mathbf{F}$ are constructed from the elemental matrices as

$$K_{ij}^{e} = -\sum_{k=1}^{4} A_{Qk} \iint_{x_{1a}\,x_{2a}}^{x_{1b}\,x_{2b}} \left(\frac{\partial N_i}{\partial x_1}\frac{\partial N_j}{\partial x_1} + \frac{\partial N_i}{\partial x_2}\frac{\partial N_j}{\partial x_2} \right) N_k \,\mathrm{d}x_1\,\mathrm{d}x_2 - 2R\omega \sum_{k=1}^{4} B_{Qk} \iint_{x_{1a}\,x_{2a}}^{x_{1b}\,x_{2b}} \frac{\partial N_i}{\partial x_1} N_j N_k \,\mathrm{d}x_1\,\mathrm{d}x_2, \tag{4.20}$$

$$F_i^e = 2\frac{\dot{m}_i r}{A} \iint_{x_{1a}\,x_{2a}}^{x_{1b}\,x_{2b}} N_i \,\mathrm{d}x_1\,\mathrm{d}x_2. \tag{4.21}$$

The variable A is the area of finite elements containing air inlet. For those the $\dot{m}_i$ is nonzero. Closed algebraic forms of the above elemental matrix and vector were found for bi-linear quadrilateral element and they were used during numerical calculations. The global matrix $\mathbf{K}$ and vector $\mathbf{F}$ are both dependent on the actual pressure (and temperature) via variables A_Q and B_Q. Iterative Newton-Raphson method (section 3.3.3) is used to approach to the weak solution of generalized Reynolds equation. Between iterations of the method, temperature and temperature dependent variables A_Q and B_Q are updated. Recalculation of all $\mathbf{K}^e$ and $\mathbf{F}^e$ follows.

4.2.4 Conservation of Energy

The equations of conservation of energy (**??**) can be rewritten in the terms of temperature, considering the ideal gas, as

$$\rho c_p \left(\frac{\partial T}{\partial t} + \mathbf{v}\cdot\nabla T \right) = \frac{\partial p}{\partial t} + \mathbf{v}\cdot\nabla p + \nabla\cdot(k\nabla T) + \Phi. \tag{4.22}$$

Dissipative function (1.11) has been simplified to account for dominant shear rates due to small thickness in comparison with the other two spatial dimensions

$$\Phi = \mu \left(\left(\frac{\partial v_1}{\partial x_3} \right)^2 + \left(\frac{\partial v_2}{\partial x_3} \right)^2 \right). \tag{4.23}$$

4.2.5 Transformation of Coordinates

The equation (4.22) describes energy conservation in the air film. It is supposed to be solved in volume described by following set

$$\Omega = \{(x_1, x_2, x_3) \in R^3 :\ x_1 \in \langle 0, 2\pi R\rangle,\ x_2 \in \langle 0, L\rangle,\ x_3 \in \langle 0, h\,(x_1, x_2)\rangle\}. \tag{4.24}$$

The thickness h of the air film is a function of spatial coordinates and its value is very small compared to the other two spatial boundaries. Such volume is not easy to mesh. Even with a very fine mesh, the elements would be highly stretched. Author of this work decided to transform the equation of energy conservation using new coordinates. The benefit of the transformation is that the new volume, on which the solution is to be searched, will become a cuboid with comparable dimensions in all three directions. The drawback of this choice is that the solved equation will become significantly more complicated. The new curvilinear coordinates ξ, η and ζ are defined as follows

$$\xi = \frac{x_1}{R}, \qquad \eta = \frac{x_2}{R}, \qquad \zeta = \frac{x_3}{h\left(x_1, x_2\right)} = \frac{x_3}{cH(\xi, \eta)}. \tag{4.25}$$

This coordinate transformation leads to the new *cuboid* set Ω_n

$$\Omega_n = \{(\xi, \eta, \zeta) \in R^3 : \ \xi \in \langle 0, 2\pi \rangle, \, \eta \in \langle 0, L/R \rangle, \, \zeta \in \langle 0, 1 \rangle\} \tag{4.26}$$

in which the transformed energy equation will be solved.

Vector $\mathbf{x}$, expressed in the original Cartesian coordinates as

$$\mathbf{x} = x_i \mathbf{e}_i = (R\xi, R\eta, cH\zeta) \tag{4.27}$$

is represented in covariant basis of the curvilinear coordinates as

$$\mathbf{x} = \xi^i \mathbf{g}_i, \quad \mathbf{g}_j = \frac{\partial x_i}{\partial \xi^j} \mathbf{e}_i. \tag{4.28}$$

The covariant basis in this particular case consists of

$$\mathbf{g}_1 = R\,\mathbf{e}_1 + c\zeta \frac{\partial H}{\partial \xi} \mathbf{e}_3, \quad \mathbf{g}_2 = R\,\mathbf{e}_2 + c\zeta \frac{\partial H}{\partial \eta} \mathbf{e}_3, \quad \mathbf{g}_3 = cH\,\mathbf{e}_3. \tag{4.29}$$

The change of the basis can be represented by means of Jacobian matrix

$$[J_{ij}] = \frac{\partial x_i}{\partial \xi^j} = \begin{pmatrix} R & 0 & 0 \\ 0 & R & 0 \\ c\zeta \frac{\partial H}{\partial \xi} & c\zeta \frac{\partial H}{\partial \eta} & cH \end{pmatrix}, \tag{4.30}$$

which rows consist of coordinates of the covariant basis vectors. The backward transformation is done by inverse matrix

$$[J_{ij}]^{-1} = \begin{pmatrix} \frac{1}{R} & 0 & 0 \\ 0 & \frac{1}{R} & 0 \\ \frac{-\zeta}{RH} \frac{\partial H}{\partial \xi} & \frac{-\zeta}{RH} \frac{\partial H}{\partial \eta} & \frac{1}{cH} \end{pmatrix}, \tag{4.31}$$

that has the coordinates of contravariant basis put in the rows ($\mathbf{g}^i \mathbf{g}_j = \delta^i_j$).

The covariant and contravariant metric tensors are

$$[g_{ij}] = \mathbf{J}^{\mathrm{T}}\mathbf{J} = \begin{pmatrix} R^2 + c^2\zeta^2\left(\frac{\partial H}{\partial \xi}\right)^2 & c^2\zeta^2\frac{\partial H}{\partial \xi}\frac{\partial H}{\partial \eta} & c^2\zeta H\frac{\partial H}{\partial \xi} \\ c^2\zeta^2\frac{\partial H}{\partial \xi}\frac{\partial H}{\partial \eta} & R^2 + c^2\zeta^2\left(\frac{\partial H}{\partial \eta}\right)^2 & c^2\zeta H\frac{\partial H}{\partial \zeta} \\ c^2\zeta H\frac{\partial H}{\partial \xi} & c^2\zeta H\frac{\partial H}{\partial \zeta} & c^2H^2 \end{pmatrix}, \tag{4.32}$$

$$\left[g^{ij}\right] = \mathbf{J}^{-1}\mathbf{J}^{-\mathrm{T}} = \begin{pmatrix} \frac{1}{R^2} & 0 & \frac{-\zeta}{HR^2}\frac{\partial H}{\partial \xi} \\ 0 & \frac{1}{R^2} & \frac{-\zeta}{HR^2}\frac{\partial H}{\partial \eta} \\ \frac{-\zeta}{HR^2}\frac{\partial H}{\partial \xi} & \frac{-\zeta}{HR^2}\frac{\partial H}{\partial \eta} & \frac{1}{c^2H^2} + \frac{\zeta^2}{R^2H^2}\left(\left(\frac{\partial H}{\partial \xi}\right)^2 + \left(\frac{\partial H}{\partial \eta}\right)^2\right) \end{pmatrix}. \tag{4.33}$$

Gradient of a scalar field can be now calculated as

$$\nabla f = \frac{\partial f}{\partial \xi^i}\mathbf{g}^i = g^{ki}\frac{\partial f}{\partial \xi^k}\mathbf{g}_i, \tag{4.34}$$

Laplacian of a scalar field as

$$\Delta f = \frac{1}{\sqrt{g}}\frac{\partial}{\partial \xi^i}\left(g^{ki}\frac{\partial f}{\partial \xi^k}\sqrt{g}\right), \tag{4.35}$$

where

$$\sqrt{g} = \sqrt{\det\left([g_{ij}]\right)}. \tag{4.36}$$

Specially, the thermal gradient coordinates are

$$[\nabla T] = \mathbf{J}^{-\mathrm{T}}\left[\frac{\partial T}{\partial \xi^i}\right] = \begin{pmatrix} \frac{1}{R}\frac{\partial T}{\partial \xi} - \frac{\zeta}{RH}\frac{\partial H}{\partial \xi}\frac{\partial T}{\partial \zeta} \\ \frac{1}{R}\frac{\partial T}{\partial \eta} - \frac{\zeta}{RH}\frac{\partial H}{\partial \eta}\frac{\partial T}{\partial \zeta} \\ \frac{1}{Hc}\frac{\partial T}{\partial \zeta} \end{pmatrix}, \tag{4.37}$$

and the Laplacian of temperature is

$$\begin{aligned} \Delta T = {} & \frac{1}{R^2}\frac{\partial^2 T}{\partial \xi^2} + \frac{1}{R^2}\frac{\partial^2 T}{\partial \eta^2} + \frac{1}{H^2c^2}\frac{\partial^2 T}{\partial \zeta^2} + \\ & \frac{1}{R^2H^2}\left(\left(\frac{\partial H}{\partial \xi}\right)^2 + \left(\frac{\partial H}{\partial \eta}\right)^2\right)\zeta^2\frac{\partial^2 T}{\partial \zeta^2} - \frac{2}{R^2H}\frac{\partial H}{\partial \xi}\zeta\frac{\partial^2 T}{\partial \xi \partial \zeta} - \frac{2}{R^2H}\frac{\partial H}{\partial \eta}\zeta\frac{\partial^2 T}{\partial \eta \partial \zeta} - \\ & \left(\frac{1}{R^2H}\frac{\partial^2 H}{\partial \xi^2} + \frac{1}{R^2H}\frac{\partial^2 H}{\partial \eta^2} - \frac{2}{R^2H^2}\left(\frac{\partial H}{\partial \xi}\right)^2 - \frac{2}{R^2H^2}\left(\frac{\partial H}{\partial \eta}\right)^2\right)\zeta\frac{\partial T}{\partial \zeta}. \end{aligned} \tag{4.38}$$

Other quantities used in the equation (4.22) are already known expressed in the Cartesian coordinate system $\{\mathbf{e}_i\}$ from the results of generalized Reynolds equation or as material properties.

The energy conservation equation now becomes (considering constant thermal conductivity k)

$$\rho c_p \left(\frac{\partial T}{\partial t} + v_1 \left(\frac{1}{R}\frac{\partial T}{\partial \xi} - \frac{\zeta}{RH}\frac{\partial H}{\partial \xi}\frac{\partial T}{\partial \zeta} \right) + v_2 \left(\frac{1}{R}\frac{\partial T}{\partial \eta} - \frac{\zeta}{RH}\frac{\partial H}{\partial \eta}\frac{\partial T}{\partial \zeta} \right) + v_3 \left(\frac{1}{Hc}\frac{\partial T}{\partial \zeta} \right) \right) =$$
$$\frac{\partial p}{\partial t} + v_1 \left(\frac{1}{R}\frac{\partial p}{\partial \xi} \right) + v_2 \left(\frac{1}{R}\frac{\partial p}{\partial \eta} \right) + k \left(\frac{1}{R^2}\frac{\partial^2 T}{\partial \xi^2} + \frac{1}{R^2}\frac{\partial^2 T}{\partial \eta^2} + \frac{1}{H^2 c^2}\frac{\partial^2 T}{\partial \zeta^2} + \right.$$
$$\frac{1}{R^2 H^2} \left(\left(\frac{\partial H}{\partial \xi} \right)^2 + \left(\frac{\partial H}{\partial \eta} \right)^2 \right) \zeta^2 \frac{\partial^2 T}{\partial \zeta^2} - \frac{2}{R^2 H}\frac{\partial H}{\partial \xi}\zeta\frac{\partial^2 T}{\partial \xi \partial \zeta} - \frac{2}{R^2 H}\frac{\partial H}{\partial \eta}\zeta\frac{\partial^2 T}{\partial \eta \partial \zeta} -$$
$$\left(\frac{1}{R^2 H}\frac{\partial^2 H}{\partial \xi^2} + \frac{1}{R^2 H}\frac{\partial^2 H}{\partial \eta^2} - \frac{2}{R^2 H^2}\left(\frac{\partial H}{\partial \xi} \right)^2 - \frac{2}{R^2 H^2}\left(\frac{\partial H}{\partial \eta} \right)^2 \right) \zeta \frac{\partial T}{\partial \zeta} \Bigg) +$$
$$\mu \left(\left(\frac{\partial v_1}{\partial x_3} \right)^2 + \left(\frac{\partial v_2}{\partial x_3} \right)^2 \right). \tag{4.39}$$

The above time dependent equation (in partial dimensionless form) has been solved by finite difference method together with the generalized Reynolds equation (4.16). The finite difference scheme was complicated, and problems with oscillations of approximate solution often occurred, when approaching steady state solution.

4.2.6 FEM formulation of Steady State Equation of Energy Conservation

Steady state form of equation (4.22),

$$\nabla \cdot (k \nabla T) - \rho c_p \left(\mathbf{v} \cdot \nabla T \right) = -\mathbf{v} \cdot \nabla p - \Phi, \tag{4.40}$$

is discretized by means of Galerkin method as

$$\int_\Omega k N_i \left(\frac{\partial^2 T}{\partial x_1^2} + \frac{\partial^2 T}{\partial x_2^2} + \frac{\partial^2 T}{\partial x_3^2} \right) \mathrm{d}\Omega - \int_\Omega \rho c_p N_i \left(v_1 \frac{\partial T}{\partial x_1} + v_2 \frac{\partial T}{\partial x_2} + v_3 \frac{\partial T}{\partial x_3} \right) \mathrm{d}\Omega =$$
$$- \int_\Omega N_i \left(v_1 \frac{\partial p}{\partial x_1} + v_2 \frac{\partial p}{\partial x_2} \right) \mathrm{d}\Omega - \int_\Omega \mu N_i \left(\left(\frac{\partial v_1}{\partial x_3} \right)^2 + \left(\frac{\partial v_2}{\partial x_3} \right)^2 \right) \mathrm{d}\Omega. \tag{4.41}$$

Applying Green's first identity leads to

$$\int_\Omega k \left(\frac{\partial N_i}{\partial x_1}\frac{\partial N_j}{\partial x_1} + \frac{\partial N_i}{\partial x_2}\frac{\partial N_j}{\partial x_2} + \frac{\partial N_i}{\partial x_3}\frac{\partial N_j}{\partial x_3} \right) T_j \, \mathrm{d}\Omega - \int_{\partial\Omega} k N_i \left(\nabla N_j \right) \cdot \mathbf{n} \, T_j \, \mathrm{d}S +$$
$$\int_\Omega \rho c_p N_i \left(v_1 \frac{\partial N_j}{\partial x_1} + v_2 \frac{\partial N_j}{\partial x_2} + v_3 \frac{\partial N_j}{\partial x_3} \right) T_j \, \mathrm{d}\Omega = \int_\Omega N_i \left(v_1 \frac{\partial p}{\partial x_1} + v_2 \frac{\partial p}{\partial x_2} \right) \mathrm{d}\Omega +$$
$$\int_\Omega \mu N_i \left(\left(\frac{\partial v_1}{\partial x_3} \right)^2 + \left(\frac{\partial v_2}{\partial x_3} \right)^2 \right) \mathrm{d}\Omega. \tag{4.42}$$

The original volume Ω is mapped onto volume Ω_n (4.26) by presented change of coordinates. The Jacobian of the transformation is

$$\det(J) = R^2 H c, \tag{4.43}$$

so that the volume integrals from (4.42) containing temperature, expressed in the new curvilinear coordinates and using the formula (4.34) for scalar gradients are as follows.

Conductive part:

$$\int_\Omega k\left(\frac{\partial N_i}{\partial x_1}\frac{\partial N_j}{\partial x_1}+\frac{\partial N_i}{\partial x_2}\frac{\partial N_j}{\partial x_2}+\frac{\partial N_i}{\partial x_3}\frac{\partial N_j}{\partial x_3}\right)T_j\,\mathrm{d}\Omega = c\int_{\Omega_n} kH\left(\frac{\partial N_i}{\partial \xi}\frac{\partial N_j}{\partial \xi}+\frac{\partial N_i}{\partial \eta}\frac{\partial N_j}{\partial \eta}\right)+ \frac{k\zeta^2}{H}\frac{\partial N_i}{\partial \zeta}\frac{\partial N_j}{\partial \zeta}\left(\left(\frac{\partial H}{\partial \xi}\right)^2+\left(\frac{\partial H}{\partial \eta}\right)^2+\left(\frac{R}{c\zeta}\right)^2\right)-k\zeta\left(\frac{\partial H}{\partial \xi}\left(\frac{\partial N_i}{\partial \xi}\frac{\partial N_j}{\partial \zeta}+\frac{\partial N_j}{\partial \xi}\frac{\partial N_i}{\partial \zeta}\right)+ \frac{\partial H}{\partial \eta}\left(\frac{\partial N_i}{\partial \eta}\frac{\partial N_j}{\partial \zeta}+\frac{\partial N_j}{\partial \eta}\frac{\partial N_i}{\partial \zeta}\right)\right)\mathrm{d}\Omega_n\,T_j. \tag{4.44}$$

Convective part:

$$\int_\Omega \rho c_p N_i\left(v_1\frac{\partial N_j}{\partial x_1}+v_2\frac{\partial N_j}{\partial x_2}+v_3\frac{\partial N_j}{\partial x_3}\right)T_j\,\mathrm{d}\Omega = \tag{4.45}$$
$$Rc\int_{\Omega_n}\rho c_p N_i\left(H\left(v_1\frac{\partial N_j}{\partial \xi}+v_2\frac{\partial N_j}{\partial \eta}+\frac{v_3 R}{Hc}\frac{\partial N_j}{\partial \zeta}\right)-\zeta\frac{\partial N_j}{\partial \zeta}\left(\frac{\partial H}{\partial \xi}+\frac{\partial H}{\partial \eta}\right)\right)\mathrm{d}\Omega_n\,T_j.$$

the integrals on the right hand side of equation (4.42) are trivial, because velocity, pressure and their gradients are known functions (in the weak sense; obtained from generalized Reynolds equation). Using finite element technique, the surface integral in (4.42) will become important only at boundaries of region Ω, where other than Dirichlet boundary condition is applied.

The region Ω_n is meshed by 8-node trilinear brick elements, all oriented with faces parallel to planes defined by $\xi = 0$, $\eta = 0$, $\zeta = 0$. Boundary of a single finite element encloses a region $\Omega_n^e = \{(\xi,\eta,\zeta) \in R^3 :\ \xi \in \langle \xi_a, \xi_b\rangle,\ \eta \in \langle \eta_a, \eta_b\rangle,\ \zeta \in \langle \zeta_a, \zeta_b\rangle\}$. The basis functions of such element are

$$N_1 = \frac{-\eta\,\xi\,\zeta+\zeta_b\eta\,\xi+\xi_b\eta\,\zeta+\eta_b\xi\,\zeta-\zeta_b\xi_b\eta-\zeta_b\eta_b\xi-\eta_b\xi_b\zeta+\zeta_b\eta_b\xi_b}{(\xi_b-\xi_a)(\eta_b-\eta_a)(\zeta_b-\zeta_a)}$$

$$N_2 = \frac{\eta\,\xi\,\zeta-\zeta_b\eta\,\xi-\xi_b\eta\,\zeta-\eta_a\xi\,\zeta+\zeta_b\xi_b\eta+\eta_a\zeta_b\xi+\xi_b\eta_a\zeta-\eta_a\xi_b\zeta_b}{(\xi_b-\xi_a)(\eta_b-\eta_a)(\zeta_b-\zeta_a)}$$

$$N_3 = \frac{\eta\,\xi\,\zeta-\zeta_a\eta\,\xi-\xi_b\eta\,\zeta-\eta_b\xi\,\zeta+\xi_b\zeta_a\eta+\zeta_a\eta_b\xi+\eta_b\xi_b\zeta-\eta_b\xi_b\zeta_a}{(\xi_b-\xi_a)(\eta_b-\eta_a)(\zeta_b-\zeta_a)}$$

$$N_4 = \frac{-\eta\,\xi\,\zeta+\zeta_a\eta\,\xi+\xi_b\eta\,\zeta+\eta_a\xi\,\zeta-\zeta_a\xi_b\eta-\zeta_a\eta_a\xi-\eta_a\xi_b\zeta+\zeta_a\eta_a\xi_b}{(\xi_b-\xi_a)(\eta_b-\eta_a)(\zeta_b-\zeta_a)}$$

$$N_5 = \frac{\eta\,\xi\,\zeta-\zeta_b\eta\,\xi-\xi_a\eta\,\zeta-\eta_b\xi\,\zeta+\xi_a\zeta_b\eta+\zeta_b\eta_b\xi+\xi_a\eta_b\zeta-\eta_b\xi_a\zeta_b}{(\xi_b-\xi_a)(\eta_b-\eta_a)(\zeta_b-\zeta_a)}$$

$$N_6 = \frac{-\eta\,\xi\,\zeta + \zeta_b\eta\,\xi + \xi_a\eta\,\zeta + \eta_a\xi\,\zeta - \xi_a\zeta_b\eta - \eta_a\zeta_b\xi - \xi_a\eta_a\zeta + \eta_a\xi_a\zeta_b}{(\xi_b - \xi_a)\,(\eta_b - \eta_a)\,(\zeta_b - \zeta_a)}$$

$$N_7 = \frac{-\eta\,\xi\,\zeta + \zeta_a\eta\,\xi + \xi_a\eta\,\zeta + \eta_b\xi\,\zeta - \xi_a\zeta_a\eta - \zeta_a\eta_b\xi - \xi_a\eta_b\zeta + \eta_b\xi_a\zeta_a}{(\xi_b - \xi_a)\,(\eta_b - \eta_a)\,(\zeta_b - \zeta_a)}$$

$$N_8 = \frac{\eta\,\xi\,\zeta - \zeta_a\eta\,\xi - \xi_a\eta\,\zeta - \eta_a\xi\,\zeta + \xi_a\zeta_a\eta + \zeta_a\eta_a\xi + \xi_a\eta_a\zeta - \eta_a\xi_a\zeta_a}{(\xi_b - \xi_a)\,(\eta_b - \eta_a)\,(\zeta_b - \zeta_a)}$$

The weak solution for temperature is searched as the solution of set of linear equations $K_{ij}T_j = F_i$. The element stiffness matrix $\mathbf{K}^e$ is given by

$$K^e_{ij} = \mathbf{I}_\mathrm{d} + \mathbf{I}_\mathrm{v} + \mathbf{I}_\mathrm{S}, \tag{4.46}$$

$$\begin{aligned}\mathbf{I}_\mathrm{d} = kc\sum_{l=1}^{8}\Bigg(&H_l\iiint_{\xi_a\,\eta_a\,\zeta_a}^{\xi_b\,\eta_b\,\zeta_b} N_l\left(\frac{\partial N_i}{\partial\xi}\frac{\partial N_j}{\partial\xi} + \frac{\partial N_i}{\partial\eta}\frac{\partial N_j}{\partial\eta}\right)\mathrm{d}\zeta\,\mathrm{d}\eta\,\mathrm{d}\xi + \\ &\frac{R^2}{c^2}Q^a_l\iiint_{\xi_a\,\eta_a\,\zeta_a}^{\xi_b\,\eta_b\,\zeta_b} N_l\frac{\partial N_i}{\partial\zeta}\frac{\partial N_j}{\partial\zeta}\,\mathrm{d}\zeta\,\mathrm{d}\eta\,\mathrm{d}\xi + Q^b_l\iiint_{\xi_a\,\eta_a\,\zeta_a}^{\xi_b\,\eta_b\,\zeta_b}\zeta^2 N_l\frac{\partial N_i}{\partial\zeta}\frac{\partial N_j}{\partial\zeta}\,\mathrm{d}\zeta\,\mathrm{d}\eta\,\mathrm{d}\xi - \\ &Q^c_l\iiint_{\xi_a\,\eta_a\,\zeta_a}^{\xi_b\,\eta_b\,\zeta_b}\zeta N_l\left(\frac{\partial N_i}{\partial\xi}\frac{\partial N_j}{\partial\zeta} + \frac{\partial N_i}{\partial\zeta}\frac{\partial N_j}{\partial\xi}\right)\mathrm{d}\zeta\,\mathrm{d}\eta\,\mathrm{d}\xi - \\ &Q^d_l\iiint_{\xi_a\,\eta_a\,\zeta_a}^{\xi_b\,\eta_b\,\zeta_b}\zeta N_l\left(\frac{\partial N_i}{\partial\eta}\frac{\partial N_j}{\partial\zeta} + \frac{\partial N_i}{\partial\zeta}\frac{\partial N_j}{\partial\eta}\right)\mathrm{d}\zeta\,\mathrm{d}\eta\,\mathrm{d}\xi\Bigg),\end{aligned} \tag{4.47}$$

$$\begin{aligned}\mathbf{I}_\mathrm{v} = Rc\rho c_p\sum_{l=1}^{8}\Bigg(&Q^e_l\iiint_{\xi_a\,\eta_a\,\zeta_a}^{\xi_b\,\eta_b\,\zeta_b} N_l N_i\frac{\partial N_j}{\partial\xi}\,\mathrm{d}\zeta\,\mathrm{d}\eta\,\mathrm{d}\xi + Q^f_l\iiint_{\xi_a\,\eta_a\,\zeta_a}^{\xi_b\,\eta_b\,\zeta_b} N_l N_i\frac{\partial N_j}{\partial\eta}\,\mathrm{d}\zeta\,\mathrm{d}\eta\,\mathrm{d}\xi + \\ &\frac{R}{c}Q^g_l\iiint_{\xi_a\,\eta_a\,\zeta_a}^{\xi_b\,\eta_b\,\zeta_b} N_l N_i\frac{\partial N_j}{\partial\zeta}\,\mathrm{d}\zeta\,\mathrm{d}\eta\,\mathrm{d}\xi - Q^h_l\iiint_{\xi_a\,\eta_a\,\zeta_a}^{\xi_b\,\eta_b\,\zeta_b}\zeta N_l N_i\frac{\partial N_j}{\partial\zeta}\,\mathrm{d}\zeta\,\mathrm{d}\eta\,\mathrm{d}\xi\Bigg),\end{aligned} \tag{4.48}$$

where

$$\begin{aligned}&Q_a = \frac{1}{H}, \qquad Q^b = \frac{1}{H}\left(\left(\frac{\partial H}{\partial\xi}\right)^2 + \left(\frac{\partial H}{\partial\eta}\right)^2\right), \qquad Q^c = \frac{\partial H}{\partial\xi}, \qquad Q^d = \frac{\partial H}{\partial\eta}, \\ &Q^e = Hv_1, \qquad Q^f = Hv_2, \qquad Q^g = v_3, \qquad Q^h = \frac{\partial H}{\partial\xi} + \frac{\partial H}{\partial\eta},\end{aligned} \tag{4.49}$$

are auxiliary functions used during matrix assembly. All integrals in (4.47) and (4.48) are calculated just once. Update during iterative numerical solution is done only by these coeffi-

cients and quick rebuilding of the elements' matrices. Matrix $\mathbf{I}_\mathrm{S}$ is the surface integral from (4.42), and it has effect only for the boundary elements at the end of bearing, where the air escapes to the atmosphere. Depending on which end of the bearing the element is positioned, the surface integral can be expressed as either one of the following

$$\mathbf{I}_\mathrm{S} = ck \sum_{l=1}^{8} \left(H_l \int_{\xi_a}^{\xi_b} \int_{\zeta_a}^{\zeta_b} N_l N_i \frac{\partial N_j}{\partial \eta} \,\mathrm{d}\zeta \,\mathrm{d}\xi - Q_l^d \int_{\xi_a}^{\xi_b} \int_{\zeta_a}^{\zeta_b} \zeta N_l N_i \frac{\partial N_j}{\partial \zeta} \,\mathrm{d}\zeta \,\mathrm{d}\xi \right) \Bigg|_{\eta=\eta_a},$$
$$\mathbf{I}_\mathrm{S} = -ck \sum_{l=1}^{8} \left(H_l \int_{\xi_a}^{\xi_b} \int_{\zeta_a}^{\zeta_b} N_l N_i \frac{\partial N_j}{\partial \eta} \,\mathrm{d}\zeta \,\mathrm{d}\xi - Q_l^d \int_{\xi_a}^{\xi_b} \int_{\zeta_a}^{\zeta_b} \zeta N_l N_i \frac{\partial N_j}{\partial \zeta} \,\mathrm{d}\zeta \,\mathrm{d}\xi \right) \Bigg|_{\eta=\eta_b}. \tag{4.50}$$

The right-hand side of (4.42) is straightforwardly integrable per finite elements, giving the forcing vectors $\mathbf{F}_i^e$. It should be mentioned that thermal conductivity k, viscosity μ, isobaric heat capacity c_p and density ρ are all treated constant over single element to simplify the process. The mesh is supposed to be fine enough to make this assumption not causing an excessive error. The pressure and the velocity are also known only in the weak sense.

4.2.7 Numerical Process of THDL Analysis

High altitude view of the process of THDL analysis is depicted in the figure 4.1. It consists of two main blocks, the generalized Reynolds equation FEM solver (section 4.2.3) and the thermal analysis FEM solver (section 4.2.6) in a closed loop. Between those two solvers, the updates of the air properties and the other shared quantities take place. The entire analysis runs iteratively, until the results seem reached converged values according to selected criteria (maximum norm of difference of two consecutive temperature vectors $\mathbf{T}_j$). Rest of the process belongs to the necessary pre and post processors. Pre-processor consists of meshers producing quadrilateral mesh for generalized Reynolds equation solver and brick mesh for the thermal analysis. The algorithms of the meshers are trivial, as both meshed regions are rectangle or cuboid. All the elements are of uniform size.

Described numerical process exhibits fast convergence of the results for analysis of bearing with Dirichlet boundary conditions applied on the journal and bushing cylindrical surfaces. With this scenario, seven iterations within the loop of generalized Reynolds and thermal analysis is sufficient number to obtain stabilized results for given number of finite elements, as can be seen in the figure 4.2.

The generalized Reynolds equation solver uses Newton-Raphson method, so does the solver developed for the isothermal bearing analysis. Thermal analysis is developed in the way, that a system of linear equations is solved every iteration loop. Iterative solver is used for solving this set, because direct sparse solver based on LU decomposition of system matrix $\mathbf{K}$ turned out to be excessively memory consuming, owing to the fact that even though system matrix $\mathbf{K}$ is sparse, its LU factorisation may produce (and it does in this particu-

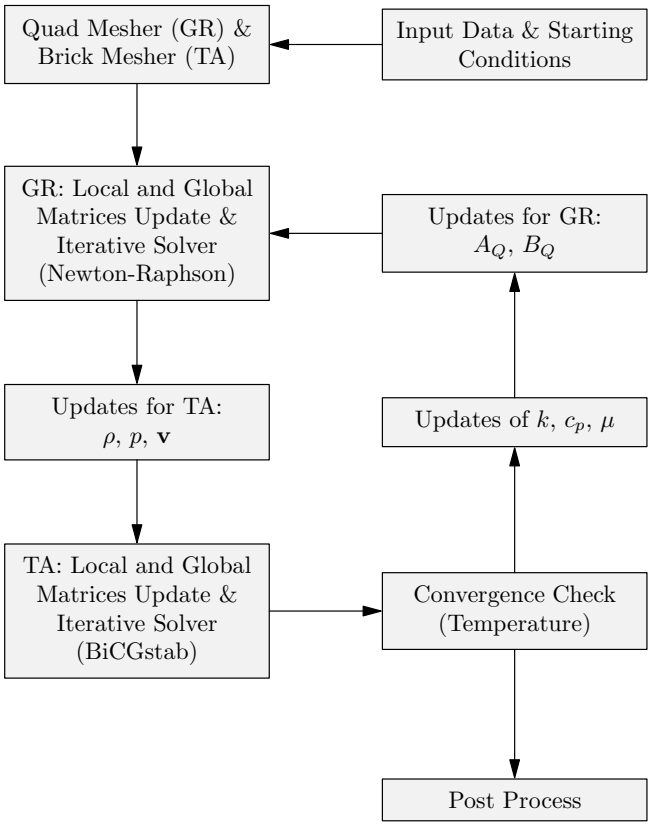

Figure 4.1: THDL analysis process chart. GR: Generalized Reynolds FEM solver, TA: Thermal analysis FEM solver

lar case) significantly denser matrices **L**, **U**. Biconjugate gradients stabilized method with preconditioning is used to solve the system instead. For preconditioning, the incomplete LU factorisation is used. Drop tolerance of this factorisation was set to 10^{-4}. This value was found experimentally in order to preserve fast convergence of biconjugate gradients method, while avoiding overflow of available physical memory. The biconjugate gradients method then converged mostly within a few iterations with relative error of order 10^{-16}.

4.3 Test Case of THDL Analysis

Bearing with eight inherently compensated orifices of diameter $d_o = 0.2\,\mathrm{mm}$, positioned in the middle of bearing length, with other dimensions $R = 15\,\mathrm{mm}$, $L = 30\,\mathrm{mm}$, $c = 20\,\mu\mathrm{m}$ was analysed to test the THDL analysis process in the terms of convergence of the results with respect to number of finite elements used. Dirichlet boundary conditions ($T = 300\,\mathrm{K}$) applied on cylindrical surfaces of the bearing bushing and journal were applied.

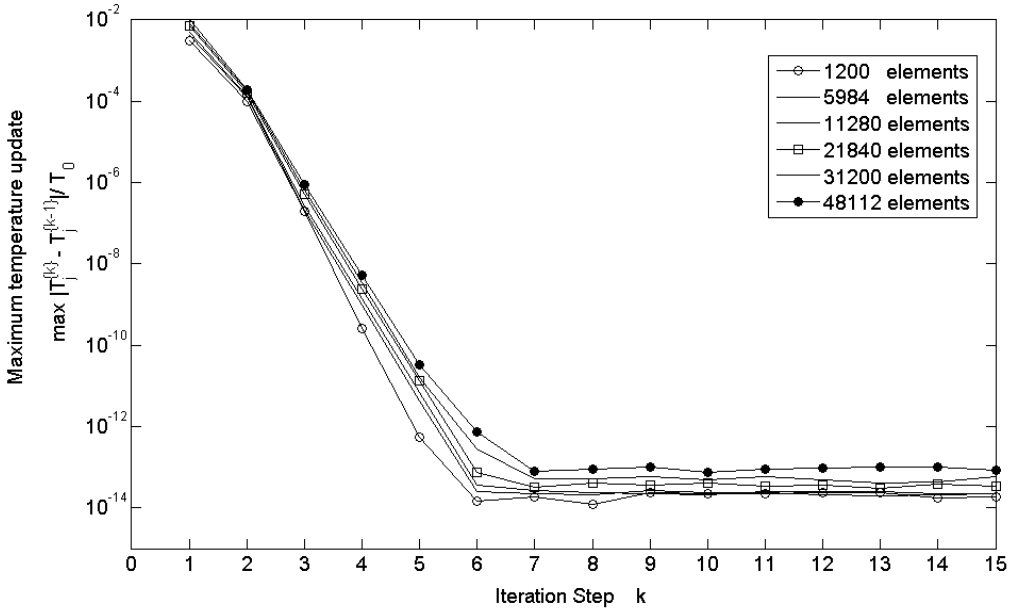

Figure 4.2: Convergence of iterative process of steady state THDL solver

4.3.1 Convergence Criteria

Firstly, minimum, maximum and average temperature of the air within the bearing was calculated for increasing number of elements. The results are plotted in the graph 4.3 for stationary and relatively fast running journal. The average temperature is virtually independent on the number of finite elements, whereas the minimum and maximum temperature show tendency to slowly diverge within the examined range of number of finite elements. This finding has the origin in the fact that both extremes of temperature appear in small regions near the air inlet orifices, where the highest pressure gradients occur. With respect to the size of elements, even for the highest number used, each air inlet acts as a singularity, which is averaged over single element surface. Presented model is not capable of providing detailed solution of temperature within the areas of air inlet orifices. To obtain accurate temperature peaks in those small areas close to air inlet orifices, a different kind of model, solving both the flow and heat transfer related problems on significantly refined mesh would have been necessary. However the maximum and minimum temperatures do not converge with more precise representation of the pressure and the temperature, the affected regions are getting smaller. Isolated force acting at a single node of structural FEM model might be good analogy to this situation.

More important than local extremes of the temperature is the overall energy balance of the system. During deriving this model, there were number of simplifications taken into process. Following criteria of convergence is provided.

Energy balance of the bearing control volume can be written in terms of stagnation enthalpy change between inlet and outlet of the control volume. For steady state situation,

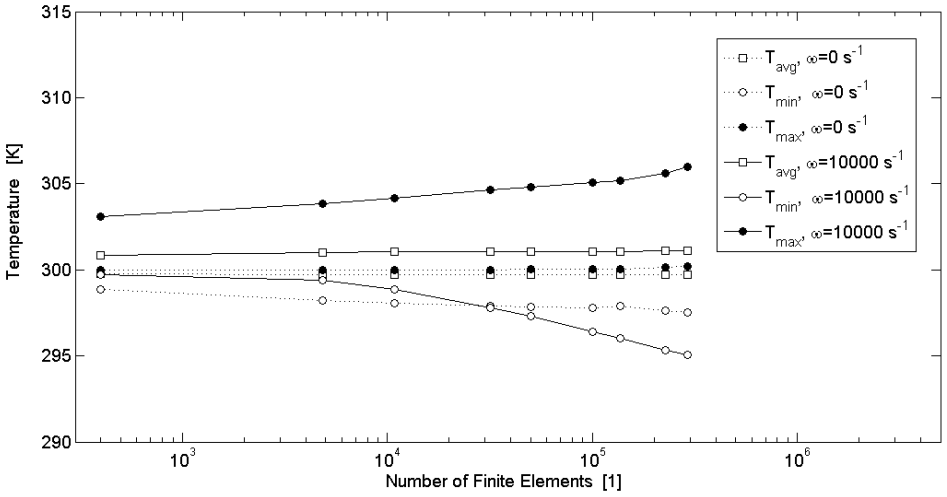

Figure 4.3: Convergence of temperature

the difference in the stagnation enthalpy is covered by shaft work and heat brought to the system, according to the next equation

$$\dot{m}\left(i_{ST}^{\{out\}} - i_{ST}^{\{in\}}\right) = \dot{Q} + \dot{W}_{sh}. \tag{4.51}$$

The heat flow $\dot{Q}$, as well as the stagnation enthalpy change, can be calculated from the results of thermal analysis by means of integrals over surfaces enclosing the bearing volume. Outlet stagnation enthalpy rate $\dot{I}_{ST}^{\{out\}} = \dot{m} i_{ST}^{\{out\}}$ is calculated as

$$\dot{I}_{ST}^{\{out\}} = \iint_{S^{\{out\}}} \rho\left(c_p T + \frac{v^2}{2}\right)\mathbf{v}\cdot\mathbf{n}\mathrm{d}S = \dot{I}^{\{out\}} + \dot{W}_{kin}^{\{out\}}, \tag{4.52}$$

$S^{\{out\}}$ being the bearing outlet area. Inlet stagnation enthalpy can be calculated directly, summing over n inlets

$$\dot{I}_{ST}^{\{in\}} = \sum_{i=1}^{n} \dot{m}_i\left(c_p T_i + \frac{v_i^2}{2}\right) = \dot{I}^{\{in\}} + \dot{W}_{kin}^{\{in\}}. \tag{4.53}$$

Heat transferred from journal and bushing can be estimated by means of integral all over the control volume surface. Noticeable value will have only heat transport through cylindrical surfaces of journal and bushing $S^{\{JB\}}$.

$$\dot{Q} = \iint_{S^{\{JB\}}} k\nabla T\cdot\mathbf{n}\mathrm{d}S. \tag{4.54}$$

Using above relations, the shaft work done on the system can be put down as

$$\dot{W}_{sh} = \dot{I}_{ST}^{\{out\}} - \dot{I}_{ST}^{\{in\}} - \dot{Q} = \dot{I} + \dot{W}_{kin} - \dot{Q}. \tag{4.55}$$

By integration of the energy equation (4.40) over entire control volume, we get

$$\dot{I} - \dot{Q} = \iiint_{\Omega} (\Phi + \mathbf{v} \cdot \nabla p) \ \mathrm{d}\Omega, \tag{4.56}$$

which should be satisfied for fully conservative model.

Let residual enthalpy change rate be defined as

$$\dot{I}_{res} = \sum_{i=1}^{n} \dot{m}_i c_p T_i - \iint_{S^{\{out\}}} \rho c_p T \mathbf{v} \cdot \mathbf{n} \mathrm{d}S + \iint_{S^{\{JB\}}} k \nabla T \cdot \mathbf{n} \mathrm{d}S + \iiint_{\Omega} (\Phi + \mathbf{v} \cdot \nabla p) \ \mathrm{d}\Omega, \tag{4.57}$$

using the last equation (4.56), enthalpy rate of change, and heat transfer rate calculated from the equations (4.52),(4.53) and (4.54). The residual enthalpy rate of change for two chosen cases is in the graph of the figure 4.4.

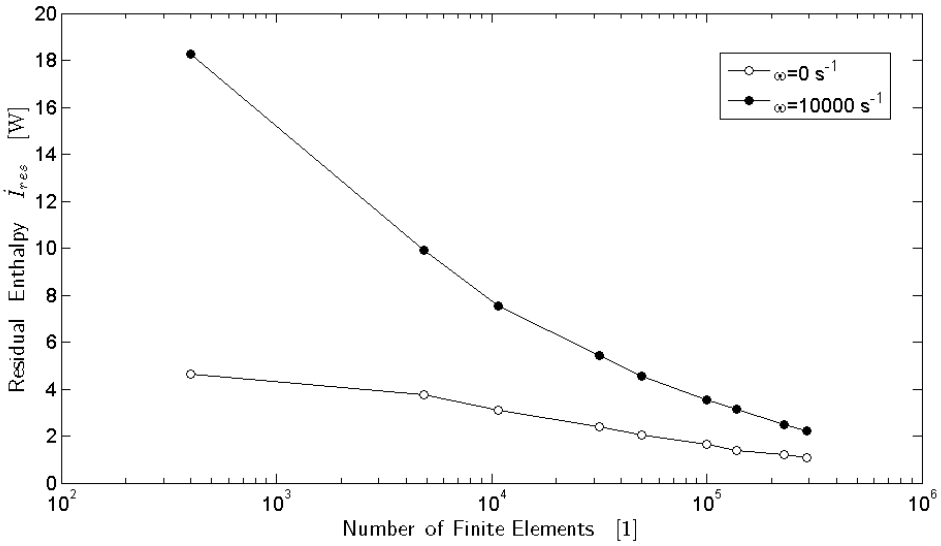

Figure 4.4: Convergence in terms of residual enthalpy rate of change

4.3.2 Results of the Test Case

Results of the analysis of the test case of bearing A, running at angular speed $\omega = 10,000\,\mathrm{s}^{-1}$ are presented in the following figures. Number of finite elements used was 291,600. The fig. 4.5 shows the calculated temperature in the middle of the air film, figs. 4.6 and 4.7 show the air temperature at bearing midplane and the temperature at the end of bearing. In the figures 4.8, 4.9, the temperature in radial-axial cuts is displayed. These results show the

temperature variations within range of several Kelvins, even with respect to the discussed fact of uncertain absolute values of the temperatures near orifices. Because Galerkin method was used to solve strongly convective problem, the stability of the method is of concern. With the number of elements used, mild non-physical spatial oscillations are becoming visible. Further increase of number of elements promotes these oscillations. For higher resolution of spatial discretization, some stabilized variant of the Galerkin method will have to be used in order to obtain the results free from non-physical oscillation. For general purpose of this analysis, level of discretization of the problem is sufficient.

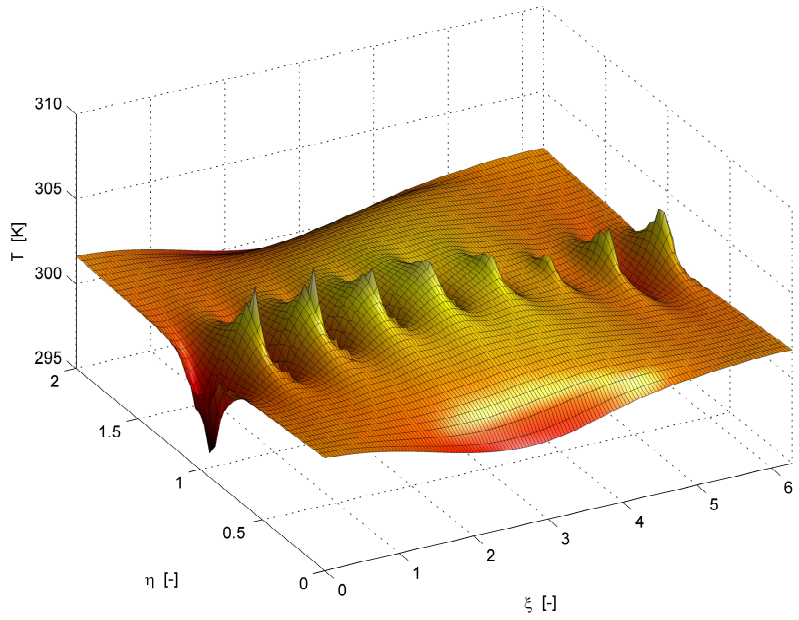

Figure 4.5: Temperature of the air, measured in the middle of air film thickness ($\zeta = 0.5$); Bearing design A, $\omega = 10000\,\mathrm{s}^{-1}$, $p_s = 0.5\,\mathrm{MPa}$, $\varepsilon = 0.5$

Pressure profile calculated by the generalized Reynolds equation is drawn in the figure 4.10. Difference between this pressure and pressure obtained by finite element model of isothermal bearing at 300 K is in the figure 4.11. Maximum difference between those two pressure profiles is less than 10% for this relatively fast running bearing configuration. Use of isothermal bearing models is justifiable in most cases of isothermal boundary conditions. Angular speed of $10,000\,\mathrm{s}^{-1}$ for this bearing design is rather excessive with respect to bearing stability. Lesser effect on pressure is expected within practical range of journal speed.

The circumferential and the axial components of air velocity, measured in the middle of air film, are in the figures 4.12 and 4.13. The figure 4.14 shows this velocity field in streamlines, together with isobaric contours. The streamlines are significantly not perpendicular to the isobars due to the Couette component of flow generated by rotation of journal.

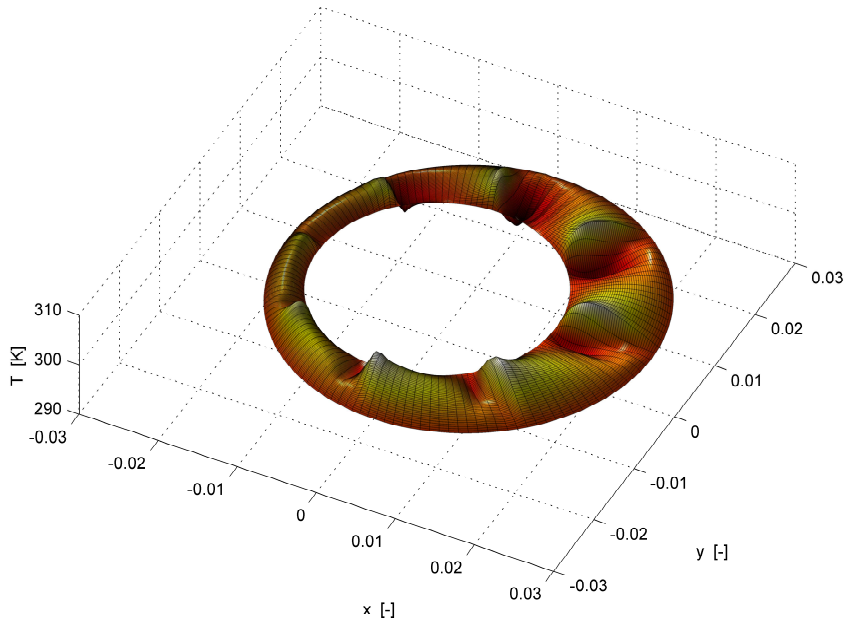

Figure 4.6: Temperature of the air, measured in the middle of the bearing ($\eta = 0.5$); Bearing design A, $\omega = 10000\,\mathrm{s}^{-1}$, $p_s = 0.5\,\mathrm{MPa}$, $\varepsilon = 0.5$

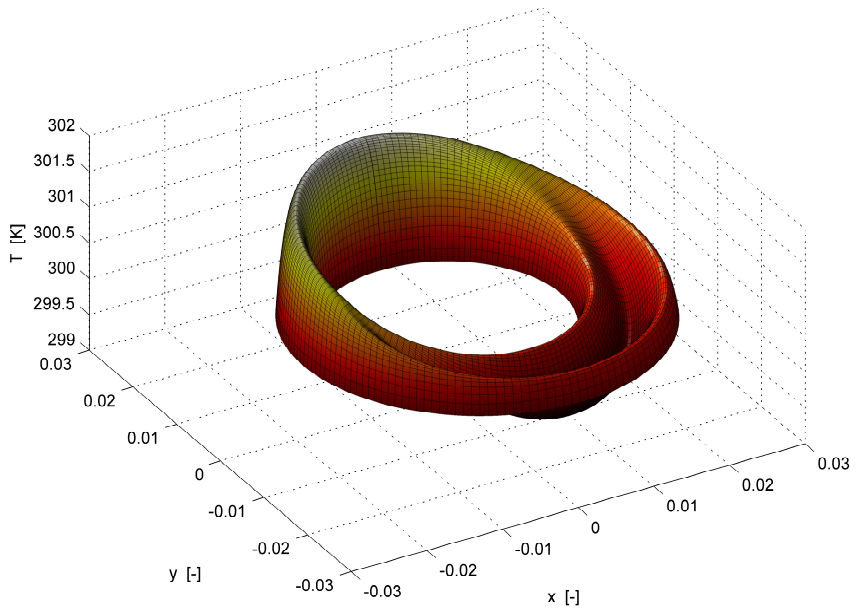

Figure 4.7: Temperature of the air leaving the bearing, measured at the bearing end ($\eta = 0$); Bearing design A, $\omega = 10000\,\mathrm{s}^{-1}$, $p_s = 0.5\,\mathrm{MPa}$, $\varepsilon = 0.5$

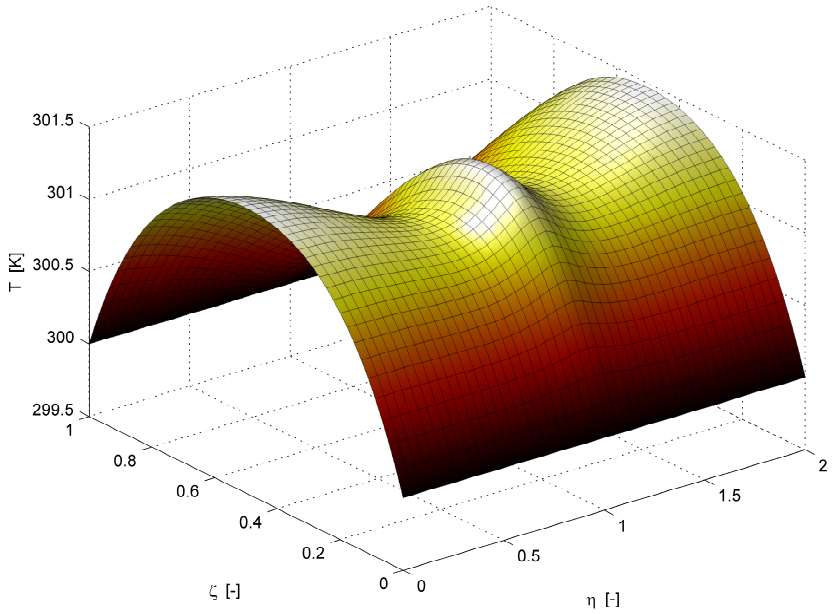

Figure 4.8: Temperature of the air, measured in between two air inlet orifices (radial-axial cut); Bearing design A, $\omega = 10000\,\mathrm{s}^{-1}$, $p_s = 0.5\,\mathrm{MPa}$, $\varepsilon = 0.5$

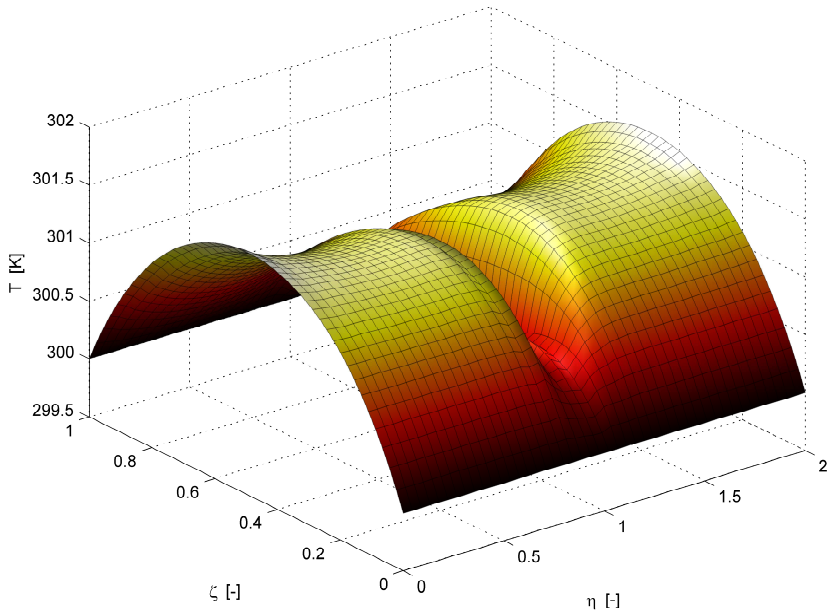

Figure 4.9: Temperature of the air, measured at position of an air inlet orifice (radial-axial cut); Bearing design A, $\omega = 10000\,\mathrm{s}^{-1}$, $p_s = 0.5\,\mathrm{MPa}$, $\varepsilon = 0.5$

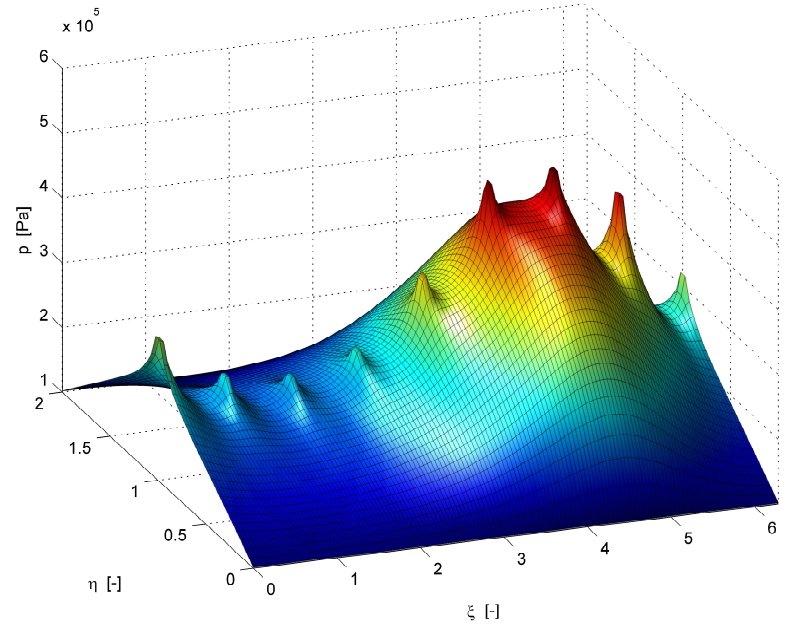

Figure 4.10: Pressure profile obtained by THDL analysis; Bearing design A, $\omega = 10000\,\mathrm{s}^{-1}$, $p_s = 0.5\,\mathrm{MPa}$, $\varepsilon = 0.5$

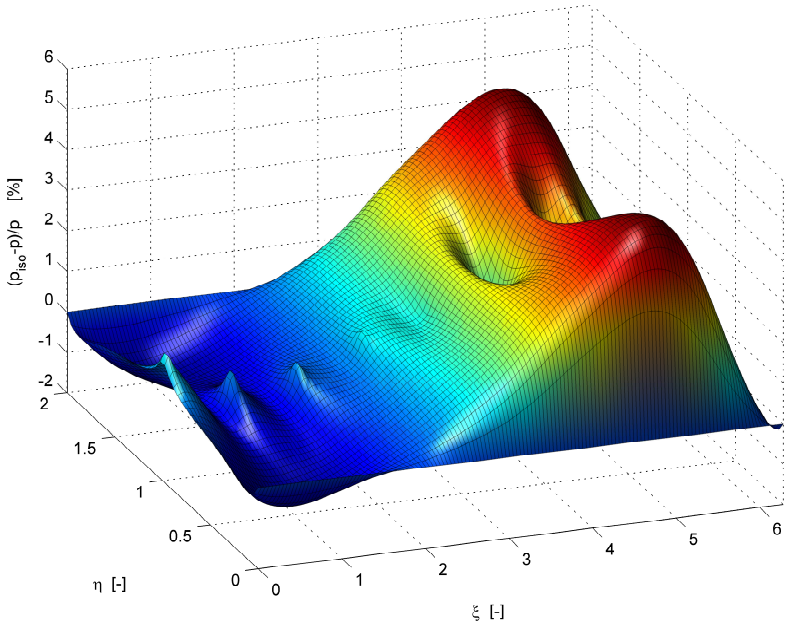

Figure 4.11: Difference between pressure profiles resulting from THDL and isothermal HDL analyses; Bearing design A, $\omega = 10000\,\mathrm{s}^{-1}$, $p_s = 0.5\,\mathrm{MPa}$, $\varepsilon = 0.5$

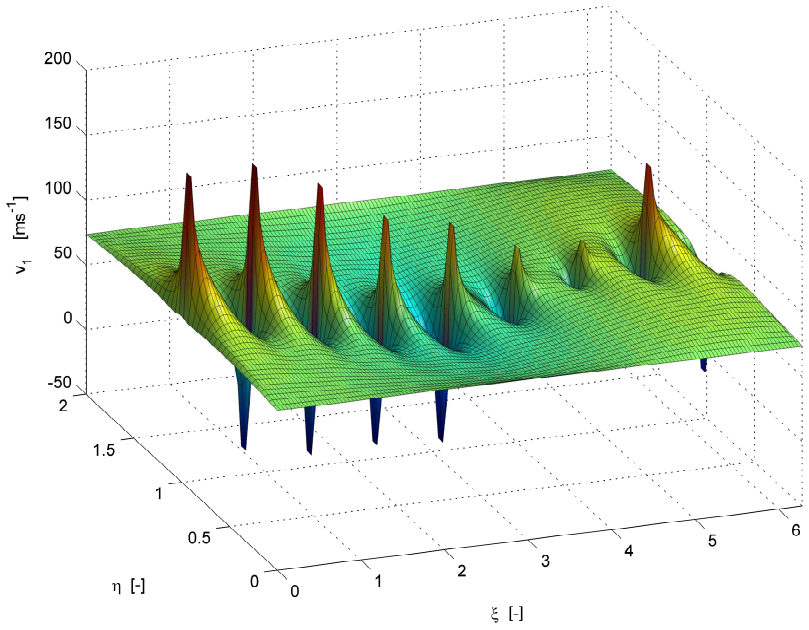

Figure 4.12: Circumferential (ξ) component of air velocity, measured in the middle of air film thickness ($\zeta = 0.5$); Bearing design A, $\omega = 10000\,\mathrm{s}^{-1}$, $p_s = 0.5\,\mathrm{MPa}$, $\varepsilon = 0.5$

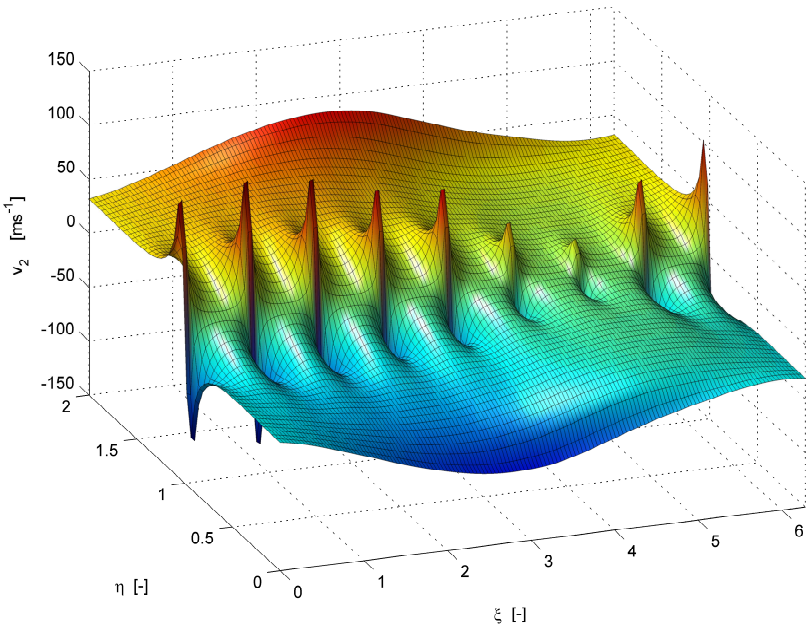

Figure 4.13: Axial (η) component of air velocity, measured in the middle of air film thickness ($\zeta = 0.5$); Bearing design A, $\omega = 10000\,\mathrm{s}^{-1}$, $p_s = 0.5\,\mathrm{MPa}$, $\varepsilon = 0.5$

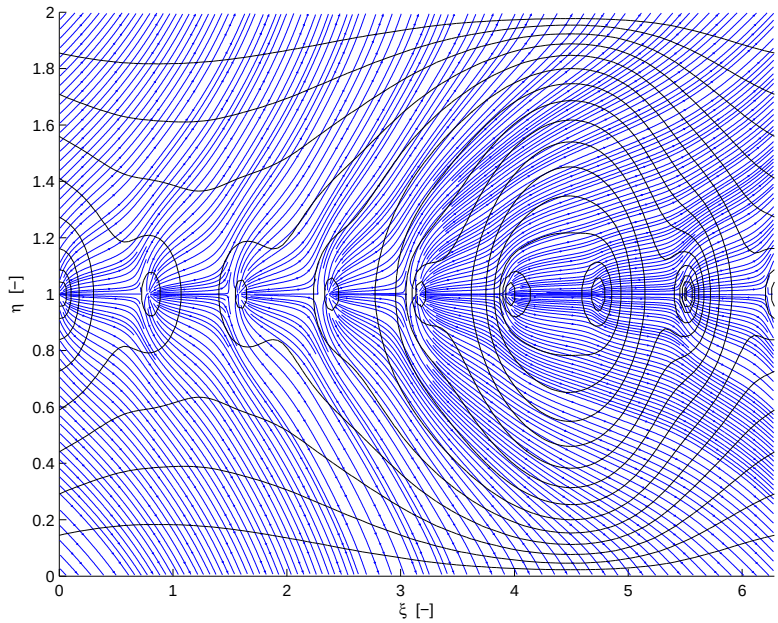

Figure 4.14: Streamlines (blue) of air flow in the middle of air film ($\zeta = 0.5$) and isobars (black); Bearing design A, $\omega = 10000\,\mathrm{s}^{-1}$, $p_s = 0.5\,\mathrm{MPa}$, $\varepsilon = 0.5$

Mean values of viscosity, thermal conductivity and isobaric thermal capacity are plotted in graphs of the figures 4.15, 4.16 and 4.17. These quantities exhibit little spatial variations caused by temperature variations within the air film.

Mechanical part of enthalpy change, taken from the right-hand side of equation (4.56) is shown in the figure 4.18 as surface density, defined as

$$\dot{I}_{Dmech} = \int_0^h (\Phi + \mathbf{v} \cdot \nabla p)\ \mathrm{d}x_3, \tag{4.58}$$

Contribution to the enthalpy change from air expansion and energy dissipation are plotted separately in the figures 4.19, 4.20, where

$$\dot{I}_{Dexp} = \int_0^h \mathbf{v} \cdot \nabla p\,\mathrm{d}x_3, \qquad \dot{I}_{Ddis} = \int_0^h \Phi\,\mathrm{d}x_3. \tag{4.59}$$

Overall contributions of these components to the enthalpy rate of change,

$$\dot{I}_{exp} = \iiint_\Omega \mathbf{v} \cdot \nabla p\,\mathrm{d}\Omega, \qquad \dot{I}_{dis} = \iiint_\Omega \Phi\,\mathrm{d}\Omega, \qquad \dot{I}_{mech} = \dot{I}_{exp} + \dot{I}_{dis}, \tag{4.60}$$

are depicted in the figure 4.21 with respect to journal angular speed. This graph shows a balance between the air expansion and the energy dissipation in the case of standstill journal, $\omega = 0$, when only Poiseuille part of flow is present. Therefore, this part of flow does not significantly contribute to the change of average temperature of the bearing. The Couette

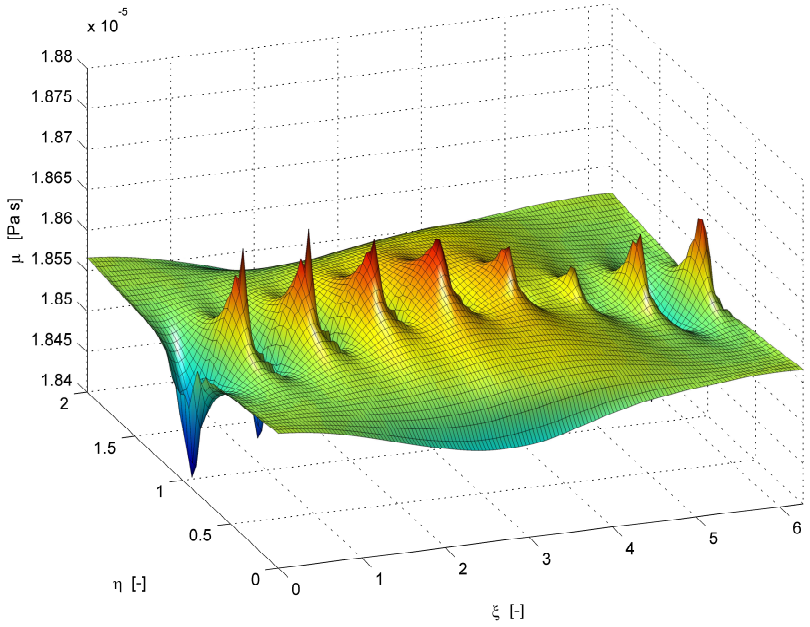

Figure 4.15: Mean value of air viscosity, averaged across air film thickness; Bearing design A, $\omega = 10000\,\mathrm{s}^{-1}$, $p_s = 0.5\,\mathrm{MPa}$, $\varepsilon = 0.5$

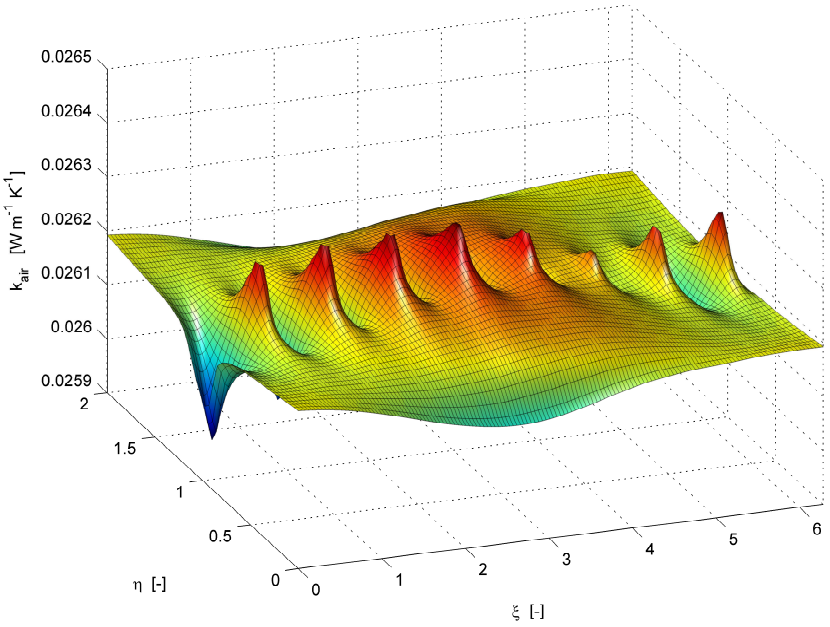

Figure 4.16: Mean value of air thermal conductivity, averaged across air film thickness; Bearing design A, $\omega = 10000\,\mathrm{s}^{-1}$, $p_s = 0.5\,\mathrm{MPa}$, $\varepsilon = 0.5$

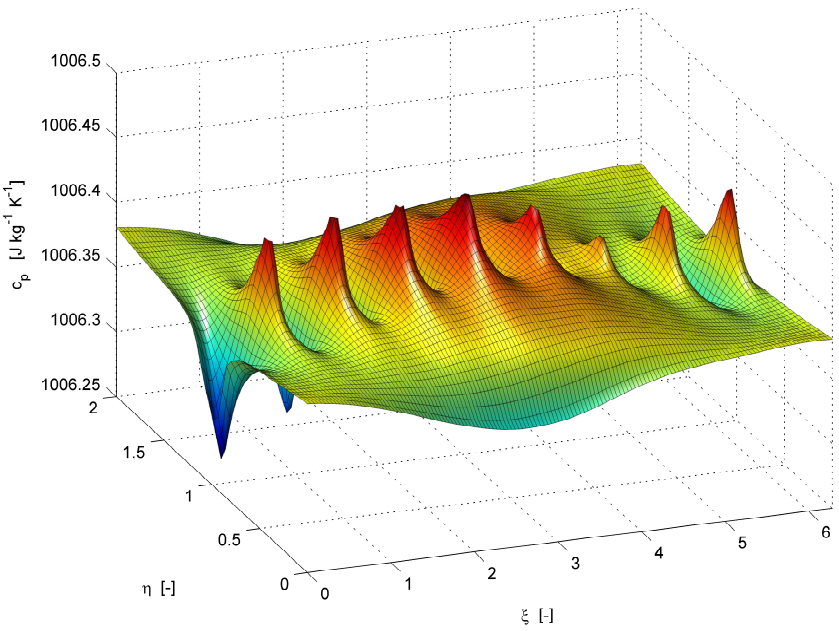

Figure 4.17: Mean value of isobaric thermal capacity of the air, averaged across air film thickness; Bearing design A, $\omega = 10000\,\mathrm{s}^{-1}$, $p_s = 0.5\,\mathrm{MPa}$, $\varepsilon = 0.5$

flow, driven by journal rotation is the main contributor to the enthalpy rate of change and as such it is mostly taken out of the control volume in the form of heat transfered through the isothermal boundaries representing journal and bushing. The quantity $\dot{I}_{mech}$ closely follows quadratic function approaching the bearing mechanical power loss.

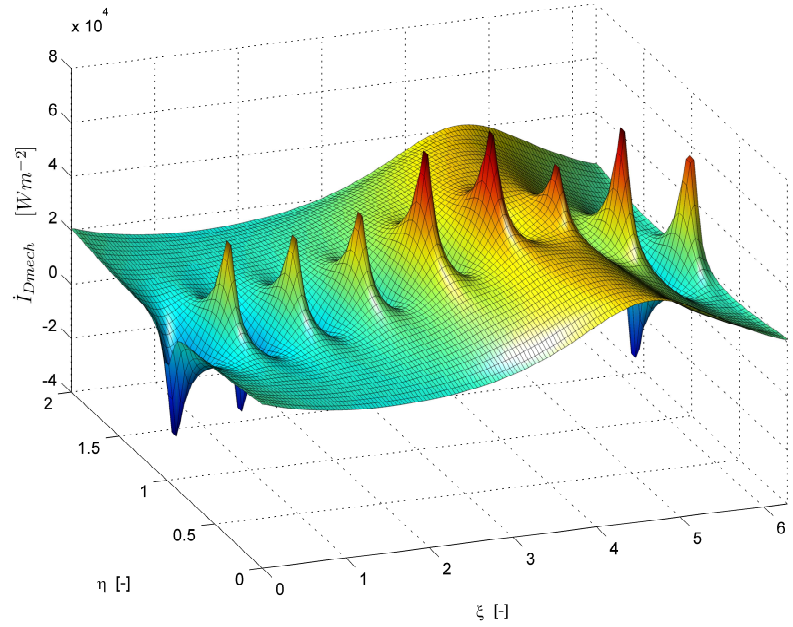

Figure 4.18: Surface density of enthalpy rate of change, isolated effect of air expansion and dissipation; Bearing design A, $\omega = 10000\,\mathrm{s}^{-1}$, $p_s = 0.5\,\mathrm{MPa}$, $\varepsilon = 0.5$

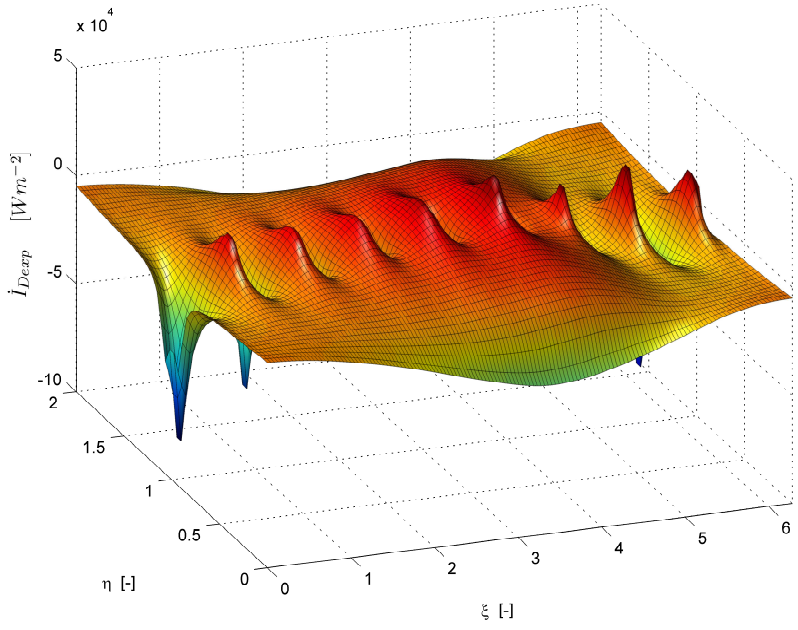

Figure 4.19: Surface density of enthalpy rate of change, isolated effect of air expansion; Bearing design A, $\omega = 10000\,\mathrm{s}^{-1}$, $p_s = 0.5\,\mathrm{MPa}$, $\varepsilon = 0.5$

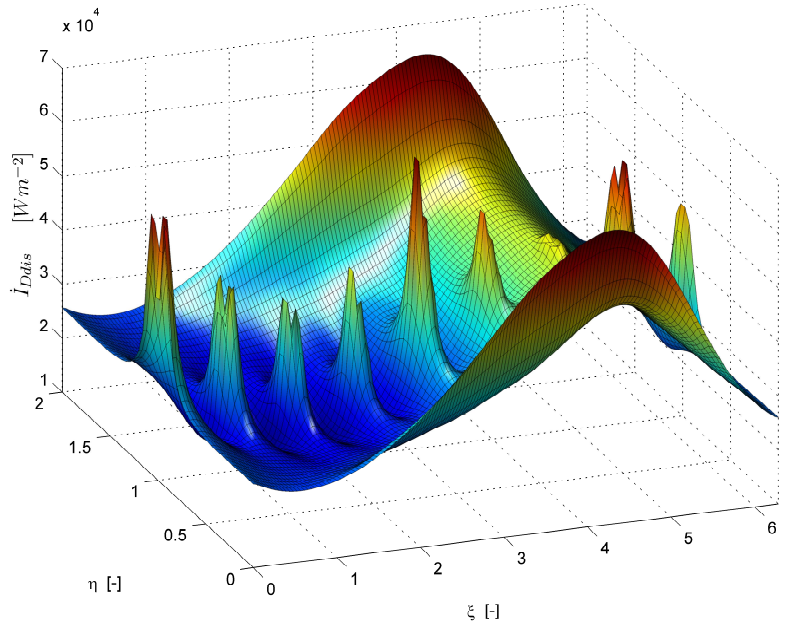

Figure 4.20: Surface density of enthalpy rate of change, isolated effect of dissipation; Bearing design A, $\omega = 10000\,\mathrm{s}^{-1}$, $p_s = 0.5\,\mathrm{MPa}$, $\varepsilon = 0.5$

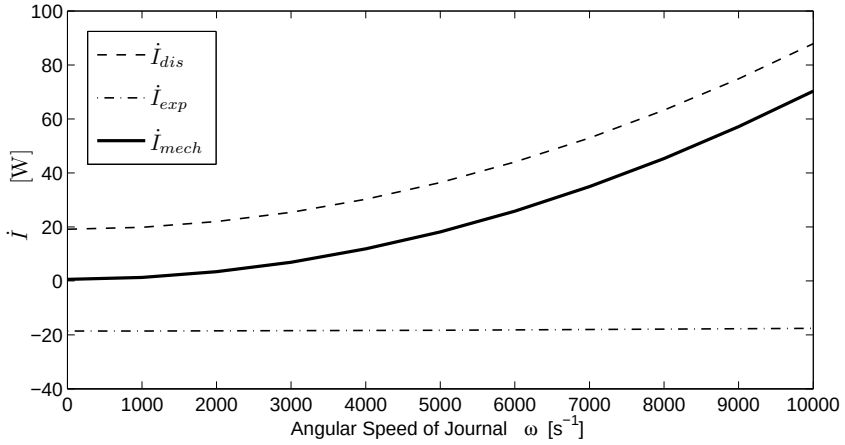

Figure 4.21: Enthalpy rate of change components vs. journal angular speed; Bearing design A, $p_s = 0.5\,\mathrm{MPa}$, $\varepsilon = 0.5$

4.4 Bearing Operating Temperature

Thermal analysis of the bearing with isothermal boundary conditions confirmed the assumption of nearly isothermal air film, which is in accordance with experimental evidence observed by Ohishi and Matsuzaki [26]. The opened question is the mean air film temperature in the case of more realistic boundary conditions of the air film. The temperatures of the shaft and bushing cylindrical surfaces are determined by solid parts of the bearing and their boundary conditions.

Using steady state heat conduction models of journal and bushing, the thermal contact temperature can be searched by means of the balance between the heat transferred through air film model boundaries to solid parts and the heat leaving those parts by natural or forced convection.

4.4.1 Steady State Heat Conduction Models of Bearing Parts

For demonstrative purposes, simple geometry of solid parts composing the bearing was chosen: Hollow shaft of 30 mm outer diameter, with inner diameter 10 mm and length of 100 mm; Cylindrical bushing of outer diameter 50 mm and 30 mm length, with neglected geometry of the air supply ducts. Bushing is positioned on the shaft so that the bearing end face is in distance of 20 mm from the end of the shaft. Other bearing parameters are identical to the test case analysed in previous section.

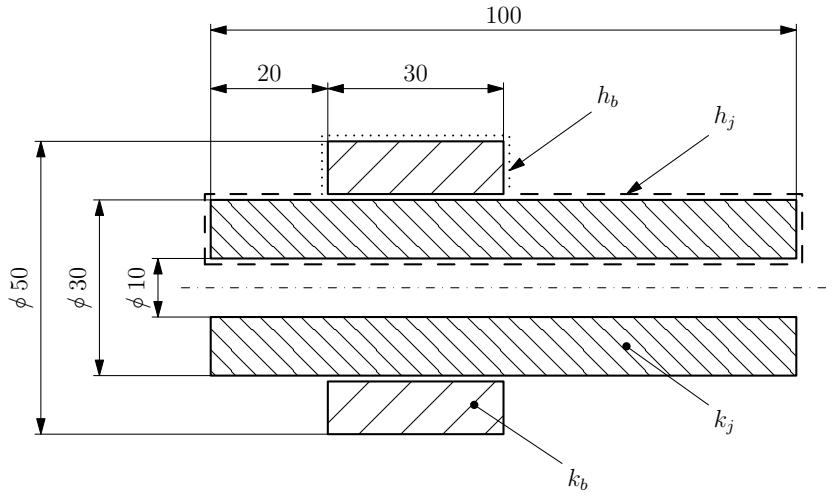

Figure 4.22: Shaft and air bearing configuration for thermal analysis

Steady state heat conduction problem for bushing was formulated in cylindrical coordinates (r, φ, z) according to Lewis et al. [69]; Galerkin method using basis functions of trilinear

brick elements was applied on equation

$$k_b \left(\frac{\partial^2 T}{\partial r^2} + \frac{1}{r}\frac{\partial T}{\partial r} + \frac{1}{r^2}\frac{\partial^2 T}{\partial \varphi^2} + \frac{\partial^2 T}{\partial z^2} \right) = 0. \tag{4.61}$$

Axisymmetric formulation was chosen for journal heat conduction, assuming the rotation of the journal will lead to uniform temperature along φ coordinate. Simplex triangular linear elements were used for journal discretization. Axisymmetric steady state heat conduction equation used for journal:

$$k_j \left(\frac{\partial^2 T}{\partial r^2} + \frac{1}{r}\frac{\partial T}{\partial r} + \frac{\partial^2 T}{\partial z^2} \right) = 0. \tag{4.62}$$

Convection boundary conditions for free surfaces of both these parts were considered with heat convection coefficients: $h_j = 200\,\mathrm{W\,m^{-2}K^{-1}}$ and $h_b = 50\,\mathrm{W\,m^{-2}K^{-1}}$. Thermal conductivity of materials of journal and bushing was $k_j = 16\,\mathrm{W\,m^{-1}K^{-1}}$, $k_b = 45\,\mathrm{W\,m^{-1}K^{-1}}$. Heat flow boundary conditions are applied on remaining surfaces. Sizes of the elements in circumferential and axial directions are equal to those of THDL model of the air film. The amount of heat transferred to the metal parts is calculated by solving the thermal analysis of the air film.

4.4.2 Results of Steady State Operating Temperature

Steady state temperature of bearing configuration described in the previous section was calculated for two journal angular speeds: $\omega = 10,000\,\mathrm{s^{-1}}$ and $\omega = 1\,\mathrm{s^{-1}}$. The second case can be considered standstill journal, but very slow rotation was set in order to satisfy assumption of uniform temperature along circumferential coordinate of journal. Results of these analyses are presented in the figures 4.23 to 4.28.

Results for standstill rotor confirmed that virtually no effect on temperature comes from the Poiseuille flow induced by supply of pressurized air. Bearing operating temperature for configuration of fast running journal is driven by particular design of the parts and the convective boundary conditions, but from obtained temperature distribution it can be concluded, that the air film remains nearly isothermal in this particular case and that it could be treated as isothermal for most technical applications, even if the operating temperature significantly differs from the ambient temperature. Accurate prediction of the operating temperature is a matter of adequate models of solid parts involved and of understanding boundary conditions of particular design case.

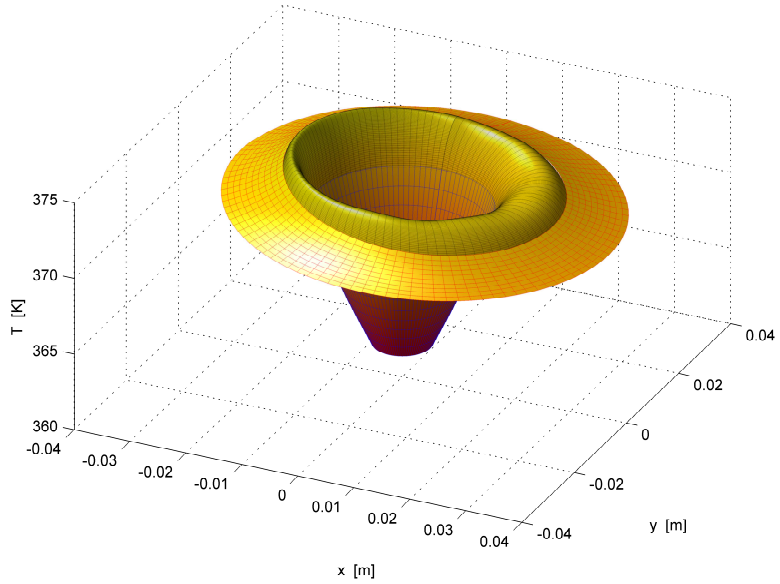

Figure 4.23: Steady state temperature of bearing, radial (r, φ) cut in quarter of bearing length. Bushing: red element edges, Journal: blue element edges, Air film: grey element edges, Air film thickness scaled up by factor 400; Bearing design A, $\omega = 10000\,\mathrm{s}^{-1}$, $p_s = 0.5\,\mathrm{MPa}$, $\varepsilon = 0.5$

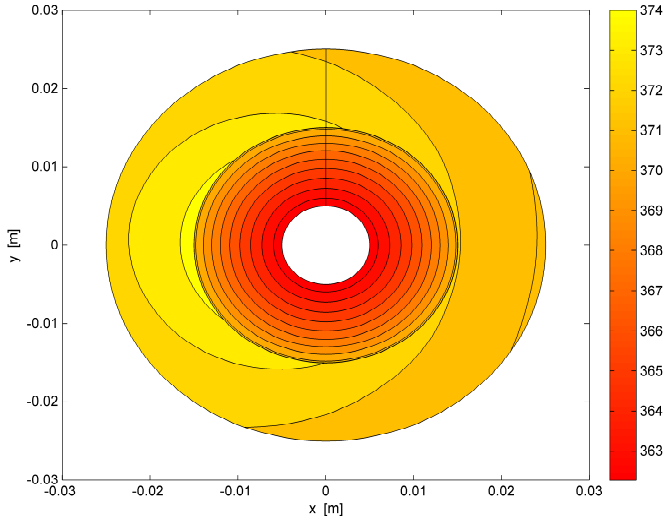

Figure 4.24: Steady state temperature of bearing, radial (r, φ) cut in quarter of bearing length, isotherms; Bearing design A, $\omega = 10000\,\mathrm{s}^{-1}$, $p_s = 0.5\,\mathrm{MPa}$, $\varepsilon = 0.5$

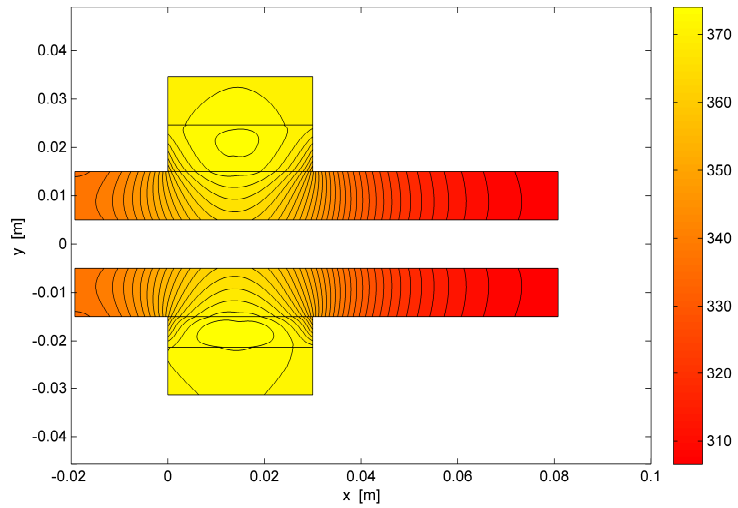

Figure 4.25: Steady state temperature of bearing, axial (r, z) cut, isotherms; Air film thickness scaled up by factor 400; Bearing design A, $\omega = 10000\,\mathrm{s}^{-1}$, $p_s = 0.5\,\mathrm{MPa}$, $\varepsilon = 0.5$

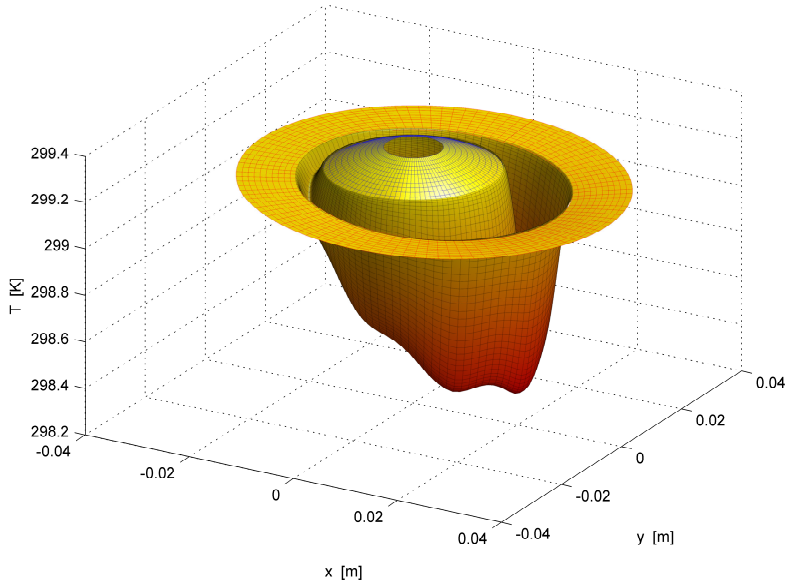

Figure 4.26: Steady state temperature of bearing, radial (r, φ) cut in quarter of bearing length. Bushing: red element edges, Journal: blue element edges, Air film: grey element edges, Air film thickness scaled up by factor 400; Bearing design A, $\omega = 1\,\mathrm{s}^{-1}$, $p_s = 0.5\,\mathrm{MPa}$, $\varepsilon = 0.5$

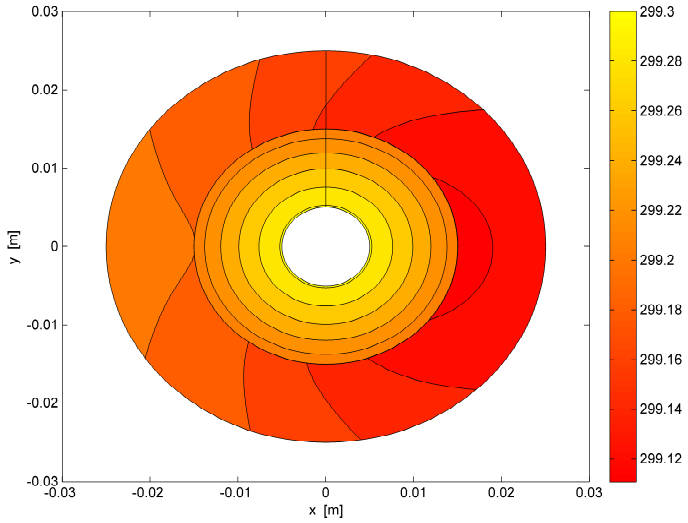

Figure 4.27: Steady state temperature of bearing, radial (r, φ) cut in quarter of bearing length, isotherms; Bearing design A, $\omega = 1\,\mathrm{s}^{-1}$, $p_s = 0.5\,\mathrm{MPa}$, $\varepsilon = 0.5$

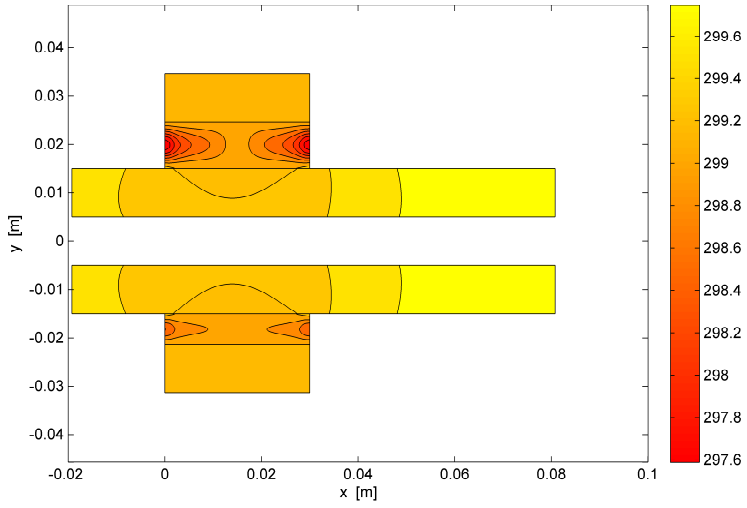

Figure 4.28: Steady state temperature of bearing, axial (r, z) cut, isotherms; Air film thickness scaled up by factor 400; Bearing design A, $\omega = 1\,\mathrm{s}^{-1}$, $p_s = 0.5\,\mathrm{MPa}$, $\varepsilon = 0.5$

Chapter 5

Conclusion

This dissertation defines and delivers a set of mathematical tools for analysis of rotor systems supported in aerostatic journal bearings, with special concerns about thermal conditions of analysed system. This work was motivated by the fact that there is little attention paid to the thermal analysis of aerostatic bearings in scientific literature despite the high sensitivity of bearing geometry and lubricant parameters to the temperature changes. Elevated temperature of aerostatic bearings during high speed operation is evident from experiments. Modelling technique capable of analysing the thermal situation of these bearings is the key aim of this work. Results of developed model, the average temperature of lubricant film, its distribution over the lubricant volume, and the resulting effect to the lubricant pressure enable the calculation of relevant properties of the air bearings. These results also provide reasoning of the use of significantly simpler isothermal hydrodynamic bearing analysis in particular design cases. Providing that the non-uniformity of bearing temperature causes little effect to the pressure distribution, the isothermal bearing models can be employed (using adequate parameters obtained from the thermal analysis). Those isothermal models can be treated in the time domain together with equations of motions of rotor system. In spite of the fact that hydrodynamic models of aerostatic bearing are non-linear, the bearings itself can behave almost linearly at certain conditions. Development of isothermal bearing models and methods of assessment of their linearity was also objective of this work. An analysis tool providing linear coefficients of bearings (respecting all four lateral degrees of freedom: two displacements and two tilts), which would be applicable to linear models of rotor systems was also in the scope of this work. Elastic rotor models, whether treated in the time domain together with a transient bearing models or approached in the frequency domain with the use linear bearing coefficients, were to be programmed. Transient analysis of rotor systems is usually time consumptive owing to a large span of eigenfrequencies of the rotor model, therefore a reliable reduction method of gyroscopic defective rotor models was intended to be implemented into resultant code package. All these objectives have been accomplished.

Thermo-hydrodynamic Lubrication model of aerostatic bearing with inherently compensated orifices is presented in the chapter 4. It consists of energy conservation equation that is

solved in three dimensions by means of finite element method. Galerkin approach is utilized in order to obtain the weak formulation of energy equation in curvilinear coordinates. Transition to curvilinear coordinates was proposed in order to transform problematic geometry of air film to simple cuboid, which can however be done only on the cost of getting more complicated form of solved equation. The energy equation is coupled with proposed generalized Reynolds equation that represents momentum and mass transfer. The generalized Reynolds equation is also discretized by means of finite elements. Both the generalized Reynolds equation and the energy equation are solved iteratively together. Results of the test problems with isothermal boundary conditions of bearing and journal surfaces suggested that the temperature inside air film is nearly uniform (less than 5 K) in the most of the air volume even for the power loss of 70 W. The exceptions were the areas close to the orifices, at which the absolute temperature was not obtainable, because the orifices were treated as point sources. Generated dissipative heat was nearly all conducted out of the air volume via these idealized isothermal boundaries. Test case also confirmed that Poiseuille part of the flow through bearing does not contribute to the total generated heat, because the dissipative heat of this part of flow is balanced out by the expansion work. Maximum local effect on the pressure, caused by observed little spatial variations of temperature, was approximately 5% in the terms of difference from the pressure of isothermal model. More realistic boundary conditions of THDL were implemented by heat conduction models of journal and bushing. This joined system has been solved and the results confirmed nearly isothermal distribution of the temperature within the air film, even if the average film temperature was elevated by nearly 75 K. It also confirmed the negligible effect of the Poiseuille flow. Both these findings, the effect of Poiseuille flow and the nearly isothermal conditions of air film are in agreement with experimental observation of Ohishi and Matsuzaki [26], who measured the air film temperatures for this kind of bearings and also did not encounter an effect of Poiseuille part of the air flow to air film temperature. The results of maintained analyses suggest that the isothermal assumption is justifiable in many cases. Therefore the isothermal models of aerostatic bearings seem appropriate on condition that the average air film temperature is understood.

Isothermal bearing models based on the Reynolds equation of classical lubrication are presented in the chapter 3 of this work. Finite element method was implemented in the steady state solver of pressure distribution. Finite element approach to transient solver is also presented, but it was excessively time-consuming in comparison to the simple finite difference method. Finite difference method was therefore preferred for transient solver. Comparison of bearing load capacities that were calculated by both these methods showed reasonable agreement for number of elements (mesh nodes resp.) exceeding 10,000. Finite difference transient solver was used in the method of obtaining bearing linear stiffness and damping coefficients. Angular displacements as well as cross-coupling between translational and angular displacements were respected. This method has been developed as an extension of existing method of Czolczyński [39]. Characteristics of aerostatic bearing corresponding to the lateral

translational displacements were recently measured by Kozánek and Půst [66]; these data were compared to the data calculated by presented numerical method. Agreement between measured and calculated stiffness coefficients was within the range of 25%, what can be considered good agreement with respect to all uncertainties involved in both processes. Linearity of aerostatic bearings was studied by means of dependence of identified linear characteristics on vibration amplitude and frequency. The biggest effects of nonlinearity were observed in diagonal stiffness and damping coefficients. These parametric studies are difficult to interpret in the terms of expected errors of bearing system response. Assessment of bearing linearity is more accessible in the frequency domain. Comparison of transfer functions of bearing-journal system that were obtained by means of calculated linear characteristics and the transfer function estimated from the transient response to a stochastic signal is more convenient option. The level of nonlinearity can be also observed by magnitude-square coherence of force input and displacement output of transient model.

Chapter 2 contains selected topics on elastic rotor models for analyses of combined systems of rotors and bearings. The most general model of rotating shaft developed in this work is a Timoshenko shaft finite element with independent tilt of shaft cross-section and internal viscous damping. The key topic of the chapter 2 is reduction of defective gyroscopic rotor models. Three reduction methods were programmed and tested in frequency and time domains. Partial decomposition of rotor system by bending modes of rotor system without gyroscopic effect exhibited faster rate of convergence of eigenfrequencies and eigenvectors than other two methods that were derived from Craig-Bampton component mode synthesis. Results of transient analyses of the test case of a rotor with significant gyroscopic effect were in accordance with this finding, although all three methods are proved feasible for reduction of presented kind of defective rotor systems. Purpose of this reduction methods is to avoid problems that are linked to computation of dynamic contributions of high frequency whirl modes. In contrast with somewhat worse approximation of the full rotor system, the modified Craig-Bampton component mode synthesis methods are better suited for transient analysis. These fixed-interface methods do not use the rigid body modes of the rotor system. In addition, the transformations from physical to modal space and vice versa each integration step are completely avoided.

Bibliography

[1] J. Frêne, D. Nicolas, B. Degueurce, D. Berthe, and M. Godet. *Hydrodynamic Lubrication. Bearings and Thrust Bearings*. Elsevier, 1997. ISBN 0-444-82366-2.

[2] K. Ramesh, S.H. Yeo, Z.W. Zhong, and Akinori Yui. ltra-high-speed thermal behavior of a rolling element upon using oilair mist lubrication. *Journal of Materials Processing Technology*, 127:191–198, 2002.

[3] Franz-Josef Ebert. Fundamentals of design and technology of rolling element bearings. *Chinese Journal of Aeronautics*, 23:123–136, 2010.

[4] Shigeo Fukada, Bin Fang, and Akira Shigeno. Experimental analysis and simulation of nonlinear microscopic behavior of ball screw mechanism for ultra-precision positioning. *Precision Engineering*, 35:650–668, 2011.

[5] Cai Tian, Zhang Ming, Zhu Yu, and Hu Chuxiong. Dynamic modeling and analysis of a 3-dof ultra-precision positioning stage with air bearing. *Procedia Engineering*, 16:264–270, 2011.

[6] E. S. Piekos. *Numerical Simulation of Gas-Lubricated Journal Bearings for Microfabricated Machines*. PhD thesis, Massachusetts Institute of Technology, 2000.

[7] Qide Zhang, Xue Chuan Shan, Guoxiao Guo, and Stephen Wong. Performance analysis of air bearing in a micro system. *Materials Science and Engineering*, A 423:25–229, 2006.

[8] An Sung Lee and Kyung Geun Bang. Fe lubrication analysis and dynamic characteristics of herringbone groove air bearing applied to color wheel for projection television. In *IFToMM*, 7th International Conference on Rotor Dynamics, Vienna, Austria, September 2006.

[9] Cheng-Chi Wang, Her-Terng Yau, Ming-Jyi Jang, and Yen-Liang Yeh. Theoretical analysis of the nonlinear behavior of a flexible rotor supported by herringbone grooved gas journal bearings. *Tribology International*, 40:533–541, 2007.

[10] J. Šimek, J. Kozánek, and M. Šafr. Some interesting features of rotors supported in aerodynamic bearings. In *IFToMM, 7th International Conference on Rotor Dynamics*, Vienna, Austria, September 2006.

[11] Luis San Andrés and Tae Ho Kim. Forced nonlinear response of gas foil bearing supported rotors. *Tribology International*, 41:704–715, 2008.

[12] D. Sudheer Kumar Reddy, S. Swarnamani, and B.S. Prabhu. Analysis of aerodynamic multileaf foil journal bearings. *Wear*, 209:115–122, 1997.

[13] Yong-Bok Lee, Dong-Jin Park, and Chang-Ho Kim. Numerical analysis for bump foil journal bearing considering top foil effect and experimental investigation. In *IFToMM*, 7th International Conference on Rotor Dynamics, Vienna, Austria, September 2006.

[14] L.-Y. Xiong, G. Wu, Y. Hou, L.-Q. Liu, M.-F. Ling, and C.-Z. Chen. Development of aerodynamic foil journal bearings for a high speed cryogenic turboexpander. *Cryogenics*, 37:221–230, 1997.

[15] Tae Ho Kim and Luis San Andrés. Analysis of advanced gas foil bearings with piecewise linear elastic supports. *Tribology International, doi: 10.1016/j.triboint.2007.01.022*, 2007.

[16] Yong-Bok Lee, Tae-Ho Kim, Chang-Ho Kim, Nam-Soo Lee, and Dong-Hoon Choi. Dynamic characteristics of a flexible rotor system supported by a viscoelastic foil bearing (vefb). *Tribology International*, 37: 679–687, 2004.

[17] Hooshang Heshmat, Piotr Hryniewicz, James F. Walton II, John P. Willis, S. Jahanmir, and Christopher DellaCorte. Low-friction wear-resistant coatings for high-temperature foil bearings. *Tribology International*, 38:1059–1075, 2005.

[18] H.M. Talukder and T.B. Stowell. Pneumatic hammer in an externally pressurized orifice compensated air journal bearing. *Tribology International*, 36:585–591, 2003.

[19] M. Brdička, L. Samek, and B. Sopka. *Mechanika kontinua*. Academia, 2000. ISBN 80-200-0772-5.

[20] Mohammad I. Younis. *Modeling and Simulation of Microelectromechanical Systems in Multi-Physics Fields*. PhD thesis, Virginia Polytechnic Institute and State University, 2004.

[21] Eddie Yin-Kwee Ng and Ningyu Liu. A multicoefficient slip-corrected reynolds equation for micro-thin film gas lubrication. *International Journal of Rotating Machinery*, 5:105–111, 2005.

[22] Jean Frêne, Mihai Arghir, and Virgil Constantinescu. Combined thin-film and Navier-Stokes analysis in high Reynolds number lubrication. *Tribology International*, 39:734–747, 2006.

[23] L. Bouard, M. Fillon, and J.Frêne. Comparison between three turbulent models - application to thermohydrodynamic performances of tilting-pad journal bearings. *Tribology International*, 29:11–18, 1996.

[24] Eric Dumont, Francine Fayolle, Václav Sobolík, and Jack Legrand. Wall shear rate in the Taylor–Couette-Poiseuille flow at low axial Reynolds number. *International Journal of Heat and Mass Transfer*, 45:679–689, 2002.

[25] Sang Myung Chun. Thermohydrodynamic lubrication analysis of high-speed journal bearing considering variable density and variable specific heat. *Tribology International*, 37:405–413, 2004.

[26] Susumu Ohishi and Yasushi Matsuzaki. Experimental investigation of air spindle unit thermal characteristics. *Precision Engineering*, 26:49–57, 2002.

[27] S. Zhang and D.B. Bogy. A heat transfer model for thermal fluctuations in a thin slider/disk air bearing. *International Journal of Heat and Mass Transfer*, 42:1791–1800, 1998.

[28] Luis San Andres, Dara Childs, and Zhou Yang. Turbulent-flow hydrostatic bearings: Analysis and experimental results. *Int. J. Mech. Sci.*, 37:815–829, 1995.

[29] B.V. Rathish Kumar, P. Srinivasa Rao, and Prawal Sinha. A numerical study of performance of a slider bearing with heat conduction to the pad. *Finite Elements in Analysis and Design*, 37:533–547, 2001.

[30] Yung-Kuang Yang and Ming-Chang Jeng. Analysis of viscosity interaction on the misaligned conical–cylindrical bearing. *Tribology International*, 37:51–60, 2004.

[31] Sang Myung Chun and Dae-Hong Ha. Study on mixing flow effects in a high-speed journal bearing. *Tribology International*, 34:397–405, 2001.

[32] Tor Syverud. Experimental investigation of the temperature fade in the cavitation zone of full journal bearings. *Tribology International*, 34:859–870, 2001.

[33] Ilmar Ferreira Santos and Rodrigo Nicoletti. Influence of orifice distribution on the thermal and static properties of hybridly lubricated bearings. *International Journal of Solids and Structures*, 38:2069–2081, 2001.

[34] Vijay Kumar, Satish C. Sharma, and S.C. Jain. On the restrictor design parameter of hybrid journal bearing for optimum rotordynamic coefficients. *Tribology International*, 39:56–368, 2006.

[35] Satish C. Sharma, Vijay Kumar, S.C. Jain, and T. Nagaraju. Study of hole-entry hybrid journal bearing system considering combined influence of thermal and elastic effects. *Tribology International*, 36:903–920, 2003.

[36] P.C. Mishra, R.K. Pandey, and K. Athre. Temperature profile of an elliptic bore journal bearing. *Tribology International*, 40:453–458, 2007.

[37] M. Fillon and J. Bouyer. Thermohydrodynamic analysis of a worn plain journal bearing. *Tribology International*, 37:129–136, 2004.

[38] J. Slavík, V. Stejskal, and V. Zeman. *Základy dynamiky strojů*. Vydavatelství ČVUT, 1997. ISBN 80-01-01622-6.

[39] K. Czolczyński. *Rotordynamics of Gas-Lubricated Journal Bearing Systems*. Springer-Verlag New York Inc., 1999.

[40] D.-C. Han, S.-S. Park, W.-J. Kim, and J-W. Kim. A study on the characteristics of externally pressurized air bearings. *Precision Engineering*, 16:164–173, 1994.

[41] K. Czolczyński. How to obtain stiffness and damping coefficients of gas bearings. *Wear*, 201:265–275, 1996.

[42] M.A. Mohiuddin. Coupled bending torsional vibration of rotating shafts using finite element. Master's thesis, University of Petroleum and Minerals, Saudi Arabia, 1992.

[43] M. Byrtus, M. Hajžman, and V. Zeman. *Dynamika rotujících soustav*. Západočeská univerzita v Plzni, Vydavatelství, 2010. ISBN 978-80-7043-953-1.

[44] Qing Hua Qin and Cheng Xiong Mao. Coupled torsional-flexural vibration of shaft systems in mechanical engineering–i. finite element model. *Computers & Structures*, 58:835–843, 1996.

[45] M. A. Mohiuddin and Y. A. Khulief. Modal characteristics of rotors using a conical shaft finite element. *Comput. Methods Appl. Mech. Engrg.*, 115:125–144, 1994.

[46] An Sung Lee, Byung Ok Kim, and Yeong-Chun Kim. A finite element transient response analysis method of a rotor-bearing system to base shock excitations using the state-space newmark scheme and comparisons with experiments. *Journal of Sound and Vibration*, 297:595–615, 2006.

[47] L.-W.Chen and W.-K. Peng. Stability analysis of a timoshenko shaft with dissimilar lateral moments of inertia. *Journal of Sound and Vibration*, 207:33–46, 1997.

[48] Jagadish BabuGunda, R.K.Gupta, G.RangaJanardhan, and G.VenkateswaraRao. Large amplitude free vibration analysis of timoshenko beams using a relatively simple finite element formulation. *International Journal of Mechanical Sciences*, 52:1597–1604, 2010.

[49] N.M. Auciello and A. Ercolano. A general solution for dynamic response of axially loaded non-uniform timoshenko beams. *International Journal of Solids and Structures*, 41:4861–4874, 2004.

[50] P. Jafarali, Mohammed Ameen, Somenath Mukherjee, and Gangan Prathap. Variational correctness and timoshenko beam finite element elastodynamics. *Journal of Sound and Vibration*, 299:196–211, 2007.

[51] Aleš Tondl. *Some problems of rotor dynamics*. Publishing House of the Czechoslovak Academy of Sciences, Chapman & Hall, 1965.

[52] Mohamed A. Kandil. *On Rotor Internal Damping Instability*. PhD thesis, Imperial College London, 2004.

[53] Giancarlo Genta and Nicola Amati. Hysteretic damping in rotordynamics: An equivalent formulation. *Journal of Sound and Vibration*, 329:4772–4784, 2010.

[54] T. Musil. *Paralelní programování v dynamice rotorů s hydrodynamickými ložisky*. PhD thesis, Vysoká škola báňská, Technická univerzita Ostrava, 2008.

[55] Roy R. Craig, Jr., and Ching-Jone Chang. A review of substructure coupling methods for dynamic analysis. Technical report, NASA. Langley Res. Center Advan. in Eng. Sci, 1976.

[56] A. Shanmugam and Chandramouli Padmanabhan. fixedfree interface component mode synthesis method for rotordynamic analysis. *Journal of Sound and Vibration*, 297:664–679, 2006.

[57] Xiao-Li Wang, Ke-Qin Zhu, and Shi-Zhu Wen. On the performance of dynamically loaded journal bearings lubricated with couple stress fluids. *Tribology International*, 35:185–191, 2002.

[58] K . Hu, N. Vlahopoulos, and Z. P. Mourelatos. A finite element formulation for coupling rigid and flexible body dynamics of rotating beams. *Journal of Sound and vibration*, 253:603–630, 2002.

[59] Jeffrey A. Morgan, Christophe Pierre, and Gregory M. Hulbert. Basebandmethodsof componentmode synthesis for non-proportionally damped systems. *Mechanical Systems and Signal Processing*, 17:589–598, 2003.

[60] Cheng-Ying Lo, Cheng-Chi Wang, and Yu-Han Lee. Performance analysis of high-speed spindle aerostatic bearings. *Tribology International*, 38:5–14, 2005.

[61] M.F. Chen, Y.P. Chen, and C.D. Lin. Research on the arc type aerostatic bearing for a PCB drilling station. *Tribology International*, 35:235–243, 2002.

[62] G. Belforte, T. Raparelli, V. Viktorov, and A. Trivella. Discharge coefficients of orifice-type restrictor for aerostatic bearings. *Tribology International*, 40:512–521, 2007.

[63] Xue-Dong Chen and Xue-Ming He. The effect of the recess shape on performance analysis of the gas-lubricated bearing in optical lithography. *Tribology International*, 39:1336–1341, 2006.

[64] Antonín Skarolek. Model of rotor supported in aerostatic journal bearings. In *Proceedings of 9th International Scientific Conference Applied Mechanics*, Malenovice, Czech Republic, 2007. ISBN 978-80-248-1389-9.

[65] Antonín Skarolek and Jan Kozánek. Computation of dynamic properties of aerostatic journal bearings. In *Proceedings of National Conference with International Participation Engineering Mechanics*, Svratka, Czech Republic, 2007. ISBN 978-80-87012-06-2.

[66] Jan Kozánek and Ladislav Půst. Spectral properties and identification of aerostatic bearings. *Acta Mech Sin*, 27:63–67, 2011.

[67] J. Kozánek, J. Šimek, P. Steinbauer, and et. al. Identification of aerostatic journal bearing stiffness and damping. In *Proceedings of Colloquium Dynamics of Machines*, Prague, Czech Republic, 2009.

[68] Jan Kozánek and Ladislav Půst. Spectral properties and dynamic characteristics of aerostatic bearings. In *Proceedings of 10th Conference on Dynamical Systems Theory and Applications*, Lodz, Poland, 2009.

[69] R. W. Lewis, P. Nithiarasu, and K. N. Seetharamu. *Fundamentals of the finite element method for heat and fluid flow*. John Willey & Sons Ltd, 2005. ISBN 0-470-84789-1.

Antonín Skarolek

Education

Since 2005: Doctoral study programme, Ph.D (PhD) in Applied Mechanics, Faculty of Mechanical Engineering, Technical University of Liberec

1999–2005: Master study programme, Ing. (MSc), Mechanical Engineering, Faculty of Mechanical Engineering, Technical University of Liberec

Professional Experience

Since April 2010: Department of Mechanics and Elasticity, Faculty of Mechanical Engineering, Technical University of Liberec

Since April 2010: R&D Mechanical/Stress Analyst, VÚTS, a.s, (Research Institute of Textile Machines), Liberec, Czech Republic

March 2008–March 2010: Engineer-Rotor Systems, Cummins Turbo Technologies, Huddersfield, United Kingdom

July 2006–July 2007: R&D Mechanical/Stress Analyst, VÚTS, a.s, (Research Institute of Textile Machines), Liberec, Czech Republic

Publications

L. Pešík and A. Skarolek. Tuning of vibration isolation differential pneumatic system by means of throttle valve. *Transactions of the Universities of Košice: Research reports from the Universities of Košice* 2nd edition. Technical University in Košice, p: 191–196, 2011. ISSN 1335-2334

L. Pešík and A. Skarolek. Variable stiffness of resilient pneumatic support. *Pneumatyka: Przemysłowe systemy sprężonego powietrza* 78:25–27, 2011. ISSN 1426-6644

J. Cerman, P. Špatenka, A. Maková, A. Skarolek. Comparison of mechanical properties of hard and wear resistant films on forms for polymer processing. *Czechoslovak Journal of Physics*, V. 56, Supplement 2, 2006. ISSN 0011-4626 (Print) 1572-9486 (Online)

L. Pešík and A. Skarolek. Aplikace kyvadlového eliminátoru torzních kmitů. *Acta Mechanica Slovaca*, 9:161–164, 2005. ISSN 1335-2393. [In Czech]

A. Skarolek. Reduction of defective gyroscopic rotor system models: Modal partial decoupling versus component mode synthesis. In: *Computational Mechanics 2011*, Pilsen, Czech Republic, 2011. ISBN 978-80-261-0027-0

A. Skarolek, M. Pustka, N. Pomp. HDL model of machine tool slideway. In: *Engineering Mechanics 2011*, Svratka, Czech Republic, 2011. ISBN 978-80-87012-33-8

A. Skarolek and J. Kozánek. Computation of Dynamic Properties of Aerostatic Journal Bearings. In: *Engineering Mechanics 2007*, Svratka, Czech Republic, May 14—17, 2007. ISBN 978-80-87012-06-2.

A. Skarolek. Model of Rotor Supported in Aerostatic Journal Bearings. In: *Applied Mechanics 2007*, Malenovice, Czech Republic, 2007. ISBN 978-80-248-1389-9.

J. Šklíba, M. Sivčák and A. Skarolek On the stability of a vibroisolation system with more degrees of freedom. In: *Conference on Vibration Problems ICOVP 2005*, Springer proceedings in physics, Vol. 111, 2007, XVIII. ISBN: 978-1-4020-5400-6

L. Pešík, A. Skarolek, M. Vančura et al. Podstavec sedadla řidiče se řízenou zatěžovací charakteristikou. In: *Sborník referátů: 52. Konference kateder částí a mechanismů strojů s mezinárodní účastí.* Vysoká škola báňská – Technická univerzita Ostrava, 2011, ISBN 978-80-248-2450-5. [In Czech]

A. Skarolek and J. Kozánek Matematický model radiálních aerostatických ložisek v interakci s rotorem. In: *Interakce a zpětné vazby '2006*, ÚT AVČR, Praha, ISBN: 80-87012-02-X. [In Czech]

J. Mevald and A. Skarolek Deterministický chaos u modelu mechanického systému s vůlemi. In: *Teorie strojů a mechanismů*, TUL, Liberec, ISBN: 80-7083-847-7. [In Czech]

Appendices

Appendix A

Quasistatic Timoshenko Shaft Finite Element

Slopes of deflection curves v, w consist of two components of cross section lateral rotations

$$\frac{\mathrm{d}v}{\mathrm{d}x} = \psi + \delta_v, \quad \frac{\mathrm{d}w}{\mathrm{d}x} = -\vartheta + \delta_w \tag{A.1}$$

Shear and bending angles are coupled by relation (2.5) in the case of static deflection. Slopes of shaft deflection can be then written as

$$\frac{\mathrm{d}v}{\mathrm{d}x} = \psi - \frac{EJ}{\kappa GA}\frac{\mathrm{d}^2\psi}{\mathrm{d}x^2}, \quad \frac{\mathrm{d}w}{\mathrm{d}x} = -\vartheta - \frac{EJ}{\kappa GA}\frac{\mathrm{d}^2\vartheta}{\mathrm{d}x^2}. \tag{A.2}$$

Actual angles of shaft cross section rotations ψ, ϑ are taken as independent state variables and are approached by quadratic polynomial

$$\psi(x) = \frac{\mathrm{d}\,\mathbf{P}_3}{\mathrm{d}x}\,\mathbf{c}_1, \quad \vartheta(x) = -\frac{\mathrm{d}\,\mathbf{P}_3}{\mathrm{d}x}\,\mathbf{c}_2, \quad \mathbf{P}_3 = (1, x, x^2, x^3). \tag{A.3}$$

Displacements v and w now involve bending and shear deformations

$$v(x) = \left(\mathbf{P}_3 - \beta\frac{\mathrm{d}^2\mathbf{P}_3}{\mathrm{d}x^2}\right)\mathbf{c}_1, \quad w(x) = \left(\mathbf{P}_3 + \beta\frac{\mathrm{d}^2\mathbf{P}_3}{\mathrm{d}x^2}\right)\mathbf{c}_2, \tag{A.4}$$

where

$$\beta = \frac{EJ}{\kappa GA}. \tag{A.5}$$

Vector of nodal displacements in terms of selected state variables is

$$\mathbf{q}^e = (\mathbf{q}_1^{\mathrm{T}}, \mathbf{q}_2^{\mathrm{T}})^{\mathrm{T}}, \tag{A.6}$$

where

$$\mathbf{q}_1^{\mathrm{T}} = \begin{pmatrix} v(0) & \psi(0) & v(l) & \psi(l) \end{pmatrix}, \quad \mathbf{q}_2^{\mathrm{T}} = \begin{pmatrix} w(0) & \vartheta(0) & w(l) & \vartheta(l) \end{pmatrix}. \tag{A.7}$$

Relation between nodal values and coefficients $\mathbf{c}_i$ of basis polynomials is given by linear transformation

$$\mathbf{q}_i = \mathbf{S}_{i\beta}\,\mathbf{c}_i, \tag{A.8}$$

where

$$\mathbf{S}_{1\beta} = \begin{pmatrix} 1 & 0 & -2\beta & 0 \\ 0 & 1 & 0 & 0 \\ 1 & l & l^2 - 2\beta & l^3 - 6l\beta \\ 0 & 1 & 2l & 3l^2 \end{pmatrix}, \quad \mathbf{S}_{2\beta} = \begin{pmatrix} 1 & 0 & 2\beta & 0 \\ 0 & -1 & 0 & 0 \\ 1 & l & l^2 + 2\beta & l^3 + 6l\beta \\ 0 & -1 & -2l & -3l^2 \end{pmatrix}. \tag{A.9}$$

Shaft deflection is now determined by means of nodal values as

$$\begin{aligned} v(x) &= \left(\mathbf{P}_3 - \beta \frac{\mathrm{d}^2 \mathbf{P}_3}{\mathrm{d}x^2} \right) \mathbf{S}_{1\beta}^{-1} \mathbf{q}_1, & w(x) &= \left(\mathbf{P}_3 + \beta \frac{\mathrm{d}^2 \mathbf{P}_3}{\mathrm{d}x^2} \right) \mathbf{S}_{2\beta}^{-1} \mathbf{q}_2, \\ \psi(x) &= \frac{\mathrm{d}\mathbf{P}_3}{\mathrm{d}x} \mathbf{S}_{1\beta}^{-1} \mathbf{q}_1, & \vartheta(x) &= -\frac{\mathrm{d}\mathbf{P}_3}{\mathrm{d}x} \mathbf{S}_{2\beta}^{-1} \mathbf{q}_2. \end{aligned} \tag{A.10}$$

Potential strain energy of shaft element contains both the bending and the shear components

$$\begin{aligned} U^e = &\frac{1}{2} \int_0^l E\, J(x) \left[\left(\frac{\partial\, \psi}{\partial\, x} \right)^2 + \left(\frac{\partial\, \vartheta}{\partial\, x} \right)^2 \right] \mathrm{d}x \\ &+ \frac{1}{2} \int_0^l \kappa\, G\, A(x) \left[\left(\frac{\partial\, v}{\partial\, x} - \psi \right)^2 + \left(\frac{\partial\, w}{\partial\, x} + \vartheta \right)^2 \right] \mathrm{d}x. \end{aligned} \tag{A.11}$$

Kinetic energy of the element:

$$\begin{aligned} T^e = &\frac{1}{2} \int_0^l \rho\, A(x) \left(\dot{v}^2 + \dot{w}^2 \right) \mathrm{d}x + \frac{1}{2} \int_0^l \rho\, J(x) \left(\dot{\psi}^2 + \dot{\vartheta}^2 \right) \mathrm{d}x \\ &+ \frac{1}{2} \int_0^l \rho\, J_p(x)\, \omega_0 \left(2\, \dot{\vartheta}\, \psi + 1 \right) \mathrm{d}x. \end{aligned} \tag{A.12}$$

Equations of motion of single finite element are obtained by means of Lagrange equations

$$\frac{\mathrm{d}}{\mathrm{d}t} \left(\frac{\partial T^e}{\partial \dot{\mathbf{q}}^e} \right) - \frac{\partial T^e}{\partial \mathbf{q}^e} + \frac{\partial U^e}{\partial \mathbf{q}^e} = \mathbf{M}_\beta^e\, \ddot{\mathbf{q}}^e + \omega_0\, \mathbf{G}_\beta^e\, \dot{\mathbf{q}}^e + \mathbf{K}_\beta^e\, \mathbf{q}^e \tag{A.13}$$

providing local stiffness matrix

$$\begin{aligned} &\mathbf{K}_\beta^e = \begin{pmatrix} \mathbf{S}_{1\beta}^{-\mathrm{T}} \left(\mathbf{I}_3 + \mathbf{I}_{3\beta} \right) \mathbf{S}_{1\beta}^{-1} & \mathbf{0} \\ \mathbf{0} & \mathbf{S}_{2\beta}^{-\mathrm{T}} \left(\mathbf{I}_3 + \mathbf{I}_{3\beta} \right) \mathbf{S}_{2\beta}^{-1} \end{pmatrix}, \qquad \mathbf{I}_3 = \int_0^l E\, J(x) \frac{\mathrm{d}^2 \mathbf{P}_3}{\mathrm{d}x^2}^{\mathrm{T}} \frac{\mathrm{d}^2 \mathbf{P}_3}{\mathrm{d}x^2} \mathrm{d}x, \\ &\mathbf{I}_{3\beta} = \int_0^l \kappa G A(x) \beta^2 \frac{\mathrm{d}^3 \mathbf{P}_3}{\mathrm{d}x^3}^{\mathrm{T}} \frac{\mathrm{d}^3 \mathbf{P}_3}{\mathrm{d}x^3} \mathrm{d}x, \end{aligned} \tag{A.14}$$

gyroscopic matrix:

$$\mathbf{G}_\beta^e = \begin{pmatrix} \mathbf{0} & 2\mathbf{S}_{1\beta}^{-\mathrm{T}} \mathbf{I}_2 \mathbf{S}_{2\beta}^{-1} \\ -2\mathbf{S}_{2\beta}^{-\mathrm{T}} \mathbf{I}_2 \mathbf{S}_{1\beta}^{-1} & \mathbf{0} \end{pmatrix}, \quad \mathbf{I}_2 = \int_0^l \rho\, J(x) \frac{\mathrm{d}\, \mathbf{P}_3}{\mathrm{d}x}^{\mathrm{T}} \frac{\mathrm{d}\, \mathbf{P}_3}{\mathrm{d}2}\, \mathrm{d}x, \tag{A.15}$$

and mass matrix

$$\mathbf{M}^e_\beta = \begin{pmatrix} \mathbf{S}_{1\beta}^{-\mathrm{T}} \left(\mathbf{I}_{1\beta} + \mathbf{I}_2\right) \mathbf{S}_{1\beta}^{-1} & \mathbf{0} \\ \mathbf{0} & \mathbf{S}_{2\beta}^{-\mathrm{T}} \left(\mathbf{I}_{2\beta} + \mathbf{I}_2\right) \mathbf{S}_{2\beta}^{-1} \end{pmatrix},$$
$$\mathbf{I}_{1\beta} = \int_0^l \rho\, A(x) \left(\mathbf{P}_3 - \beta \frac{\mathrm{d}^2 \mathbf{P}_3}{\mathrm{d}x}\right)^{\mathrm{T}} \left(\mathbf{P}_3 - \beta \frac{\mathrm{d}^2 \mathbf{P}_3}{\mathrm{d}x}\right) \mathrm{d}x,$$
$$\mathbf{I}_{2\beta} = \int_0^l \rho\, A(x) \left(\mathbf{P}_3 + \beta \frac{\mathrm{d}^2 \mathbf{P}_3}{\mathrm{d}x}\right)^{\mathrm{T}} \left(\mathbf{P}_3 + \beta \frac{\mathrm{d}^2 \mathbf{P}_3}{\mathrm{d}x}\right) \mathrm{d}x. \tag{A.16}$$

Assuming prismatic shaft element, integrals $\mathbf{I}_{1\beta}$, $\mathbf{I}_{2\beta}$, $\mathbf{I}_2$, $\mathbf{I}_3$ and $\mathbf{I}_{3\beta}$ can be evaluated in closed form in advance

$$\mathbf{I}_{1\beta} = \rho A l \begin{pmatrix} 1 & l/2 & l^2/3 - 2\beta & l\left(l^2 - 12\beta\right)/4 \\ & l^2/3 & l\left(l^2 - 4\beta\right)/4 & l^2\left(l^2 - 10\beta\right)/5 \\ & & l^4/5 - 4\beta l^2/3 + 4\beta^2 & l\left(l^4 - 12\beta l^2 + 36\beta^2\right)/6 \\ sym. & & & l^2\left(5l^4 - 84\beta l^2 + 420\beta^2\right)/35 \end{pmatrix},$$
$$\mathbf{I}_{2\beta} = \rho A l \begin{pmatrix} 1 & l/2 & l^2/3 + 2\beta & l\left(l^2 + 12\beta\right)/4 \\ & l^2/3 & l\left(l^2 + 4\beta\right)/4 & l^2\left(l^2 + 10\beta\right)/5 \\ & & l^4/5 + 4\beta l^2/3 + 4\beta^2 & l\left(l^4 + 12\beta l^2 + 36\beta^2\right)/6 \\ sym. & & & l^2\left(5l^4 + 84\beta l^2 + 420\beta^2\right)/35 \end{pmatrix},$$
$$\mathbf{I}_2 = \rho J l \begin{pmatrix} 0 & 0 & 0 & 0 \\ & 1 & l & l^2 \\ & & 4l^2/3 & 3l^3/2 \\ sym. & & & 9l^4/5 \end{pmatrix}, \tag{A.17}$$
$$\mathbf{I}_3 = EJl \begin{pmatrix} 0 & 0 & 0 & 0 \\ & 0 & 0 & 0 \\ & & 4 & 6l \\ sym. & & & 12l^2 \end{pmatrix}, \qquad \mathbf{I}_{3\beta} = \kappa G A l \begin{pmatrix} 0 & 0 & 0 & 0 \\ & 0 & 0 & 0 \\ & & 0 & 0 \\ sym. & & & 36\beta^2 \end{pmatrix}.$$

For convenience, parameter β can be substituted by

$$\beta = \frac{l^2}{12}\Phi, \quad \Phi = \frac{12EJ}{\kappa G A l^2}. \tag{A.18}$$

When β=0 (Φ=0), then Timoshenko $\mathbf{K}^e_\beta$, $\mathbf{G}^e_\beta$, $\mathbf{M}^e_\beta$ and Rayleigh $\mathbf{K}^e$, $\mathbf{G}^e$,$\mathbf{M}^e$ matrices become identical. Transformation by means of matrix $\mathbf{T}$ (1.69) provides local matrices in global coordinates of nodal displacements

$$\tilde{\mathbf{q}}^e = (v(0),\, \psi(0),\, w(0),\, \vartheta(0),\, v(l),\, \psi(l),\, w(l),\, \vartheta(l))^{\mathrm{T}}. \tag{A.19}$$

Appendix B

Classification of Rotor Vibration Modes

Complex eigenvectors describing vibration modes (higher than rigid ones) of rotor can be of four kinds: Planar bending, Forward whirl, Backward whirl and Mixed whirl. One method to determine which type particular eigenvector $\mathbf{v}$ belongs to is to assess motion orbit $\mathbf{v} \cdot \mathrm{e}^{j\omega t}$ of each node separately, and decide as follows

1. Planar bending: All nodes follow linear trajectories
2. Forward whirl: All nodes follow elliptic trajectories in the same direction as $(1, -j)^{\mathrm{T}} \mathrm{e}^{j\omega t}$
3. Backward whirl: All nodes follow elliptic trajectories in oposite direction to $(1, -j)^{\mathrm{T}} \mathrm{e}^{j\omega t}$
4. Mixed whirl: Nodes follow elliptic trajectories, only part of them in the same direction as $(1, -j)^{\mathrm{T}} \mathrm{e}^{j\omega t}$

Orbit trajectory of i-th node is

$$y(t) = \mathrm{Re}\left(\hat{v}_i \cdot \mathrm{e}^{j\omega t}\right), \quad z(t) = \mathrm{Re}\left(\hat{w}_i \cdot \mathrm{e}^{j\omega t}\right), \tag{B.1}$$

where $\hat{v}$ and $\hat{w}$ are components of eigenvector $\mathbf{v}$. Substitutions $\hat{v}_i = v \cdot \mathrm{e}^{j\phi_v}$ and $\hat{w}_i = w \cdot \mathrm{e}^{j\phi_w}$ to (B.1) renders the orbit trajectory as parametric equations of ellipse

$$y(t) = v \cos\left(\omega t + \phi_v\right), \quad z(t) = w \cos\left(\omega t + \phi_w\right).$$

Phase difference between cosines determines following possibilities ($\mathbb{Z}$ denotes the set of whole numbers)

$$\phi_w - \phi_v \in \begin{cases} n\pi, \quad n \in \mathbb{Z}; & \text{Ellipse degenerated into line segment} \\ \left((2n-1)\pi, 2n\pi\right), n \in \mathbb{Z}; & \text{Forward (anti-clockwise) rotation of vector } (y, z)^{\mathrm{T}} \\ \left(2n\pi, (2n+1)\pi\right), n \in \mathbb{Z}; & \text{Backward (clockwise) rotation of vector } (y, z)^{\mathrm{T}} \end{cases}$$

Appendix C

Dynamic Parameters of Bearings

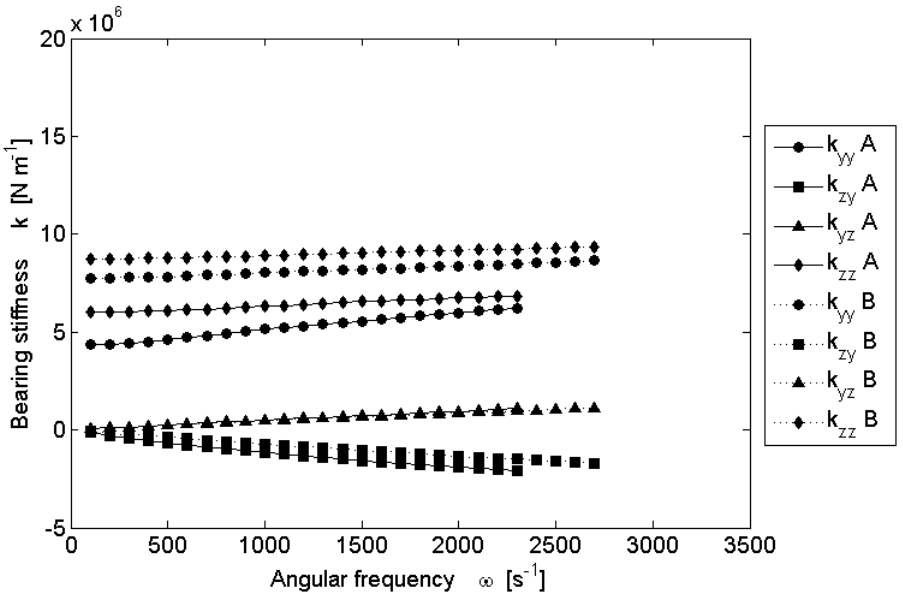

Figure C.1: Translational stiffness v. angular velocity of journal ω, Bearing design A&B, Supply pressure $p_s = 0.4$MPa

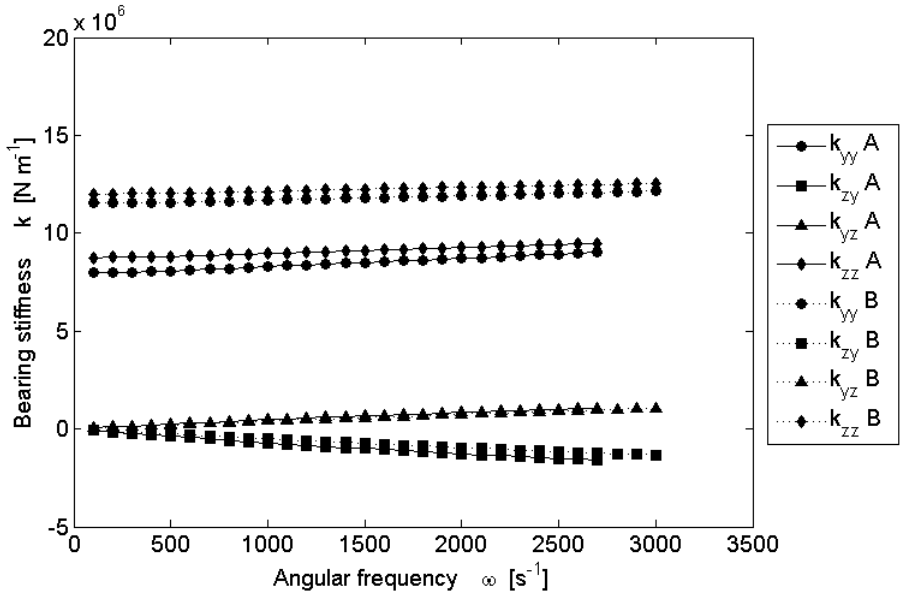

Figure C.2: Translational stiffness v. angular velocity of journal ω, Bearing design A&B, Supply pressure $p_s = 0.5$MPa

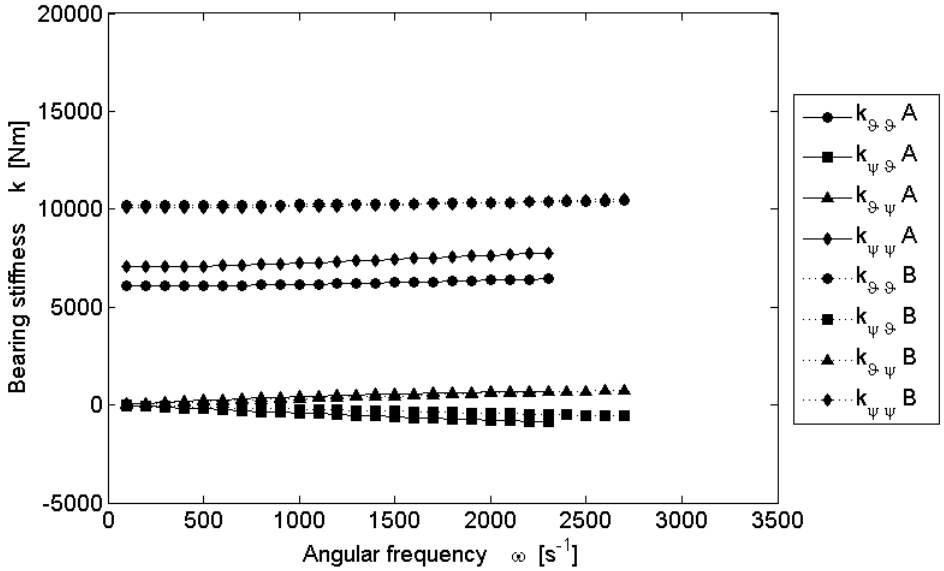

Figure C.3: Angular stiffness v. angular velocity of journal ω, Bearing design A&B, Supply pressure $p_s = 0.4$MPa

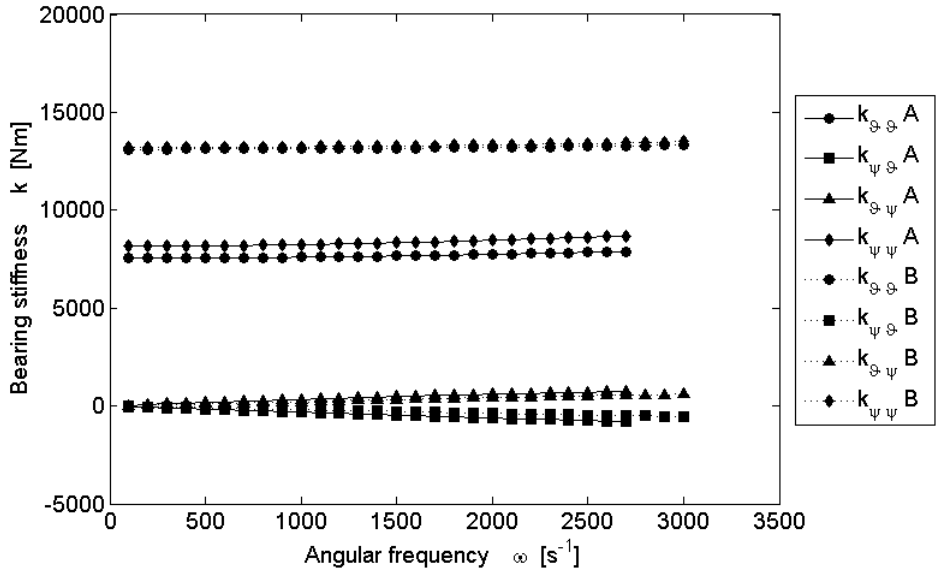

Figure C.4: Angular stiffness v. angular velocity of journal ω, Bearing design A&B, Supply pressure $p_s = 0.5$MPa

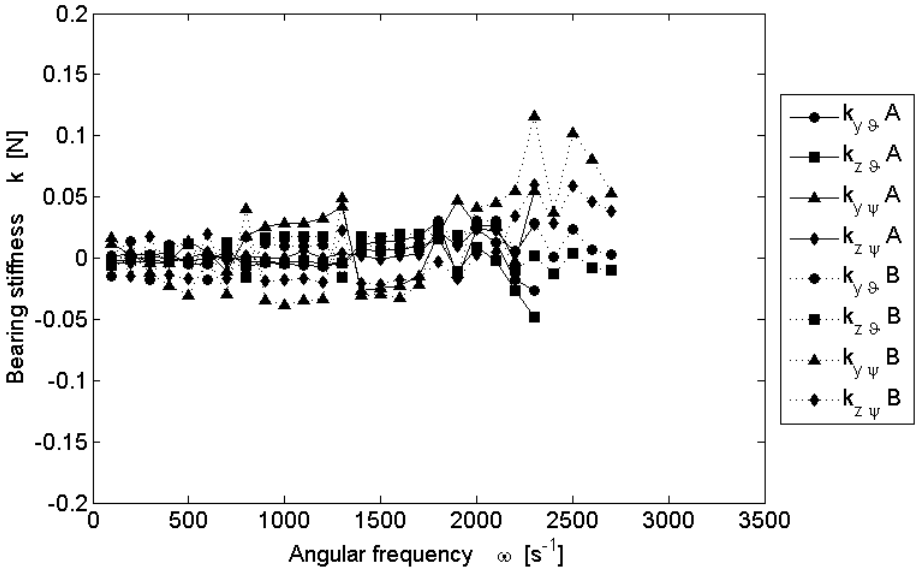

Figure C.5: Cross-coupling stiffness v. angular velocity of journal ω, Bearing design A&B, Supply pressure $p_s = 0.4$MPa

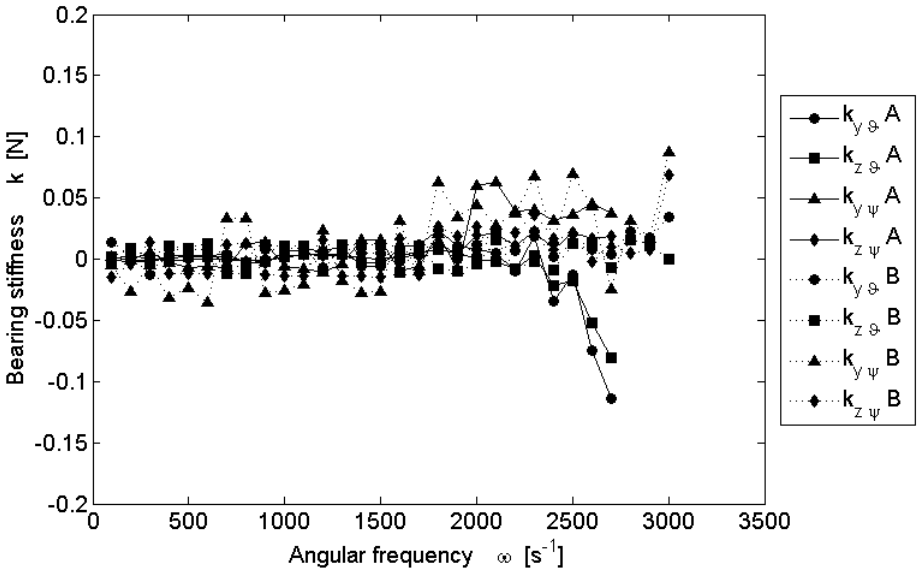

Figure C.6: Cross-coupling stiffness v. angular velocity of journal ω, Bearing design A&B, Supply pressure $p_s = 0.5$MPa

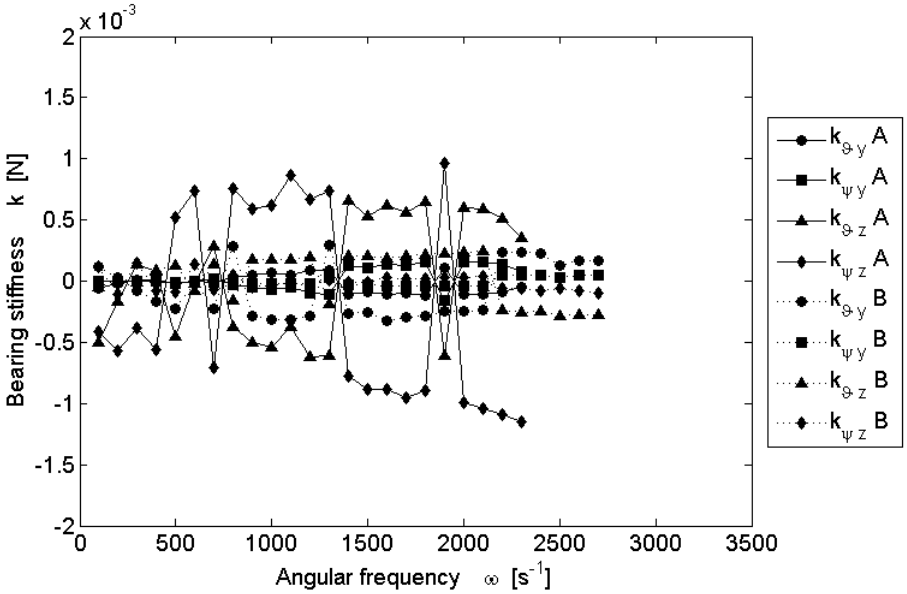

Figure C.7: Cross-coupling stiffness v. angular velocity of journal ω, Bearing design A&B, Supply pressure $p_s = 0.4$MPa

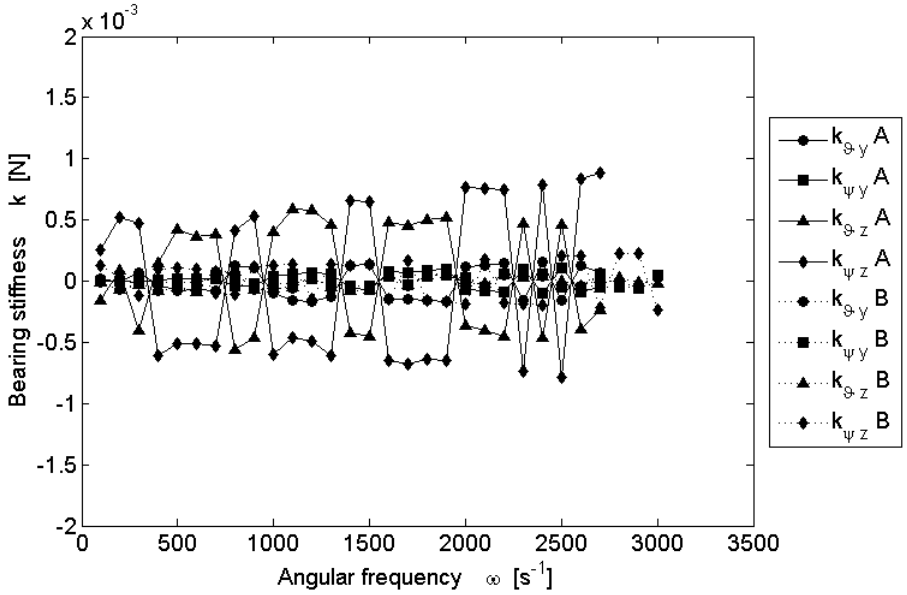

Figure C.8: Cross-coupling stiffness v. angular velocity of journal ω, Bearing design A&B, Supply pressure $p_s = 0.5$MPa

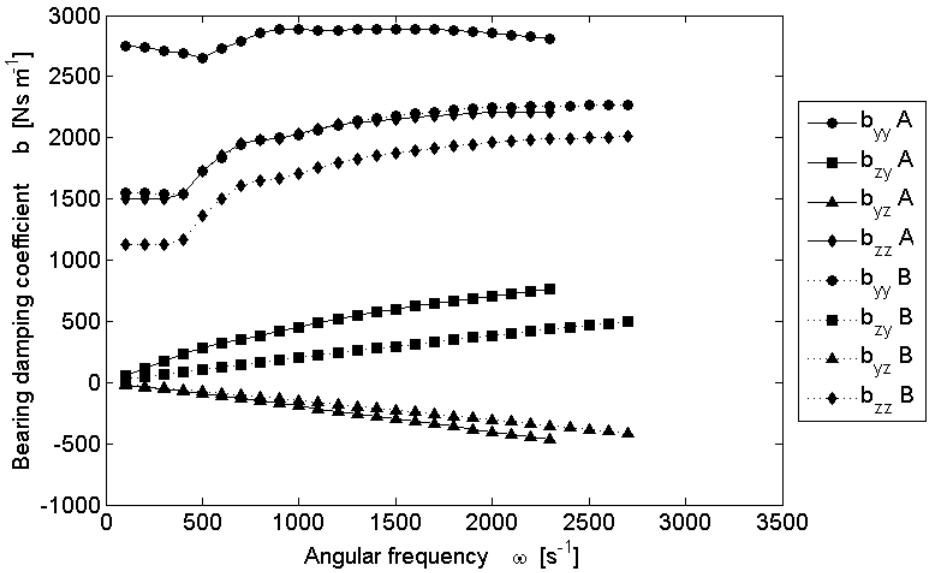

Figure C.9: Translational damping coeff. v. angular velocity of journal ω, Bearing design A&B, Supply pressure $p_s = 0.4$MPa

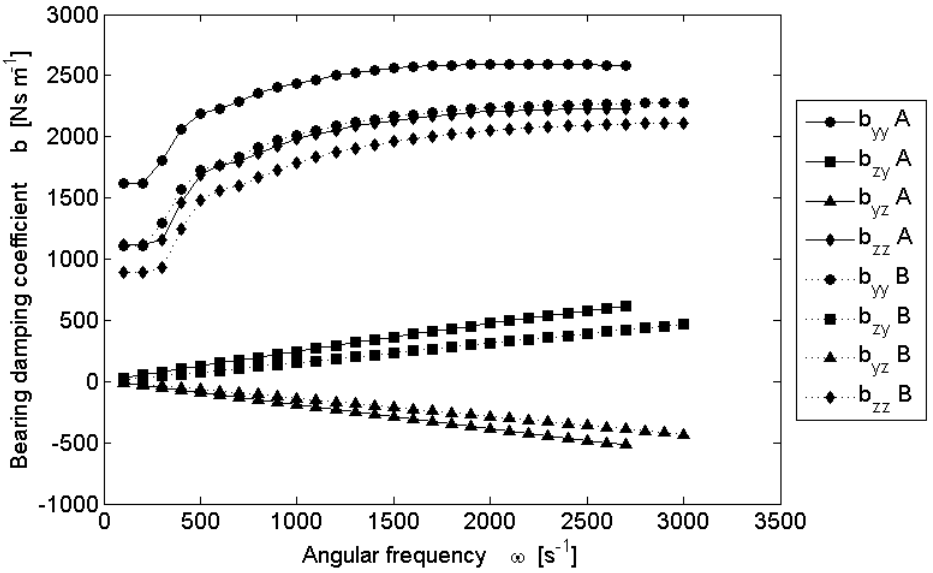

Figure C.10: Translational damping coeff. v. angular velocity of journal ω, Bearing design A&B, Supply pressure $p_s = 0.5$MPa

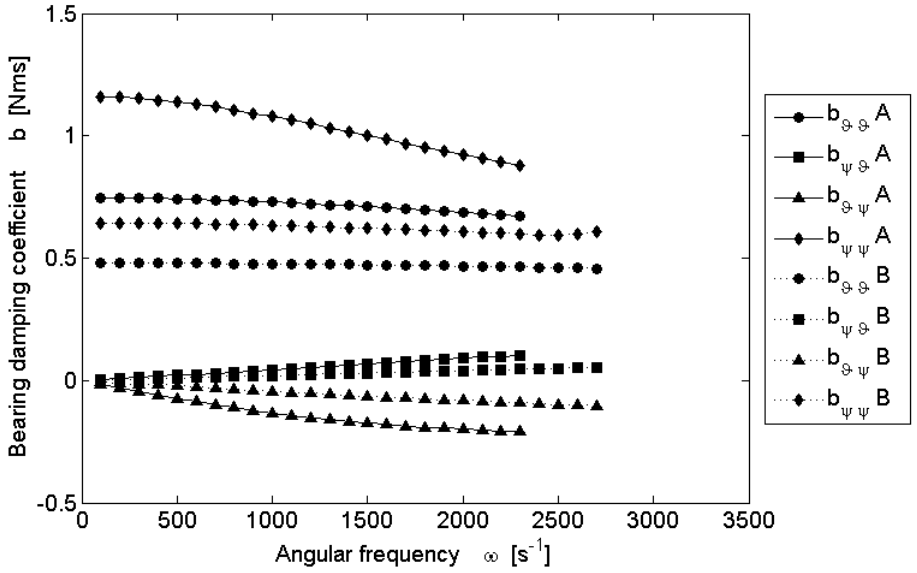

Figure C.11: Angular damping coeff. v. angular velocity of journal ω, Bearing design A&B, Supply pressure $p_s = 0.4$MPa

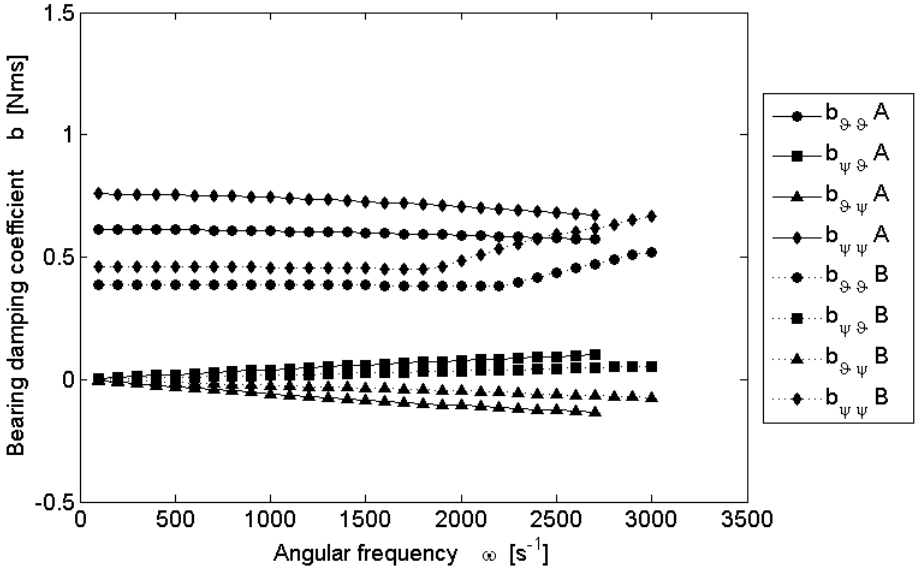

Figure C.12: Angular damping coeff. v. angular velocity of journal ω, Bearing design A&B, Supply pressure $p_s = 0.5$MPa

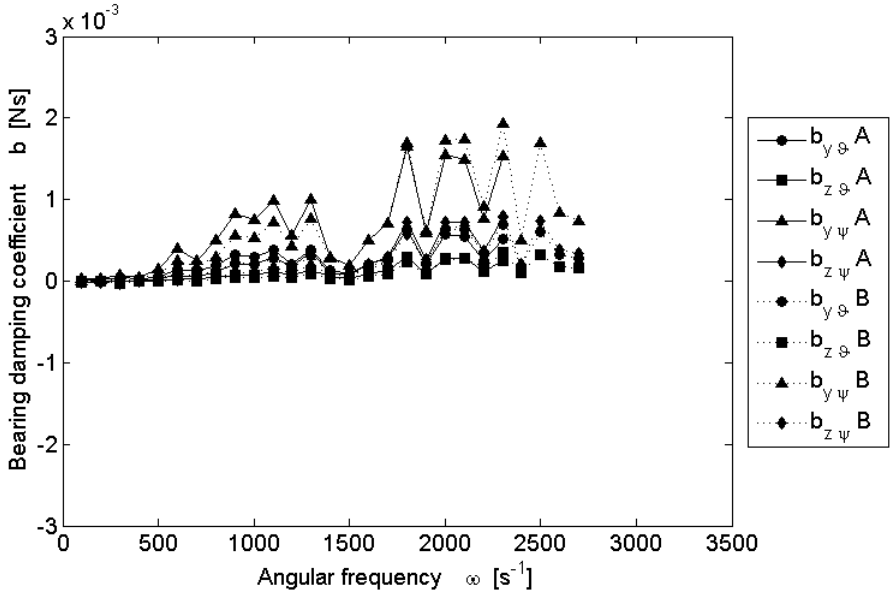

Figure C.13: Cross-coupling damping coeff. v. angular velocity of journal ω, Bearing design A&B, Supply pressure $p_s = 0.4$MPa

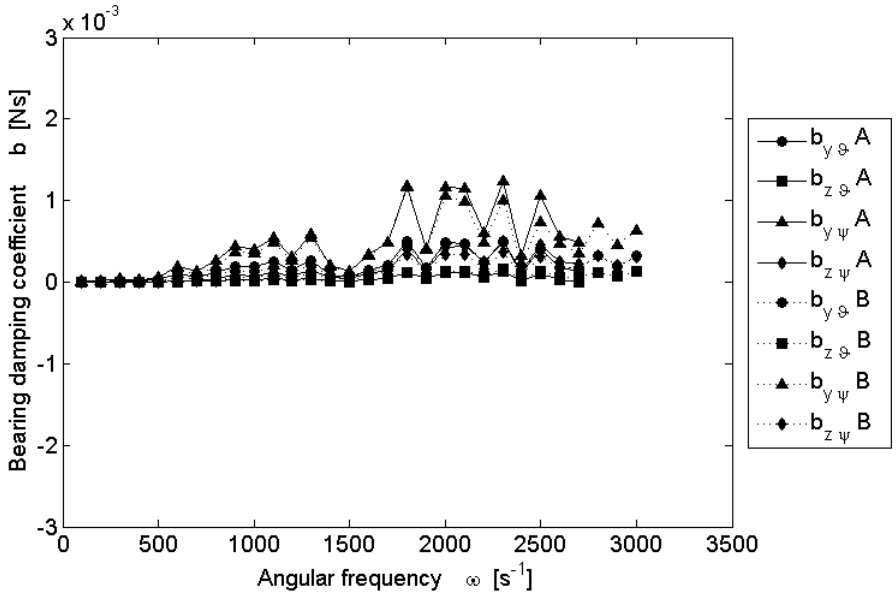

Figure C.14: Cross-coupling damping coeff. v. angular velocity of journal ω, Bearing design A&B, Supply pressure $p_s = 0.5$MPa

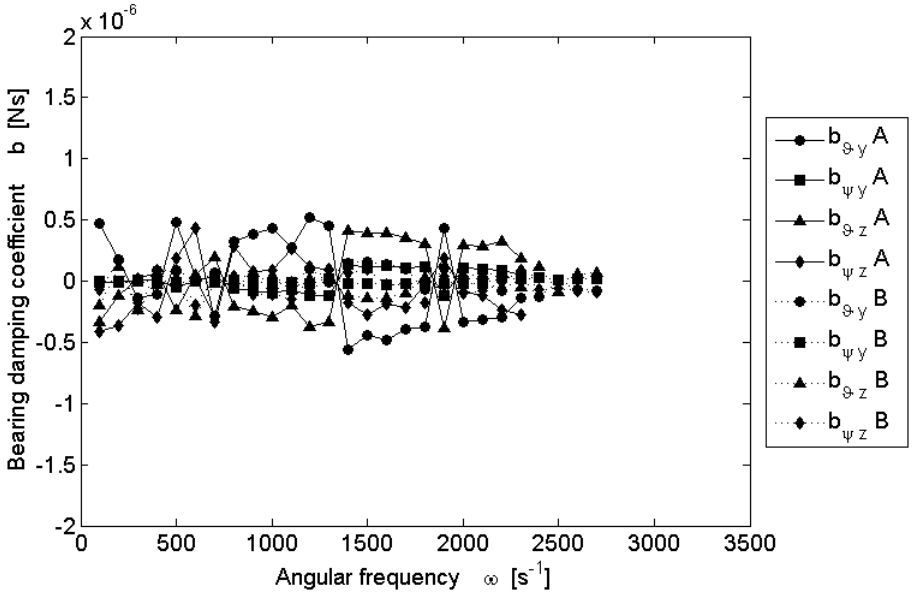

Figure C.15: Cross-coupling damping coeff. v. angular velocity of journal ω, Bearing design A&B, Supply pressure $p_s = 0.4$MPa

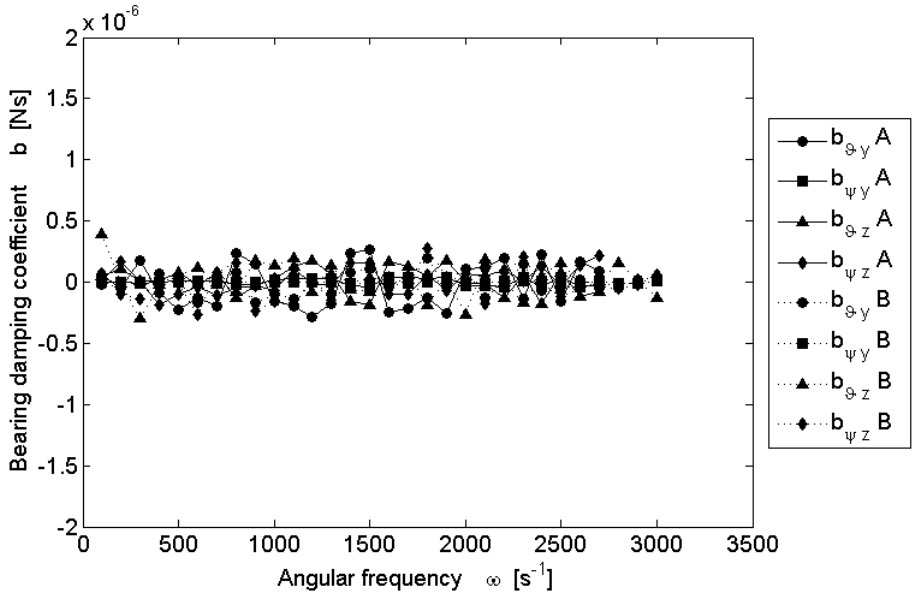

Figure C.16: Cross-coupling damping coeff. v. angular velocity of journal ω, Bearing design A&B, Supply pressure $p_s = 0.5$MPa